International Year of
CHEMISTRY
2011

Journal of the Serbian Chemical Society

Available on line at

СХД
1897

www.shd.org.rs/JSCS/

CONTENTS

Available online at www.shd.org.rs/JSCS/

Thiazolidin-4-one, azetidin-2-one and 1,3,4-oxadiazole derivatives of isonicotinic acid hydrazide: synthesis and their biological evaluation

SADAF J. GILANI[1,2]*, SUROOR A. KHAN[1], OZAIR ALAM[1], VIJENDER SINGH[2] and ALKA ARORA[2]

[1]*Department of Pharmaceutical Chemistry, Faculty of Pharmacy, Jamia Hamdard, New Delhi-110062 and* [2]*Department of Pharmaceutical Chemistry, KIET School of Pharmacy, Ghaziabad, U.P. 201206, India*

Abstract: A series of thiazolidin-4-one (**2a**–**h**; **3a**–**h**), azetidin-2-one (**4a**–**h**) and 1,3,4-oxadiazole (**5a**–**h**) derivatives of isoninicotinic acid hydrazide (INH) were synthesized in order to obtain new compounds with potential anti-inflammatory, analgesic, ulcerogenic and lipid peroxidation activities. The structures of the new compounds were supported by their IR, ^{1}H-NMR and mass spectral data. All compounds were evaluated for their anti-inflammatory activity by the carrageenan-induced rat paw edema test method. Eleven of the new compounds, out of 32, showed very good anti-inflammatory activity in the carrageenan-induced rat paw edema test, with significant analgesic activity in the tail immersion method together with negligible ulcerogenic action. The compounds, which showed less ulcerogenic action, also showed reduced malondialdehyde content (MDA), which is one of the by-products of lipid peroxidation. The study showed that the compounds inhibited the induction of gastric mucosal lesions and it can be suggested from the results that their protective effects may be related to inhibition of lipid peroxidation in the gastric mucosa.

Keywords: anti-inflammatory activity; analgesic activity; ulcerogenic activity; lipid peroxidation.

INTRODUCTION

The currently available non-steroidal anti-inflammatory drugs (NSAIDs), such as ibuprofen, flurbiprofen, fenbufen and naproxen, exhibit gastric toxicity. Long-term use of these drugs has been associated with gastro-intestinal (GI) ulceration, bleeding and nephrotoxicity.[1] The pharmacological activity of NSAIDs is related to the suppression of prostaglandin biosynthesis from arachidonic acid

---

by inhibiting the enzyme cyclooxygenases (COXs).[2,3] Recently, it was discovered that COX exists in two isoforms, COX-1 and COX-2, which are regulated differently.[4–6] COX-1 provides cytoprotection in the gastrointestinal (GI) tract, whereas inducible COX-2 mediates inflammation.[7–9] Since most of the NSAIDs on the market show greater selectivity for COX-1 than COX-2,[10] chronic use of NSAIDs may elicit appreciable GI irritation, bleeding and ulceration.

The GI damage from NSAIDs is generally attributed to two factors, *i.e.*, local irritation by the carboxylic acid moiety common to most NSAIDs (topical effect); and decreased tissue prostaglandin production, which undermines the physiological role of the cytoprotective prostaglandins in maintaining GI health and homeostasis.[11] The incidence of clinically significant GI side effects due to NSAIDs is high (30 %) and causes some patients to abandon NSAID therapy.[12] Thus, the discovery of COX-2 provided the rationale for the development of drugs devoid of GI disorders while retaining clinical efficacy as anti-inflammatory agents. However, recent reports showed that selective COX-2 inhibitors (coxibs) could lead to adverse cardiovascular effects.[13] Therefore, the development of novel compounds having anti-inflammatory and analgesic activity with improved safety profiles is still a necessity.

Synthetic approaches based on chemical modification of NSAIDs have been undertaken with the aim of improving their safety profiles. A literature survey revealed that derivatization of the carboxylate function of NSAIDs resulted in retained anti-inflammatory activity with reduced ulcerogenic potential.[14–17] It has also been reported in the literature that certain compounds bearing a thiazolidin-4-one, azetidin-2-one or 1,3,4-oxadiazole nucleus possess significant anti-inflammatory activity.[18–20]

In view of the important biological properties of the thiazolidin-4-one, azetidin-2-one and 1,3,4-oxadiazole nuclei, it was planned to suitably incorporate the above-mentioned ring systems into the isoniazide moiety to explore the possibilities of some altered biological actions. Hence, the thiazolidin-4-one, azetidin-2-one and 1,3,4-oxadiazole derivatives reported herein were designed and synthesized. They were found to possess an interesting profile of anti-inflammatory and analgesic activity with significant reduction in their ulcerogenic risks to the stomach.

EXPERIMENTAL

Materials, methods and instrumentation

All the solvents were of AR grade and were obtained from Merck, CDH and S.D. Fine chemicals. Melting points were determined in open capillary tubes and are uncorrected. All the compounds were subjected to elemental analysis (CHN) and the measured values agreed within ±0.4 % with the calculated ones. Thin layer chromatography was performed on silica gel G (Merck). The spots were developed in an iodine chamber and visualized with an ultraviolet lamp. The solvent systems used were benzene:acetone (8:2, v/v) and toluene:ethyl ace-

tate:formic acid (5:4:1, v/v). Ashless Whatman No. 1 filter paper was used for vacuum filtration. The IR spectra were recorded in KBr pellets on a (BIO-RAD FTS 135) WIN-IR spectrophotometer. The FAB mass spectra of all the compounds were recorded on a JEOL SX102/ /DA-600 mass spectrometer using argon/xenon (6 kV, 10 mA) as the FAB gas. The ^{1}H-NMR spectra were recorded on a Bruker model DPX 300 FT-NMR spectrometer in CDCl$_3$ using tetramethylsilane (Me$_4$Si, TMS) as an internal standard. The chemical shifts are reported in the δ ppm scale.

*General procedure for the preparation of the new (*E*)-N'-(substituted benzylidene)-isonicotinohydrazides (**1a**–**h**)*

To an equimolar methanolic solution of isonicotinic acid hydrazide (0.1 mol) and substituted benzaldehyde (0.1 mol), a few drops of glacial acetic acid were added. The mixture was then refluxed on water bath for 5–6 h. It was then allowed to cool, poured onto crushed ice and recrystallised from methanol.

*General procedure for the preparation of the new N-(2-(substituted phenyl)-4-oxothiazolidin-3-yl)isonicotinamides (**2a**–**h**)*

A mixture of **1** (0.01 mol) and thioglycolic acid (0.01 mol) was heated on an oil-bath at 120–125 °C for 12 h. The reaction mixture was cooled and treated with 10 % sodium bicarbonate solution. The product was isolated and recrystallised from methanol–dioxane (4:1).

*General procedure for the preparation of new 2-(2-(2-substituted phenyl)-3-(isonicotin-amido)-4-oxothiazolidin-5-yl)acetic acids (**3a**–**h**)*

A mixture of **1** (0.01 mol) and thiomalic acid (0.01 mol) was heated on an oil-bath at 120–125 °C for 12 h. The reaction mixture was cooled and treated with 10 % sodium bicarbonate solution. The product was isolated and recrystallised from methanol–dioxane (4:1).

*General procedure for the synthesis of N-(3-chloro-2-(2-substituted phenyl)-4-oxoazetidin-1-yl)isonicotinamide (**4a**–**h**)*

A solution of **1** (0.01 mol) in dioxane (20 mL) was added to a well-stirred mixture of chloroacetyl chloride (0.012 mol) and triethylamine (Et$_3$N) (0.012 mol) in dioxane (10 mL) at 0–5 °C. The reaction mixture was then stirred for 8 h, kept for 2 days at room temperature and then treated with cold water. The solid thus obtained was filtered, washed with water and recrystallised from methanol.

*General procedure for the synthesis of 1-(2-(2-substituted phenyl)-5-(pyridin-4-yl)-1,3,4-oxadiazol-3(2H)-yl)ethanone (**5a**–**h**)*

A mixture of **1** (0.003 mol) and acetic anhydride (10 mL) was heated under reflux for 4 h. After the reaction mixture attained room temperature, the excess acetic anhydride was decomposed by water and the mixture was stirred for further 30 min. The separated product was filtered, washed with water, dried and recrystallised from appropriate solvent systems.

Biological evaluation

Animals. Adult Wistar strain rats of either sex weighing 150–200 g were used for the evaluation of the anti-inflammatory, ulcerogenic and lipid peroxidation activities, whereas Swiss albino mice weighing 25–30 g were used for assessing the analgesic activity. The animals were allowed food and water *ad libitum* except during the experiments. They were housed in a room at 25±2 °C, and 50±5 % relative humidity with a 12 h light/dark cycle. The animals were randomly allocated into groups at the beginning of all the experiments. All the experimental protocols were performed with permission from the Institutional Animal Ethics Committee (IAEC), form No. 520. The animals were obtained from the Central Animal House

Facility, Hamdard University, New Delhi-110062, India. Registration number and date of registration of the Animal House Facility (173/CPCSEA, 28, JAN-2000). All the test compounds and the reference drug were administered orally suspended in 0.5 % carboxymethyl cellulose (CMC) solutions.

Anti-inflammatory activity

The synthesized compounds were evaluated for their anti-inflammatory activity using the carrageenan-induced hind paw edema method.[21] The animals were randomly allocated into groups of six animals each and were fasted for 24 h before the experiment with free access to water. The control group received only 0.5 % carboxymethyl cellulose solution. The standard drug naproxen was administered orally at a dose of 10 mg kg^{-1}. The test compounds were administered orally at an equimolar oral dose relative to 10 mg kg^{-1} naproxen. Into the sub-plantar region of the right hind paw of each rat, 0.1 ml of 1 % carrageenan solution in saline was injected subcutaneously, 1 h after the administration of the test compounds or the standard drug. The right hind paw volume was measured before and after 3 and 4 h of carrageenan treatment by means of a plethysmometer. The percent edema inhibition was calculated from the mean effect in the control and treated animals according to the following equation:

$$\text{Percent edema inhibition} = (V_c - V_t / V_c) \times 100$$

where V_t represents the mean increase in paw volume in rats treated with test compounds and V_c represents the mean increase in paw volume in the control group of rats.

Analgesic activity

The analgesic activity was evaluated by the tail immersion method.[22] Swiss albino mice allocated into different groups consisting of six animals of either sex in each, weighing 25–30 g, were used for the experiment. The analgesic activity was evaluated after oral administration of the test compounds at an equimolar dose relative to 10 mg kg^{-1} naproxen. The test compounds and the standard drug were administered orally as a suspension in carboxymethyl cellulose solution in water (0.5 %, w/v). The analgesic activity was assessed before and 4 h after the administration of test compounds and standard drug. The lower 5 cm portion of the tail was gently immersed into thermostatically controlled water at 55±0.5 °C. The time in seconds for tail withdrawal from the water was taken as the reaction time with a cut-off time of immersion set at 10 s for both the control as well as the treated group of animals.

Acute ulcerogenicity

Acute ulcerogenicity was determined according to the method of Cioli *et al.*[23] The animals were allocated into different groups consisting of six animals in each group. The ulcerogenic activity was evaluated after oral administration of the test compounds at an equimolar dose relative to 30 mg kg^{-1} naproxen. The control group received only 0.5 % carboxymethyl cellulose solution. Food but not water was removed 24 h before administration of the test compounds. After the drug treatment, the rats were fed with a normal diet for 17 h and then sacrificed. The stomach was removed and opened along the greater curvature, washed with distilled water and cleaned gently by dipping in normal saline. The mucosal damage was examined by means of a magnifying glass. For each stomach the mucosal damage was assessed according to the following scoring system: 0.5, redness, 1.0, spot ulcers, 1.5, hemorrhagic streaks, 2.0, ulcers < 3, 3.0, ulcers > 3 but ≤ 5. The mean score of each treated group minus the mean score of control group was regarded as the severity index of gastric mucosal damage.

Lipid peroxidation

Lipid peroxidation in the gastric mucosa was determined according to the method of Ohkawa *et al.*[24] After screening for ulcerogenic activity, the gastric mucosa was scraped with two glass slides, weighed (100 mg) and homogenized in 1.8 ml of 1.15 % ice-cold KCl solution. The homogenate was supplemented with 0.2 ml of 8.1 % sodium dodecyl sulphate (SDS), 1.5 ml of acetate buffer (pH 3.5) and 1.5 ml of 0.8 % thiobarbituric acid (TBA). The mixture was heated at 95 °C for 60 min. After cooling, the reactants were supplemented with 5 ml of the mixture of *n*-butanol and pyridine (15:1 v/v), shaken vigorously for 1 min and centrifuged for 10 min at 4000 rpm. The supernatant organic layer was removed and the absorbance measured at 532 nm using a UV/Vis spectrophotometer. The results were expressed as nmol MDA 100 mg^{-1} tissue, using an extinction coefficient 1.56×10^5 cm^{-1} M^{-1}.

Statistical analysis of data

The data are expressed as mean±standard error of mean (*SEM*). In the anti-inflammatory, ulcerogenic and lipid peroxidation studies, statistical differences between the treatments and the standard were tested by one-way ANOVA followed by the Dunnett multiple comparison test. A value of $p < 0.01$ was considered significant. In analgesic activity study, the statistical differences in treatments and standard were tested by the paired Student's *t*-test.

RESULTS AND DISCUSSION

Chemistry

The key intermediates used in the synthesis of thiazolidin-4-ones **2a**–**h** and **3a**–**h**, azetidin-2-one **4a**–**h** and 1,3,4-oxadiazole derivatives **5a**–**h**, (*E*)-*N'*-(2-substituted benzylidene)isonicotinohydrazides **1a**–**h** were prepared starting from isonicotinic acid hydrazide. The reaction of isonicotinic acid hydrazide with substituted benzaldehyde in refluxing methanol with few drops of glacial acetic acid gave the (*E*)-*N'*-(2-substituted benzylidene)isonicotinohydrazides **1a**–**h.** In the present study, the reaction of the substituted benzylidene isonicotinohydrazides **1a**–**h** with thioglycolic acid, thiomalic acid, chloroacetyl chloride and acetic anhydride in presence of various reagents gave the new thiazolidin-4-ones **2a**–**h** and **3a**–**h**, azetidin-2-one **4a**–**h** and 1,3,4-oxadiazole derivatives **5a**–**h**, respectively.

The synthesis routes to the compounds are outlined in Scheme 1. The analytical and spectral data of the newly prepared compounds are given in the supplementary material to this paper.

The IR spectra of compounds **1a**–**h** showed absorption peaks at 3300, 1680 and 1600 cm^{-1} due to N–H, C=O and –N=CH stretching vibrations. The appearance of the stretching of the C=O of thiazolidinone, *β*-lactam ring and the acetyl of the oxadiazole ring at 1700, 1745 and 1660 cm^{-1}, respectively, in the spectra of the derivatives, together with the C=O stretching at 1680 cm^{-1} confirmed the formation of the compounds **2a**–**h**, **3a**–**h**, **4a**–**h** and **5a**–**h**.

The ^{1}H-NMR spectra of compounds **1a**–**h** revealed a multiplet at *δ* 7.72 and 8.63 ppm for pyridine and *δ* 7.12–7.15 ppm for the aromatic ring and singlets at *δ* 6.1 and 7.9 ppm for –NH and –N=CH, respectively. The disappearance of the singlet peak of –N=CH and presence of a singlet peak at *δ* 3.5, 10.0, 7.7 and 7.19

ppm of –CH$_2$ of thiazolidinone, COOH, –N–CH and –CH oxadiazole, respectively, proved that these compounds participated in the cyclisation reaction and formed the desired compounds.
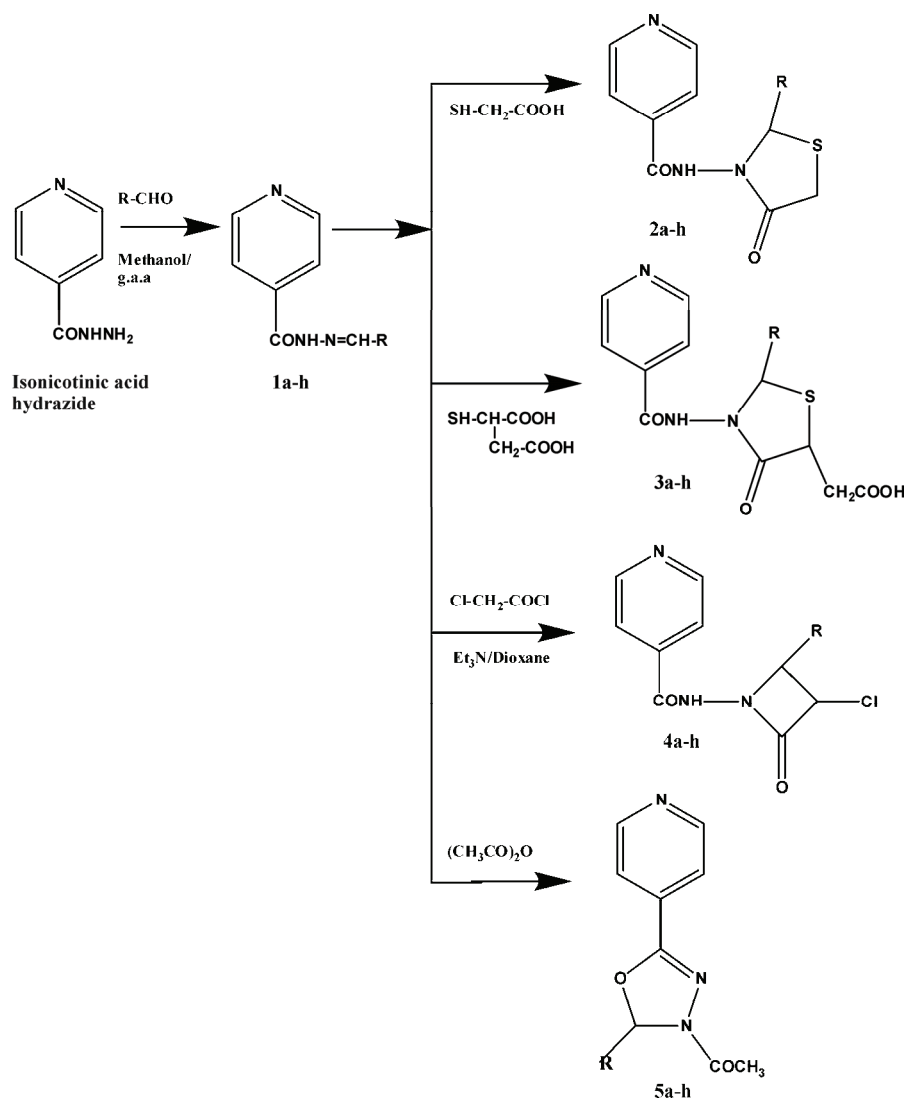
Scheme 1. The synthesis routes to the title compounds.

Anti-inflammatory activity

The anti-inflammatory activities of the synthesized compounds **2a–h**, **3a–h**, **4a–h** and **5a–h** were evaluated by the carrageenan-induced paw edema method of Winter *et al.*[15] The compounds were tested at a 10 mg kg^{-1} oral dose and were

compared with the standard drug naproxen at the same oral dose. The tested compounds showed anti-inflammatory activity ranging from 31.81–84.54 % (Table I), whereas the standard drug naproxen showed 81.86 % inhibition after 4 h.

TABLE I. Biological data of isonicotinic aid hydrazide derivatives (anti-inflammatory and analgesic activities of the test compounds with reference to the control. Ulcerogenic and lipid peroxidation were compared with reference to the standard drug, *i.e.*, naproxen. Data were only analyzed by the Student's *t*-test for $n = 6$)

Compd.	R	Anti-inflammatoryactivity (% inhibition±*SEM*)	Analgesic activity (% inhibition±*SEM*)	Ulcerogenic activity (severity index±*SEM*)	(nmol MDA content± *SEM*)/100 mg tissue
Control	–	–	–	0.000±0.00	3.25±0.005
Naproxen	–	81.86±3.71[c]	71.42±1.31[a]	2.250±0.11	9.04±0.24
2a	o-C_6H_4Cl	78.00±2.53[c]	70.32±1.31[a]	0.583±0.18[a]	5.715±0.14[a]
2b	p-C_6H_4Cl	64.64±3.79[c]	59.09±3.60[c]	2.750±0.19[c]	8.808±0.06[c]
2c	o-C_6H_4OH	57.57±3.45[c]	65.15±1.51[c]	1.000±0.31[c]	7.904±0.19[c]
2d	m-C_6H_4OH	34.08±3.47c	44.05±3.76c	1.667±0.24[c]	6.715±0.16[a]
2e	p-$C_6H_4OCH_3$	39.54±2.27c	31.81±3.71c	2.140±0.11[c]	8.155±0.14[c]
2f	p-C_6H_4F	82.81±2.17[a]	71.57±1.85[a]	0.666±0.16[a]	5.608±0.02[a]
2g	o-$C_6H_4NO_2$	84.24±0.95[a]	72.42±1.31[a]	0.510±0.08[a]	5.876±0.13[a]
2h	p-$C_6H_4N(CH_3)_2$	65.15±1.51[c]	59.23±3.71[c]	2.427±0.14[c]	8.128±0.06[c]
3a	o-C_6H_4Cl	77.27±1.92[c]	70.45±3.26[a]	0.833±0.24[c]	6.110±0.04[a]
3b	p-C_6H_4Cl	63.63±1.96[c]	54.28±3.76c	2.466±0.20[c]	8.742±0.17[c]
3c	o-C_6H_4OH	68.93±3.60[c]	62.85±1.65[c]	0.917±0.12[c]	7.788±0.10[c]
3d	m-C_6H_4OH	31.81±3.45c	47.27±2.73c	2.835±0.18[c]	8.110±0.13[c]
3e	p-$C_6H_4OCH_3$	56.81±1.94[c]	66.46±2.38[c]	0.814±0.24[c]	7.337±0.16[c]
3f	p-C_6H_4F	75.00±2.53[c]	70.04±1.64[a]	0.541±0.10[a]	6.854±0.14[a]
3g	o-$C_6H_4NO_2$	82.27±1.84[a]	72.72±1.66[a]	0.516±0.11[a]	5.788±0.10[a]
3h	p-$C_6H_4N(CH_3)_2$	59.09±3.60[c]	49.54±2.27c	2.413±0.10[c]	8.371±0.12[c]
4a	o-C_6H_4Cl	70.45±3.26[c]	64.80±1.28[c]	2.683±0.10[c]	7.874±0.15[c]
4b	p-C_6H_4Cl	68.93±3.60[c]	59.61±1.00[c]	1.751±0.16[c]	5.192±0.22[a]
4c	o-C_6H_4OH	84.54±1.94[a]	73.06±2.61[a]	0.517±0.25[a]	6.651±0.17[a]
4d	m-C_6H_4OH	44.05±3.76c	57.14±2.20[c]	1.836±0.11[c]	7.327±0.19[c]
4e	p-$C_6H_4OCH_3$	54.28±3.45c	44.19±2.76c	2.432±0.24[c]	8.418±0.11[c]
4f	p-C_6H_4F	77.14±2.20[c]	71.12±1.24[a]	0.750±0.18[c]	5.62±0.29[a]
4g	o-$C_6H_4NO_2$	76.50±1.82[c]	69.54±3.19[c]	0.817±0.12[c]	8.364±0.24[c]
4h	p-$C_6H_4N(CH_3)_2$	72.72±1.66[c]	52.48±3.76c	1.342±0.23[c]	7.821±0.14[c]
5a	o-C_6H_4Cl	82.86±1.84[a]	70.45±3.26[a]	0.750±0.14[c]	7.51±0.68[c]
5b	p-C_6H_4Cl	69.23±3.71[c]	62.69±1.65[c]	1.967±0.17[c]	7.441±0.12[c]
5c	o-C_6H_4OH	63.46±2.38[c]	55.32±1.96[c]	1.834±0.22[c]	7.652±0.17[c]
5d	m-C_6H_4OH	51.28±3.61[c]	42.45±3.16c	2.667±0.14[c]	8.345±0.19[c]
5e	p-$C_6H_4OCH_3$	31.81±3.41[c]	57.80±2.84[b]	1.684±0.26[b]	6.791±0.13[a]
5f	p-C_6H_4F	76.92±1.58[b]	71.72±1.66[a]	0.667±0.18[a]	6.338±0.20[a]
5g	o-$C_6H_4NO_2$	83.80±1.85[a]	72.52±1.00[a]	0.412±0.11[a]	5.742±0.17[a]
5h	p-$C_6H_4N(CH_3)_2$	68.26±2.31[b]	61.82±1.65[b]	1.327±0.20[b]	7.155±0.22[b]

[a] $p < 0.0001$; [b] $p < 0.001$; [c] $p < 0.01$

The anti-inflammatory activities of the thiazolidin-4-one derivatives (**2a**–**h** and **3a**–**h**) were in the range 34.08–84.24 %. When the CH_2 of thiazolidin-4-one moiety (**2a**–**h**) at the position 5 was substituted by CH_2COOH (**3a**–**h**), no substantial change was observed in the activity. It was observed that thaiazolidin-4--one derivatives having *o*-Cl, *p*-F and *o*-NO_2 phenyl group showed better or equivalent activity (78.00, 82.81, 84.24 (in series **2**), 77.27, 75.00 and 82.27 % (in series **3**), respectively) to that of the standard drug. The other thiazolidin-4-one derivatives showed moderate activity.

The anti-inflammatory activities of the azetidin-2-one derivatives were between 44.05 and 84.54 %. The highest activity (84.54 %) was found with the azetidin-2-one derivative **4c** having an *o*-hydroxyphenyl group at the position 4. It was observed that the azetidin-2-one derivative having a *p*-dimethylaminophenyl group (**4h**) also showed good activity, *viz.* 72.72 % as did those having an *o*-chloro, *p*-fluoro and *o*-nitrophenyl group (70.45, 77.14 and 76.50 %, respectively). The other derivatives showed moderate activity.

The 1,3,4-oxadiazole derivatives of isonicotinic acid hydrazide showed anti--inflammatory activities ranging from 31.81 to 83.80 %.The highest activity (83.80 %) of the oxadiazole derivative was found for compound **5g** having a *o*-nitrophenyl group at the position 2. When this group was replaced by the *o*-chloro phenyl group, the activity was found to be decreased but equivalent to that of the standard drug (82.86 %). Furthermore, the oxadiazole derivative having a *p*-fluorophenyl group (**5f**) at the position 2 also showed good activity (76.92 %). The remaining oxadiazole derivatives showed moderate activity.

Analgesic activity

The thiazolidin-4-one derivatives **2f, 2g** and **3g** showed analgesic activities ranging from 71.57 to 72.72 %, *i.e.*, better than that of the standard drug naproxen (71.42 %). The presence of a *o*-nitrophenyl group, at the position 2 of the thiazolidinone ring (**2g** and **3g**) gave the maximum activity (72.42 and 72.72 %, respectively). When this group was replaced by *o*-chlorophenyl (**2a** and **3a**) and *p*-fluorophenyl (**2f** and **3f**), the activity was found to be slightly decreased (70.32–71.57 %). When these groups were replaced by *p*-OCH_3 and *m*-OH phenyl group (**2e** and **3d**)**,** the activity decreased drastically (31.81 and 47.27 %, respectively). The results show that an electron-withdrawing group increased the analgesic activity of the compounds.

When the thiazolidin-4-one nucleus was replaced by the azetidin-2-one nucleus, the analgesic activity of most of the compounds decreased, except for compound **4c** having an *o*-hydroxylphenyl group at the position 4, which exhibited the highest activity (73.06 %). 1,3,4-Oxadiazole derivatives (**5a**–**h**) were also screened and showed 42.45–72.52 % analgesic activity. The compounds having a *p*-fluorophenyl (**5f**) and a *o*-nitrophenyl group (**5g**) at the position 2 of the oxa-

diazole nucleus showed a slight difference in their activity (71.72 and 72.52 %). There was a decrease in the activity when these groups were replaced by an *m*--hydroxyphenyl group (**5d**).

Acute ulcerogenesis

The tested compounds showed significant reductions in ulcerogenic activity, ranging from 0.417±0.08 to 2.835±0.18, whereas the standard drug naproxen exhibited a high severity index (2.250±0.11). The ulcerogenic activity of the thiazolidin-4-one derivatives **2a–h** and **3a–h** ranged from 0.510±0.08 to 2.835±0.18. The compounds with a *o*-nitrophenyl group (**2g** and **3g**) showed minimum ulcerogenic activity (0.510±0.08 and 0.516±0.11, respectively). Moreover, their anti--inflammatory activity was found to be high *viz.* 84.24 and 82.27 %, respectively. The other three thiazolidinone derivatives **2a**, **2f** and **3f** also showed reductions in ulcerogenic activity (0.583±0.08, 0.666±0.16 and 0.541±0.10, respectively) in comparison to the standard drug.

The azetidin-2-one derivatives **4c**, **4f** and **4g** also showed reductions in ulcerogenic activity (0.517±0.11, 0.750±0.14 and 0.817±0.13). The 1,3,4-oxadiazole derivatives showed minimal ulcerogenic activity, when compared to the thiazolidin-4-one and azetidin-2-one derivatives. Compound **5g** having a *o*-nitrophenyl group showed the minimum severity index (0.412±0.11).

Lipid peroxidation

It was reported in the literature that compounds showing less ulcerogenic activity also showed reduced malondialdehyde (MDA) content, a by-product of lipid peroxidation.[25] Therefore, an attempt was made to correlate the decrease in ulcerogenic activity of the compounds with that of lipid peroxidation. All the compounds screened for ulcerogenic activity were also analyzed for lipid peroxidation.

The lipid peroxidation was measured as nmol of MDA per 100 mg of tissue. The naproxen (standard drug) showed the maximum lipid peroxidation (9.04± ±0.24), whereas the control group showed 3.25±0.05. It was found that all the cyclised derivatives showing lower ulcerogenic activity also exhibited reduced lipid peroxidation (Table I). Thus, these studies showed that the synthesized compounds inhibited the induction of gastric mucosal lesions and the results further suggested that their protective effect might be related to the inhibition of lipid peroxidation in the gastric mucosa.

CONCLUSIONS

Various thiazolidin-4-one, azetidin-2-one and 1,3,4-oxadiazole derivatives of isonicotinic acid hydrazide were prepared with the objective of developing better anti-inflammatory molecules with minimum ulcerogenic activity. It was interesting to note that six of the cyclised compounds, **2f**, **2g**, **3g**, **4c**, **5a** and **5g**, were

found to have anti-inflammatory activity greater than that of the standard drug (naproxen, 81.86 %) at 10 mg kg^{-1} *p.o.* Furthermore, five compounds, **2a**, **3a**, **4f**, **4g** and **5f**, exhibited anti-inflammatory activity equivalent to the standard drug in the carrageenan-induced paw edema test in rats. When these compounds were subjected to the analgesic activity test, they showed increased activity over the reference drug.

The presence of *p*-fluorophenyl and *o*-nitrophenyl groups at the 2nd position of the thiazolidinone nucleus increased the anti-inflammatory activity whereas the presence of *m*-hydroxryphenyl and *p*-methoxyphenyl groups decreased the anti-inflammatory activity. It was further noted that the presence of *o*-hydroxy, *o*--chloro and *o*-nitrophenyl groups at the and positions 4 and 2 of azetidinone and oxadiazole nucleus, respectively, increased the anti-inflammatory activity compared to the standard drug, whereas presence of the *p*-fluorophenyl group showed anti-inflammatory activity slightly less than that of the standard drug.

These compounds tested for ulcerogenic activity showed a significant decrease in activity compared to that of the standard drug. It was noted that the oxadiazole derivatives showed maximum reduction in ulcerogenic activity followed by the thiazolidinone and azetidinone derivatives. It was further concluded that the presence of *p*-fluorophenyl and *o*-nitrophenyl groups at the positions 2, 4 and 2 of thiazolidione, azetidinone and oxadiazole nucleus, respectively, showed maximum anti-inflammatory and analgesic activity, minimum ulcerogenic activity together with minimum lipid peroxidation.

SUPPLEMENTARY MATERIAL

Analytical and spectral data of the synthesized compounds are available electronically at http://www.shd.org.rs/JSCS/, or from the corresponding author on request.

ИЗВОД

ТИАЗОЛИДИН-4-ОНСКИ, АЗЕТИДИН-2-ОНСКИ И 1,3,4-ОКСАДИАЗОЛСКИ ДЕРИВАТИ ХИДРАЗИДА ИЗОНИКОТИНСКЕ КИСЕЛИНЕ: СИНТЕЗА И ЊИХОВА БИОЛОШКА АКТИВНОСТ

SADAF J. GILANI[1,2], SUROOR A. KHAN[1], OZAIR ALAM[1], VIJENDER SINGH[2] и ALKA ARORA[2]

[1]*Department of Pharmaceutical Chemistry, Faculty of Pharmacy, Jamia Hamdard, New Delhi-110062 u* [2]*Department of Pharmaceutical Chemistry, KIET School of Pharmacy, Ghaziabad, U.P. 201206, India*

Синтетисана је серија нових тиазолидин-4-онских (**2a**–**h** и **3a**–**h**), азетидин-2-онских (**4a**–**h**) и 1,3,4-оксадиазолских (**5a**–**h**) деривата хидразида изоникотинске киселине (INH) са циљем да се испита њихова анти-инфламаторна, аналгетичка и улцерогена активност и активност према пероксидацији липида. Структура синтетисаних једињења одређена је на основу IC, NMR и масених спектара. Анти-инфламаторна активност једињења одређена је

тестом карагененом идукованог отока на шапи пацова. Од 32 испитана једињења, 11 показује врло добру анти-инфламаторну активност и изражену аналгетичку активност, уз незнатну улцерогену активност. Једињења која показују најмању улцерогену активност доводе до снижавања количине малондиалдехида (MDA), који је споредни производ липидне пероксидације. Резултати показују да једињења инхибирају индукцију оштећења слузокоже желуца и може се претпоставити да је њихова заштитна улога повезана са инхибицијом липидне пероксидације у слузокожи желуца.

REFERENCES

1. M. Amir, H. Kumar, S. A. Javed, *Eur. J. Med. Chem*. **39** (2004) 535
2. C. J. Smith, Y. Zhang, C. M. Koboldt, J. Muhammad, B. S. Zwefel, A. Shaffer, J. J. Talley, J. L. Masferrer, K. Serbert, P. C. Isakson, *Proc. Natl. Acad. Sci. USA* **95** (1998) 13313
3. T. D. Warner, F. Giuliano, I. Vaynovie, A. Bukasa, J. A. Mitchell, J. R. Vave, *Proc. Natl. Acad. Sci. USA* **96** (1999) 7563
4. L. J. Marnett, A. S. Kalgutkar, *Trends Pharmacol. Sci.* **20** (1999) 465
5. G. Dannhardt, W. Kiefer, *Eur. J. Med. Chem*. **36** (2001) 109
6. L. J. Marnett, A. S. Kalgutkar, *Curr. Opin. Chem. Biol*. **2** (1998) 482
7. P. Parsit, D. Reindeau, *Annu. Rep. Med. Chem*. **32** (1997) 211
8. A. G. Habeeb, P. N. P. Rao, E. D. Knaus, *J. Med. Chem*. **44** (2001) 2921
9. C. A. Imansa, J. Alfon, A. F. de Arriba, F. L. Cavalcanti, I. Escamilla, L. A. Gomez, A. Mirralles, R. Solvia, J. Bartroli, E. Carceller, M. Merlos, J. G. Rafanell, *J. Med. Chem*. **46** (2003) 3643
10. L. M. Jackson, C. J. Hawkey, *Exp. Opin. Invest. Drugs* **8** (1999) 963
11. C. Hawkey, L. Laine, T. Simon, A. Beaulieu, J. Maldonado-Cocco, E. Acevedo, A. Shahane, H. Quan, J. Bolognese, E. Mortensen, *Arthritis Rheum*. **43** (2000) 370
12. V. K. Tammara, M. M. Narurkar, A. M. Crider, M. A. Khan, *J. Pharm. Sci*. **83** (1994) 644
13. J. M. Dogne, C. T. Supuran, D. Pratico, *J. Med. Chem*.**48** (2005) 2251
14. D. Galanakis, A. P. Kourounakis, K. C. Tsiakitzis, C. Doulgkeris, E. A. Rekka, A. Gavalas, C. Kravaritou, C. Charitos, P. N. Kourounakis, *Bioorg. Med. Chem. Lett.* **14** (2004) 3639
15. A. S. Kalgutkar, A. B. Marnett, B. C. Crews, R. P. Remmel, *J. Med. Chem.* **43** (2000) 2860
16. M. Duflos, M. R. Nourrisson, J. Brelet, J. Courant, G. Le Baut, N. Grimaud, J. Y. Petit, *Eur. J. Med. Chem.* **36** (2001) 545
17. A. S. Kalgutkar, B. Crews, S. Rowlinson, C. Garner, K. Seibert, L. Marnett, *Science* **280** (1998) 1268
18. M. Tuncbilek, N. Altanlar, *Farmaco* **54** (1999) 475
19. K. Mogilaiah, R. B. Rao, K. N. Reddy, *Ind. J. Chem*. B **38** (1999) 818
20. M. S. Y. Khan, G. Chawla, M. A. Mueed, *Ind. J. Chem*. B **43** (2004) 1302
21. C. A. Winter, E. A. Risley, G. W. Nuss, *Proc. Soc. Exp. Biol. Med.* **111** (1962) 544
22. O. O. Adeyemi, O. S. Okpo, O. J. Okpaka, *J. Ethnopharmacol*. **90** (2004) 45
23. V. Cioli, S. Putzolu, V. Rossi, S. P. Barcellona, C. Corradino, *Toxicol. Appl. Pharmacol*. **50** (1979) 283
24. H. Ohkawa, M. Ohishi, K. Yagi, *Anal. Biochem*. **95** (1979) 351
25. Y. Naito, T. Yoshikawa, N. Yoshinda, M. Kondo, *Dig. Dis. Sci*. **43** (1998) 30s.

SUPPLEMENTARY MATERIAL TO

Thiazolidin-4-one, azetidin-2-one and 1,3,4-oxadiazole derivatives of isonicotinic acid hydrazide: synthesis and their biological evaluation

SADAF J. GILANI[1,2]*, SUROOR A. KHAN[1], OZAIR ALAM[1], VIJENDER SINGH[2] and ALKA ARORA[2]

[1]Department of Pharmaceutical Chemistry, Faculty of Pharmacy, Jamia Hamdard, New Delhi-110062 and [2]Department of Pharmaceutical Chemistry, KIET School of Pharmacy, Ghaziabad, U.P. 201206, India

ANALYTICAL AND SPECTRAL DATA OF THE NEWLY PREPARED COMPOUNDS

(E)-N'-(2-Chlorobenzylidene)isonicotinohydrazide (1a). Yield: 90 %; m.p. 184–186 °C. Anal. Calcd. for $C_{13}H_{10}N_3OCl$ (*FW* 259.69): C, 60.12; H, 3.88; N, 16.18 %. Found: C, 60.10; H, 3.86; N, 16.16 %. IR (KBr, cm⁻¹): 3300 (N–H stretching), 1680 (C=O stretching of carbonyl), 1600 (–N=CH–Ar stretching of aromatic ring), 830 (C–Cl stretching of chlorine). ¹H-NMR (300 MHz, CDCl₃, *δ* / ppm): 7.9 (1H, *s*, –N=CH), 7.72, 8.63 (4H, *m*, Py), 7.12–7.15 (4H, *m, J* = 9 Hz, aromatic), 6.1 (1H, *s*, NH). MS (*m/z*): 259 [M]⁺.

(E)-N'-(4-Chlorobenzylidene)isonicotinohydrazide (1b). Yield: 90 %; m.p. 192–194 °C. Anal. Calcd. for $C_{13}H_{10}N_3OCl$ (*FW* 259.69): C, 60.12; H, 3.88; N, 16.18 %. Found: C, 60.11; H, 3.87; N, 16.17 %. IR (KBr, cm⁻¹): 3310 (N–H stretching), 1676 (C=O stretching of carbonyl), 1615 (–N=CH–Ar stretching of aromatic ring), 822 (C–Cl stretching of chlorine). ¹H-NMR (300 MHz, CDCl₃, *δ* / ppm): 7.72, 8.63 (4H, *m*, Py), 7.12–7.15 (4H, *m, J* = 9 Hz, aromatic,), 7.7 (1H, *s*, –N=CH), 6.4 (1H, *s*, NH). MS (*m/z*): 259 [M]⁺.

(E)-N'-(2-Hydroxybenzylidene)isonicotinohydrazide (1c). Yield: 80 %; m.p. 168–170 °C. Anal. Calcd. for $C_{13}H_{11}N_3O_2$ (*FW* 241.25): C, 64.72; H, 4.60; N, 17.42 %. Found: C, 64.70; H, 4.59; N, 17.40 %. IR (KBr, cm⁻¹): 3308 (N–H stretching), 1684 (C=O stretching of carbonyl), 1612 (–N=CH–Ar stretching of aromatic ring). ¹H-NMR (300 MHz, CDCl₃, *δ* / ppm): 9.40 (1H, *br*, OH), 7.8 (1H, *s*, –N=CH), 7.13–7.16 (4H, *m, J* = 9 Hz, aromatic), 7.70, 8.61 (4H, *m,* Py), 6.2 (1H, *s*, NH). MS (*m/z*): 241[M]⁺.

---

* Corresponding author. E-mail: gilanisadaf@gmail.com

(E)-N'-(3-Hydroxybenzylidene)isonicotinohydrazide (1d). Yield: 75 %; m.p. 186–188°C. Anal. Calcd. for $C_{13}H_{11}N_3O_2$ (FW 241.25): C, 64.72; H, 4.60; N, 17.42 %. Found: C, 64.70; H, 4.59; N, 17.40 %. IR (KBr, cm^{-1}): 3318 (N–H stretching), 1688 (C=O stretching of carbonyl), 1607 (–N=CH–Ar stretching of aromatic ring). ^{1}H-NMR (300 MHz, CDCl$_3$, δ / ppm): 9.40 (1H, *br*, OH), 7.7 (1H, *s*, –N=CH), 7.74, 8.62 (4H, *m*, Py), 7.11–7.14 (4H, *m*, *J* = 9 Hz, aromatic), 6.3 (1H, *s*, NH). MS (*m/z*): 241 [M]$^+$.

(E)-N'-(4-Methoxybenzylidene)isonicotinohydrazide (1e). Yield: 80 %; m.p. 194–196 °C. Anal. Calcd. for $C_{14}H_{13}N_3O_2$ (*FW* 255.27): C, 65.87; H, 5.13; N, 16.46 %. Found: C, 65.85; H, 5.10; N, 16.44 %. IR (KBr, cm^{-1}): 3314 (N–H stretching), 1687 (C=O stretching of carbonyl), 1604 (–N=CH–Ar stretching of aromatic ring). ^{1}H-NMR (300 MHz, CDCl$_3$, δ / ppm): 7.73, 8.64 (4H, *m*, Py), 7.3 (1H, *s*, –N=CH), 7.13–7.16 (4H, *m*, *J* = 9 Hz, aromatic), 6.4 (1H, *s*, NH), 3.83 (3H, *s*, OCH$_3$). MS (*m/z*): 255 [M]$^+$.

(E)-N'-(4-Fluorobenzylidene)isonicotinohydrazide (1f). Yield: 90 %; m.p. 182–184 °C. Anal. Calcd. for $C_{13}H_{10}FN_3O$ (*FW* 243.24): C, 64.19; H, 4.14; N, 17.28 %. Found: C, 64.16; H, 4.12; N, 17.26 %. IR (KBr, cm^{-1}): 3305 (N–H stretching), 1684 (C=O stretching of carbonyl), 1611 (–N=CH–Ar stretching of aromatic ring). ^{1}H-NMR (300 MHz, CDCl$_3$, δ / ppm): 7.70–8.61 (4H, *m*, Py), 7.6 (1H, *s*, –N=CH), 7.11–7.14 (4H, *m*, *J* = 9.0 Hz, aromatic), 6.3 (1H, *s*, NH). MS (*m/z*): 243 [M]$^+$.

(E)-N'-(2-Nitrobenzylidene)isonicotinohydrazide (1g). Yield: 85 %; m.p. 188–189 °C. Anal. Calcd. for $C_{13}H_{10}N_4O_3$ (*FW* 270.24): C, 57.78; H, 3.73; N, 20.73 %. Found: C, 57.76; H, 3.70; N, 20.71 %. IR (KBr, cm^{-1}): 3311 (N–H stretching), 1685 (C=O stretching of carbonyl), 1610 (–N=CH– Ar stretching of aromatic rings), 1366 (NO$_2$). ^{1}H-NMR (300 MHz, CDCl$_3$, δ / ppm): 7.8 (1H, *s*, –N=CH), 7.73, 8.61 (4H, *m*, Py), 7.10–7.13 (4H, *m*, *J* = 9.0 Hz, aromatic), 6.2 (1H, *s*, NH). MS (*m/z*): 270 [M]$^+$.

(E)-N'-(4-(Dimethylamino)benzylidene)isonicotinohydrazide (1h). Yield: 85 %; m.p. 196–198 °C. Anal. Calcd. for $C_{15}H_{16}N_4O$ (*FW* 268.31): C, 67.15; H, 6.01; N, 20.88 %. Found: C, 67.12; H, 6.00; N, 20.86 %. IR (KBr, cm^{-1}): 3313 (N–H stretching), 1683(C=O stretching of carbonyl), 1613 (–N=CH–Ar stretching of aromatic rings). ^{1}H-NMR (300 MHz, CDCl$_3$, δ / ppm): 7.9 (1H, *s*, –N=CH), 7.72, 8.63 (4H, *m*, Py), 7.12–7.15 (4H, *m*, *J* = 9.0 Hz aromatic), 6.1 (1H, *s*, NH), 2.63 (6H, *s*, N(CH$_3$)$_2$). MS (*m/z*): 268 [M]$^+$.

N-(2-(2-Chlorophenyl)-4-oxothiazolidin-3-yl)isonicotinamide (*2a*). Yield: 85 %; m.p. 198–200 °C. Anal. Calcd. for $C_{15}H_{12}ClN_3O_2S$ (*FW* 333.79): C, 53.97; H, 3.62; N, 12.59 %. Found: C, 53.94; H, 3.60; N, 12.57 %. IR (KBr, cm^{-1}): 3300 (N–H stretching), 1700 (C=O thiazolidinone), 1670 (C=O stretching of carbonyl), 1610 (C=N), 1574 (C=C stretching of chlorine), 830 (C–Cl stretching of chlorine), 700 (C–S–C). ^{1}H-NMR (300 MHz, CDCl$_3$, δ / ppm): 9.8 (1H, *s*, CONH–),

7.74–8.64 (4H, *m, * Py), 7.20 (1H, *s*, N–CH–), 7.12–7.15 (4H, *m,* aromatic), 5.96 (1H, *s*, –S–CH–), 3.50 (2H, *s*, CH$_2$). ^{13}C-NMR (100 MHz, CDCl$_3$, δ / ppm): 168.8, 163.7, 149.7, 140.8, 134.0, 130.1, 128.7, 128.5, 126.7, 121.7, 102.5, 59.2, 35.6. MS (*m/z*): 333 [M$^+$].

N-*(2-(4-Chlorophenyl)-4-oxothiazolidin-3-yl)isonicotinamide (2b)*. Yield: 85 %; m.p. 202–204 °C. Anal. Calcd. for C$_{15}$H$_{12}$ClN$_3$O$_2$S (*FW* 333.79): C, 53.97; H, 3.62; N, 12.59 %. Found: C, 53.96; H, 3.61; N, 12.58 %. IR (KBr, cm^{-1}): 3310 (N–H stretching), 1706 (C=O thiazolidinone), 1666 (C=O stretching of carbonyl), 1612 (C=N), 1573 (C=C), 830 (C–Cl stretching of chlorine), 700 (C–S–C). ^{1}H-NMR (300 MHz, CDCl$_3$, δ / ppm): 9.8 (1H, *s,* CONH–), 7.74, 8.64 (4H, *m*, Py), 7.2 (1H, *s*, N–CH–), 7.12–7.15 (4H, *m*, aromatic), 5.96 (1H, *s*, –S–CH–), 3.50 (2H, *s*, CH$_2$). ^{13}C-NMR (100 MHz, CDCl$_3$, δ / ppm): 168.8, 163.7, 149.7, 140.8, 134.0, 130.1, 128.7, 128.5, 126.7, 121.7, 102.5, 59.2, 35.6. MS (*m/z*): 333 [M$^+$].

N-*(2-(2-Hydroxyphenyl)-4-oxothiazolidin-3-yl)isonicotinamide (2c)*. Yield: 70 %; m.p. 200–202 °C. Anal. Calcd. for C$_{15}$H$_{13}$N$_3$O$_3$S (*FW* 315.07): C, 57.13; H, 4.16; N, 13.33 %. Found: C, 57.11; H, 4.14; N, 13.31 %. IR (KBr, cm^{-1}): 3318 (N–H stretching), 1716 (C=O thiazolidinone), 1674 (C=O stretching of carbonyl), 1626 (C=N), 1587 (C=C), 644 (C–S–C). ^{1}H-NMR (300 MHz, CDCl$_3$, δ / ppm): 9.41 (1H, *br*, OH), 9.14 (1H, *s,* CONH–), 7.77–8.68 (4H, *m,* Py), 7.20 (1H, *s*, N–CH–), 7.17–7.20 (4H, *m*, Ar–H), 5.16 (1H, *s*, –S–CH–), 3.50 (2H, *s*, CH$_2$). ^{13}C-NMR (100 MHz, CDCl$_3$, δ / ppm): 168.8, 163.7, 153.7, 149.7, 140.8, 128.5, 128.0, 121.2, 121.7, 118.1, 115.8, 58.1, 35.6. MS (*m/z*): 315 [M$^+$].

N-*(2-(3-Hydroxyphenyl)-4-oxothiazolidin-3-yl)isonicotinamide (2d)*. Yield: 70 %; m.p. 208–210 °C. Anal. Calcd. for C$_{15}$H$_{13}$N$_3$O$_3$S (*FW* 315.07): C, 57.13; H, 4.16; N, 13.33 %. Found: C, 57.10; H, 4.13; N, 13.32 %. IR (KBr, cm^{-1}): 3317 (N–H stretching), 1717 (C=O thiazolidinone), 1672 (C=O stretching of carbonyl), 1624 (C=N), 1588 (C=C), 642 (C–S–C). ^{1}H-NMR (300 MHz, CDCl$_3$, δ / / ppm): 9.42 (1H, *br*, OH), 9.13 (1H, *s*, CONH–), 7.76–8.67 (4H, *m*, Py), 7.10 (1H, *s*, N–CH–), 7.17–7.20 (4H, *m*, aromatic), 5.16 (1H, *s*, –S–CH–), 3.50 (2H, *s*, CH$_2$). ^{13}C-NMR (100 MHz, CDCl$_3$, δ / ppm): 168.8, 163.7, 153.7, 149.7, 140.8, 128.5, 128.0, 121.2, 121.7, 118.1, 115.8, 58.1, 35.6. MS (*m/z*): 315 [M$^+$].

N-*(2-(4-Methoxyphenyl)-4-oxothiazolidin-3-yl)isonicotinamide (2e)*. Yield: 75 %; m.p. 204–206 °C. Anal. Calcd. for C$_{16}$H$_{15}$N$_3$O$_3$S (*FW* 329.37): C, 58.34; H, 4.59; N, 12.76 %. Found: C, 58.33; H, 4.58; N, 12.74 %. IR (KBr, cm^{-1}): 3302 (N–H stretching), 1760 (C=O thiazolidinone), 1632 (C=O stretching of carbonyl), 1667 (C=N), 1546 (C=C), 628 (C–S–C). ^{1}H-NMR (300 MHz, CDCl$_3$, δ / / ppm): 9.06 (1H, *s*, CONH–), 7.70, 8.64 (4H, *m*, Py), 7.40 (1H, *s*, N–CH–), 7.26––7.32 (4H, *m*, aromatic), 5.22 (1H, *s*, –S–CH–), 3.84 (3H, *s*, OCH$_3$), 3.80 (2H, *s*, CH$_2$). ^{13}C-NMR (100 MHz, CDCl$_3$, δ / ppm): 168.8, 163.7, 159.0, 149.7, 121.7, 140.8, 131.5, 129.7, 121.7, 114.2, 64.3, 55.8, 35.6. MS (*m/z*): 329 [M$^+$].

N-*(2-(4-Fluorophenyl)-4-oxothiazolidin-3-yl)isonicotinamide (2f)*. Yield: 85 %; m.p. 196–200 °C. Anal. Calcd. for $C_{15}H_{12}FN_3O_2S$ (*FW* 317.34): C, 56.77; H, 3.81; N, 5.99 %. Found: C, 56.76; H, 3.80; N, 5.98 %. IR (KBr, cm^{-1}): 3316 (N–H stretching), 1769 (C=O thiazolidinone), 1661 (C=N), 1649 (C=O stretching of carbonyl), 1535 (C=C), 623 (C–S–C). ^{1}H-NMR (300 MHz, CDCl$_3$, δ / ppm): 9.02 (1H, *s*, CONH–), 7.80 (1H, *s*, N–CH–), 7.75–8.60 (4H, *m*, Py), 7.30, 7.36 (4H, *m*, aromatic), 5.28 (1H, *s*, –S–CH–), 3.10 (2H, *s*, CH$_2$). ^{13}C-NMR (100 MHz, CDCl$_3$, δ / ppm): 168.8, 163.7, 161.3, 149.7, 140.8, 134.8, 130.3, 121.7, 115.4, 64.3, 35.6. MS (*m/z*): 317 [M$^+$].

N-*(2-(2-Nitrophenyl)-4-oxothiazolidin-3-yl)isonicotinamide (2g)*. Yield: 80 %; m.p. 210–212 °C. Anal. Calcd. for $C_{15}H_{12}N_4O_4S$ (*FW* 344.35): C, 52.32; H, 3.51; N, 16.27 %. Found: C, 52.31; H, 3.50; N, 16.25 %. IR (KBr, cm^{-1}): 3328 (N–H stretching), 1774 (C=O thiazolidinone), 1660 (C=N), 1652 (C=O stretching of carbonyl), 1532 (C=C), 620 (C–S–C). ^{1}H-NMR (300 MHz, CDCl$_3$, δ / ppm): 9.05 (1H, *s*, CONH–), 7.90 (1H, *s*, N–CH–), 7.78, 8.64 (4H, *m*, Py), 7.31–7.34 (4H, *m*, aromatic), 5.21 (1H, *s*, –S–CH–), 3.11 (2H, *s*, CH$_2$). ^{13}C-NMR (100 MHz, CDCl$_3$, δ / ppm): 168.8, 163.7, 149.7, 149.0, 140.8, 134.7, 133.4, 129.6, 128.0, 124.8, 121.7, 59.7, 35.6. MS (*m/z*): 344 [M$^+$].

N-*(2-(4-(Dimethylamino)phenyl)-4-oxothiazolidin-3-yl)isonicotinamide (2h)*. Yield: 75 %; m.p. 204–206 °C. Anal. Calcd. for $C_{17}H_{18}N_4O_2S$ (*FW* 342.42): C, 59.63; H, 5.30; N, 16.36 %. Found: C, 59.61; H, 5.29; N, 16.34 %. IR (KBr, cm^{-1}): 3336 (N–H stretching), 1777 (C=O thiazolidinone), 1661 (C=N), 1635 (C=O stretching of carbonyl), 1539 (C=C), 625 (C–S–C). ^{1}H-NMR (300 MHz, CDCl$_3$, δ / ppm): 9.03 (1H, *s*, CONH–), 7.71, 8.60 (4H, *m*, Py), 7.70 (1H, *s*, N–CH–), 7.28–7.32 (4H, *m*, aromatic), 5.20 (1H, *s*, –S–CH–), 3.09 (2H, *s*, CH$_2$), 2.65 (6H, *s*, N(CH$_3$)$_2$). ^{13}C-NMR (100 MHz, CDCl$_3$, δ / ppm): 168.8, 163.7, 149.7, 149.5, 140.8, 128.7, 127.4, 121.7, 112.8, 64.3, 41.3, 35.6. MS (*m/z*): 342 [M$^+$].

2-(2-(2-Chlorophenyl)-3-isonicotinamido-4-oxothiazolidin-5-yl)acetic acid (3a). Yield: 80 %; m.p. 210–212 °C. Anal. Calcd. for $C_{17}H_{14}ClN_3O_4S$ (*FW* 391.83): C, 52.11; H, 3.60; N, 10.72 %. Found: C, 52.10; H, 3.59; N, 10.70 %. IR (KBr, cm^{-1}): 3200 (N–H stretching), 1700 (C=O thiazolidinone), 1666 (C=O stretching of carbonyl), 1610 (C=N), 1572 (C=C), 700 (C–S–C), 830 (C–Cl stretching of chlorine). ^{1}H-NMR (300 MHz, CDCl$_3$, δ / ppm): 10.00 (1H, *s*, COOH), 9.40 (1H, *s*, CONH–), 7.71–8.60 (4H, *m*, Py), 7.20 (1H, *s*, N–CH–), 6.17—6.15 (4H, *m*, Ar–H), 5.95 (1H, *s*, –S–CH–Ar). ^{13}C-NMR (100 MHz, CDCl$_3$, δ / ppm): 175.3, 173.3, 163.7, 149.7, 140.8, 134.0, 130.1, 121.7, 128.7, 128.5, 126.7, 102.5, 56.7, 47.5, 39.2. MS (*m/z*): 391 [M$^+$].

2-(2-(4-Chlorophenyl)-3-isonicotinamido-4-oxothiazolidin-5-yl)acetic acid (3b). Yield: 85 %; m.p. 216–218 °C. Anal. Calcd. for $C_{17}H_{14}ClN_3O_4S$ (*FW* 391.83): Calcd: C, 52.11; H, 3.60; N, 10.72 %. Found: C, 52.09; H, 3.58; N, 10.71 %. IR (KBr, cm^{-1}): 3204 (N–H stretching), 1702 (C=O thiazolidinone),

1664 (C=O stretching of carbonyl), 1611 (C=N), 1572 (C=C), 701 (C–S–C), 832 (C–Cl stretching of chlorine). ^{1}H-NMR (300 MHz, CDCl$_3$, δ / ppm): 10.10 (1H, *s*, COOH), 9.50 (1H, *s*, CONH–), 7.72–8.61 (4H, *m*, Py), 7.10 (1H, *s*, N–CH–), 6.18–6.16 (4H, *m*, aromatic), 5.94 (1H, *s*, –S–CH–Ar). ^{13}C-NMR (100 MHz, CDCl$_3$, δ / ppm): 175.3, 173.3, 163.7, 149.7, 140.8, 134.0, 130.1, 121.7, 128.7, 128.5, 126.7, 102.5, 56.7, 47.5, 39.2. MS (*m/z*): 391 [M$^+$].

2-(2-(2-Hydroxyphenyl)-3-isonicotinamido-4-oxothiazolidin-5-yl)acetic acid (3c). Yield: 75 %; m.p. 222–224 °C. Anal. Calcd. for C$_{17}$H$_{15}$N$_3$O$_5$S (*FW* 373.38): C, 54.68; H, 4.05; N, 11.25 %. Found: C, 54.67; H, 4.03; N, 10.23 %. IR (KBr, cm^{-1}): 3324 (N–H stretching), 1714 (C=O thiazolidinone), 1660 (C=O stretching of carbonyl), 1625 (C=N), 1579 (C=C), 710 (C–S–C). ^{1}H-NMR (300 MHz, CDCl$_3$, δ / ppm): 10.02 (1H, *s*, COOH), 9.40 (1H, *s*, CONH–), 9.33 (1H, *br*, OH), 7.69––8.51 (4H, *m*, Py), 7.50 (1H, *s*, N–CH–), 6.20–6.17 (4H, *m*, aromatic), 5.90 (1H, *s*, –S–CH–Ar). ^{13}C-NMR (100 MHz, CDCl$_3$, δ / ppm): 175.3, 173.3, 163.7, 153.7, 149.7, 140.8, 128.5, 128.0, 121.2, 118.1, 55.6, 47.5, 39.2. MS (*m/z*): 373 [M$^+$].

2-(2-(3-Hydroxyphenyl)-3-isonicotinamido-4-oxothiazolidin-5-yl)acetic acid (3d). Yield: 60 %; m.p. 238–240 °C. Anal. Calcd. for C$_{17}$H$_{15}$N$_3$O$_5$S (*FW* 373.38): C, 54.68; H, 4.05; N, 11.25 %. Found: C, 54.66; H, 4.04; N, 10.24 %. IR (KBr, cm^{-1}): 3325 (N–H stretching), 1713 (C=O thiazolidinone), 1662 (C=O stretching of carbonyl), 1624 (C=N), 1580 (C=C), 711 (C–S–C). ^{1}H-NMR (300 MHz, CDCl$_3$, δ / ppm): 10.02 (1H, *s*, COOH), 9.40 (1H, *s*, CONH–), 9.32 (1H, *br*, OH), 7.68–8.52 (4H, *m*, Py), 7.50 (1H, *s*, N–CH–), 6.20–6.17 (4H, *m*, aromatic), 5.90 (1H, *s*, –S–CH–Ar). ^{13}C-NMR (100 MHz, CDCl$_3$, δ / ppm): 175.3, 173.3, 163.7, 153.7, 149.7, 140.8, 128.5, 128.0, 121.2, 118.1, 55.6, 47.5, 39.2. MS (*m/z*): 373 [M$^+$].

2-(3-Isonicotinamido-2-(4-methoxyphenyl)-4-oxothiazolidin-5-yl)acetic acid (3e). Yield: 65 %; m.p. 220–222 °C. Anal. Calcd. for C$_{18}$H$_{17}$N$_3$O$_5$S (*FW* 387.41): C, 55.80; H, 4.42; N, 10.85 %. Found: C, 55.78; H, 4.41; N, 10.83 %. IR (KBr, cm^{-1}): 3330 (N–H stretching), 1720 (C=O thiazolidinone), 1669 (C=O stretching of carbonyl), 1629 (C=N), 1574 (C=C), 714 (C–S–C). ^{1}H-NMR (300 MHz, CDCl$_3$, δ / ppm): 10.01 (1H, *s*, COOH), 9.60 (1H, *s*, CONH–), 7.70 (1H, *s*, N–CH–), 7.63, 8.55 (4H, *m*, Py), 6.22–6.18 (4H, *m*, Ar–H), 5.91 (1H, *s*, –S–CH–Ar), 3.80 (3H, *s*, –OCH$_3$). ^{13}C-NMR (100 MHz, CDCl$_3$, δ / ppm): 175.3, 173.3, 163.7, 159.0, 149.7, 140.8, 131.5, 129.7, 121.7, 114.2, 61.8, 55.8, 47.5, 39.2. MS (*m/z*): 387 [M$^+$].

2-(2-(4-Fluorophenyl)-3-isonicotinamido-4-oxothiazolidin-5-yl)acetic acid (3f). Yield: 75 %; m.p. 190–192 °C. Anal. Calcd. for C$_{17}$H$_{14}$FN$_3$O$_4$S (*FW* 375.37): C, 54.39; H, 3.76; N, 11.19 %. Found: C, 54.38; H, 3.74; N, 11.18 %. IR (KBr, cm^{-1}): 3316 (N–H stretching), 1714 (C=O thiazolidinone), 1670 (C=O stretching of carbonyl), 1634 (C=N), 1578 (C=C), 720 (C–S–C). ^{1}H-NMR (300 MHz,

CDCl$_3$, δ / ppm): 10.04 (1H, *s*, COOH), 9.20 (1H, *s*, CONH–), 7.90 (1H, *s*, N–CH–), 7.66–8.58 (4H, *m*, Py), 6.20–6.17 (4H, *m*, aromatic), 5.93 (1H, *s*, –S–CH–Ar). ^{13}C-NMR (100 MHz, CDCl$_3$, δ / ppm): 175.3, 173.3, 163.7, 161.3, 149.7, 140.8, 134.8, 130.3, 121.7, 115.4, 61.8, 47.5, 39.2. MS (*m/z*): 375 [M$^+$].

2-(3-Isonicotinamido-2-(2-nitrophenyl)-4-oxothiazolidin-5-yl)acetic acid (3g). Yield: 80 %; m.p. 232–234 °C. Anal. Calcd. for C$_{17}$H$_{14}$N$_4$O$_6$S (*FW* 402.38): C, 50.74; H, 3.51; N, 13.92 %. Found: C, 50.73; H, 3.50; N, 13.91 %. IR (KBr, cm^{-1}): 3310 (N–H stretching), 1704 (C=O thiazolidinone), 1660 (C=O stretching of carbonyl), 1632 (C=N), 1580 (C=C), 727 (C–S–C). ^{1}H-NMR (300 MHz, CDCl$_3$, δ / / ppm): 10.03 (1H, *s*, COOH), 9.40 (1H, *s*, CONH–), 7.63, 8.31 (4H, *m*, Py), 7.50 (1H, *s*, N–CH), 6.24–6.20 (4H, *m*, Ar–H), 5.90 (1H, *s*, –S–CH–Ar). ^{13}C-NMR (100 MHz, CDCl$_3$, δ / ppm): 175.3, 173.3, 163.7, 149.0, 149.7, 140.8, 133.4, 134.7, 129.6, 128.0, 124.8, 121.7, 57.2, 47.5, 39.2. MS (*m/z*): 402 [M$^+$].

2-(2-(4-(Dimethylamino)phenyl)-3-isonicotinamido-4-oxothiazolidin-5-yl)-acetic acid (3h). Yield: 70 %; m.p. 248–250 °C. Anal. Calcd. for C$_{19}$H$_{20}$N$_4$O$_4$S (*FW* 400.45): C, 56.99; H, 5.03; N, 13.99 %. Found: C, 56.97; H, 5.01; N, 13.98 %. IR (KBr, cm^{-1}): 3315 (N–H stretching), 1710 (C=O thiazolidinone), 1666 (C=O stretching of carbonyl), 1632 (C=N), 1584 (C=C), 727 (C–S–C). ^{1}H-NMR (300 MHz, CDCl$_3$, δ / ppm): 10.06 (1H, *s*, COOH), 9.10 (1H, *s*, CONH–), 7.68–8.33 (4H, *m*, Py), 6.22–6.19 (4H, *m*, Ar–H), 7.10 (1H, *s*, N–CH–), 5.93 (1H, *s*, –S–CH–Ar), 2.72 (6H, *s*, N(CH$_3$)$_2$). ^{13}C-NMR (100 MHz, CDCl$_3$, δ / ppm): 175.3, 173.3, 163.7, 149.7, 149.5, 140.8, 128.7, 127.4, 121.7, 112.8, 57.2, 47.5, 39.2. MS (*m/z*): 400 [M$^+$].

N-(3-Chloro-2-(2-chlorophenyl)-4-oxoazetidin-1-yl)isonicotinamide (4a). Yield: 75 %; m.p. 322–324 °C. Anal. Calcd. for C$_{15}$H$_{11}$Cl$_2$N$_3$O$_2$ (*FW* 336.17): C, 53.59; H, 3.30; N, 12.50 %. Found: C, 53.58; H, 3.29; N, 12.48 %. IR (KBr, cm^{-1}): 3250 (N–H stretching), 1745 (C=O β-lactam ring), 1616 (C=O stretching of carbonyl), 1600 (C=N), 1560 (C=C), 742 (C–Cl stretching of chlorine). ^{1}H-NMR (300 MHz, CDCl$_3$, δ / ppm): 9.40 (1H, *s*, CONH–), 7.70 (1H, *s*, N–CH–), 7.68–8.33 (4H, *m*, Py), 6.61–6.63 (4H, *m*, aromatic). ^{13}C-NMR (100 MHz, CDCl$_3$, δ / ppm): 163.7, 163.5, 149.7, 143.5, 140.8, 132.2, 128.6, 128.1, 126.6, 121.7. MS (*m/z*): 335 [M$^+$].

N-(3-Chloro-2-(4-chlorophenyl)-4-oxoazetidin-1-yl)isonicotinamide (4b). Yield: 65 %; m.p. 328–330 °C. Anal. Calcd. for C$_{15}$H$_{11}$Cl$_2$N$_3$O$_2$ (*FW* 336.17): C, 53.59; H, 3.30; N, 12.50 %. Found: C, 53.57; H, 3.27; N, 12.46 %. IR (KBr, cm^{-1}): 3252 (N–H stretching), 1746 (C=O β-lactam ring), 1612 (C=O stretching of carbonyl), 1599 (C=N), 1562 (C=C), 741 (C–Cl stretching of chlorine). ^{1}H-NMR (300 MHz, CDCl$_3$, δ / ppm): 9.80 (1H, *s*, CONH–), 7.60 (1H, *s*, N–CH–), 7.67–8.32 (4H, *m*, Py), 6.62–6.64 (4H, *m*, Ar–H). ^{13}C-NMR (100 MHz, CDCl$_3$, δ / ppm): 163.7, 163.5, 149.7, 143.5, 140.8, 132.2, 128.6, 128.1, 126.6, 121.7. MS (*m/z*): 335 [M$^+$].

N-*(3-Chloro-2-(2-hydroxyphenyl)-4-oxoazetidin-1-yl)isonicotinamide* **(4c)**. Yield: 70 %; m.p. 346–348 °C. Anal. Calcd. for $C_{15}H_{12}ClN_3O_3$ (*FW* 317.73): C, 56.70; H, 3.81; N, 13.23 %. Found: C, 56.68; H, 3.80; N, 13.21 %. IR (KBr, cm^{-1}): 3256 (N–H stretching), 1749 (C=O β-lactam ring), 1614 (C=O stretching of carbonyl), 1602 (C=N), 1561 (C=C). ^{1}H-NMR (300 MHz, CDCl$_3$, δ / ppm): 9.20 (1H, *br*, OH), 9.90 (1H, *s*, CONH–), 7.64–8.31 (4H, *m*, Py), 7.40 (1H, *s*, N–CH–), 6.60–6.61 (4H, *m*, aromatic). ^{13}C-NMR (100 MHz, CDCl$_3$, δ / ppm): 163.7, 163.5, 154.0, 149.7, 140.8, 130.9, 128.1, 126.5, 121.7, 121.1, 115.7, 64.4, 61.2. MS (*m/z*): 317 [M$^+$].

N-*(3-Chloro-2-(3-hydroxyphenyl)-4-oxoazetidin-1-yl)isonicotinamide* **(4d)**. Yield: 60 %; m.p. 330–332 °C. Anal. Calcd. for $C_{15}H_{12}ClN_3O_3$ (*FW* 317.73): C, 56.70; H, 3.81; N, 13.23 %. Found: C, 56.69; H, 3.80; N, 13.22 %. IR (KBr, cm^{-1}): 3259 (N–H stretching), 1752 (C=O β-lactam ring), 1672 (C=O stretching of carbonyl), 1605 (C=N), 1562 (C=C). ^{1}H-NMR (300 MHz, CDCl$_3$, δ / ppm): 9.30 (1H, *br*, OH), 9.80 (1H, *s*, CONH–), 7.64–8.31 (4H, *m*, Py), 7.40 (1H, *s*, N–CH–), 6.60–6.61 (4H, *m*, Ar–H). ^{13}C-NMR (100 MHz, CDCl$_3$, δ / ppm): 163.7, 163.5, 156.8, 149.7, 144.9, 140.8, 129.9, 121.7, 113.9, 112.6, 67.7, 64.1. MS (*m/z*): 317 [M$^+$].

N-*(3-Chloro-2-(4-methoxyphenyl)-4-oxoazetidin-1-yl)isonicotinamide* **(4e)**. Yield: 55 %; m.p. 344–346 °C. Anal. Calcd. for $C_{16}H_{14}ClN_3O_3$ (*FW* 331.75): C, 57.93; H, 4.25; N, 12.67 %. Found: C, 57.91; H, 4.22; N, 12.65 %. IR (KBr, cm^{-1}): 3260 (N–H stretching), 1748 (C=O β-lactam ring), 1670 (C=O stretching of carbonyl), 1603 (C=N), 1558 (C=C). ^{1}H-NMR (300 MHz, CDCl$_3$, δ / ppm): 9.40 (1H, *s*, CONH–), 7.62, 8.31 (4H, *m*, Py), 7.20 (1H, *s*, N–CH–), 6.63–6.65 (4H, *m*, aromatic), 3.78 (3H, *s*, OCH$_3$). ^{13}C-NMR (100 MHz, CDCl$_3$, δ / ppm): 163.7, 163.5, 158.6, 149.7, 140.8, 135.8, 126.6, 121.7, 114.1, 67.4, 64.1. MS (*m/z*): 331 [M$^+$].

N-*(3-Chloro-2-(4-fluorophenyl)-4-oxoazetidin-1-yl)isonicotinamide* **(4f)**. Yield: 75 %; m.p. 298–300 °C. Anal. Calcd. for $C_{15}H_{11}ClFN_3O_2$ (*FW* 319.72): C, 56.35; H, 3.47; N, 13.14 %. Found: C, 56.33; H, 3.46; N, 13.12 %. IR (KBr, cm^{-1}): 3264 (N–H stretching), 1747 (C=O β-lactam ring), 1672 (C=O stretching of carbonyl), 1613 (C=N), 1560 (C=C). ^{1}H-NMR (300 MHz, CDCl$_3$, δ / ppm): 9.60 (1H, *s*, CONH–), 7.60, 8.31 (4H, *m*, Py), 7.80 (1H, *s*, N–CH–), 6.62–6.67 (4H, *m*, Ar–H). ^{13}C-NMR (100 MHz, CDCl$_3$, δ / ppm): 163.7, 163.5, 160.9, 149.7, 140.8, 139.1, 128.5, 121.7, 115.3, 67.4, 64.1. MS (*m/z*): 319 [M$^+$].

N-*(3-Chloro-2-(2-nitrophenyl)-4-oxoazetidin-1-yl)isonicotinamide* **(4g)**. Yield: 60 %; m.p. 294–296 °C. Anal. Calcd. for $C_{15}H_{11}ClN_4O_4$ (*FW* 346.73): C, 51.96; H, 3.20; N, 16.16 %. Found: C, 51.94; H, 3.19; N, 16.14 %. IR (KBr, cm^{-1}): 3268 (N–H stretching), 1740 (C=O β-lactam ring), 1662 (C=O stretching of carbonyl), 1614 (C=N), 1562 (C=C). ^{1}H-NMR (300 MHz, CDCl$_3$, δ / ppm): 9.40 (1H, *s*, CONH–), 7.63, 8.34 (4H, *m*, Py), 7.30 (1H, *s*, N–CH–), 6.64–6.66 (4H, *m*,

Ar–H). ^{13}C-NMR (100 MHz, CDCl$_3$, δ / ppm): 163.7, 163.5, 149.7, 147.2, 140.8, 137.5, 134.6, 127.6, 124.7, 121.7, 63.1, 62.8. MS (*m/z*): 346 [M$^+$].

N-*(3-Chloro-2-(4-(dimethylamino)phenyl)-4-oxoazetidin-1-yl)isonicotinami-de (4h)*. Yield: 65 %; m.p. 360–362 °C. Anal. Calcd. for C$_{17}$H$_{17}$ClN$_4$O$_2$ (*FW* 344.80): C, 59.22; H, 4.97; N, 16.25 %. Found: C, 59.21; H, 4.96; N, 16.23 %. IR (KBr, cm^{-1}): 3266 (N–H stretching), 1747 (C=O β-lactam ring), 1668 (C=O stretching of carbonyl), 1611 (C=N), 1565 (C=C). ^{1}H-NMR (300 MHz, CDCl$_3$, δ / ppm): 9.10 (1H, *s*, CONH–), 7.90 (1H, *s*, N–CH–), 7.67, 8.32 (4H, *m*, Py), 6.65–6.69 (4H, *m*, Ar–H), 2.70 (6H, *s*, N(CH$_3$)$_2$). ^{13}C-NMR (100 MHz, CDCl$_3$, δ / ppm): 163.7, 163.5, 149.7, 149.1, 140.8, 133.0, 129.2, 121.7, 112.7, 67.4, 64.1, 41.3. MS (*m/z*): 344 [M$^+$].

1-(2-(2-Chlorophenyl)-5-(pyridin-4-yl)-1,3,4-oxadiazol-3(2H)-yl)ethanone (5a). Yield: 65 %; m.p. 182–184 °C. Anal. Calcd. for C$_{15}$H$_{12}$ClN$_3$O$_2$ (*FW* 301.73): C, 59.71; H, 4.01; N, 13.93 %. Found: C, 59.70; H, 4.00; N, 13.91 %. IR (KBr, cm^{-1}): 1660 (acetyl C=O), 1614 (C=N), 1560 (C=C), 830 (C–Cl stretching of chlorine), 1500 (C–O–C). ^{1}H-NMR (300 MHz, CDCl$_3$, δ / ppm): 7.72–8.64 (4H, *m*, Py), 7.12–7.14 (4H, *m*, aromatic), 7.19 (1H, *s*, CH– oxadiazole). ^{13}C--NMR (100 MHz, CDCl$_3$, δ / ppm): 168.8, 157.0, 149.4, 142.8, 138.4, 132.2, 128.6, 128.3, 128.1, 126.6, 124.1, 78.4, 23.4. MS (*m/z*): 301 [M$^+$].

1-(2-(4-Chlorophenyl)-5-(pyridin-4-yl)-1,3,4-oxadiazol-3(2H)-yl)ethanone (5b). Yield: 60 %; m.p. 186–188°C. Anal. Calcd. for C$_{15}$H$_{12}$ClN$_3$O$_2$ (*FW* 301.73): C, 59.22; H, 4.97; N, 16.25 %. Found: C, 59.21; H, 4.95; N, 16.23. IR (KBr, cm^{-1}): 1662 (acetyl C=O), 1616 (C=N), 1562 (C=C), 834 (C–Cl stretching of chlorine), 1504 (C–O–C). ^{1}H-NMR (300 MHz, CDCl$_3$, δ / ppm): 7.73, 8.65 (4H, *m*, Py), 7.20 (1H, *s*, CH–oxadiazole), 7.13–7.15 (4H, *m*, aromatic). ^{13}C--NMR (100 MHz, CDCl$_3$, δ / ppm): 168.8, 157.0, 149.4, 138.4, 132.3, 128.6, 128.3, 124.1, 83.5, 23.4. MS (*m/z*): 301 [M$^+$].

1-(2-(2-Hydroxyphenyl)-5-(pyridin-4-yl)-1,3,4-oxadiazol-3(2H)-yl)ethanone (5c). Yield: 50 %; m.p. 198–200 °C. Anal. Calcd. for C$_{15}$H$_{13}$N$_3$O$_3$ (*FW* 283.28): C, 63.60; H, 4.63; N, 14.83 %. Found: C, 63.58; H, 4.61; N, 14.81 %. IR (KBr, cm^{-1}): 1664 (acetyl C=O), 1618 (C=N), 1563 (C=C), 1510 (C–O–C). ^{1}H-NMR (300 MHz, CDCl$_3$, δ / ppm): 9.32 (1H, *br*, OH), 7.62, 8.34 (4H, *m*, Py), 7.20 (1H, *s*, CH–oxadiazole), 7.10–7.13 (4H, *m*, aromatic). ^{13}C-NMR (100 MHz, CDCl$_3$, δ / ppm): 168.8, 157.0, 149.4, 138.4, 129.6, 128.3, 128.1, 124.1, 121.1, 115.7, 77.3, 23.4. MS (*m/z*): 283 [M$^+$].

1-(2-(3-Hydroxyphenyl)-5-(pyridin-4-yl)-1,3,4-oxadiazol-3(2H)-yl)ethanone (5d). Yield: 65 %; m.p. 210–212 °C. Anal. Calcd. for C$_{15}$H$_{13}$N$_3$O$_3$ (*FW* 283.28): C, 63.60; H, 4.63; N, 14.83 %. Found: C, 63.59; H, 4.62; N, 14.82. IR (KBr, cm^{-1}): 1664 (acetyl C=O), 1618 (C=N), 1563 (C=C), 1510 (C–O–C). ^{1}H-NMR (300 MHz, CDCl$_3$, δ / ppm): 9.32 (1H, *br*, OH), 7.62, 8.34 (4H, *m*, Py), 7.20 (1H, *s*, CH–oxadiazole), 7.10–7.13 (4H, *m*, aromatic). ^{13}C-NMR (100 MHz, CDCl$_3$, δ /

/ ppm): 168.8, 157.0, 156.8, 149.4, 141.7, 138.4, 129.9, 124.1, 113.9, 112.6, 83.8, 23.4. MS (*m/z*): 283 [M$^+$].

*1-(2-(4-Methoxyphenyl)-5-(pyridin-4-yl)-1,3,4-oxadiazol-3(2*H*)-yl)ethanone (5e)*. Yield: 55 %; m.p. 202–204 °C. Anal. Calcd. for C$_{16}$H$_{15}$N$_3$O$_3$ (*FW* 297.31): C, 64.64; H, 5.09; N, 14.13 %. Found: C, 64.62; H, 5.07; N, 14.11 %. IR (KBr, cm^{-1}): 1667 (acetyl C=O), 1615 (C=N), 1561 (C=C), 1515 (C–O–C). ^{1}H-NMR (300 MHz, CDCl$_3$, δ / ppm): 7.66, 8.38 (4H, *m*, Py), 7.22 (1H, *s*, CH–oxadiazole), 7.14–7.17 (4H, *m*, aromatic), 3.71 (3H, *s*, OCH$_3$). ^{13}C-NMR (100 MHz, CDCl$_3$, δ / ppm): 168.8, 157.0, 156.5, 149.4, 138.4, 127.9, 127.7, 124.1, 120.8, 112.1, 77.6, 23.4. MS (*m/z*): 297 [M$^+$].

*1-(2-(4-Fluorophenyl)-5-(pyridin-4-yl)-1,3,4-oxadiazol-3(2*H*)-yl)ethanone (5f)*. Yield: 65 %; m.p. 206–208 °C. Anal. Calcd. for C$_{15}$H$_{12}$FN$_3$O$_2$ (*FW* 285.27): C, 63.15; H, 4.24; N, 14.73 %. Found: C, 63.14; H, 4.23; N, 14.71 %. IR (KBr, cm^{-1}): 1663 (acetyl C=O), 1620 (C=N), 1565 (C=C), 1518 (C–O–C). ^{1}H-NMR (300 MHz, CDCl$_3$, δ / ppm): 7.69, 8.37 (4H, *m*, Py), 7.25 (1H, *s*, CH–oxadiazole), 7.13–7.18 (4H, *m*, aromatic). ^{13}C-NMR (100 MHz, CDCl$_3$, δ / ppm): 168.8, 157.0, 159.4, 149.4, 138.4, 129.4, 128.5, 128.3, 124.1, 76.7, 23.4. MS (*m/z*): 285 [M$^+$].

*1-(2-(2-Nitrophenyl)-5-(pyridin-4-yl)-1,3,4-oxadiazol-3(2*H*)-yl)ethanone (5g)*. Yield: 70 %; m.p. 196–198 °C. Anal. Calcd. for C$_{15}$H$_{12}$N$_4$O$_4$ (*FW* 312.28): C, 57.69; H, 3.87; N, 17.94 %. Found: C, 57.67; H, 3.85; N, 17.93 %. IR (KBr, cm^{-1}): 1669 (acetyl C=O), 1619 (C=N), 1563 (C=C), 1517 (C–O–C). ^{1}H-NMR (300 MHz, CDCl$_3$, δ / ppm): 7.67, 8.35 (4H, *m*, Py), 7.23 (1H, *s*, CH–oxadiazole), 7.12–7.15 (4H, *m*, aromatic). ^{13}C-NMR (100 MHz, CDCl$_3$, δ / ppm): 168.8, 157.0, 149.4, 148.2, 139.4, 138.4, 130.9, 129.4, 127.6, 124.7, 78.9, 23.4. MS (*m/z*): 312 [M$^+$].

*1-(2-(4-(Dimethylamino)phenyl)-5-(pyridin-4-yl)-1,3,4-oxadiazol-3(2*H*)-yl)-ethanone (5h)*. Yield: 75 %; m.p. 204–206 °C. Anal. Calcd. for C$_{17}$H$_{18}$N$_4$O$_2$ (*FW* 310.35): C, 65.79; H, 5.85; N, 18.05 %. Found: C, 65.78; H, 5.83; N, 18.03 %. IR (KBr, cm^{-1}): 1664 (acetyl C=O), 1624 (C=N), 1570 (C=C), 1511 (C–O–C). ^{1}H-NMR (300 MHz, CDCl$_3$, δ / ppm): 7.65, 8.33 (4H, *m*, Py), 7.26 (1H, *s*, CH–oxadiazole), 7.14–7.18 (4H, *m*, aromatic), 2.73 (6H, *s*, N(CH$_3$)$_2$). ^{13}C-NMR (100 MHz, CDCl$_3$, δ / ppm): 168.8, 157.0, 149.4, 149.1, 138.4, 129.8, 127.8, 124.1, 83.5, 41.3, 23.4. MS (*m/z*): 310 [M+].

Facile syntheses of Mannich bases of 3-[*p*-(5-arylpyrazolin-3--yl)phenyl]sydnones, as anti-tubercular and anti-microbial agents, under ionic liquid/tetrabutylammonium bromide catalytic conditions

TASNEEM TAJ[1], RAVINDRA R. KAMBLE[1]*, TEGGINMATH M. GIREESH[1]
and RAVINDRA K. HUNNUR[2]

[1]*PG Department of Studies in Chemistry, Karnatak University Dharwad-580 003 and* [2]*APL Research Centre, A Division of Aurobindo Pharma Ltd. 313, Batchupally, Hyderabad-500 072, India*

Abstract: Novel methylene bridged Mannich bases **2a**–**j** were synthesized in good to excellent yields from the pyrazoline derivative **1** using various primary/secondary amines, 37 % formalin in presence of ionic liquids/TBAB as catalyst. The structures of the newly synthesized compounds were confirmed by IR, ^{1}H- and ^{13}C-NMR and GC–MS spectroscopy, as well as elemental analysis. The title compounds were screened for their anti-tubercular and antimicrobial activities. Some of the compounds exhibited very good anti-tubercular, antifungal and antibacterial activities.

Keywords: pyrazoline; Mannich base; ionic liquids; TBAB; *MIC*; anti-tubercular activity.

INTRODUCTION

Multidrug-resistant tuberculosis is perceived as a growing hazard to human health worldwide. The fear is that the number of cases resistant to anti-tubercular drugs is on the increase.[1] One of the strategies suggested for overcoming this problem is to exploit the potential of standard short course chemotherapy based on the cheap and safe first line drugs. Furthermore, there is an urgent need for the development of new potent anti-tubercular drugs without cross resistance with known antimycobacterial agents.[2,3] This has stimulated scientists to develop novel molecules to combat these illnesses. Pantothenate synthetase (PS) is one of the potential new antimicrobial targets which are useful for the treatment of non-replicating persistent forms of *Mycobacterium tuberculosis* (*Mtb*). Therefore, the

---

discovery and development of drugs effective against non-replicating persistence (NRP) *Mtb* are considered as the highest priority among tetrabutyl (TB) drug discovery efforts.[4]

Reports convey that Mannich bases possess anti-inflammatory, antibacterial, antifungal and antihistamine activities. The synthesis of pyrazole and its *N*-aryl analogues has been the subject of consistent interest because of the wide range of applications of such heterocycles in the pharmaceutical and agrochemical Industries. Numerous compounds containing the pyrazole moiety have exhibited anti-hyperglycemic, analgesic, anti-inflammatory, antipyretic, antibacterial and seda-tive–hypnotic activity.[5–9] The role of the added pyrazole ring could be to in-crease the electron density of the system and makes the chromophore more re-sistant towards enzymatic reduction by radical species. In addition, some syd-none derivatives have been reported as potential anti-tubercular agents.[10]

Recently, ionic liquids (ILs), a kind of ion solvent, which combine the ad-vantages of both traditional molecular solvents and melt salts, have been consi-dered as promising new reaction media, and have found wide use in catalytic and non-catalytic reactions as these materials dissolve many organic as well as in-organic substances. In addition, they can be easily recycled. Moreover, their pro-perties are tunable to satisfy specific chemical tasks.[11–14]

The above observations prompted us to explore the synthetic utility of pyra-zoline derivatives using ionic liquids or tetrabutylammonium bromide (TBAB) as catalysts in the synthesis of novel Mannich bases intact with the sydnone moiety, giving novel biodynamic molecules **2a**–**j** in order to evaluate their antimicrobial and anti-tuberculosis activity.

<div align="center">EXPERIMENTAL</div>

Chemistry

Melting points were determined in open capillaries and are uncorrected. The IR spectra were recorded on a Nicolet Impact 5200 USA FT-IR instrument using KBr pellets. The ^{1}H--NMR and ^{13}C-NMR spectra were recorded on a Bruker Varian 300-MHz FT-NMR spectro-meter with TMS as the internal standard. The mass spectra were recorded on Shimadzu Japan QP2010 S spectrometer and the elemental analyses were realized using Heraeus CHN rapid analyzer. The purity of the compounds was checked by thin layer chromatography (TLC) on silica gel plates using benzene and ethyl acetate as eluents. The pharmacological evaluations were performed at the Department of Microbiology and Immunology, NGH College of Dental sciences, Belgaum, Karnataka, India. The log *P* values were calculated using ACD Chem-sketch software for the structural analogues of the synthesized compounds and are uncor-rected.

The pyrazoline derivative **1** required for the present work was prepared by the reaction of the chalcone and hydrazine hydrate according to a reported method.[15] The acidic ionic liquid catalysts were synthesized according to literature procedures.[16] Commercially available TBAB was used for the reaction at 10 mol %. The pyrazoline derivative **1** upon reaction with primary/secondary amines in presence of 37 % formalin and an ionic liquid as catalyst gave

the Mannich bases **2a**–**j** (Scheme 1). All the products are solids, with exception of the compounds **2d** and **2f** which were isolated as semisolids.
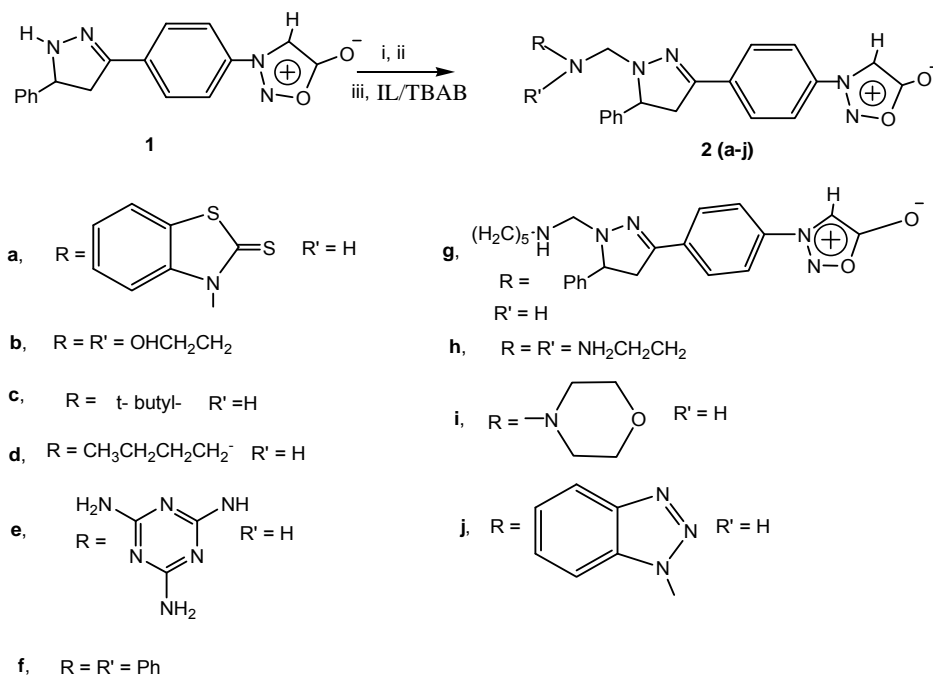
Scheme 1. Synthesis of Mannich bases **2a**–**j**.

*Preparation of 3-[4-(5-phenyl-4,5-dihydro-1*H-*pyrazol-3-yl)phenyl]sydnone (1)*

The pyrazoline derivative **1** was synthesized according to a literature method.[17] Yellow solid. Yield: 80 %, m.p. 171–173 °C.

Preparation of 2a–j

To the slurry of compound **1** (0.01 mol), 50 % aqueous ethanol (5 ml) and 37 % formalin (5 ml) was added dropwise an amine (0.01 mol) and an ionic liquid catalyst (0.01 mmol) with cooling and shaking. The reaction mixture was allowed to stand at RT for 1 h with occasional stirring after which it was warmed on a steam bath for 3 h for the conventional synthesis method. When using an ionic liquid 10 mol %, the reaction time was unchanged. The catalyst was recovered by extracting with diethyl ether.

When TBAB was used as catalyst, the reaction time was 2 h. At the end of this period, the solvent was evaporated and the contents were cooled. The products thus separated were filtered and recrystallized (except **2d** and **2f**) in ethanol, petroleum ether and chloroform.

Biological assays

Antimicrobial assay. Preliminary screening was conducted for all the compounds at 100 µg ml^{-1} concentration against two Gram-positive bacteria, *Staphylococcus aureus* – ATCC 25293 and *Bacillus subtilis* – ATCC 6633 and Gram-negative bacteria *Pseudomonas aeruginosa* – ATCC 10145 and *Escherichia coli* – ATCC 35218, and against two fungal strains *Candida albicans* 10231 and *Candida fumigatus* 74359.

The protocol for the antimicrobial activity assay was as follows.[18]

Dimethylformamide was used as the solvent control. The bacterial cultures were inoculated on Mueller Hinton Agar (Merck) and fungal cultures on Potato Dextrose Agar. Media (20 ml) were poured into each sterilized Petri dish (99 mm) and media were inoculated homogeneously with the liquid cultures by the spread plate method. All the compounds were dissolved in dimethyl sulfoxide (DMSO) to obtain a concentration of 100 µg/µl. Each sample (100 µl) was directly loaded into the wells of agar plates. The plates inoculated with bacteria were incubated at 37 °C for 24 h and the fungal cultures were incubated at 25 °C for 72 h. All the determinations were performed in triplicate. The standards ampicillin (100 µg ml^{-1}) for the antibacterial and clotrimazole (100 µg ml^{-1}) for the antifungal assays were used as the positive controls and 100 µl of DMSO was used as the negative control. The zones of inhibition were recorded in mm.

Different series of dilutions of the compounds were made (0.5–10.0 µg ml^{-1}) to determine the minimum inhibitory concentration (*MIC*).

Anti-tubercular assay. The anti-tubercular activity of the test compounds were evaluated against the standard strain of *Mycobacterium tuberculosis* H37Rv. The antibiotic standards used were streptomycin and pyrazinamide. The procedure followed for the anti-tubercular activity assay involved the use of Middlebrook 7H-9 broth. The basal medium was prepared according to the manufacturer's instructions (Hi-Media) and sterilized by autoclaving. Then, 4.5 ml of broth was poured into every sterile bottle. To this, 0.5 ml of albumin dextrose catalase (ADC) supplement consisting of catalase, dextrose and bovine serum albumin (BSA) fraction v was added. Then, a stock solution of the test compound was prepared (10 mg ml^{-1}). From this, appropriate amounts of the solution were transferred to the media bottles to achieve final concentrations of 25, 50, 100 µg ml^{-1}. Finally, 10 µl of a suspension of *M. tuberculosis* H37Rv strain (10^5 organisms ml^{-1}, adjusted by the McFarmland turbidity standard) was transferred to each of the bottles and incubated at 37 °C. Together with these, a growth control without the compound and drug controls were also set up. The bottles were inspected for growth twice a week for a period of three weeks. The appearance of turbidity indicated the growth and inferred resistance to the compound. The growth was confirmed by making a smear from each bottle and performing a Ziehl–Neelsen (ZN) stain.

RESULTS AND DISCUSSION

The synthesis of the investigated compounds by the conventional method resulted into low yields. Use of ionic liquids **1**–**4** enhanced the yields, but phase transfer catalyst (PTC) method using TBAB gave excellent yields along with increased reaction rates. Various ionic liquids (IL1–IL4) and TBAB catalysts were tried at different concentrations and finally it was observed that 10 mol % of the catalyst (ionic liquids and TBAB) gave good yields (Table I). For the synthesis of long chain alkylated Mannich bases, *viz.*, **2d** and **2g**, IL3 and IL4 gave poor yields as the products could not be isolated in the desired quantity as either solids or semisolids, which posed great difficulty for product characterization. For the other compounds, the catalyst used and the range of yields are depicted in Table II. The ionic liquids which gave better results are also reported. It is interesting to note that the TBAB catalyst gave excellent yields for all the final compounds. The reaction time was unchanged when an ionic liquid (10 mol %)

was used, whereas the use of TBAB reduced the reaction time to 2 h. The ionic liquid Hmim Tsa⁻ (IL1) gave better yields for the final compounds **2a**, **2e** and **2i**, whereas the yields of compounds **2b, 2c**, **2f** and **2j** were good when Hmim SO_4^- (IL2) was used. The catalytic activities of Bmim $[H_2PO_4]^-$ (IL3) and Bmim $[HSO_4]^-$ (IL4) were much lower and the yields of **2d** and **2h** were negligible under IL3 and IL4 conditions. The ionic liquids IL1 and IL2 did not give the products **2d** and **2g**.

TABLE I. Methods and catalysts employed for the reactions (10 mol %) and the obtained yields

Catalyst	Yield range, %
Conventional method	
Without catalyst	60–70
Ionic liquids method	
Hmim Tsa⁻ (IL1)	65–75
Hmim SO_4^- (IL2)	68–76
Bmim $[H_2PO_4]^-$ (IL3)	30–35
Bmim $[HSO_4]^-$ (IL4)	25–34
TBAB	80–85

TABLE II. Yields of the respective compounds using the conventional method and employing catalysts

Compound	Method			
	Conventional	Ionic liquids		TBAB
	Yield, %	Catalyst	Yield,%	Yield, %
2a	67	IL1	70	82
2b	65	1L2	72	85
2c	68	IL2	75	84
2d	69	IL3	–	78
2e	70	IL1	70	87
2f	64	IL2	72	89
2g	66	IL4	34	85
2h	67	IL2	74	80
2i	69	IL1	75	88
2j	66	IL2	77	85

The structures of the Mannich bases **2a**–**j**, given in the Supplementary material, were confirmed by IR, NMR ([1]H- and [13]C-), MS and elemental analyses, the data are also given as Supplementary material. In their IR spectra, all the compounds exhibited a common strong absorption band at around 1748–1754 cm⁻¹ and a medium intensity sharp band at around 2950–3150 cm⁻¹, due to ν(C–H) of sydnone ring. In addition, another common sharp band was observed at around 1580–1595 cm⁻¹, due to C=N stretching frequencies of the pyrazoline ring.

Compound **2a** showed a weak absorption band at around 1420 cm⁻¹ due to C=S stretching. Compound **2b** exhibited a broad band at about 3427 cm⁻¹ due to

the two OH groups. Similarly, **2c** and **2d** showed sharp medium bands at 3426 and 3444 cm^{-1} arising from N–H stretching. Two weak stretching bands at around 3405 and 3415 cm^{-1} were present in the spectrum of compound **2e** due to the symmetric and asymmetric stretching frequencies of NH$_2$ groups attached to the triazine ring. Compound **2g** did not show any other significant bands except strong absorption at 2930 and 2922 cm^{-1} due to CH$_2$ stretching. Compound **2h** also presented two weak bands at around 3439 and 3445 cm^{-1} due to N–H stretching. Compounds **2i** and **2j** did not show any other significant stretching bands.

The ^{1}H-NMR spectral analysis of the title compounds resulted in the following observations. All the compounds gave a singlet in the range δ 6.65–6.75 ppm due to the proton attached at the C$_4$ carbon of the sydnone ring. The protons of the pyrazole ring, *i.e.*, the methine proton and the diastereotopic methylene protons exhibited a characteristic ABX pattern. The methylene protons can be assigned as H$_A$ and H$_B$ and the methine proton as Hx. H$_A$ and H$_B$ are diastereotopic and also anisochronous as they differ in their chemical shift and since this difference is not large, they are identified as AB protons. The methine proton on the adjacent carbon with a larger downfield shift is the Hx proton and all together, they form an ABX pattern. The H$_A$ and H$_B$ protons appear as doublet of doublets due to geminal and vicinal coupling. These H$_A$ and H$_B$ differ in coupling with Hx and hence they are also anisogamous. The H$_A$ proton appears as a doublets of doublet in the range δ 3.48–3.73 ppm with two coupling constants, $J_{AB} = 17.6$ Hz and $J_{Ax} = 4.5$ Hz. H$_B$ also appears as doublet of doublets at 3.08––3.47 ppm, whereby $J_{BA} = 17.6$ Hz and $J_{BX} = 11.8$ Hz. The Hx proton always appears as a four-line spectrum with $J_{XA} = 4.49$ Hz and $J_{XB} = 11.84$ in the δ range 4.32–4.92 ppm. The methylene protons attached to the nitrogen of pyrazole appear in the δ range 3.50–3.75 ppm.

The ^{1}H-NMR spectrum of **2a** showed a singlet at δ 3.45 ppm for two protons due to presence of methylene groups. The aromatic protons appear as a multiplet in the δ range 7.32–7.76 ppm due to protons on benzothiazoline-2-thione and the phenyl ring attached to the pyrazoline ring. The ^{1}H-NMR spectrum of **2b** showed a singlet at δ 3.64 ppm for two protons due to the presence of methylene groups attached to the nitrogen atom of the pyrazoline ring. The remaining two sets of methylene groups appeared as two sets of triplets at δ 4.38 (those attached to nitrogen) and 4.83 ppm (those attached to the OH group). The aromatic protons appeared as a multiplet in the region δ 7.27–7.87 ppm for nine protons.

Compound **2c** exhibited the following ^{1}H-NMR signature. A singlet for 9 protons was observed at δ 1.78 ppm due to *t*-butyl and another singlet at δ 3.64 ppm for 2 protons due to the methylene group. Similarly, a broad singlet was observed at 5.15 ppm (D$_2$O exchangeable) due to NH protons. Compound **2d** showed a singlet at δ 3.71 ppm due to the methylene group present in between the pyrazoline ring and the butylamine moiety and another singlet at δ 4.92 ppm (D$_2$O

exchangeable). The *n*-butyl group attached to the nitrogen atom gave a triplet at δ 1.05 ppm due to the methyl protons and another triplet in the range δ 4.11 ppm due to methylene protons attached to the nitrogen. The two methylene groups present in between the methyl and the methylene adjacent to the nitrogen appear as a multiplet in the range δ 2.70–2.96 ppm. The aromatic protons appear as multiplets in the region δ 6.77–7.83 ppm.

Compound **2e** showed a singlet at δ 3.71 ppm and a broad singlet at δ 5.08 (D_2O exchangeable) due to NH_2 protons, whereas compound **2f** showed a complex multiplet within the range 7.03–8.21 ppm for 19 aromatic protons. A multiplet at δ 1.34–2.40 ppm of 10 aliphatic protons was observed for compound **2g**, in which the 5 methylene group chain is flanked by two pyrazoline phenylsydnone groups. This compound also exhibited two doublets of doublets for 4 protons and one four line spectrum as a doublet of doublets for 2 methine protons, one in each lead pyrazoline ring. Compound **2h** showed a multiplet for 4 protons at δ 0.88–2.17 ppm due to the two sets of methylene protons attached to nitrogen atoms and another set of 2 protons as a singlet at 3.53 ppm.

A multiplet at δ 2.45–2.63 ppm appeared due to the methylene protons of morpholine in the spectrum of compound **2i**. Compound **2j** exhibited a singlet due to the methylene group spaced between the benzotriazole and the pyrazole ring at δ 3.75 ppm. The aromatic protons appeared as multiplet in the range δ 7.28–7.89 ppm.

The ^{13}C-NMR spectra of all the compounds showed signals in the respective regions.

Furthermore, in the electron impact studies, all the compounds showed molecular ion peaks at their respective *m/z* value.

Antibacterial activity assay

The *MIC* values for compounds **2a**–**j** and the standard obtained in the *in vitro* anti-bacterial studies, which ranged from 0.5–4 µg ml^{-1}, are given in Table III. These activities are comparable to those of a number of common pyrazole derivatives reported in the literature. The anti-bacterial activity of all the compounds against *S. aureus*, *B. subtilis*, *P. aeruginosa* and *E. coli* showed good potencies compared to the control drug ampicillin. From the results, it is apparent that among the synthesized compounds **2a**, **2b** and **2f** showed excellent activity against *B. subtilis* with *MIC* values 0.5–1.5 µg ml^{-1}, and *P. aeruginosa* with values of 1–2.5 µg ml^{-1}. Compounds **2c**, **2e**, **2f**, **2h** and **2j** showed potent inhibition against *S. aureus* with values ranging from 1–3 µg ml^{-1}. Compounds **2a**, **2f** and **2j** showed good activity against *E. coli* with values of 1–3 µg ml^{-1}. Among the ten screened compounds, almost all of them exhibited promising inhibition against the bacterial cultures compared to the control drug ampicillin.

Antifungal activity assay

The *MIC* values for compounds **2a**–**j** and the standard in the *in vitro* anti--fungal studies are represented in Table III. Among the test compounds, interesting activities were found for compounds **2a**, **2b**, **2f**, **2e**, **2g**, and **2i**, which showed potent inhibition against *C. albicans* with *MIC* values in the range 1.5–3 µg ml^{-1}. Compounds **2b**, **2c** and **2i** possessed favorable *MIC* values against *C. fumigatus*, having values in the range 2–3.5 µg ml^{-1}. The anti-fungal activities indicated that some of the derivatives exhibited a broad spectrum of activity against the tested fungi, with compounds having electron donating groups appended to the pyrazole moiety exhibiting a better spectrum of activity than the reference drug clotrimazole.

TABLE III. Antibacterial and antifungal activities (*MIC* / µg ml^{-1}) of the compounds **2a**–**j** (control: DMSO)

Entry No.	*B. subtilis* ATCC 6633	*S. aureus* ATCC 25293	*E. coli* ATCC 35218	*P. aeruginosa* ATCC 10145	*C. albicans* ATCC 10145	*C. fumigates* ATCC 74359
2a	1.5	1	3	3.5	3	2
2b	2	1	2	3.5	4	3.5
2c	0.5	3	1.5	2	1.5	3.5
2d	0.5	3	1	2.5	2	2.5
2e	0.5	2.5	2	2	3	2
2f	1	3	3	3.5	3.5	2
2g	0.5	1.5	2	1	4	3
2h	0.5	2	2	2	2	3
2i	1	2	2	1.5	3	2
2j	1	2	3	1.5	1.5	2.5
Ampicillin	0.5	1	2	2	–	–
Clotrimazole	–	–	–	–	2	2

Anti-tubercular activity assay

The results of the anti-tubercular activity studies are given in Table IV, from which it can be seen that the compounds with electron donating groups *viz.*, **2c**, **2d**, **2e**, **2g** and **2i** exhibited excellent inhibition (*MIC*) at a concentration of less than 5 µg ml^{-1}. Compounds **2b**, **2f**, **2h** and **2j** showed moderate inhibition at a concentration of 10 µg ml^{-1}. Compound **2a** with benzothiazoline-2-thione showed activity only at a concentrations of 25 µg ml^{-1} as compared to the standards used, *viz.*, streptomycin (7.5 µg ml^{-1}) and pyrazinamide (10 µg ml^{-1}). The encouraging activities are attributed to the presence of long alkylating chains with electron donating groups, *viz.*, OH, NH$_2$, methylene and ethylene through mesomeric effect, appended to the pyrazoline moiety.

The log *P* values of the compounds are given in Table V. To qualify a compound as a drug candidate, it is analyzed by the parameters set by the Lipinski rule of five. The log *P* value is an important physico-chemical property indi-

cating lipophilicity and the ability of a molecule to cross the various biological membranes. According to the Lipinski rule of five, with a log P value below 5, it is feasible for a compound to be future drug. The synthesized compounds showed marginal lipophilicity within the range of 1.20–5.0. The molecular weight of a compound is related to its *in vivo* administration. All the synthesized compounds had a molecular weight within the acceptable range, *i.e.*, 400–500 g mol^{-1}.

TABLE IV. Anti-tubercular activity of the synthesized compounds (Strain H37Rv); standard: streptomycin, 7.5 µg ml^{-1}, pyrazinamide, 10 µg ml^{-1}; all compounds tested at concentrations of 5, 10 and 25 µg ml^{-1}

Entry No.	MIC / µg ml^{-1}
2a	25
2b	4.5
2c	5
2d	3.5
2e	5
2f	10
2g	5
2h	10
2i	3.5
2j	12

TABLE V. The calculated log P values of the newly synthesized compounds

Entry No.	log P
1	1.83
2a	3.73
2b	1.49
2c	2.41
2d	2.77
2e	1.20
2f	5.03
2g	Not applicable
2h	1.38
2i	1.62
2j	2.96
INH	0.887
Nifuroxazide	0.059

According to the Lipinski rule, a less than five-heteroatom moiety can be considered as a probable candidate as a drug. The log P values depict the penetration of the drug into the cell membrane. As value of log P value increases, the penetration also increases. Compounds **2b**, **2c**, **2d**, **2e** and **2i** showed low MIC values and high log P values, which show that these moieties have better penetration values and can be considered for further studies as drugs.

CONCLUSIONS

A simple and efficient method for the synthesis of novel methylene-bridged Mannich bases of benzothiazoline-2-thione, morpholine, biphenyl and benzotriazole derivatives was developed. It is believed that the procedural simplicity, the efficiency and the easy accessibility of the reaction partners give access to a wide array of heterocyclic frameworks equipped with a pendant pyrazoline unit. The use of environmental friendly catalysts, *viz.*, an ionic liquid and TBAB is an added advantage. TBAB as a catalyst gave excellent results in terms of yields.

The results of the anti-tubercular screening revealed that of the ten synthesized compounds, five showed good inhibition while the other five compounds displayed moderate to low inhibition.

SUPPLEMENTARY MATERIAL

Structures of the prepared compounds and their spectral data are available electronically at http://www.shd.org.rs/JSCS/, or from the corresponding author on request.

И З В О Д

ЈЕДНОСТАВНА СИНТЕЗА МАНИХОВИХ БАЗА 3-[*p*-(5-АРИЛ-ПИРАЗОЛИН-3-ИЛ)- -ФЕНИЛ]СИДНОНА У ПРИСУСТВУ КАТАЛИТИЧКИХ КОЛИЧИНА ТВАВ/ЈОНСКЕ ТЕЧНОСТИ, КАО АНТИ-ТУБЕРКУЛОЗНИХ И АНТИ-МИКРОБНИХ АГЕНАСА

TASNEEM TAJ[1], RAVINDRA R. KAMBLE[1], T. M. GIREESH[1] и RAVINDRA K. HUNNUR[2]

[1]*PG Department of Studies in Chemistry, Karnatak University Dharwad-580 003 u* [2]*APL Research Centre, A Division of Aurobindo Pharma Ltd. 313, Batchupally, Hyderabad-500 072, India*

Синтетисане су нове Манихове базе **2a**–**j**, у добром до одличном приносу, полазећи од пиразолинског деривата **1** употребом различитих примарних/секундарних амина и 37 % формалдехида, у присуству каталитичких количина ТВАВ/јонске течности. Структура нових једињења потврђена је IC, NMR (^{1}H-, ^{13}C-), GC-MS и елементалном анализом. Испитана је антитуберкулозна и антимикробна активност добијених једињења. Нека од њих показују веома добру антитуберкулозну, антифунгалну и антибактеријску активност.

(Примљено 8. јула 2010, ревидирано 7. јануара 2011)

REFERENCES

1. S. Rollas, S. Güniz Küçükgüzel, *Molecules* **12** (2007) 1910
2. T. AbouI-Fadl, A. H. Faragany Mohammed, E. A. S. Hassan, *Arch. Pharm. Res.* **26** (2003) 778
3. R. K. Mali, R. R. Somani, M. P. Toraskar, K. K. Mali, P. P. Naik, P. Y. Shirodkar, *Int. J. Chem. Tech. Res.* **1** (2009) 168
4. S. Velaparthi, M. Brunsteiner, R. Uddin, B. Wan, S. G. Franzblau, P. A. Petukhov, *J. Med. Chem.* **51** (2008) 1999
5. S. Peruncheralathan, T. A. Khan, H. Ila, H. Junjappa, *J. Org. Chem.* **70** (2005) 10030
6. K. L. Kees, J. J. Fitzgerald, K. E. Steiner Jr., J. F. Mattes, B. Mihan, T. Tosi, D. Mondoro, M. L. McCaleb, *J. Med. Chem.* **39** (1996) 3920
7. S. Manfredini, R. Bazzanini, P. G. Baraldi, M. Guarneri, D. Simoni, M. E. Marongiu, A. Pani, E. Tramontano, P. L. Colla, *J. Med. Chem.* **6** (1992) 917

8. L. N. Jungheim, *Tetrahedron Lett.* **30** (1989) 1889
9. P. Kim, S. Kang, H. I. Boshoff, J. Jiricek, M. Collins, R. Singh, U. H. Manjunatha, P. Niyomrattanakit, L. Zhang, M. Goodwin, T. Dick, T. H. Keller, C. S. Dowd, C. E. Barry, *J. Med. Chem.* **52** (2009) 1329
10. J. J. Jogul, B. V. Badami, *J. Serb. Chem. Soc.* **71** (2006) 851
11. A. C. Cole, J. L. Jensen, I. Ntai, K. L. T. Tran, K. J. Weaver, D. C. Forbes, J. H. Davis Jr., *J. Am. Chem. Soc.* **124** (2002) 5962
12. T. Welton, *Chem. Rev.* **99** (1999) 2071
13. P. Wasserscheid, W. Keim, *Angew. Chem. Int. Ed.* **39** (2000) 3773
14. R. Sheldon, *Chem. Commun.* **23** (2001) 2399
15. G. Zhao, T. Jiang, H. Gao, B. Han, J. Huang, D. Sun, *Green Chem.* **6** (2004) 75
16. G. V. P. Rao, P. N. Reddy, Y. T. Reddy, V. N. Kumar, B. Rajitha, *Ind. J. Chem.* **44B** (2005) 1109
17. D. B. Dambal, P. P. Pattanashetti, R. K. Tikare, B. V. Badami, G. S. Puranik, *Indian J. Chem.* **23B** (1984) 186
18. A. M. Revol-Junelles, R. Mathis, F. Krier, A. Delfour, G. Lefebvre, *Lett. Appl. Microbiol.* **23** (1996) 120.

SUPPLEMENTARY MATERIAL TO

Facile syntheses of Mannich bases of 3-[*p*-(5-arylpyrazolin-3--yl)phenyl]sydnones, as anti-tubercular and anti-microbial agents, under ionic liquid/tetrabutylammonium bromide catalytic conditions

TASNEEM TAJ[1], RAVINDRA R. KAMBLE[1]*, TEGGINMATH M. GIREESH[1]
and RAVINDRA K. HUNNUR[2]

PG Department of Studies in Chemistry, Karnatak University Dharwad-580 003 and [1]APL Research Centre, A Division of Aurobindo Pharma Ltd. 313, Batchupally, Hyderabad-500 072, India

STRUCTURES OF THE PREPARED COMPOUNDS

2a

2b
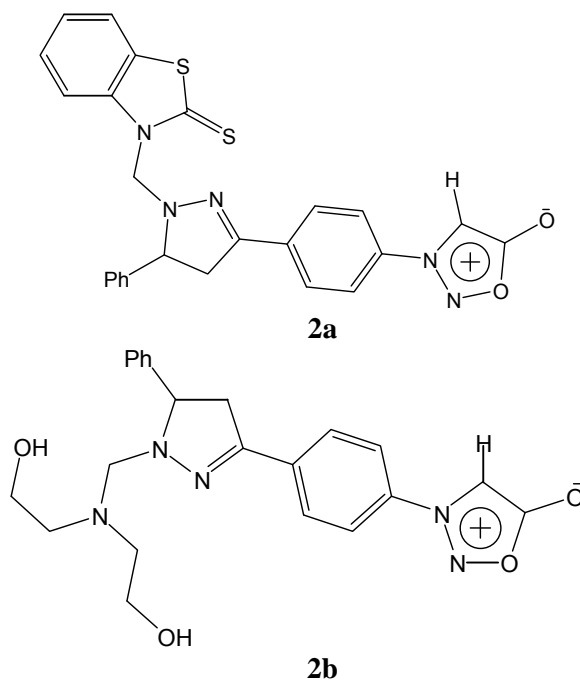
* Corresponding author. E-mail: kamchem9@gmail.com

TASNEEM TAJ *et al.*

2c

2d

2e

2f

2g
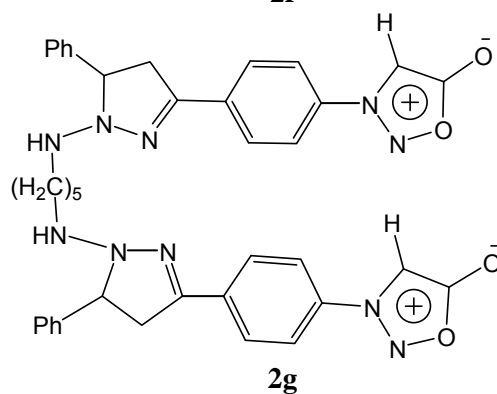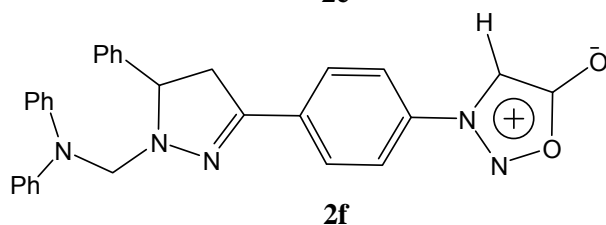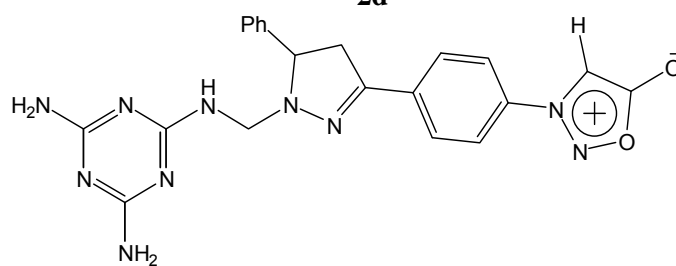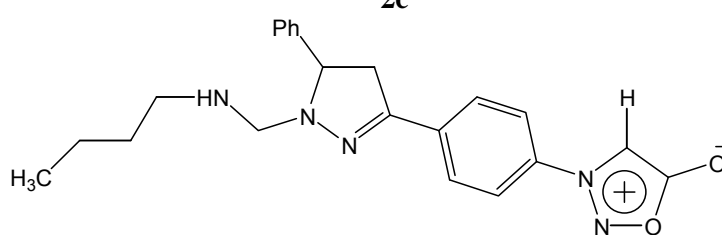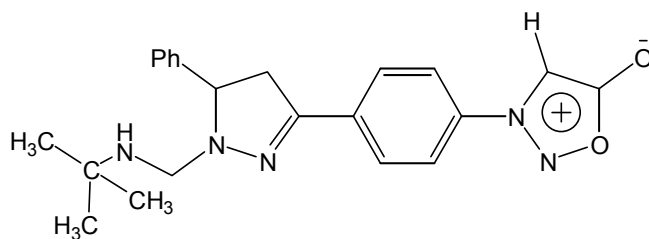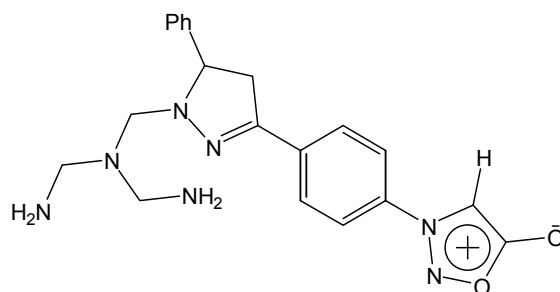
2h
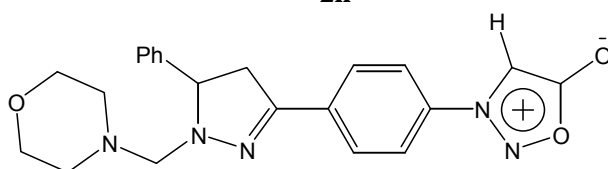
2i
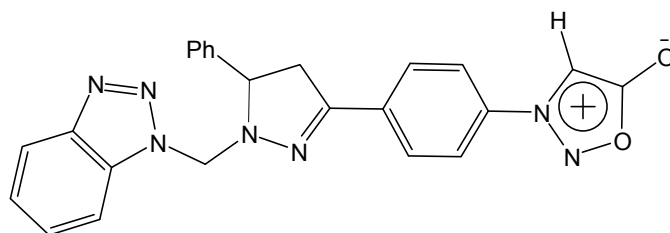
2j

ANALYTICAL AND SPECTRAL DATA OF THE SYNTHESIZED COMPOUNDS **2a**–**j**

3-{4-[5-Phenyl-1-(2-thioxobenzothiazol-3-ylmethyl)-4,5-dihydro-1H-pyrazol-3--yl]phenyl}sydnone (2a). Yellow amorphous solid (ethanol), R_f 0.88*, m.p. 95–96 °C. Anal. Calcd. for $C_{25}H_{19}N_5O_2S_2$: C, 68.85; H, 3.91; N, 14.43 %. Found: C, 68.84, H, 3.89, N, 14.41 %. IR (KBr, cm^{-1}): 2854 (–CH stretching of sydnone ring), 1754 (–C=O stretching of sydnone ring), 1595 (–C=N stretching of pyrazole ring). ^{1}H-NMR (300 MHz, CDCl$_3$, δ / ppm): 3.00 (1H, *dd*, –CH$_2$, H$_A$, *J* = = 12.05 Hz), 3.45 (2H, s, –CH$_2$, N–CH$_2$–N), 3.48 (1H, *dd*, –CH$_2$, H$_B$, *J* = 12.45 Hz), 4.56 (1H, *dd*, –CH, H$_X$, J_{XA} = 3Hz, J_{XB} = 9 Hz), 6.65 (1H, *s*, –C$_4$–H of sydnone), 7.32–7.43 (9H, *m*, aromatic), 7.70 (2H, *m*, N$_3$-aromatic), 7.76 (4H, *d*, N$_3$-aromatic). ^{13}C-NMR (300 MHz, CDCl$_3$, δ / ppm): 193.9 (C=S), 161 (C=O), 155.6 (C=N), 140.1, 137.2, 131.6, 131.0, 129.9, 129.8, 129.6, 129.5, 129.5, 129.3, 129.2, 128.3, 128.2, 128.1, 128.0, 126.8, 125.6, 125.5, 124.8, 116.7 (CH), 72.7 (CH$_2$), 48.7 (CH), 40.1 (CH$_2$). MS (*m/z*, (relative abundance, %)): 485 (M$^+$, 85), 321, 413, 457, 180.8, 161.0, 102.0, 84, 71, 57, 42.

---

* The eluents used were hexane or ethyl acetate for all compounds.

3-{4-[1-(Bis(2-hydroxyethyl)aminomethyl)-5-phenyl-4,5-dihydro-1H-pyrazol-3-yl]phenyl}sydnone (2b). Yellow amorphous solid (pet. ether), R_f 0.91, m.p. 85–86 °C. Anal. Calcd. for $C_{22}H_{25}N_5O_4$: C, 62.41; H, 5.91; N, 16.54 %. Found: C, 62.39, H, 5.89, N 16.51 %. IR (KBr, cm^{-1}): 3427 (–OH stretching of CH_2OH), 2922 (–CH stretching of sydnone ring), 1749 (–C=O stretching of sydnone ring), 1594 (–C=N stretching of pyrazole ring). ^{1}H-NMR (300 MHz, CDCl$_3$, δ / ppm.): 3.09 (1H, *dd*, –CH_2, H_A, J = 10.88 Hz), 3.53 (1H, *dd*, –CH_2, H_B, J = 11.00 Hz), 3.64 (2H, *s*, –CH_2, N–CH_2–N), 4.32 (1H, *dd*, –CH, H_X, J_{XA} = 4.38 Hz, J_{XB} = 11.31 Hz), 4.38 (4H, *t*, –CH_2N), 4.83 (4H, *t*, –CH_2OH), 5.02 (2H, *s*, –OH, D_2O exchangeable) 6.75 (1H, *s*, –C_4–H of sydnone), 7.27–7.81 (9H, *m*, aromatic). ^{13}C-NMR (300 MHz, CDCl$_3$, δ / ppm): 161 (C=O), 155.6 (C=N), 137.2, 131.5, 131.0, 129.8, 129.7, 129.5, 129.4, 128.3, 128.3, 128.1, 128.0, 126.8, 116.7, 73.4, 62.4, 62.4, 54.5, 54.5 (CH_2), 49.0 (CH), 40.1 (CH_2). MS (*m/z*, (relative abundance, %)): 424 (M$^+$, 35), 404, 381, 367, 247, 323, 305, 291, 263, 242, 230, 214, 200, 172, 183, 155, 144,129, 117, 103, 84, 71, 57, 42, 40.

3-{4-[1-(t-Butylaminomethyl)-5-phenyl-4,5-dihydro-1H-pyrazol-3-yl]phenyl}-sydnone (2c). Yellow amorphous solid (chloroform), R_f 0.93, m.p. 76–77 °C. Anal. Calcd. for $C_{22}H_{25}N_5O_2$: C, 67.51; H, 6.39; N, 17.90 %. Found: C, 67.50, H, 6.37, N 17.92 %. IR (KBr, cm^{-1}): 3130 (–NH stretching of secondary amine), 2924 (–CH stretching of sydnone ring), 1748 (–C=O stretching of sydnone ring), 1593 (–C=N stretching of pyrazole ring). ^{1}H-NMR (300 MHz, CDCl$_3$, δ / ppm): 1.78 (9H, *s*, (–CH_3)$_3$C), 3.09 (1H, *dd*, –CH_2, H_A, J = 14.95 Hz), 3.53 (1H, *dd*, –CH_2, H_B, J = 15.10 Hz), 3.64 (2H, *s*, –CH_2, N–CH_2–N), 4.38 (1H, *dd*, –CH, H_X, J_{XA} = 4.42 Hz, J_{XB} = 11.38 Hz), 5.15 (1H, *s*, –NH, D_2O exchangeable), 6.76 (1H, *s*, –C_4–H of sydnone ring), 7.27–7.87 (9H, *m*, aromatic). ^{13}C-NMR (300 MHz, CDCl$_3$, δ / ppm): 161 (C=O), 155.6 (C=N), 137.2, 131.6, 131.0 (C–aromatic), 129.9, 129.6, 129.4, 129.0, 128.3, 128.3, 128.1, 128.0, 126.8 (CH-aromatic), 116.7 (CH), 63.4 (CH_2), 48.7 (CH), 45.4 (**C**–(CH_3)$_3$), 40.1 (CH_2), 31.0 (CH_3). MS (*m/z*, (relative abundance, %)): 391 (M$^+$, 40), 382, 339, 328, 313, 298, 284, 269, 260, 247, 232, 220, 201, 195, 173, 160, 156, 146, 131, 116, 104, 91, 77, 65, 41.

3-[4-(1-(Butylaminomethyl)-5-phenyl-4,5-dihydro-1H-pyrazol-3-yl)phenyl]sydnone (2d). Brown semi-solid (pet ether), R_f 0.90. Anal. Calcd. for $C_{22}H_{25}N_5O_2$: C, 67.51; H, 6.39; N, 17.90 %. Found: C, 67.50, H, 6.37, N, 17.92 %. IR (KBr, cm^{-1}): 3414 (–NH stretching of secondary amine), 2956 (–CH_2 stretching of *n*-butyl amine), 2929 (–CH stretching of sydnone ring), 1751 (–C=O stretching of sydnone ring), 1594 (–C=N stretching of pyrazole ring). ^{1}H-NMR (300 MHz, CDCl$_3$, δ / ppm): 1.05 (3H, *t*, –CH_3), 2.70–2.96 (4H, *m*, –CH_2) 3.57 (1H, *dd*, –CH_2, H_A, J = 12.69 Hz), 3.90 (1H, *dd*, –CH_2, H_B, J = 12.89 Hz), 3.94 (2H, *s*, –CH_2, N–CH_2–N), 3.92 (2H, *t*, –CH_2), 4.11 (2H, *t*, –CH_2), 4.23 (1H, *dd*, –CH, H_X, J_{XA} = 3.60 Hz, J_{XB} = 10.44 Hz), 4.92 (1H, *s*, NH, D_2O exchangeable), 6.77–7.83 (9H,

m, aromatic), 6.75 (1H, *s*, –C$_4$–H of sydnone). ^{13}C-NMR (300 MHz, CDCl$_3$, δ / ppm): 163.5 (C=O), 155.6 (C=N), 137.2, 132.0, 131.5, 129.7, 129.5, 129.4, 129.0, 128.3, 128.3, 128.1, 128.0, 126.8, 116.7 (CH), 68.7 (CH$_2$), 48.7 (CH), 46.6, 40.1, 34.1, 20.5, 13.7 (CH$_2$). MS (*m/z*, (relative abundance, %)): 391 (M$^+$,30), 381, 367, 347, 323, 305, 291, 263, 242, 230, 214, 200, 183, 172, 155, 144, 129, 117, 103, 84, 71, 57, 42.

3-(4-{1-[(4,6-Diamino-1,3,5-triazin-2-ylamino)methyl]-5-phenyl-4,5-dihydro-1H-pyrazol-3-yl}-phenyl)sydnone (2e). Yellow amorphous solid (chloroform), *R*$_f$ 0.88, m.p., 89–90 °C. Anal. Calcd. for C$_{21}$H$_{20}$N$_{10}$O$_2$: C, 56.75; H, 4.50; N, 31.53 %. Found: C, 56.77, H, 4.50, N 31.50 %. IR (KBr, cm^{-1}): 3415 (–NH$_2$ stretching for primary amine), 3106 (–NH stretching for secondary amine), 2921 (–CH$_2$ stretching), 2852 (–CH stretching for sydnone ring), 1753 (–C=O stretching for sydnone ring), 1560 (–C=N stretching for pyrazole ring). ^{1}H-NMR (300 MHz, CDCl$_3$, δ / ppm): 3.09 (1H, *dd*, –CH$_2$, H$_A$, *J* = 15.12 Hz), 3.52 (1H, *dd*, –CH$_2$, H$_B$, *J* = 15.35 Hz), 3.71 (2H, *s*, –CH$_2$, N–CH$_2$–N), 4.73 (1H, *dd*, –CH, H$_X$, *J*$_{XA}$ = = 4.50 Hz, *J*$_{XB}$ = 10.68 Hz), 4.90 (4H, *d*, –NH$_2$, D$_2$O exchangeable), 5.08 (1H, *s*, –NH, D$_2$O exchangeable), 6.75 (1H, *s*, –C$_4$–H of sydnone ring), 7.27–7.84 (9H, *m*, aromatic). ^{13}C-NMR (300 MHz, CDCl$_3$, δ / ppm): 164.0 (C=O), 155.6 (C=N), 149.0, 148.3, 145.1, 137.2, 133.0, 131.5, 129.8, 129.6, 129.5, 128.9, 128.3, 128.2, 128.0, 126.8, 116.7, 90.1, 88.9 (CH), 70.8 (CH$_2$), 48.7 (CH), 40.1 (CH$_2$). MS (*m/z*, (relative abundance, %)): 444 (M$^+$, 25), 441, 335, 313, 297, 285, 262, 248, 235, 221, 200, 191, 172, 155, 144, 129, 117, 103, 85, 76, 57, 44, 40.

3-(4-{1-[(Diphenylamino)methyl]-5-phenyl-4,5-dihydro-1H-pyrazol-3-yl}phenylsydnone (2f). Brown semi-solid (pet. ether), *R*$_f$ 0.928. Anal. Calcd. for C$_{30}$H$_{25}$N$_5$O$_2$: C,73.92; H, 5.11; N, 14.37 %. Found: C, 73.90, H, 5.13, N 14.35 %. IR (KBr, cm^{-1}): 2924 (–CH stretching for sydnone ring), 1749 (–C=O stretching for sydnone ring), 1593 (–C=N stretching of pyrazole ring). ^{1}H-NMR (300 MHz, CDCl$_3$, δ / ppm): 3.08 (1H, *dd*, –CH$_2$, H$_A$, *J* = 14.89 Hz), 3.52 (1H, *dd*, –CH$_2$, H$_B$, *J* = 15.01 Hz), 3.98 (2H, *s*, –CH$_2$, N–CH$_2$–N), 4.42 (1H, *dd*, –CH, H$_X$, *J*$_{XA}$ = = 4.80 Hz, *J*$_{XB}$ = 8.25 Hz), 6.75 (1H, *s*, –C$_4$–H of sydnone), 7.03–8.21 (19H, *m*, aromatic). ^{13}C-NMR (300 MHz, CDCl$_3$, δ / ppm.): 160.0 (C=O), 155.6 (C=N), 144.0, 143.2, 137.2, 135.0, 131.0, 129.5, 129.4, 129.3, 129.1, 129.0, 128.9, 128.7, 128.6, 128.3, 128.3, 128.1, 128.0, 126.8, 118.0, 118.0, 117.9, 116.7 (CH), 77.6 (CH$_2$), 49.0 (CH), 40.1 (CH$_2$). MS (*m/z*, (relative abundance, %)): 487 (M$^+$ 35), 456, 428, 395, 364, 334, 306, 288, 276, 260, 248, 233, 221, 204, 191, 178, 165, 144, 129, 116, 104, 89, 77, 63, 44, 40.

3,3'-{1,5-Pentanediylbis[imino(5-phenyl-4,5-dihydropyrazole-1,3-diyl)-1,4-phenylene]}bis[sydnone] (2g). Yellow solid (pet. ether), *R*$_f$ 0.88, m.p. 99–100 °C. Anal. Calcd. for C$_{22}$H$_{27}$N$_7$O$_2$: C, 69.6; H, 6.07; N, 15.46 %. Found: C, 69.4, H, 6.07, N, 15.44 %. IR (KBr, cm^{-1}): 3150 (–NH stretching for secondary amine), 2930 (–NH stretching for secondary amine), 2922 (–CH stretching for sydnone

ring), 1750 (–C=O stretching for sydnone ring), 1594 (C=N stretching of pyrazole ring); ^{1}H-NMR (300 MHz, CDCl$_3$, δ / ppm): 1.34–2.40 (10H, *m*, –CH$_2$), 3.08 (1H, *dd*, –CH$_2$, H$_A$, *J* = 15.06 Hz), 3.52 (1H, *dd*, –CH$_2$, H$_B$, *J* = 15.68 Hz), 3.98 (2H, *s*, –CH$_2$, N–CH$_2$–N), 4.42 (1H, *dd*, –CH, H$_X$, J_{XA} = 3.60 Hz, J_{XB} = = 10.44 Hz), 3.2 (4H, *s*, –CH$_2$), 3.62 (2H, *s*, –CH$_2$), 5.05 (1H, *s*, –NH, D$_2$O exchangeable), 6.72 (1H, *s*, –C$_4$–H of sydnone), 7.28–7.70 (18H, *m*, aromatic). ^{13}C--NMR (300 MHz, CDCl$_3$, δ / ppm.): 163.0 (C=O), 155.6, 155.6 (C=N), 137.2, 131.6, 131.5, 131.4, 131.0, 129.9, 129.8, 129.7, 129.6, 129.5, 129.4, 129.3, 129.2, 128.3, 128.2, 128.1, 128.0, 126.8, 116.7, 116.5 (CH), 68.7 (CH$_2$), 48.7 (CH), 47.7, 46.9, 42.3, 40.2, 40.1, 34.1, 33.6, 31.6, 24.8, 24.6 (CH$_2$). MS (*m/z*, (relative abundance, %)): 724 (M$^+$,15), 717, 678, 647, 633, 600, 579, 551, 520, 494, 473, 456, 421, 407, 406, 377, 379, 377, 345, 318, 301, 288, 276, 260, 250, 234, 218, 205, 178, 152, 132, 119, 103, 91, 77, 64, 44, 41.

3-(4-{1-[Bis(aminomethylamino)methyl]-5-phenyl-4,5-dihydro-1H-pyrazol-3--yl}phenyl)sydnone (2h). Yellow solid (ethanol), R$_f$ 0.89, m.p. 141–142 °C. Anal. Calcd. for C$_{21}$H$_{22}$N$_6$O$_2$: C, 77; H, 3.66; N, 14.0 %. Found: C, 77.01, H, 3.67, N, 14.02. IR (KBr, cm^{-1}): 3140 (–NH$_2$ stretching for primary amine), 2032 (–NH stretching for secondary amine), 2920 (–CH stretching for sydnone ring), 1754 (–C=O stretching for sydnone ring), 1590 (–C=N stretching for pyrazole ring). ^{1}H-NMR (300 MHz, CDCl$_3$, δ / ppm): 0.88–2.17 (4H, *m*, –CH$_2$), 3.07 (1H, *dd*, –CH$_2$, H$_A$, *J* = 12.03 Hz), 3.53 (2H, *s*, –CH$_2$, N–CH$_2$–N), 3.52 (1H, *dd*, –CH$_2$, H$_B$, *J* = 12.46 Hz), 4.64 (1H, *dd*, –CH, H$_X$, J_{XA} = 4.50 Hz, J_{XB} = 8.70 Hz), 5.04 (1H, *s*, –NH, D$_2$O exchangeable), 6.74 (1H, *s*, –C$_4$–H of sydnone), 7.28–7.70 (9H, *m*, aromatic). ^{13}C-NMR (300 MHz, CDCl$_3$, δ / ppm): 160.0 (C=O), 155.6 (C=N), 137.2, 132.0, 131.0, 129.9, 129.8, 129.6, 129.5, 128.3, 128.2, 128.1, 128.0, 126.8, 116.7 (CH), 72.8, 55.4 (CH$_2$), 49.0 (CH), 41.7, 40.1 (CH$_2$). MS (*m/z*, (relative abundance, %)): 422 (M$^+$, 25), 407, 406, 377, 379, 377, 345, 318, 301, 288, 276, 260, 250, 234, 218, 205, 178, 152, 132, 119, 103, 91, 77, 64, 44, 41.

3-{4-[1-(Morpholin-4-ylmethyl)-5-phenyl-4,5-dihydro-1H-pyrazol-3-yl)]-phenyl}sydnone (2i). Yellow shiny solid (chloroform), *R*$_f$ 0.85, m.p. 160–161 °C. Anal. Calcd. for C$_{22}$H$_{23}$N$_5$O$_3$: C, 65.18; H, 5.67; N, 11.85 %. Found: C, 65.15, H, 5.65, N, 17.30 %. IR (KBr, cm^{-1}): 2922 (–CH stretching for sydnone ring), 1749 (–C=O stretching for sydnone ring), 1596 (–C=N stretching for pyrazole ring). ^{1}H-NMR (300 MHz, CDCl$_3$, δ / ppm.): 2.45 (2H, *dd*, –CH$_2$), 2.47 (2H, *dd*, –CH$_2$), 2.63 (2H, *s*, –CH$_2$), 3.09 (1H, *dd*, –CH$_2$, H$_A$, *J* = 12.13 Hz), 3.55 (1H, *dd*, –CH$_2$, H$_B$, *J* = 12.78 Hz), 3.71 (2H, *dd*, –CH$_2$), 3.75 (2H, *dd*, –CH$_2$), 3.94 (2H, *s*, –CH$_2$, N–CH$_2$–N), 4.39 (1H, *dd*, –CH, H$_X$, J_{XA} = 4.80 Hz, J_{XB} = 9.00 Hz), 6.74 (1H, *s*, –C$_4$–H of sydnone), 7.28–7.70 (9H, *m*, aromatic). ^{13}C-NMR (300 MHz, CDCl$_3$, δ / ppm): 168.8 (C=O), 144.2 (C=N), 139.79, 128.8, 128.7, 128.5, 128.1, 128.0, 127.7, 127.58, 127.52, 126.85, 126.78, 126.57, 120.9 (CH), 73.83, 67.70, 51.39 (CH$_2$), 49.0 (CH), 41.0 (CH$_2$). MS (*m/z* (relative abundance, %)): 406 (M$^+$,

30), 379, 363, 334, 300, 288, 270, 260, 248, 235, 221, 206, 191, 178, 165, 150, 145, 130, 116, 105, 91, 77, 63, 44, 40.

3-[4-(1-1H-Benzotriazol-1-ylmethyl)-5-phenyl-4,5-dihydro-1H-pyrazol-3-yl)-phenylsydnone (2j). Straw colored solid (ethanol), R_f 0.88, m.p. 150–152 °C. Anal. Calcd. for $C_{24}H_{19}N_7O_2$: C, 65.90; H, 4.34; N, 22.42 %. Found: C, 65.87, H, 4.37, N, 22.43 %. IR (KBr, cm^{-1}): 2921 (CH stretching for sydnone ring), 1745.5 (C=O stretching for sydnone ring), 1595 (C=N stretching for sydnone ring). ^{1}H-NMR (300 MHz, CDCl$_3$, δ / ppm): 3.08 (1H, *dd*, CH$_2$, H$_A$, J = 11.93 Hz), 3.73 (1H, *dd*, CH$_2$, H$_B$, J = 12.87 Hz), 3.75 (2H, *s*, CH$_2$, N–CH$_2$–N), 4.52 (1H, *dd*, CH, H$_X$, J_{XA} = 3.60 Hz, J_{XB} = 8.43 Hz), 6.73 (1H, *s*, C$_4$–H), 7.28–7.89 (13H, *m*, aromatic). ^{13}C-NMR (300 MHz, CDCl$_3$, δ / ppm): 164.0 (C=O), 155.6 (C=N), 137.2, 134.0, 132.0, 131.0, 130.7, 129.9, 129.8, 129.7, 129.5, 128.5, 128.4, 128.3, 128.3, 128.2, 128.1, 128.0, 126.8, 116.7 (CH), 74.5 (CH$_2$), 48.7 (CH), 40.1 (CH$_2$). MS (*m/z* (relative abundance, %)): 437 (M$^+$, 25), 406, 379, 377, 345, 318, 301, 290, 276, 260, 248, 234, 225, 205, 178, 165, 152, 132, 119, 103, 91, 77, 64, 50, 44, 41.

Production of lipase from *Pseudozyma aphidis* and determination of the activity and stability of the crude lipase preparation in polar organic solvents

ALEKSANDRA DIMITRIJEVIĆ[1#], DUŠAN VELIČKOVIĆ[1#], DEJAN BEZBRADICA[2#], FILIP BIHELOVIĆ[1#], RATKO JANKOV[1#] and NENAD MILOSAVIĆ[1*#]

[1]Faculty of Chemistry, University of Belgrade, Studentski trg 12, 11000 Belgrade and [2]Faculty of Technology and Metallurgy, University of Belgrade, Karnegijeva 4, 11000 Belgrade, Serbia

Abstract: The production of lipase from *Pseudozyma aphidis* (DSM 70725) was determined in six different media. The highest lipase production was observed in a medium with glucose as the sole carbon source, and yeast extract and sodium nitrate as the nitrogen sources. The time course studies of growth and lipase production in the optimal medium revealed that the highest lipase production was achieved at the end of the log phase of growth, reaching the value of 35.0 U cm^{-3} in the fifth day of cultivation. The effects of various polar, water-miscible, organic solvents on the activity and stability of the crude lipase produced by *P. aphidis* were evaluated. The hydrolytic activity of the crude lipase towards *p*-nitrophenyl palmitate (*p*-NPP) in aqueous media and in organic solvents was determined, using the same spectrophotometric assay in both the aqueous and organic media. The crude lipase preparation exhibited activity towards *p*-NPP only in acetone and acetonitrile, while the lipase was stable only in acetone, with 23 % residual activity after 24 h of incubation. These results suggested that lipase from *P. aphidis* can be used as a biocatalyst for potential applications in such organic solvents.

Keywords: lipase; activity; stability; organic solvents.

INTRODUCTION

Lipases (triacylglycerol acylhydrolases, EC 3.1.1.3) are serine hydrolases that catalyze the hydrolysis of triacylglycerols to glycerol and free fatty acids. They also catalyze a variety of synthesis reactions under reduced aqueous conditions (*e.g.*, esterification, transesterification, alcoholysis, acidolysis, aminolysis,

acylation and resolution of racemic mixtures).[1,2] Thus, lipases have become important for biotechnological and industrial applications.[3]

Biocatalysis in organic solvents offers several advantages over biocatalysis in aqueous media, due to the increased solubility of hydrophobic compounds, the ability to perform new reactions which are kinetically or thermodynamically restricted in water, suppression of undesirable side reactions, control or modification of enzyme selectivity, the possibility of recovery of some products by employment of low-boiling-point organic solvents and an increased enzyme thermostability in organic solvents.[2,4] Although enzymes exhibit many advantages, they do not always meet the desired levels of activity, productivity and, most importantly, stability in organic solvents.[5] Generally, hydrophobic solvents lead to higher enzymatic activity and stability than hydrophilic solvents, which strip water required for the enzymatic function, and lower the catalytic activity.[4,6] Thus, lipases that are active and stable in polar organic solvents would enable new applications in biotechnological processes involving polar substrates. For these reasons, it is necessary to find lipases that are active and stable in polar organic solvents.[2]

A considerable number of bacterial and fungal lipases have been commercially produced, the latter being preferable because fungi generally produce extracellular enzymes, which facilitate recovery of the enzyme from the fermentation broth.[7] *Pseudozyma* (*Candida*) *antarctica* is one of the most important sources of lipases for industrial applications.[8,9] Lipases from *P. antarctica* have many excellent characteristics and they are widely used for preparative purposes in organic synthesis in many industrial applications and scientific research projects.[10–13] However, the aim of research dealing with enzymes in non-aqueous media is to determine the optimal conditions for a specific application.[14] Very few studies have been devoted to direct comparisons of lipase activity in aqueous and organic media.[15–17] This comparison is made difficult by the fact that, generally, different reactions are used in both media for the activity assay.[14] A simple colorimetric assay based on the hydrolysis of *p*-nitrophenyl fatty acids esters was introduced by Pencreac'h and Berrati in order to compare the hydrolytic activity of thirty two commercial lipase preparations in water and heptane.[14,17] The main advantage of this assay is the use of the same hydrolytic reaction in both aqueous and organic media, which facilitates the activity comparison.[17] Hitherto, the hydrolytic activity of commercial lipase preparations was determined only in a non-polar organic solvent (heptane).[14] However, commercial lipase preparations usually contain non-protein additives that can greatly increase the enzyme activity in organic media and cause activity differences among different preparations of the same enzyme.[14]

In the present study, the objective was to produce a crude lipase synthesized by *P. aphidis* and to examine the hydrolytic activity and stability of the lipase in

polar, water-miscible organic solvents from five organic classes (ketone, nitrile, ether, alcohol, sulphoxide) using the same spectrophotometric method in aqueous and organic media. *P. aphidis* is closely related to *P.* (*Candida*) *antarctica*, but is considered a separate species.[18] To the best of our knowledge, this is the first time that the hydrolytic activity and stability of lipase produced by *P. aphidis* has been determined in organic solvents.

EXPERIMENTAL

All employed chemicals were of the highest available purity, purchased from Sigma, Merck, Bio-Rad or Aldrich.

Microorganism

Pseudozyma aphidis DSM 70725 was obtained from the German Collection of Microorganisms and Cell Cultures (DSMZ). Stock cultures were cultivated for 2 days at 25 °C on agar medium containing 3 g dm^{-3} yeast extract, 3 g dm^{-3} malt extract, 5 g dm^{-3} peptone from soybeans and 10 g dm^{-3} glucose. The culture was stored at 4 °C and renewed every 4 weeks.

Media preparation and culture conditions

Seed cultures were prepared by inoculating cells grown on slants into a growth medium (4 g dm^{-3} glucose, 2 g dm^{-3} sodium nitrate (NaNO$_3$), 0.2 g dm^{-3} magnesium sulphate (MgSO$_4$·7H$_2$O), 0.2 g dm^{-3} potassium dihydrogen phosphate (KH$_2$PO$_4$) and 1 g dm^{-3} yeast extract) at 25 °C on a rotary shaker (300 rpm) for 2 days.

Seed cultures (1 cm^3) were transferred into six 250 cm^3 Erlenmeyer flasks containing 100 cm^3 of six different cultivation media containing various carbon (glucose, glycerol, soybean oil or rapeseed oil) and nitrogen sources (yeast extract, peptone or sodium nitrate (NaNO$_3$) and ammonium chloride (NH$_4$Cl)) and incubated at 25 °C on a rotary shaker (300 rpm) for 6 days.[19,20] Detailed descriptions of the compositions of the cultivation media composition are given in Table I. After six days of cultivation, the lipase activity in the cultivation media was determined.

TABLE I. Media composition (g dm^{-3}) for *P. aphidis* cultivation

Component	Medium					
	M1	M2	M3	M4	M5	M6
Glucose	10	10	–	120	–	40
Glycerol	–	–	6	–	–	
Rapeseed oil	5	–	5	–	–	
Soybean oil	–	5	–	–	40	
Yeast extract	10	10	10	1	1	1
Peptone	10	10	10	–	–	
NH$_4$Cl	5	5	5	–	–	
MgSO$_4$·7H$_2$O	–	–	–	0.3	0.3	0.3
NaNO$_3$	–	–	–	–	–	3
KH$_2$PO$_4$	–	–	–	0.3	0.3	0.3

Time course of P. aphidis *cultivation in the optimal medium for lipase production*

After the optimal medium for lipase production was determined, the seed culture (1 cm^3) was transferred into three 250-cm^3 Erlenmeyer flasks containing 100 cm^3 of optimal (M6) me-

dium (triplicate), and incubated at 25 °C on a rotary shaker (300 rpm) for 7 days. Aliquots were withdrawn each day and the following parameters were determined: pH; absorbance at 610 nm; wet biomass; protein concentration, C_p (mg cm^{-3}); lipase concentration, C_e (U cm^{-3}), and specific activity, S_p (U mg^{-1} of protein). The mean value of each parameter was calculated from the data obtained in the triplicate trials.

Determination of growth parameters

The absorbance at 610 nm was measured. Additionally for biomass determination, 1 cm^3 of fermentation broth was centrifuged at 14,000×*g* for 15 min, the supernatant removed and the remaining biomass was dried for 15 min at room temperature and weighed.

Protein determination

The amount of protein was estimated by the Bradford dye-binding method, using bovine serum albumin (BSA) as the standard.[21]

Preparation of crude P. aphidis *lipase*

In order to produce the crude lipase preparation for the determination of the activity and stability of lipase in organic solvents, 1 cm^3 of the seed culture (prepared as described above) was transferred into 100 cm^3 of optimal (M6) media, and cultivated at 25 °C on a rotary shaker (300 rpm). After five days of cultivation, when the highest lipase production was reached, the cells were removed by centrifuging (3000 rpm, 30 min) and the supernatant was lyophilized and used as the crude lipase preparation. The specific activity of the crude lipase preparation was 705.88 U mg^{-1} of proteins.

Lipase activity in aqueous media

The lipase activity in aqueous media was measured spectrophotometrically using an assay based on the hydrolysis of *p*-nitrophenyl palmitate (*p*-NPP), as described previously, with modifications.[22] The substrate was prepared as follows: 0.1586 g *p*-NPP, 0.0017 g sodium dodecyl sulphate (SDS) and 0.1 g Triton X-100 were dissolved in 10 cm^3 of 0.1 M Tris-HCl buffer pH 8.2 (the final concentration of *p*-NPP was 0.0042 M) mixed vigorously and heated at 80 °C for 15 min.[22] The enzyme and substrate were mixed and the increase of absorbance at 410 nm was monitored every 30 s for 3 min. The reaction rate was calculated from the slope of the curve absorbance *versus* time using a molar extinction coefficient of 13,000 dm^3 mol^{-1} cm^{-1} for *p*-nitrophenol (*p*-NP). This value was determined from the absorbance of standard solutions of *p*-NP in the reaction medium. One enzyme unit was the amount of enzyme liberating one µmol of *p*-NP per minute under the above conditions.

Lipase activity in organic solvents

The hydrolytic activities of the lipase preparation in organic media were determined according to Pencreac'h and Baratti with modifications.[17] A crude lipase preparation dissolved in water was transferred to Eppendorf tubes containing 0.0042 M *p*-NPP dissolved in different organic solvents (acetone, acetonitrile, dimethyl sulphoxide, *t*-butanol or 1,2-dimethoxyethane), so that the final concentrations of the organic solvents in the assay were 95 %. The mixture was incubated for 10 s at 25 °C under reciprocal agitation at 1000 strokes per min. Mixing was stopped and after 30 s the enzyme precipitated, since its is insoluble in organic solvents and the clear supernatant was transferred to a cuvette containing 0.1 M Tris-HCl buffer pH 8.2 and the absorbance was read at 410 nm. The same was repeated in the next 30 min at regular time intervals. The reaction rate was calculated from the slope of the curve absorbance *versus* time using the molar extinction coefficients of *p*-NP in different organic solvents. The values of extinction coefficients were determined from the absorbance of standard solutions of *p*-NP

in the appropriate organic solvent, treated in the same way as in the assay. The extinction coefficients of *p*-NP were determined in organic solvents in which lipase activity was detected, *i.e.*, in acetone and acetonitrile, and they were 880 and 810 dm^3 $mol^{-1}cm^{-1}$, respectively, under the assay conditions. One enzyme unit was the amount of enzyme liberating one µmol of *p*-NP per min under the above conditions. In order to compare the activity in water and in organic solvents, the $R_{O/A}$ value was introduced. $R_{O/A}$ is the ratio between the activity in the organic solvent and the activity in the aqueous medium.[14]

Lipase stability in organic solvents

0.025 cm^3 of enzyme solution (*P. aphidis* lipase lyophilizate dissolved in water in an appropriate concentration) and 0.475 cm^3 of an organic solvent (the same solvents used for the examination of the lipase activity) were added into Eppendorf tubes, making the final concentration of organic solvent 95 %. The solutions were incubated at 25 °C for 24 h. In order to examine the denaturation kinetics of lipase, the remaining activity in the different organic solvents was determined at different time intervals. The remaining activity in the organic solvents was calculated from the absorbance change at 410 nm, considering the enzyme activity at zero time as 100 %.

RESULTS AND DISCUSSION

Production of P. aphidis *lipase and the cultivation time course*

The production of lipase from *P. aphidis* was monitored in six different media.[19,20] After six days of cultivation, the lipolytic activity of *P. aphidis* in the media supplemented with a lipid substrate (rapeseed oil or soybean oil) was between 1.5 and 2.5 U cm^{-3} (Fig. 1), which is in accordance with the results obtained by other authors.[23] However, a higher production of lipase was detected in the media supplemented with rapeseed oil (M1 and M3 in Fig. 1) than in the media supplemented with soybean oil (M2 and M5 in Fig. 1). This was expected, since it was reported that rapeseed oil induces lipase production by *P. aphidis*.[20] Generally, a slightly higher production of lipase was observed in nutrient-rich media (M1, M2 and M3 in Fig. 1) with both types of nitrogen sources (organic and mineral) and two carbon sources (carbohydrate/glycerol and oil) as also reported by other authors.[20] The lowest values of lipolytic activity were obtained in the M4 medium, in which glucose was the sole carbon source and yeast extract was the only nitrogen source. This is in accordance with a previous report, where the lowest values of lipolytic activity were obtained in media supplemented with carbohydrates as the sole carbon sources.[23] The highest value of lipase production was detected in the M6 medium (Fig. 1), which was similar in composition to the medium used for seed preparation. It is interesting that the only difference between the medium with the highest (M6) and lowest (M4) lipase production was the presence of an inorganic nitrogen source ($NaNO_3$) in the M6 medium. This interesting observation indicates that selection of an inorganic nitrogen source plays an important role in lipase production, although in some cases, it could reduce lipase production.[24] Factors controlling lipase synthesis and transport have been investigated in only a few cases, *e.g.*, the production of lipase by

Pseudomonas sp. was shown to be strongly induced by triacylglycerols and detergents and not repressed by glucose or glycerol.[25,26] However, lipase production is strongly strain-dependent, for example Dalmau *et al.* indicated the request for lipid substrates and the inhibition effect of glucose in the production of lipase by *Candida rugosa.*[23,27,28]
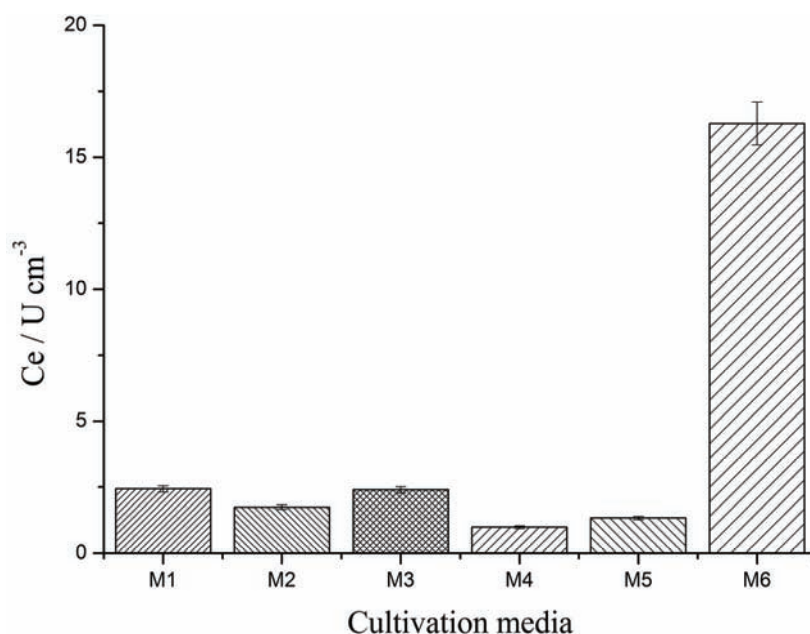
Fig. 1. Lipolytic activity of *P. aphidis* in different cultivation media after 6 days of cultivation.

Since lipase production was the highest in the M6 medium (Fig. 1), time course studies were conducted in order to determine the growth and lipase production characteristics of *P. aphidis* in the optimal medium. Different parameters were determined, including growth (biomass and absorbance at 610 nm), pH, C_p, C_e and S_p at regular intervals (24 h) during seven days. The results obtained are shown in Fig. 2. The highest lipase production (35.0 U cm^{-3}) in the M6 medium was achieved after five days of cultivation. This value was over four times higher than in previous reports dealing with *P. aphidis.*[23,20] From the values of the biomass and absorbance at 610 nm, it is clear that after five days of cultivation *P. aphidis* reached a stationary phase of growth. Thus, the maximum of lipase production was reached at the end of the log-phase. As *P. aphidis* entered the stationary phase, the lipase production decreased and the protein concentration increased, probably as a result of cell death.[25] From Fig. 2, it is clear that the specific activity was the highest at the end of the log-phase and significantly decreased in the stationary phase of growth, due to a decrease of

lipase activity and an increase of the protein concentration. Although it was reported that lipase from *C. antarctica* showed the highest activity at pH 8.0 and the enzyme was stable in the pH range of 7–9, the pH values during the cultivation of *P. aphidis* ranged from 5–6 (Fig. 2).[23]
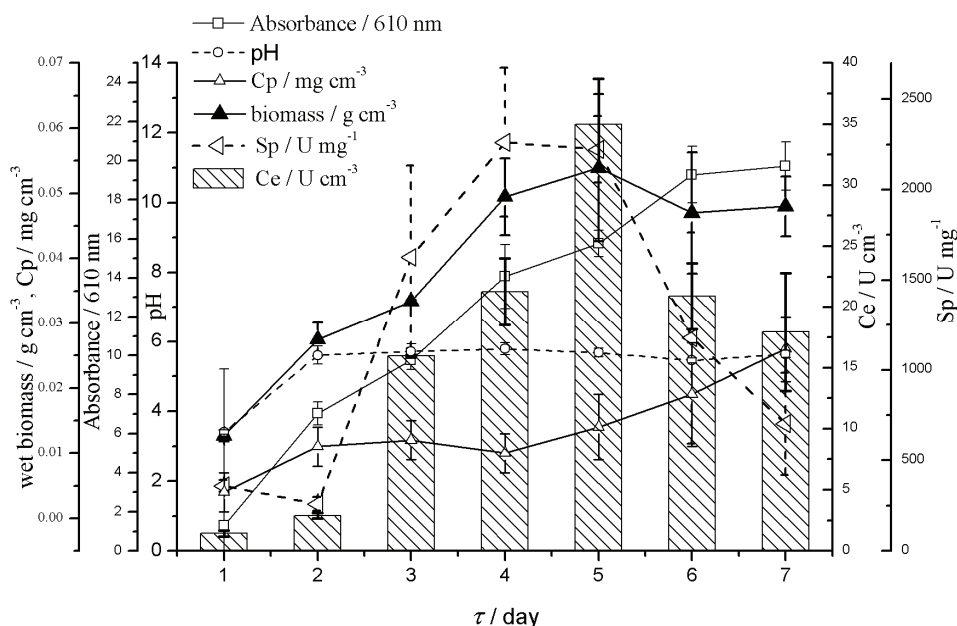
Fig. 2. Time course of the growth and lipase production of *P. aphidis* in the optimal (M6) medium.

Lipase activity in aqueous medium and in organic solvents towards p-*NPP hydrolysis*

Pencreac'h and Baratti proposed a method to compare the activity of lipases towards *p*-NPP in aqueous and organic medium.[14] Since the same reaction was used in both aqueous and organic media, the authors introduced the activity ratio $R_{O/A}$ to characterize the activity in organic media. Using this method, Pencreac'h and Baratti compared the hydrolytic activity of 32 commercial lipase preparations towards *p*-NPP in aqueous media and in *n*-heptane.[14] Since polar organic solvents have technological advantages, such as low toxicity, low boiling points, low costs and offer the possibility of using polar substrates for novel reactions, the method proposed by Pencreac'h and Baratti was modified in the present and used to compare the activity of crude *P. aphidis* lipase in aqueous media and in various, polar, water-miscible organic solvents (Table II).[2] The activity of *P. aphidis* lipase towards *p*-NPP in an aqueous medium was considered as 100 %. Among the organic solvents, lipase activity towards *p*-NPP was only observed in

acetone and acetonitrile (Table II), giving values of $R_{O/A}$ of 0.006 and 0.002, respectively. In all other tested solvents, no activity was detected. It is clear that lipase activity was detected in solvents with similar log P values. However, the activity of lipase in acetone was three times higher than in acetonitrile (Table II), indicating that a specific functional group also has an effect on the enzyme activity, as was also observed in the case of *C. antarctica* lipase.[29] From Table II, it is obvious that the $R_{O/A}$ values for acetone and acetonitrile were smaller than one. This was not surprising since reported activities in organic media are usually lower than those observed in aqueous media.[7,14] There are several possible explanations for the low activity in organic solvents. First, the amount of available water, necessary for the hydrolysis reaction, could be too low to allow good reaction rates. Second, the structural flexibility of the enzyme molecules is lower in an organic solvent than in water, which may reduce its activity. Third, the heterogeneous catalysis, which is a consequence of enzyme insolubility in organic solvents, may lead to reduced activity due to limited substrates and/or product diffusion.[14]

TABLE II. Activity of crude lipase from *P. aphidis* in 95 % organic solvents

Solvent	Log P (o/w)	Activity, %	$R_{O/A}$
Water	–	100	1
Acetone	−0.24	0.62	0.006
Acetonitrile	−0.15	0.21	0.002
Dimethyl sulphoxide	−1.22	0	0
t-Butanol	0.35	0	0
1,2-Dimethoxyethane	0.09	0	0

Lipase stability in organic solvents

The stability in organic solvents is an important characteristic of lipases. It can determine whether the enzyme can be used to catalyze synthetic reactions and also to predict which solvent would be better for performing the reaction.[29] Lipases are diverse in their sensitivity to solvents, but there is a general agreement that polar water-miscible solvents (−2.5 < log P < 0) are more destabilizing than water immiscible solvents (2 < log P < 4).[30] According to Klibanov, hydrophilic solvents exhibit a higher affinity to water and hence it is more likely that they will strip essential water from enzyme molecules, than hydrophobic solvents.[31] Although in most cases, lipases have good stability in water immiscible organic solvents and are highly denatured in hydrophilic solvents, it was reported that *A. niger* lipase exhibited better activity in acetone than in hexane and heptane, indicating that the effect of water immiscible organic solvents on enzyme stability differs from lipase to lipase.[7,30,32,33] However, in general, water immiscible organic solvents are not appropriate for reactions with polar substrates or in cases where the two substrates greatly differ in terms of polarity.[34]

Thus, lipases that are active and stable in polar solvents would open new opportunities in biocatalysis with polar substrates.[2]

Therefore, the stability of the crude lipase preparation produced by *P. aphidis* in five water-miscible, 95 % organic solvents, from five organic classes was studied. In zero time of incubation in 95 % organic solvents, the enzyme was stable in all organic solvents except in dimethyl sulphoxide (DMSO), indicating that enzyme deactivation in DMSO was immediate. Low enzyme stability and a highly destabilizing effect of DMSO were also reported by other authors.[29] After 1 h of incubation, the enzyme was stable only in acetone, with a residual activity of 82.2 %. In all other solvents, the stability was reduced drastically after 1 h. The kinetics of denaturation of the lipase in acetone is given in Fig. 3. Although, the enzyme had lost almost 50 % of its activity after 3 h, it remained active even after 24 h (Fig. 3).
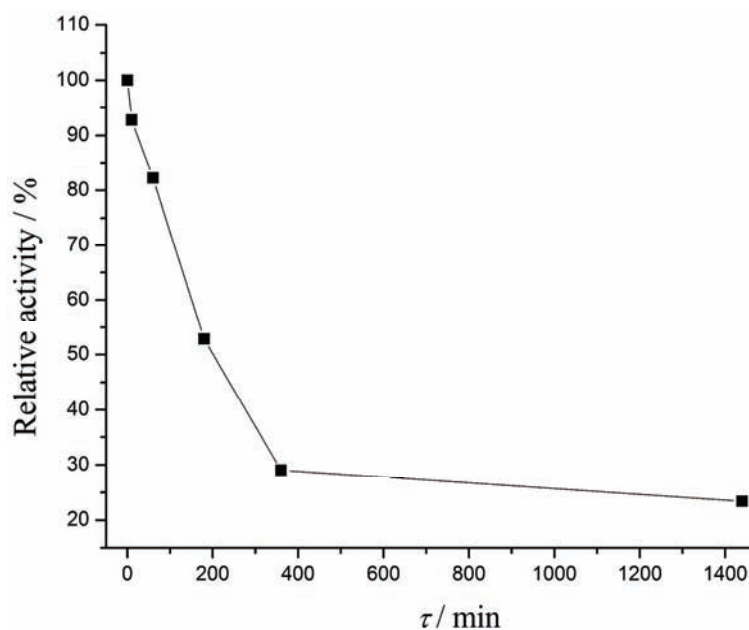
Fig. 3. Denaturation kinetics of *P. aphidis* lipase in acetone.

The low stability of the crude *P. aphidis* lipase in water-miscible organic solvents was the consequence of enzyme denaturation, due to stripping of water from the enzyme surface, as described above. The high relative activity of *P. aphidis* lipase (82.2 %) in acetone after 1 h of incubation corresponds to the results obtained by other authors.[2] Only a few reports show a high stability of lipases in acetone after a prolonged period. For example, the lipase produced by *Pseudomonas* sp. had relative activity values from 100 to 110 % after 15 h at

room temperature in acetone, and the lipase from *Mucor javanicus* exhibited high stability and an increased activity after 2 h of incubation at 25 °C in acetone.[35,36]

CONCLUSIONS

The production of lipase from *P. aphidis* was the highest in the medium with glucose as the carbon source, and yeast extract and $NaNO_3$ as the nitrogen sources. It was shown that the nitrogen source, especially an inorganic nitrogen source, plays an important role in lipase production. The highest lipase production (35.0 U cm^{-3}) in the optimal medium was achieved at the end of the log phase of growth during the fifth day of cultivation. The crude lipase preparation exhibited activity towards *p*-NPP in acetone and acetonitrile. The activity in acetone was three times higher. The results obtained indicate that besides the log *P* values, specific functional groups of the solvent affect the enzyme activity. Of the solvents tested, the lipase was stable only in acetone, even after 24 h. The stability and activity of the crude *P. aphidis* lipase preparation in acetone justifies the search for potential applications of the enzyme in biocatalysis in such a medium.

И З В О Д

ПРОИЗВОДЊА ЛИПАЗЕ ИЗ *Pseudozyma aphidis* И УТВРЂИВАЊЕ АКТИВНОСТИ И СТАБИЛНОСТИ ЛИПАЗЕ У ПОЛАРНИМ ОРГАНСКИМ РАСТВАРАЧИМА

АЛЕКСАНДРА ДИМИТРИЈЕВИЋ[1], ДУШАН ВЕЛИЧКОВИЋ[1], ДЕЈАН БЕЗБРАДИЦА[2], ФИЛИП БИХЕЛОВИЋ[1], РАТКО ЈАНКОВ[1] и НЕНАД МИЛОСАВИЋ[1]

[1]*Хемијски факулūеū, Универзиūеū у Беоīраду, Сūуденūски ūрī 12, 11000 Беоīрад и*
[2]*Технолошко—меūалуршки факулūеū, Универзиūеū у Беоīраду, Карнеīијева 4, 11000 Беоīрад*

Производња липазе из *Pseudozyma aphidis* утврђена је у шест различитих медијума. Највиша производња уочена је у медијуму где је глукоза била извор угљеника, а екстракт квасца и натријум-нитрат извори азота. Праћењем динамике раста и производње липазе у оптималном медијуму, уочено је да се највиша производња липазе достиже пред крај логаритамске фазе раста, и достиже вредност од 35 U cm^{-3} у петом дану култивације, што је четири пута већа производња од оне до сада пријављене у литератури. Утврђен је ефекат различитих поларних органских растварача, мешљивих са водом, на активност и стабилност липазе из *P. aphidis*. Хидролитичка активност липазе према пара-нитрофенил-палмитату (*p*-NPP-у) у воденој средини и органским растварачима утврђена је употребом истог спектрофотометријског теста. Показано је да липаза има активност према *p*-NPP-у само у ацетону и ацетонитрилу, док је ензим стабилан једино у ацетону и задржава 23 % активности након 24 часа инкубације. Добијени резултати указују да липаза из *P. aphidis* може бити коришћена као биокатализатор за потенцијалне примене у ацетону као медијуму.

(Примљено 28. априла, ревидирано 7. јуна 2011)

REFERENCES

1. S. Z. Grbavčić, S. I. Dimitrijević-Branković, D. I. Bezbradica, S. S. Šiler-Marinković, Z. D. Knežević, *J. Serb. Chem. Soc.* **72** (2007) 757
2. B. Hernandez-Rodriguez, J. Cordova, E. Barzana, E. Favela-Torres, *J. Mol. Catal., B* **61** (2009) 136
3. N. Ognjanović, D. Bezbradica, Z. Knežević, *J. Serb. Chem. Soc.* **73** (2008) 147
4. A. Zaks, A. M. Klibanov, *J. Biol. Chem.* **263** (1988) 3194
5. G. Correa, S. Riva, *Angew. Chem. Int. Ed.* **39** (2000) 2226
6. A. Zaks, A. M. Klibanov, *J. Biol. Chem.* **263** (1988) 8017
7. V. M. G. Lima, N. Krieger, D. A. Mitchell, J. D. Fontana, *Biochem. Eng. J.* **18** (2004) 65
8. Z. Cabrera, G. Fernandez-Lorente, R. Fernandez-Lafuente, J. M. Palomo, J. M. Guisan, *J. Mol. Catal., B* **57** (2009) 171
9. P. Trodler, J. Nieveler, M. Rusnak, R. D. Schmid, J. Pleiss, *J. Chromatogr., A* **1179** (2008) 161
10. J. H. Liu, Y. Y. Zhang, Y. M. Xia, F. Su, *Chem. Biochem. Eng. Q.* **24** (2010) 203
11. Z. Knežević-Jugović, D. Bezbradica, Z. Jakovljević, S. Branković-Dimitrijević, D. Mijin, *J. Serb. Chem. Soc.* **73** (2008) 1139
12. H. Stamatis, V. Sereti, F. N. Kolisis, *J. Mol. Catal. B: Enzym.* **11** (2001) 323
13. S. Karboune, M. Safari, B. M. Lue, F. K. Yeboah, S. Kermasha, *J. Biotechnol.* **119** (2005) 281
14. G. Pencreac'h, J. C. Baratti, *Enzym. Microb. Technol.* **28** (2001) 473
15. P. Trodler, J. Pleiss, *BMC. Struct. Biol.* **9** (2009) 39
16. C. Li, T. Tan, H. Zhang, W. Feng, *J. Biol. Chem.* **285** (2010) 28434
17. G. Pencreac'h, J. C. Baratti, *Enzym. Microb. Technol.* **18** (1996) 417
18. Y. H. Wei, F. L. Lee, W. H. Hsu, S. R. Chen, C. C. Chen, C. Y. Wen, S. J. Lin, W. S. Chu, G. F. Yuan, G. Y. Liou, *Bot. Bull. Acad. Sin.* **46** (2005) 223
19. T. Morita, M. Konishi, T. Fukuoka, T. Imura, D. Kitamoto, *Appl. Microbiol. Biotechnol.* **74** (2007) 307
20. A. A. Chirvase1, C. Ungureanu, L. Tcacenco, N. Radu, *Rev. Chim.* **9** (2010) 61
21. M. M. Bradford, *Anal. Biochem.* **72** (1976) 248
22. R. G. Jensen, *Lipids* **18** (1983) 650
23. M. Adamczak, *Pol. J. Food Nutr. Sci.* **12** (2003) 3
24. R. N. Zaliha, R. A. Rahman, S. N. Baharum, A. B. Salleh, M. Basri, *J. Microbiol.* **44** (2006) 583
25. A. Dimitrijević, D. Veličković, M. Rikalović, N. Avramović, N. Milosavić, R. Jankov, I. Karadžić, *Carbohydr. Polym.* **83** (2011) 1397
26. E. J. Gilbert, J. W. Drozd, C. W. Jones, *J. Gen. Microbiol.* **137** (1991) 2215
27. A. Dominguez, F. J. Deive, M. A. Sanroman, M. A. Longo, *J. Chem. Technol. Biotechnol.* **78** (2003) 1166
28. E. Dolman, J. L. Montesinos, M. Lotti, C. Casos, *Enzyme Microb. Technol.* **26** (2000) 657
29. B. Fu, P. T. Vasudevan, *Energy Fuels* **23** (2009) 4105
30. L. M. Pera, C. M. Romero, M. D. Baigori, G. R. Castro, *Food Technol. Biotechnol.* **44** (2006) 247
31. A. M. Klibanov, *Chem. Tech.* **6** (1986) 354
32. M. G. B. Koblitz, G. M. Pastore, *Cienc. Agrotecnol.* **30** (2006) 494

33. R. N. Zaliha, R. A. Rahman, S. N. Baharum, M. Basri, A. B. Salleh, *Anal. Biochem.* **341** (2005) 267
34. P. Villeneuve, *Biotechnol. Adv*. **25** (2007) 515
35. M. Pogorevc, H. Stecher, K. Faber, *Biotechnol. Lett.* **24** (2002) 857
36. J. C. Wu, S. S. Lee, M. M. B. Mahmood, Y. Chow, M. M. R. Talukder, W. J. Choi, *J. Mol. Catal. B: Enzym.* **45** (2007) 108.

Journal of the Serbian Chemical Society

SHORT COMMUNICATION

Degradation kinetics of six sulfonamides in hen eggs under simulated cooking temperatures

XIN-HUAI ZHAO[1,2*], PENG WU[1] and YING-HUA ZHANG[1]

[1] Key Laboratory of Dairy Science, Ministry of Education, Northeast Agricultural University, Harbin 150030, P. R. China and [2] Department of Food Science, Northeast Agricultural University, Harbin 150030, P. R. China

Abstract: Six sulfonamides, *i.e*., sulfadiazine, sulfadimethoxine, sulfamerazine, sulfamethazine, sulfamethoxazole and sulfamonomethoxine, were applied to spike whole hen eggs at 0.1 mg kg^{-1} eggs. The spiked hen eggs were heated at 80 and 100 °C to investigate the degradation kinetics of the sulfonamides under simulated cooking conditions. The sulfonamides added were extracted twice from the spiked eggs with dichloromethane by an ultrasonic-assisted extraction, and analyzed by a HPLC method after purification. The first-order rate constants and half-life times of the sulfonamides were calculated, and the corresponding apparent activation energy of their degradation was also obtained by application of the Arrhenius equation. The results indicated that all six sulfonamides degraded faster at the higher heating temperature, with first-order rate constants ranging from 0.0056 to 0.0108 min^{-1} at 80 °C and from 0.0147 to 0.0394 min^{-1} at 100 °C. The apparent activation energies for the degradation of the sulfonamides were estimated to be in the range 30.9 to 77.5 kJ mol^{-1}. Sulfadiazine and sulfadimethoxine had the shortest and longest half-life time, respectively, and were the most instable and stable.

Keywords: sulfonamide; hen eggs; thermal degradation; kinetics; HPLC.

INTRODUCTION

Sulfonamides are synthetic antibiotics with a wide spectrum against most gram-positive and many gram-negative organisms, and are used in human medicine for therapeutic and prophylactic purposes. Sulfonamides are also sometimes used as additives in animal feed for the prevention and treatment of bacterial diseases in livestock, and might be accumulated in meat, eggs, milk and

---

1093

fish. In a recent study, Wang *et al.* found that 24 of 56 egg samples had sulfadiazine contents larger than 100 μg kg^{-1}.[1] Sulfonamide residues remaining in foods are considered to be a harmful risk for consumers. A legal maximum residue limit for sulfonamides was set at 100 μg kg^{-1} in the United States and the European Union.[2] Various LC-based analysis methods with UV,[3] diode array or photo-diode array detector,[4,5] fluorescence detector,[6] and MS or MS/MS detection [7–9] have been developed to determine sulfonamide residues in various food matrices. Other analysis techniques based on immunoassay[10,11] and capillary zone electrophoresis[12] were also applied in recent studies.

The residue levels of sulfonamides in foods are affected by food processing, especially heat treatment. It is of interest to determine if sulfonamide residues can be decreased by the usual cooking methods of foods. Furusawa and Hanabusa used three different cooking procedures to study the net change of four sulfonamide residues in chicken muscles.[13] Rose *et al.* studied the heat stability of sulfamethazine in animal tissues subjected to a range of cooking processes, including boiling, roasting, grilling, frying, pressure cooking and microwaving.[14] Fischer *et al.* reported cooking-related changes in sulfamethazine residues and its metabolites in pork products.[15] Xu *et al.* also investigated the effect of cooking on sulfadimethoxine residues in the muscle of channel catfish.[16] All these mentioned results showed that heat treatment decreased the residue levels of sulfonamides to different extents. Unfortunately, the degradation kinetics of the sulfonamides were neither measured nor studied.

In the present work, six sulfonamides, *i.e.*, sulfadiazine (SDZ), sulfadimethoxine (SDM), sulfamerazine (SMR), sulfamethazine (SMZ), sulfamethoxazole (SMX) and sulfamonomethoxine (SMM), were selected to study their degradation kinetics in hen eggs under simulated cooking conditions. The spiked whole hen eggs were heated at two temperatures for different periods. The sulfonamide residues left in the cooked eggs were separated by ultrasonic-assisted extraction and analyzed by a HPLC method. The degradation kinetics of the sulfonamides were calculated and compared, whereby the degradations of the sulfonamides were treated as first-order reactions.

EXPERIMENTAL

Reagents and materials

Six sulfonamide standards, SDZ, SDM, SMR, SMZ, SMX and SMM, were purchased from Sigma (St. Louis, MO, USA) with declared purity of more than 99.5 %, and stored at −18 °C. The first stock solutions (200 mg L^{-1}) of the individual sulfonamides were prepared by dissolving the sulfonamides in methanol separately. The second stock solutions of the individual sulfonamide were prepared daily by diluting the first stock solution with mobile phase to 10 mg L^{-1}. Working solution of the mixed sulfonamides was daily prepared by combining the second stock solution of the single sulfonamide in different volumes and diluting to a fixed volume with mobile phase. These were used to determine the standard curve or to spike hen eggs. The first stock solutions of the sulfonamides were stored at 4 °C for one week and

then discarded later. The methanol used was of chromatographic grade; other employed chemicals and solvents were analytical grade, and all were procured from Sigma-Aldrich (Schnelldorf, Germany). Water used was highly purified water prepared with Milli-Q PLUS (Millipore Corporation, New York, NY, USA). Hen eggs were purchased from a supermarket in Harbin, Heilongjiang Province and stored at 4 °C before use.

Preparation of spiked hen eggs

Some hen eggs were broken by hand and the contents of the eggs (whole hen eggs) were collected and mixed well with a hand blender. After this, working solution of the mixed sulfonamides was added to the eggs to insure the content of the sulfonamides was 100 µg kg^{-1} eggs. The spiked eggs were mixed well to distribute the sulfonamides. Portions of spiked eggs, about 50.0 g, were put in beakers of 100 mL capacity, stood at ambient temperature for 1 h, and then heated gently in a water bath to 80 or 100 °C with gentle stirring at the beginning. After the central temperature of the sample had reached the selected cooking temperature, zero reaction time was set and the eggs were heated continuously for different periods (4, 8, 12, 16 and 20 min). Then, the portions were rapidly cooled in ice–water to ambient temperature and stored at 4 °C until sulfonamide extraction and analysis. These samples were used for the kinetics study.

Whole hen eggs were heated at 100 °C for 20 min without sulfonamide addition. The heated eggs were cooled in ice–water both to ambient temperature and milled into fine particles. The cooked eggs were spiked and mixed well with the six sulfonamides at three levels, 0, 0.05 and 0.1 mg kg^{-1} egg, left at ambient temperature for 1 h, and then used as the controls for recovery evaluation. The cooked eggs were also spiked and mixed well with the six sulfonamides at 6, 8, 10, 15 and 20 µg kg^{-1} eggs, and used to determine detection limits of the sulfonamides.

Extraction and purification of sulfonamides from spiked hen eggs

The procedure for the extraction of the sulfonamides from the prepared samples was as per the method of Kishida[17] and our previous work[18] with some modifications. The spiked, cooked eggs, 3.0 g, were put in a centrifuge tube together with 15.0 mL of dichloromethane, and homogenized for 30 s with a handheld homogenizer. Then, the tube was put in an ultrasonic extractor and subjected to further extraction for 10 min at 10 °C. The mixture was centrifuged at 400×g for 5 min, and the liquid phase was collected. The residue left was re-extracted once with 15.0 mL of dichloromethane as above. The combined liquid phase was filtered through anhydrous sodium sulfate (2.0 g) into a 50 mL heart-shaped flask.

Glycol about 0.1 mL was added to the flask and the content in the flask was evaporated with nitrogen gas in an evaporation station to remove the dichloromethane. The residue was reconstituted to a volume of 1.50 mL with mobile phase, extracted with 3.0 mL *n*-hexane three times to remove the lipids, and filtered through a 0.45 µm microporous membrane before HPLC analysis.

HPLC analysis of sulfonamides

The analysis of six sulfonamides was performed in a liquid chromatograph 2695 Series (Waters Corporation, Milford, MA, US) with a diode array detector (DAD), a C_{18} reversed phase column (Hypersil ODS 250 mm×4.6 mm i.d. 5 µm, Elite Technologies, Dalian, Liaoning, China) at ambient temperature. The mobile phase consisted of methanol and 0.08 % acetic acid in a volume ratio of 38:62. The flow rate was 0.7 mL min^{-1}. Detection was realized at a wavelength of 275 nm and the injection volume of the sample was 20 µL. Qualitative identification of each sulfonamide in the samples was performed by comparing its UV spec-

trum and elution time with those of the corresponding standard. Quantification of six sulfonamides was performed by comparing the peak areas of the sulfonamides to a calibration curve of the standards, and used for the calculation of their degradation kinetics. Multitude-point calibration was used in this work.

Statistical analysis

All data are expressed as means from at least five independent trials. The rate constants of degradation of the sulfonamides were calculated by linear regression analysis using SPSS 13.0 software (SPSS Inc., Chicago, IL, USA).

RESULTS AND DISCUSSION

Analysis of sulfonamides by HPLC

Chemical structures of six sulfonamides are given in Fig. 1. With the procedure employed in this work, the six sulfonamides were extracted efficiently from the cooked hen eggs and measured accurately by HPLC. Typical HPLC profiles of the six sulfonamides obtained from the standard solutions and the samples are given in Fig. 2, which shows that the six sulfonamides were well separated by the column with elution times ranging from about 6 to 17 min. SMM was identified in the raw hen eggs by its UV spectrum obtained using the DAD and its retention time. The analysis result revealed that the linear range for the determination of the six sulfonamides was from 0.01 to 1.0 mg kg^{-1} eggs ($R^2 \geq$ ≥ 0.999). The data listed in Table I demonstrates that the detection limits for the six sulfonamides ranged from 8 to 10 µg kg^{-1} eggs (peak area three times larger than the noise), and the addition recovery of the six sulfonamides at two addition levels ranged from 78.8 (SMR, at 0.1 mg kg^{-1} eggs) to 103 % (SMM, at 0.1 mg kg^{-1} eggs). The lower recovery of SMR might be due to its lower stability, *i.e.*, easier degradation during analysis sample preparation. The relative standard deviation of the recovery of the six sulfonamides was less than 8.5 %. This means that the applied extraction and purification procedure appeared to be efficient, and the HPLC analysis procedure was applicable to detect sulfonamide residues in the prepared egg samples.
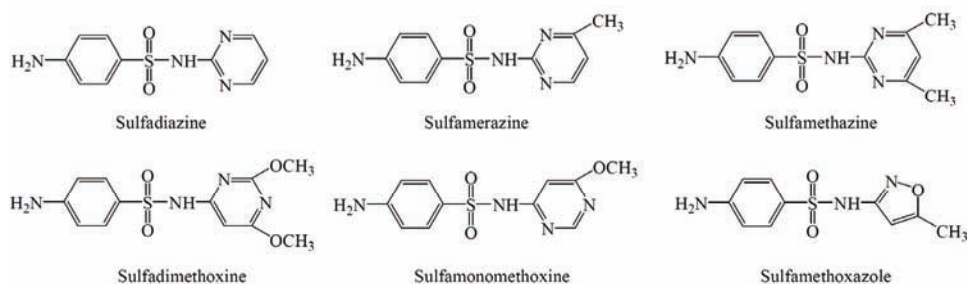
Fig. 1. Chemical structures of the six studied sulfonamides.
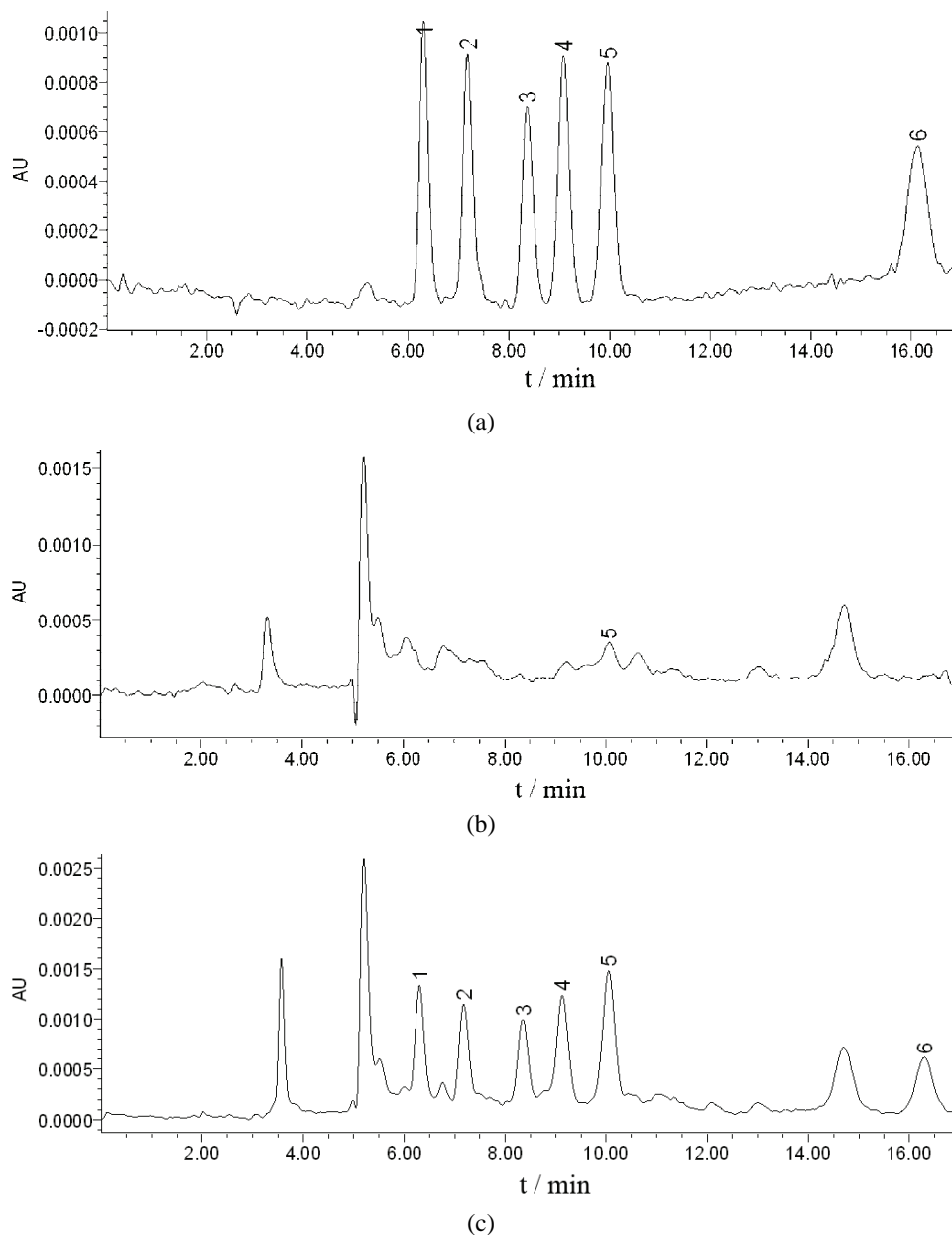
Fig. 2. Typical HPLC profiles of the six sulfonamides obtained from standard solution of 0.05 mg kg^{-1} (a), control (b) and extract of 0.1 mg kg^{-1} spiked whole hen eggs heated at 80 °C for 4 min (c). Peaks 1 to 6 in the profiles represent SDZ, SMR, SMZ, SMX, SMM and SDM, respectively. As SMM was identified in the raw hen eggs, its content served as the background and it was discarded from the experimental data of the degradation kinetics.

TABLE I. Mean recovery and limits of detection (*LOD* / %) of six sulfonamides from the spiked hen egg using HPLC analysis (the number of replicate measurements was five)

Sulfonamide	Spiking level of the sulfonamides				*LOD* / μg kg^{-1}
	0.05 mg kg^{-1}		0.1 mg kg^{-1}		
	Recovery, %	*RSD* / %	Recovery, %	*RSD* / %	
SDM	83.5	7.7	91.8	5.8	10
SDZ	83.0	7.6	79.4	8.4	8
SMM	98.6	6.3	103.0	8.2	8
SMR	89.1	5.2	78.8	7.6	8
SMX	85.2	5.7	83.5	3.3	8
SMZ	86.8	4.3	89.7	4.1	10

Degradation parameters of the six sulfonamides in hen eggs during cooking

The sulfonamide residues remaining in the cooked hen eggs subjected to different heating times were extracted and analyzed. Significant loss of the six sulfonamides was found before zero reaction time. The final results are given in Table II. The amount of sulfonamide residues showed a decreasing trend as the heating time increased, indicating the degradation of the six sulfonamides.

TABLE II. Contents of six sulfonamides remaining in the spiked hen eggs after heating at different temperatures for various times (the number of replicate measurements was five)

Cooking temperature, °C	Heat time, min	Content of the sulfonamides, μg kg^{-1}					
		SDM	SDZ	SMM	SMR	SMX	SMZ
80	4	78.4	41.0	69.1	65.8	67.1	76.7
	8	76.9	40.0	68.0	64.0	65.7	75.0
	12	74.4	38.9	64.4	63.0	64.0	73.0
	16	73.3	36.1	62.7	60.8	61.8	69.1
	20	71.7	34.8	61.0	57.8	61.0	65.5
100	4	68.0	29.3	53.5	47.5	59.1	61.9
	8	64.0	25.2	51.5	45.4	54.0	60.5
	12	60.0	24.5	44.2	40	47.2	54.9
	16	56.4	17.5	37.6	32.1	46.4	49.2
	20	54.0	16.0	36.0	29.7	42.6	48.5

Furusawa and Hanabusa found that when chicken muscles were cooked by boiling, roasting or microwaving, the amount of SDM, SMX, SMM and sulfaquinoxaline (SQ) remaining could be well-described by exponential equations.[13] Their result meant that the degradation of four sulfonamides might be first-order reaction, and the content variation of each sulfonamide in chicken muscles at different cooking times would behave as Eq. (1).

$$-\frac{\mathrm{d}c}{\mathrm{d}t} = kt \tag{1}$$

where c is the content of the sulfonamide, t is cooking time and k is the first-order rate constant of degradation of the sulfonamides.

The first-order rate constant of degradation and the half-life times of the six sulfonamides in hen eggs at two cooking temperatures were thus calculated from the data listed in Table II using Eqs. (2) and (3):

$$\ln c = -kt + A \tag{2}$$

$$t_{1/2} = \frac{0.693}{k} \tag{3}$$

where A is a constant and $t_{1/2}$ is the half-life time of the sulfonamide. The obtained values are given in Table III.

TABLE III. Kinetic parameters of degradation of six sulfonamides in hen eggs at two cooking temperatures (k / min^{-1}, first-order rate constant of degradation; R, coefficient of regression; $t_{1/2}$ / min, half-life time)

Sulfonamide	Kinetic parameter	80 °C	100 °C	R^2
SDM	k	0.00560	0.0147	0.990–0.996
	$t_{1/2}$	124	47.1	
SDZ	k	0.0108	0.0394	0.933–0.960
	$t_{1/2}$	64.2	17.6	
SMM	k	0.00830	0.0277	0.957–0.976
	$t_{1/2}$	83.5	25.0	
SMR	k	0.00780	0.0321	0.956–0.960
	$t_{1/2}$	88.8	21.6	
SMX	k	0.00630	0.0202	0.957–0.985
	$t_{1/2}$	110	34.3	
SMZ	k	0.00990	0.0174	0.943–0.962
	$t_{1/2}$	70.0	39.8	

The data listed in Table III indicate that first-order rate constant of degradation was the highest for SDZ and the lowest for SDM, meaning they were the most instable and stable, respectively, at the two studied cooking temperatures. When the cooking temperature was elevated from 80 to 100 °C, all six sulfonamides degraded faster with the increases ranging from about 1.8 (SMZ) to 4.1 (SMR) folds. Based on the relationship between the first-order rates of degradation and temperature, the apparent activation energy for degradation could be estimated from the Arrhenius equation; the calculated activation energies for the six studied sulfonamides ranged from 30.9 (SMZ) to 77.5 kJ mol^{-1} (SMR).

It was reported that the loss of SMZ from animal tissue cooked in oil at 260 °C was obvious, with a half-life time of about 5 min.[14] Fischer *et al.* found that cooking causeed on average a 46.1 % reduction of SDM in raw fillet of fish fried in vegetable oil at 190 °C.[15] In addition, SDM residues in fish muscles cooked at 190 °C for 45 min were decreased by 54 %.[16] The present result and the previously published results all demonstrate that the procedure of cooking could

decrease the residue levels of sulfonamides in food of animal-origin. The results from Furusawa and Hanabusa showed that the reductions of SDZ, SMX, SMM and SQ were 45–61 % after 12-min boiling and 38–54 % after 12-min roasting at 170 °C.[13] In their paper, it was also stated that when chicken muscle was cooked by boiling or other methods, SDZ appeared to be the most unstable and SMM the most stable, which is in agreement with the present finding. The study of Furusawa and Hanabusa also showed that the half-lives of SDZ, SMX, SMM and SQ in chicken muscle cooked by boiling and roasting decreased in the range from 7.3 to 20.3 min, which might support the results obtained in the present study at 100 °C.

CONCLUSIONS

The degradation kinetics of six sulfonamides, i.e., sulfadiazine, sulfadimethoxine, sulfamerazine, sulfamethazine, sulfamethoxazole and sulfamonomethoxine, in hen eggs at two simulated cooking temperatures were studied in the present work by measuring the sulfonamide residues in the cooked eggs by HPLC. The degradation of the sulfonamides was enhanced at higher temperature. The degradation rate constants of the sulfonamides were obtained assuming first-order reactions, and were found to range from 0.00560 to 0.0108 min^{-1} at 80 °C, or from 0.0147 to 0.0394 min^{-1} at 100 °C. The apparent activation energy for the degradation of the six sulfonamides was estimated to be 30.9 to 77.5 kJ mol^{-1}. Sulfadiazine appeared to be the least stable and sulfadimethoxine the most stable.

ИЗВОД

КИНЕТИКА РАЗЛАГАЊА ШЕСТ СУЛФОНАМИДА У КОКОШИЈЕМ ЈАЈЕТУ У СИМУЛИРАНИМ УСЛОВИМА КУВАЊА

XIN-HUAI ZHAO[1,2], PENG WU[1] и YING-HUA ZHANG[1]

[1]Key Laboratory of Dairy Science, Ministry of Education, Northeast Agricultural University, Harbin 150030 и [2]Northeast Agricultural University, Harbin 150030, P. R. China

Шест сулфонамида је унето у кокошије јаје (0,1 mg kg^{-1} јаја): сулфадиазин, сулфадиметоксин, сулфамеразин, сулфаметазин, сулфаметоксазол и сулфамонометоксин. Јаја су загревана на 80 и 100 °C да би се испитала кинетика разлагања ових сулфонамида у симулираним условима кувања. Суфонамиди су екстраховани из јаја дихлорметаном у ултразвучном купатилу и анализирани методом HPLC. Израчунате су константе реакције првог реда, полуживот сулфонамида и енергије активације применом Аренијусове једначине. Резултати су показали да се свих шест сулфонамида брже распада на вишим температурама, а константе брзине су биле 0,0056–0,0108 min^{-1} на 80 °C и 0,0147–0,0394 min^{-1} на 100 °C. Израчуната енергија активације за разлагање сулфонамида је била 30,9–77,5 kJ mol^{-1}. Сулфадиазин је имао најкраћи полуживот и био је најмање стабилан, док је најдужи полуживот и највећу стабилност имао сулфадиметоксин.

(Примљено 7. септембра, ревидирано 12. новембра 2010)

REFERENCES

1. X. Wang, K. Li, D. Shi, X, Jin, N. Xiong, F. Peng, D. Peng, D. Bi, *J. Chromatogr., B* **847** (2007) 289
2. M. Muldoon, C. Holtzapple, S. Deshpande, R. Beier, L. Stanker, *J. Agric. Food Chem.* **48** (2000) 537
3. F. de Zayas-Blanco, M. S. García-Falcón, J. Simal-Gándara, *Food Control* **15** (2004) 375
4. X. Huanga, D. Yuan, B. Huang, *Talanta* **72** (2007) 1298
5. A. K. Biswas, G. S. Rao, N. Kondaiah, A. S. R. Anjaneyulu, J. K. Malik, *J. Agric. Food Chem.* **55** (2007) 8845
6. G. F. Pang, Y. Z. Cao, C. L. Fan, J. J. Zhang, X. M. Li, Z. Y. Li, G. Q. Jia, *Anal. Bioanal. Chem.* **376** (2003) 534
7. S. Bogialli, R. Curini, A. D. Corcia, M. Nazzari, R. Samperi, *Anal. Chem.* **75** (2003) 1798
8. R. Sheridan, B. Policastro, S. Thomas, D. Rice, *J. Agric. Food Chem.* **56** (2008) 3509
9. S. Bogialli, R. Curini, A. Di Corcia, M. Nazzari, M. L. Polci, *J. Agric. Food Chem.* **51** (2003) 4225
10. T. Korpimäki, E. C. Brockmann, O. Kuronen, M. Saraste, U. Lamminmäki, M. Tuomola, *J. Agric. Food Chem.* **52** (2004) 40
11. H. Zhang, S. Wang, *J. Immunol. Methods* **350** (2009) 1
12. Q. Chu, D. Zhang, J. Wang. J. Ye, *J. Sci. Food Agric.* **89** (2009) 2498
13. N. Furusawa, R. Hanabusa, *Food Res. Int*. **35** (2002) 37
14. M. D. Rose, W. H. H. Farrington, G. Shearer, *Food Addit. Contam.* **12** (1995) 39
15. L. J. Fischer, A. J. Thulin, M. E. Zabik, A. M. Booren, R. H. Poppenga, K. J. Chapman, *J. Agric. Food Chem.* **40** (1992) 1677
16. D. Xu, J. M. Grizzle, W. A. Rogers, C. R. Santerre, *Food Res. Int*. **29** (1996) 339
17. K. Kunihiro, *Food Chem.* **101** (2007) 281
18. P. Wu, X. H. Zhao, *J. Food Sci. (Shi Pin Ke Xue)* **12** (2007) 38 (in Chinese).

Synthesis and characterization of new complexes of some divalent transition metals with *N*-isonicotinamido-4-chlorobenzalaldimine

LUCICA VIORICA ABABEI[1]*, ANGELA KRIZA[2], CRISTIAN ANDRONESCU[3]
and ADINA MAGDALENA MUSUC[3]

[1]*The House of Teaching Staff Giurgiu, 8, Nicholae Droc Barcian Street, Giurgiu,* [2]*University of Bucharest, Faculty of Chemistry, 23 Dumbrava Rosie Street, Bucharest and* [3]*Romanian Academy, "Ilie Murgulescu" Institute of Physical Chemistry, 202 Independence Avenue, 060021 Bucharest, Romania*

Abstract: New complexes of *N*-isonicotinamido-4-chlorobenzalaldimine (INHCBA) with Cu(II), Co(II) and Cd(II), having formula of the type $[M(INHCBA)(ac)_2]\cdot xH_2O$ (M = Cu^{2+}, $x = 1$, M = Co^{2+}, $x = 2$, M = Cd^{2+}, $x = 0$, ac = CH_3COO^-), and with Cu(II), Mn(II) and Zn(II), having formula of the type $[M(INHCBA)_2(H_2O)_2]SO_4\cdot xH_2O$ (M = Cu^{2+}, Mn^{2+}, $x = 2$ and Zn^{2+} $x = 2.5$) were synthesized and characterized by analytical and physico-chemical techniques, *i.e.*, elemental analyses, IR, UV–Vis–NIR and EPR spectroscopy as well as thermal analysis and the determination of the molar conductivity and magnetic moments. The thermal behaviour of complexes was studied by thermogravimetry (TG), differential thermal analysis (DTA) and differential scanning calorimetry (DSC). The ligand behaves as bidentate NO, being coordinated through the azomethine nitrogen and carbonylic oxygen. The heats of decomposition, Δ*H*, associated with the exothermal effects, were also determined.

Keywords: *N*-isonicotinamido-4-chlorobenzalaldimine; template synthesis; transition metal complexes; thermal analysis.

INTRODUCTION

Schiff bases play an important role in inorganic chemistry due to their ability to form stable complexes with most transition metal ions. The coordination compounds of aroylhydrazones were reported to act as enzyme inhibitors and be useful due to their pharmacological applications.[1–3]

The tuberculostatic activity of isonicotinic acid hydrazide and its aroylhydrazones containing azomethine nitrogen was attributed to their ability to form

1103

stable complexes with d- and f-block metal ions.[4] Boraey presented the thermal behaviour of some aroylhydrazone Schiff bases with transition metal complexes.[5] The chromism of these complexes was discussed in terms of change in the ligand field strength and/or coordination geometry. In the context of previous research, a number of complexes of transition metals with ligands derived from 1-naphthaldehyde isonicotinoylhydrazone[6] and 2-(phenyl-2-pyridinylmethylene)-isonicotinohydrayide[7] were obtained and characterized.

Thermal analysis techniques provided information concerning the stability and decomposition of these compounds in the solid state.[8–11] The results led to information concerning the composition, dehydration and thermal behaviour of the complexes.

The synthesis and characterization of three combinations of Cu(II), Co(II) and Cd(II) acetate and three combinations of Cu(II), Mn(II) and Zn(II) sulphate with *N*-isonicotinamido-4-chlorobenzalaldimine are reported herein. The structural formula of the ligand is shown in Fig. 1.
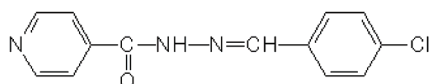

Fig. 1. The structural formula of *N*-isonicotinamido-4-chlorobenzalaldimine (INHCBA).

EXPERIMENTAL

Materials

All chemicals were of pure analytical grade and were purchased from Sigma-Aldrich and Fluka.

Synthesis of N-*isonicotinamido-4-chlorobenzalaldimine*

N-Isonicotinamido-4-chlorobenzalaldimine was obtained by refluxing a mixture of isoniazid (0.002 mol) and 4-chlorobenzaldehyde (0.002 mol) (molar ratio 1:1) on a water bath for 5 h. Ethanol (30 mL) was used as the solvent. After cooling, a white precipitate formed which was filtered, washed with ethanol and dried under vacuum over $CaCl_2$.

Synthesis of complexes

To ethanolic solution of isoniazid (0.002 mol in 30 mL of ethanol) was added an ethanolic solution of 4-chlorobenzaldehyde (0.002 mol in 30 mL ethanol). The mixture was stirred at 50 °C for 30 min and then either an ethanolic solution of Cu (II), Co (II) or Cd (II) acetate (0.002 mol in 30 ml ethanol), or an ethanolic solution of Cu(II), Mn(II) or Zn(II) sulphate (0.001 mol in 15 mL ethanol) was added under stirring. The mixtures were refluxed on water bath for 2 h. On cooling, the metallic complexes precipitated. The solid products (**I**–**VI**) were filtered, washed with ethanol and dried under vacuum over anhydrous $CaCl_2$.

Techniques

Elemental analyses (C, H and N) were realised with an Elemental Combustion System CHNS-O, using a Costech device, type ECS 4010. The metal content was determined by gravimetric methods: Cu with salicylaldoxime, and Co, Mn, Zn and Cd as pyrophosphates.[12]

The melting temperatures of the complexes were directly determined using an SMPI Melting Point Apparatus (Stuart Scientific). The molar conductances of the complexes at room

temperature were measured as 10^{-3} M solutions in DMF using a Consort type C-533 conductivity instrument.

The IR spectra (4000–400 cm^{-1}) were recorded in KBr pellets using a BIO-RAD FTS--135 spectrometer. The reflectance spectra of the complexes were recorded on a JASCO V 670 spectrophotometer.

The magnetic susceptibilities were determined at room temperature using the Faraday method and the electronic paramagnetic resonance (EPR) spectra of the Cu(II) complexes were recorded at room temperature on a Jeol JESS FA 100 spectrometer, with a 100 Hz field modulation.

The thermal experiments were performed on a Mettler Toledo TGA/SDTA 851e thermal analyzer, within the temperature range 300–1300 K, and a Mettler Toledo DSC 853e differential scanning calorimeter, within the temperature range 300–900 K. The TG curves were recorded under a dynamic nitrogen atmosphere with a flow rate of 50 mL min^{-1} and at a heating rate of 10 K min^{-1}. The DSC curves were obtained under a dynamic nitrogen atmosphere with 80 mL min^{-1} flow rate and a 10 K min^{-1} heating rate. The samples were placed in aluminium crucibles for the DSC experiments and alumina crucibles for TG/SDTA experiments, with a pinhole in the lid to prevent pressure build-up due to gaseous products. The sample mass was between 0.8 and 1.5 mg for both methods. At the end of the heating process, the mass of the sample remaining after the DSC experiments represented approximately 35 % from its initial values for all the studied complexes. The TG/DTA and DSC curves were used to characterize the accompanying mass and heat changes during linear heating.

RESULTS AND DISCUSSION

A new Schiff base, named *N*-isonicotinamido-4-chlorobenzalaldimine, was obtained by condensation of *p*-chlorobenzaldehyde (CBA) with isoniazid (INH).

Complexes with INHCBA were obtained by template synthesis. The compounds were soluble in DMF and insoluble in other common organic solvents (methanol, ethanol, acetone, diethyl ether and chloroform). The molar conductivity measurements in DMF showed that the sulphate complexes were 1:1 electrolytes and the acetate complexes non-electrolytes.[13]

The analytical data showed that the complexes may be formulated as [M(INHCBA)(ac)$_2$] (M = Cu(II), Co(II) or Cd(II), ac = CH_3COO^-), and [M(INHCBA)$_2$(H$_2$O)$_2$]SO$_4$ (M = Cu(II), Mn(II) or Zn(II)).

The results of elemental analysis for the prepared complexes are listed below.

*[Cu(INHCBA)(ac)$_2$]·H$_2$O (**I**)*. Anal. Calcd. for $C_{17}H_{18}ClCuN_3O_6$: C, 44.42; H, 3.954; Cu, 13.85; N, 9.146 %. Found: C, 44.16; H, 3.745; Cu, 13.46; N, 9.376 %.

*[Co(INHCBA)(ac)$_2$]·2H$_2$O (**II**)*. Anal. Calcd. for $C_{17}H_{20}ClCoN_3O_7$: C, 43.166; H, 4.265; Co, 12.46; N, 8.887 %. Found: C, 43.421; H, 4.435; Co, 12.64; N, 8.645 %.

*[Cd(INHCBA)(ac)$_2$] (**III**)*. Anal. Calcd. for $C_{17}H_{16}CdClN_3O_5$: C, 41.63; H, 3.29; Cd, 22.93; N, 8.57 %. Found: C, 41.47; H, 3.61; Cd, 22.61; N, 8.90 %.

ABABEI *et al.*

[Cu(INHCBA)₂(H₂O)₂](SO₄)·2H₂O *(IV)*. Anal. Calcd. for $C_{26}H_{28}ClCuN_3O_{10}S$: C, 46.34; H, 4.192; Cu, 9.43; N, 6.23 %. Found: C, 46.78; H, 4.365; Cu, 9.14; N, 6.48 %.

[Mn(INHCBA)₂(H₂O)₂](SO₄)·2H₂O *(V)*. Anal. Calcd. for $C_{26}H_{28}ClMnN_3O_{10}S$: C, 46.94; H, 4.246; Mn, 8.26; N, 6.318 %. Found: C, 46.60; H, 4.564; Mn 8.41; N, 6.63 %.

[Zn(INHCBA)₂(H₂O)₂](SO₄)·2.5H₂O *(VI)*. Anal. Calcd for $C_{26}H_{29}ClN_3O_{10.5}SZn$: C, 45.60; H, 4.272; N, 6.139; Zn, 9.55 %. Found: C, 45.89; H, 4.601; N, 6.42; Zn, 9.30 %.

Some physical properties (colour, melting point, molar conductivity in DMF 10^{-3} M) of the complexes are given in Table I.

TABLE I. Analytical and physical data of the complexes (INHCBA = *N*-isonicotinamido-4--chlorobenzalaldimine; ac = CH_3COO^-)

Compound	Colour	M. p., °C	$\Lambda_M{}^a / \Omega^{-1}$ cm^2 mol^{-1}	μ_{eff} / μ_B
[Cu(INHCBA)(ac)₂]·H₂O (**I**)	Brown	270	5.5	2.25
[Co(INHCBA)(ac)₂] 2 H₂O (**II**)	Brown	255	4.1	5.51
[Cd(INHCBA)(ac)₂] (**III**)	Yellow	299	2.6	Diamagnetic
[Cu(INHCBA)₂(H₂O)₂](SO₄) 2H₂O (**IV**)	Green	239	86	2.07
[Mn(INHCBA)₂(H₂O)₂](SO₄) 2H₂O (**V**)	White	>325	80	5.78
[Zn(INHCBA)₂(H₂O)₂](SO₄) 2.5H₂O (**VI**)	Yellow	>325	82	Diamagnetic

$^a 10^{-3}$ M in DMF at 20 °C

Infrared spectra

The main bands from the IR spectra of the ligand and its metal complexes are presented in Table II.

INHCBA is expected to act as tridentate ligand, the possible coordination sites being the pyridinic nitrogen, the azomethine nitrogen and the amide group. A study and a comparison of the IR spectrum of INHCBA and those of its metal complexes imply that the ligand is bidentate in nature with the carbonyl oxygen and the azomethine nitrogen as the two coordination sites.

In the IR spectrum of the ligand, an intense band appears at 1668 cm^{-1}, which is assigned to the frequency vibration ν(C=O) amide **I**. In the IR spectra of the complexes, the band group corresponding to amide **I** appear shifted by 5–69 cm^{-1} towards lower frequencies, which indicates the involvement of the carbonyl group in the coordination.[14]

The NH stretching bands of the free ligand occur at 3192 and 3091 cm^{-1}, respectively,[15] and remain unaffected after complexation. This excludes the possibility of coordination through the imine nitrogen atom.

Another important band occurs at 1592 cm^{-1}, attributed to the ν(C=N) azomethine mode, appears in the IR spectrum of INHCBA.[16] Shifts towards lower values of Δν, 6–45 cm^{-1}, were also observed for the frequencies charac-

teristic of the azomethine group in all the spectra of the metal complexes. This suggests the involvement of the azomethine nitrogen in the coordination of INHCBA with the metal ions.[17]

The spectra of complexes show bands assigned to both bridging and chelating binding coordination modes of the acetate anion.[18] A correlation between antisymmetric and symmetric carboxylate group infrared absorption frequencies and carboxylate group types has been developed. The acetate ion in aqueous solution is characterized by bands at 1578 and 1411 cm^{-1}, which are commonly assigned to the antisymmetric (v_{asym}) and the symmetric (v_{sym}) stretching vibrations of the carboxylate group. These frequencies and, in particular, their difference, $\Delta v = v_{as} - v_{sym}$ have been used as an empirical indicator of the coordination modes of acetates. According to Deacon and Phillips,[18] a difference larger than 200 cm^{-1} indicates monodentate coordination, whereas one smaller than 150 cm^{-1} indicates a bidentate coordination mode. Moreover, it is accepted that values of Δv smaller than 200 cm^{-1} can indicate a bidentate coordination mode. In complexes **I**–**III**, the frequency of v_{asym}(COO) appears at 1490 cm^{-1}, while those characteristic of v_{sym}(COO) ranged from 1358–1414 cm^{-1}. For these complexes, $\Delta v = v_{asym} - v_{sym} < 150$ cm^{-1}, which is an indication of a bridge or a chelating binding mode for the coordination of the acetate group. Furthermore, an increase of v_{asym} as compared to free acetate corresponds to acetate in a bridging coordination mode, while a decrease of v_{asym} suggests a chelating binding mode.[19]

The IR spectra of the complexes **IV**–**VI** show a band attributed to the counter anion SO$_4$$^{2-}$.[14]

The bands in the domain 3479–3400 cm^{-1} and 911–902 cm^{-1} in the IR spectra of the complexes **IV**–**VI** suggest the presence of coordination water.[20]

The overall IR spectral evidence suggests that INHCBA acts as a bidentate ligand and is coordinated to the metal ions by the azomethine nitrogen and the carbonyl oxygen, whereby a five-member chelate ring is formed.

Electronic and EPR spectra. Magnetic moments

The electronic spectral data and the magnetic moments of the complexes are presented in Table III.

The UV spectrum of the Schiff base presents two bands at 37037 and 28248 cm^{-1}, assigned to $\pi \rightarrow \pi^*$ and $n \rightarrow \pi^*$ transitions.

The electronic spectra of the two Cu(II) complexes exhibit bands at 14450 cm^{-1} for complex **I**, and at 13774 cm^{-1} for complex **IV**, which can be attributed to $xy \rightarrow x^2 - y^2$ transitions. These values together with the magnetic moments (2.25 and 2.07 μ_B) suggest an octahedral geometry for the Cu(II) ions.[21]

The EPR spectrum of polycrystalline [Cu(INHCBA)(ac)$_2$]·H$_2$O complex (**I**) was recorded at room temperature (Fig. 2a). This complex exhibited a broad and

TABLE II. Selected infrared absorption frequencies (cm^{-1}) of INHCBA and its complexes

Compound	ν(OH)	ν(C=O) Amide **I**	ν(C=N) Azomethine	δ(H$_2$O) Coordinated	ν(N–N)	ν(SO$_4^{2-}$) Ionic	ν(COO$^-$)		
							ν_{asym}	ν_{sym}	$\Delta\nu$
INHCBA	–	1668	1592	–	850	–	–	–	–
[Cu(INHCBA)(ac)$_2$]·H$_2$O (**I**)	–	1603	1569	–	842	–	1489	1380	109
[Co(INHCBA)(ac)$_2$]·2H$_2$O (**II**)	–	1653	1569	–	855	–	1490	1414	76
[Cd(INHCBA)(ac)$_2$] (**III**)	–	1599	1570	–	856	–	1490	1358	132
[Cu(INHCBA)$_2$(H$_2$O)$_2$](SO$_4$)·2H$_2$O (**IV**)	3400	1646	1586	911	854	1111	–	–	–
[Mn(INHCBA)$_2$(H$_2$O)$_2$](SO$_4$)·2H$_2$O (**V**)	3400	1662	1547	910	859	1197	–	–	–
[Zn(INHCBA)$_2$(H$_2$O)$_2$](SO$_4$)·2.5H$_2$O (**VI**)	3479	1663	1549	902	860	1123	–	–	–

TABLE III. Electronic spectral data and geometries for the ligand and complexes

Compound	Frequency, cm^{-1}	Assignment	Geometry	$10\Delta q$ / cm^{-1}	B	β
INHCBA	37037	$\pi \rightarrow \pi^*$	–	–	–	–
	28248	$n \rightarrow \pi^*$				
[Cu(INHCBA)(ac)$_2$]·H$_2$O (**I**)	38167	$\pi \rightarrow \pi^*$	Octahedral	–	–	–
	28901	$n \rightarrow \pi^*$				
	14450	$xy \rightarrow x^2 - y^2$				
[Co(INHCBA)(ac)$_2$]·2H$_2$O (**II**)	37878	$\pi \rightarrow \pi^*$	Octahedral	8802	860.4	0.886
	29239	$n \rightarrow \pi^*$				
	21834	$^4T_{1g} \rightarrow {}^4T_{1g}(P)$				
	17667	$^4T_{1g}(F) \rightarrow {}^4A_{2g}$				
	8875	$^4T_{1g} \rightarrow {}^4T_{2g}$				
[Cd(INHCBA)(ac)$_2$] (**III**)	38062	$\pi \rightarrow \pi^*$	Octahedral	–	–	–
	30487	$n \rightarrow \pi^*$				
[Cu(INHCBA)$_2$(H$_2$O)$_2$](SO$_4$)·2H$_2$O (**IV**)	38461	$\pi \rightarrow \pi^*$	Octahedral	–	–	–
	29069	$n \rightarrow \pi^*$				
	13774	$xy \rightarrow x^2 - y^2$				
[Mn(INHCBA)$_2$(H$_2$O)$_2$](SO$_4$)·2H$_2$O (**V**)	39370	$\pi \rightarrow \pi^*$	Octahedral	–	–	–
	34246	$n \rightarrow \pi^*$				
	30487	CT				
[Zn(INHCBA)$_2$(H$_2$O)$_2$](SO$_4$)·2.5H$_2$O (**VI**)	39682	$\pi \rightarrow \pi^*$	Octahedral	–	–	–
	34482	$n \rightarrow \pi^*$				

intense slightly anisotropic signal ($g_{isotropic}$ = 2.1096, $H_{isotropic}$ = 319.971 mT), assigned to the Cu(II) ion in a quasi-isotropic octahedral environment.[22]

The [Cu(INHCBA)$_2$(H$_2$O)$_2$](SO$_4$)·2H$_2$O complex (**IV**) was also examined by EPR spectroscopy and the values for $g_\parallel$ and $g_\perp$ were determined for the proper magnetic field (Table IV). The EPR spectrum (Figure 2b) and the values of the magnetic field parameters require an octahedral symmetry for the Cu(II) complex **IV**.

TABLE IV. EPR data of complex **IV**

Compound	g		H / mT	
	$g_\parallel$	$g_\perp$	$H_\parallel$	$H_\perp$
[Cu(INHCBA)$_2$(H$_2$O)$_2$](SO$_4$)·2H$_2$O (**IV**)	2.2648	2.1129	298.063	319.491
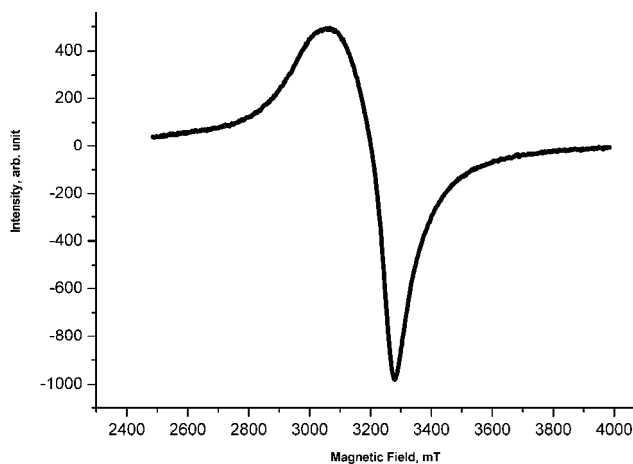
(a)
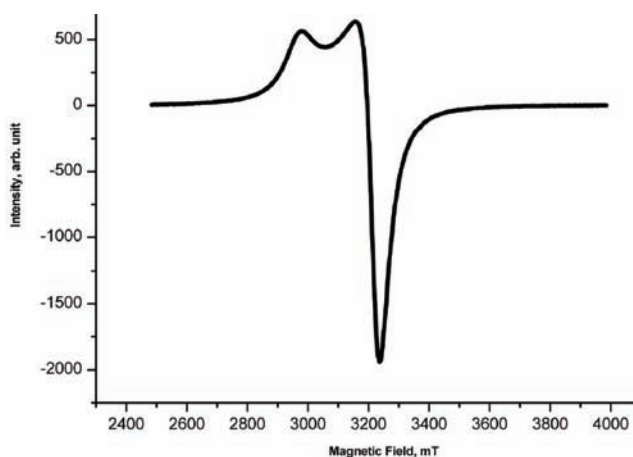
(b)

Fig. 2. The EPR spectra for complex **I** (a) and **IV** (b) at room temperature.

The electronic spectrum of the Co(II) complex presents three bands at 8875, 17667 and 21834 cm^{-1}, attributed to the d–d transitions $^4T_{1g} \rightarrow ^4T_{2g}$, $^4T_{1g}(F) \rightarrow \rightarrow ^4A_{2g}$ and $^4T_{1g} \rightarrow ^4T_{1g}(P)$, respectively. These transitions and the values of the field parameters correspond to those characteristic for an octahedral geometry.[21] For this complex, the experimentally determined magnetic moment was 5.51 μ_B, indicating a high-spin character and excluding oxidation to Co(III). This value is within the range of 4.3–5.7 μ_B corresponding to an octahedral geometry for a cobalt ion.[17]

The ligand field splitting energy ($10\Delta q$), the interelectronic repulsion parameter (B) and the nephelauxetic ratio (β) for the Co(II) complex were calculated using the secular equations given by König[23] and the values are presented in Table III.

In the spectra of the Cd(II) and Zn(II) complexes, the bands of the ligand appear displaced to lower values. For d^{10} ions, the UV spectrum provides no information about the environment. However, according to the IR spectra, an octahedral environment of the metallic ion is proposed.

The Cd(II) and Zn(II) complexes are diamagnetic, as expected for the d^{10} configuration.[24]

The Mn(II) complex presents a signal in UV domain at 30487 cm^{-1} assigned to a transfer of electric load, according to the theory data for a d^5 ion. It is well known that d–d transitions occur in d^5 systems but these transitions are of very low intensity and hence no d–d bands for such transitions were observed.[25]

The magnetic moment determined for the Mn(II) complex was 5.78 μ_B. This value falls in the range of 5.65–6.10 μ_B and it is appropriate for manganese ions in an octahedral environment.[25]

Thermal behaviour of the complexes

The determined temperatures ranges and percent mass losses are given in Table V.

The thermal TG/DTA and DSC curves of ligand are presented in Fig. 1-S, Supplementary material. The TG/DTA curves of Schiff base ligand shows an exothermal decomposition with a maximum at $T_{max} = 603$ K on the DTG curve. The evaluation of the exothermal peak area (DSC curve) gave a value of $\Delta H = -122.5$ J g^{-1}.

The TG/DTA and DSC curves of complex **I** are shown in Fig. 2-S, Supplementary material. The mass loss observed between 323 and 373 K, corresponding to an endothermic peak at 310 K on DTG curve, is due to dehydration with a loss of one molecule of water (Calcd., 4.08 %; exp., 4.04 %). The thermal decomposition occurred in two steps between 373–483 K and 483–1260 K with total mass loss of 60.15 %. It can be observed from the TG curve that the decomposition process was not completed. Decomposition of the complex was

also confirmed by a strong exothermic effect on DSC curve with a maximum at 585 K. The evaluation of the exothermal peak area gave a value of $\Delta H = -9708.7$ J g^{-1}. The final residue, estimated as CuO and unreacted compound,[26,27] had an observed mass of 35.81 %.

TABLE V. Thermoanalytical results for the M(II) complexes

Compound	TG range, K	Mass loss found (calcd.), %	Assignment
[Cu(INHCBA)(ac)$_2$]·H$_2$O (**I**)	323–373	4.04 (4.08)	Loss of lattice water molecule
	373–483	10.15 (10.45)	Loss of CO$_2$ molecule
	483–1260	50.00	Removal of the ligand (the thermal decomposition was not completed)
	>1260	35.81	Leaving CuO and unreacted compounds
[Co(INHCBA)(ac)$_2$]·2H$_2$O (**II**)	323–460	8.27 (8.26)	Loss of lattice water molecule
	460–1260	69.16 (69.44)	Loss of CO$_2$ molecules and decomposition of ligand
	>1260	22.57 (17.16)	Leaving Co$_2$O$_3$
[Cd(INHCBA)(ac)$_2$] (**III**)	500–670	72.73 (70.97)	Loss of CO$_2$ molecules and decomposition of ligand
	>670	24.48 (26.12)	Leaving CdO
[Cu(INHCBA)$_2$(H$_2$O)$_2$](SO$_4$) 2H$_2$O (**IV**)	323–383	7.31 (7.34)	Loss of lattice water molecule
	383–470	6.86 (7.34)	Removal of coordinated water molecule
	470–1240	67.71 (69.13)	Removal of one molecule of SO$_3$ and ligand
	>1240	18.12 (17.48)	Leaving CuO
[Mn(INHCBA)$_2$(H$_2$O)$_2$](SO$_4$) 2H$_2$O (**V**)	323–388	8.00 (7.46)	Loss of lattice water molecule
	388–523	7.83 (7.46)	Removal of coordinated water molecule
	523–653	16.31 (17.92)	Removal of molecule of SO$_3$
	653–1270	38.48 (43.89)	Removal of ligand
	>1270	29.38 (29.00)	Leaving MnO
[Zn(INHCBA)$_2$(H$_2$O)$_2$](SO$_4$)·2.5H$_2$O (**VI**)	323–383	9.11 (9.05)	Loss of lattice water molecule
	383–473	6.28 (6.72)	Removal of coordinated water molecule

TABLE V. Continued

Compound	TG range, K	Mass loss found (calcd.), %	Assignment
[Zn(INHCBA)$_2$(H$_2$O)$_2$](SO$_4$)·2.5H$_2$O (**VI**)	473–673	16.32 (17.51)	Removal of molecule of SO$_3$
	673–1270	37.29 (38.43)	Removal of ligand
	>1270	31.00 (32.33)	Leaving ZnSO$_4$

The thermal decomposition of [Co(INHCBA)(ac)$_2$]·2H$_2$O proceeded in four stages (Fig. 3-S, Supplementary material). Thermal dehydration occurred between 323 and 460 K with a mass loss of 8.27 %. The subsequent steps corresponded to the total decomposition of the complex. The DSC curve had a wide range of thermal change with several exothermal superposed peaks with maxima at 580, 660, 705 and 830 K. These are correlated with the decomposition of the ligand molecules and loss of CO$_2$ molecules. The evaluation of the exothermal peaks area (neglecting the partial superposition) gave a value of $\Delta H = -4657.9$ J g^{-1} for the first peak and $\Delta H = -601.5$ J g^{-1} for the second one. The final decomposition process corresponded to the formation of cobalt(III) oxide as the final product.

The TG/DTA and DSC curves of [Cd(INHCBA)(ac)$_2$] complex are presented in Fig. 4-S, Supplementary material. The complex was stable up to 500 K. The thermal decomposition progressed in one stage, as a complex process with two superposed peaks. The end product, estimated as CdO, had an observed mass of 24.48 %, compared with the calculated value of 26.12 %.

The complexes:

[Cu(INHCBA)$_2$(H$_2$O)$_2$](SO$_4$)·2H$_2$O (**IV**),

[Mn(INHCBA)$_2$(H$_2$O)$_2$](SO$_4$)·2H$_2$O (**V**) and

[Zn(INHCBA)$_2$(H$_2$O)$_2$](SO$_4$) 2.5H$_2$O (**VI**)

underwent decomposition mainly in four stages (Figs. 5-S–7-S, Supplementary material). The first stage occurred in the 323–383, 323–388 and 323–383 K ranges, respectively, corresponding to dehydration process and release of two crystallization water molecules for complexes **IV** and **V**, and 2.5 molecules for complex **VI**. The second decomposition

stage of the complexes corresponded to removal of coordinated water molecules. The third decomposition stage of the complexes corresponded to partial decomposition. The third stage for complex **IV** was in the 470–773 K temperature range with two strong exothermic peaks on the DSC curve with maxima at 484 K and 625 K. This correlated with the decomposition of the ligand molecule and expulsion of SO$_3$ molecules. The evaluation of the areas of the exothermal peaks gave a value of $\Delta H = -290.5$ J g^{-1}, and $\Delta H = -1735.9$ J g^{-1}, respectively.

The third decomposition stage of the complexes **V** and **VI** is in continuation of the second stage, in the 523–653 K and 473–673 K temperature ranges, respectively.

The final decomposition process for complexes **IV** and **V** corresponded to the formation of copper oxide and manganese oxide, respectively, as the final product. The final residue for complex **VI** was estimated as $ZnSO_4$.

Based on the above analytical and spectral data and the thermal analysis, the structural formula and stoichiometry for complexes indicated in Fig. 3 were proposed.

(a)

(b)
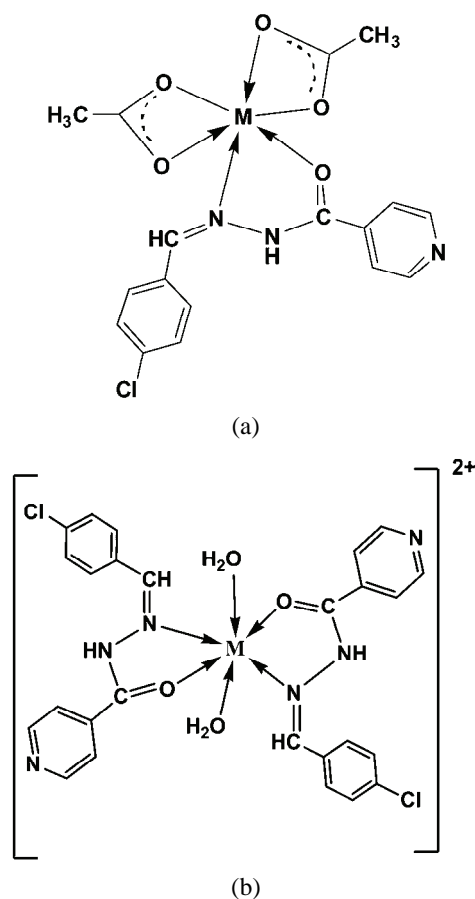
Fig. 3. Structural formula proposed for a) [M(INHCBA)(ac)$_2$]·xH$_2$O (M = Cu^{2+}, x = 1, M = Co^{2+}, x = 2, M = Cd^{2+}, x = 0, ac = CH$_3$COO$^-$) and b) [M(INHCBA)$_2$(H$_2$O)$_2$]SO$_4$·xH$_2$O (M = = Cu^{2+}, Mn^{2+}, x = 2 and Zn^{2+}, x = 2.5.

CONCLUSIONS

Six new complexes of *N*-isonicotinamido-4-chlorobenzalaldimine (INHCBA) with Cu(II), Co(II), Cd(II), Mn(II) and Zn(II), were synthesized and characterized. The spectroscopic data showed that the Schiff base ligand acted as bidentate NO, being coordinated through the azomethine nitrogen and carbonylic

oxygen. The structural formula of the complexes were proposed based on elemental analysis, molar conductance, magnetic moment values, IR, UV–Vis and EPR spectra and thermal analysis. The number of water molecules of crystallization was determined by differential thermal analysis. The thermal results allowed information concerning the stoichiometry of these compounds to be acquired.

SUPPLEMENTARY MATERIAL

The thermal TG/DTA and DSC curves of the ligand and complexes are available electronically at http://www.shd.org.rs/JSCS/, or from the corresponding author on request.

ИЗВОД

СИНТЕЗА И КАРАКТЕРИЗАЦИЈА НОВИХ КОМПЛЕКСА НЕКИХ ДВОВАЛЕНТНИХ ЈОНА ПРЕЛАЗНИХ МЕТАЛА СА *N*-ИЗОНИКОТИНАМИДО-4-ХЛОРБЕНЗАЛАЛДИМИНОМ

LUCICA VIORICA ABABEI[1], ANGELA KRIZA[2], CRISTIAN ANDRONESCU[3] и ADINA MAGDALENA MUSUC[3]

[1]*The House of Teaching Staff Giurgiu, 8, Nicholae Droc Barcian Street, Giurgiu,* [2]*University of Bucharest, Faculty of Chemistry, 23 Dumbrava Rosie Street, Bucharest u* [3]*Romanian Academy, "Ilie Murgulescu" Institute of Physical Chemistry, 202 Independence Avenue, 060021 Bucharest, Romania*

Описана је синтеза и структурна карактеризација нових комплекса двовалентних јона прелазних метала са *N*-изоникотинамидо-4-хлорбензалалдимином (INHCBA) као лигандом. Нађено је да комплекси Cu(II), Co(II) и Cd(II) имају општу формулу типа [M(INHCBA)(ac)$_2$]·xH$_2$O (M = Cu^{2+}, x = 1, M = Co^{2+}, x = 2, M = Cd^{2+}, x = 0, ac = CH$_3$COO$^-$), док је код комплекса Cu(II), Mn(II) и Zn(II) нађена општа формула типа [M(INHCBA)$_2$(H$_2$O)$_2$]SO$_4$·xH$_2$O (M = Cu^{2+}, Mn^{2+}, x = 2 и Zn^{2+} x = 2.5). За карактеризацију комплекса употребљене су различите аналитичке и физичко-хемијске методе, као што су елементална микроанализа, IR, UV–Vis–NIR и EPR спектроскопија, термална анализа, као и различита кондуктометријска и магнетна мерења. Термална анлиза комплекса урађена је на бази термогравиметријске (TG) и диференцијалне термалне анализе (DTA), као и диферен-цијалне скенирајуће калориметрије (DSC). Нађено је да се испитивани лиганд бидентатно (NO) координује, и то преко азометинског атома азота и карбонилног атома кисеоника.

(Примљено 27. октобра 2010, ревидирано 2. фебруара 2011)

REFERENCES

1. J. R. Dilworth, *Coord. Chem. Rev.* **21** (1976) 29
2. J. R Merchant, D. S. Clothia, *J. Med. Chem.* **13** (1970) 335
3. N. S. Biradar, B. R. Havinale, *Inorg. Chim. Acta* **17** (1976) 157
4. Z. Y. Yang, R. D. Yang, F. S. Li, K. B. Yu, *Polyhedron* **19** (2000) 2529
5. H. A. El-Boraey, *J. Therm. Anal. Calorim.* **81** (2005) 339
6. A. Kriza, L. V. Ababei, N. Cioatera, I. Rau, N. Stanica, *J. Serb. Chem. Soc*. **75** (2010) 229
7. L. V. Ababei, A. Kriza., A. M. Musuc, C. Andronescu, E A. Rogozea., *J. Therm. Anal. Calorim.* **101** (2010) 987
8. S. S. Konstantinović, B. S. Radovanović, A. Krklješ, *J. Therm. Anal. Calorim.* **90** (2007) 525

9. F. Dogan, M. Ulusoy, O. F. Ozturk, I. Kaya, B. Salih, *J. Therm. Anal. Calorim.* **96** (2009) 267
10. D. A. Kose, G. Gokce, S. Gokce, I. Uzun, *Coord. Chem. Rev.* **7** (1971) 81
11. A. Kriza., M. L. Dianu, C. Andronescu, E A. Rogozea, A. M. Musuc, *J. Therm. Anal. Calorim.* **100** (2010) 929
12. A. I. Vogel, *A text book of quantitative inorganic analysis*, 2nd ed., Longmans, London, UK, 1961
13. W. J. Geary, *Coord. Chem. Rev*. **7** (1971) 81
14. K. Nakamoto, *Infrared Spectra of Inorganic and Coordination Compounds*, 2nd ed., Wiley-Interscience, New York, 1970
15. L. J. Bellamy, *The Infrared Spectra of Complex Molecules*, Methuen, London, UK, 1954
16. G. R. Burns, *Inorg. Chem.* **7** (1968) 277
17. R. K. Agarwal, D. Sharma, L. Shing, H. Agarwal, *Bioinorg. Chem. Appl.* **2006** (2006) ID 29234, 1
18. G. B. Deacon, R. J. Philips, *Coord. Chem. Rev.* **33** (1980) 227
19. G. B. Deacon, F. Hubor, R. J. Philips, *Inorg. Chim. Acta* **104** (1985) 41
20. A. B. P. Lever, *Inorganic electronic spectroscopy*, Elsevier, Amsterdam, The Netherlands, 1984
21. B. Singh, K. K. Narang, R. Srivastava, *Synth. React. Inorg. Met.-Org. Chem.* **32** (2002) 1577
22. A. Jaggj, S. Chandra, K. K. Sharma. *Polyhedron* **4** (1985) 163
23. E. König, *Struct. Bond.* **9** (1971) 175
24. P. W. Selwood, *Magnetochemistry*, Interscience Publisher, New York, London, 1956
25. R. Aurkie, S. Banerjee, S. Sen, R. J. Butcher, G. M. Rosair, M. T. Garland, S. Mitra, *Struct. Chem*. **19** (2008) 209
26. M. Lalia-Kantouri, L. Tzavellas, D. Paschalidis, *J Therm. Anal. Calorim.* **91** (2008) 937
27. S. U. Din, M. Umar, *J. Therm. Anal. Calorim.* **58** (1999) 61.

SUPPLEMENTARY MATERIAL TO

Synthesis and characterization of new complexes of some divalent transition metals with *N*-isonicotinamido-4-chlorobenzalaldimine

LUCICA VIORICA ABABEI[1]*, ANGELA KRIZA[2], CRISTIAN ANDRONESCU[3] and ADINA MAGDALENA MUSUC[3]

[1]*The House of Teaching Staff Giurgiu, 8, Nicholae Droc Barcian Street, Giurgiu,* [2]*University of Bucharest, Faculty of Chemistry, 23 Dumbrava Rosie Street, Bucharest and* [3]*Romanian Academy, "Ilie Murgulescu" Institute of Physical Chemistry, 202 Independence Avenue, 060021 Bucharest, Romania*
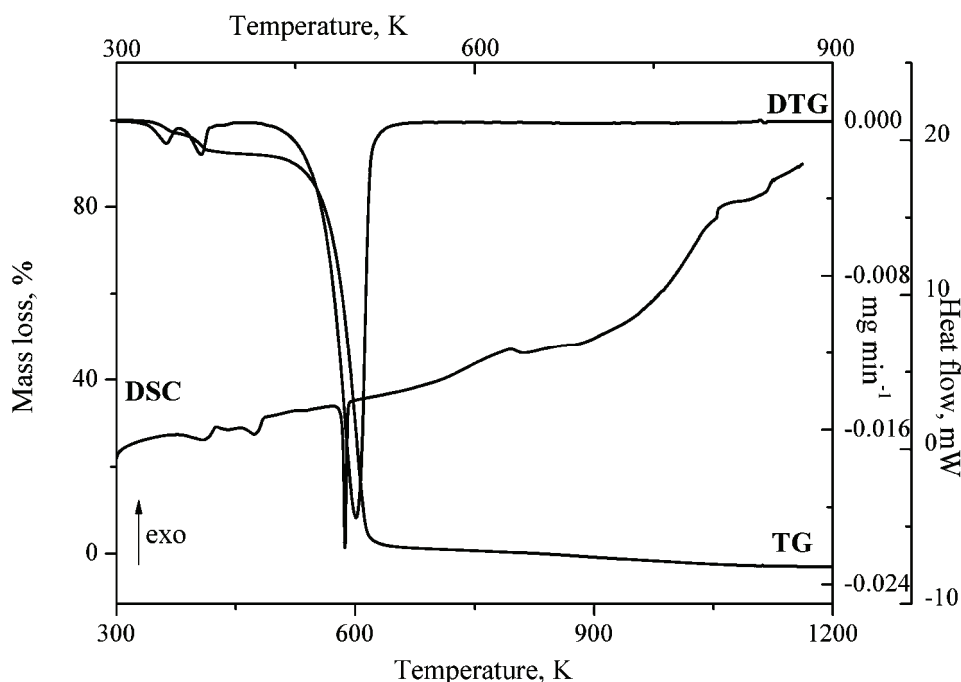
Fig. 1-S. TG/DTA and DSC curves of INHCBA.

* Corresponding author. E-mail: lucica_32@yahoo.com

S19
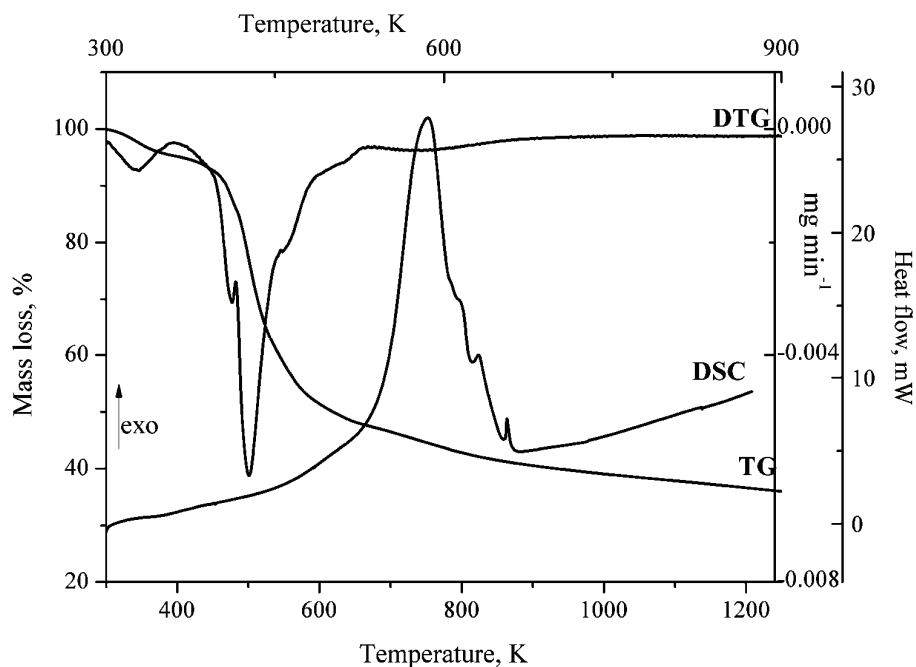
Fig. 2-S. TG/DTA and DSC curves of [Cu(INHCBA)(ac)$_2$]·H$_2$O.
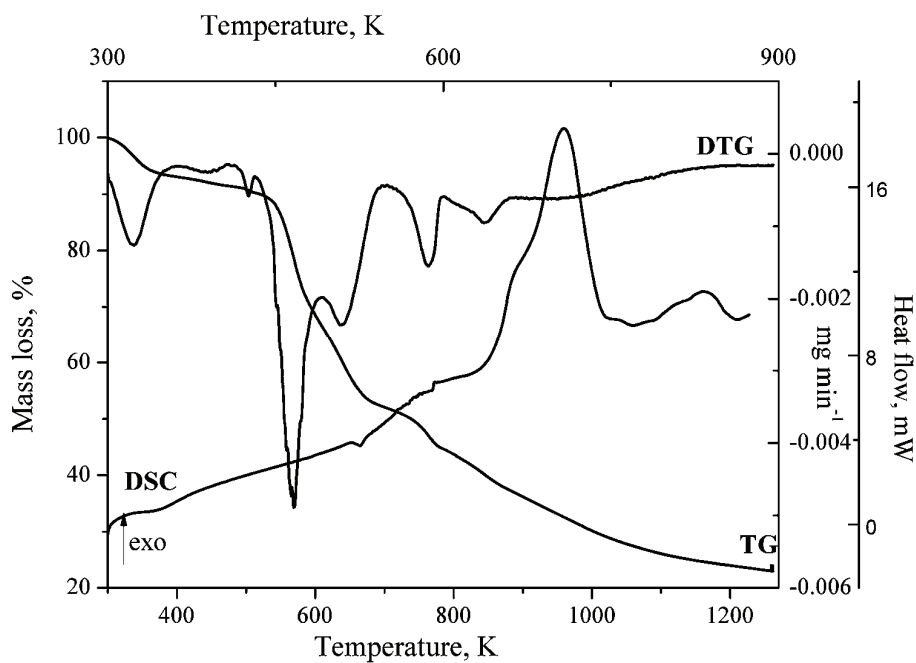
Fig. 3-S. TG/DTA and DSC curves of [Co(INHCBA)(ac)$_2$]·2H$_2$O.
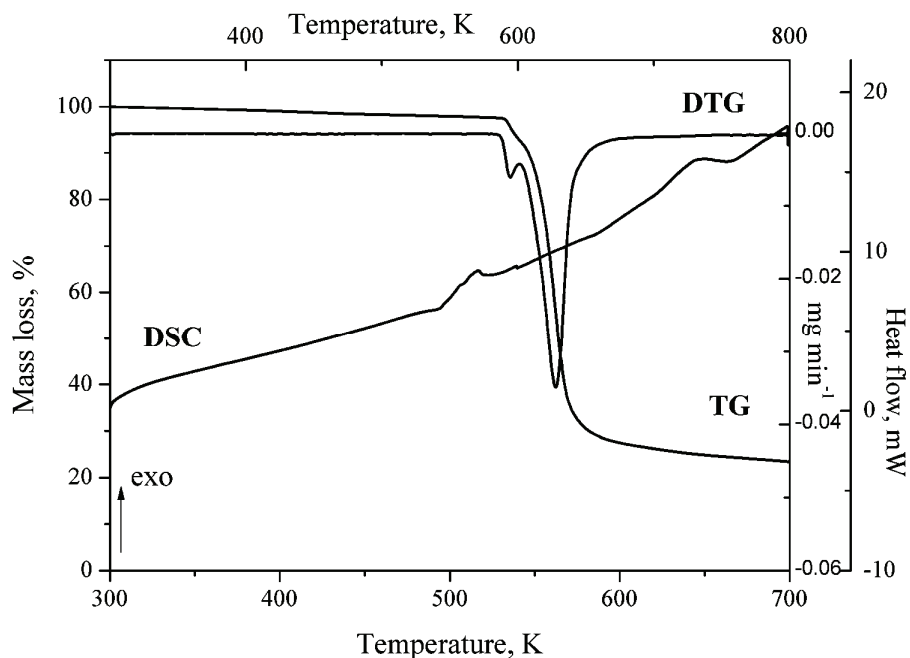
Fig. 4-S. TG/DTA and DSC curves of [Cd(INHCBA)(ac)$_2$].
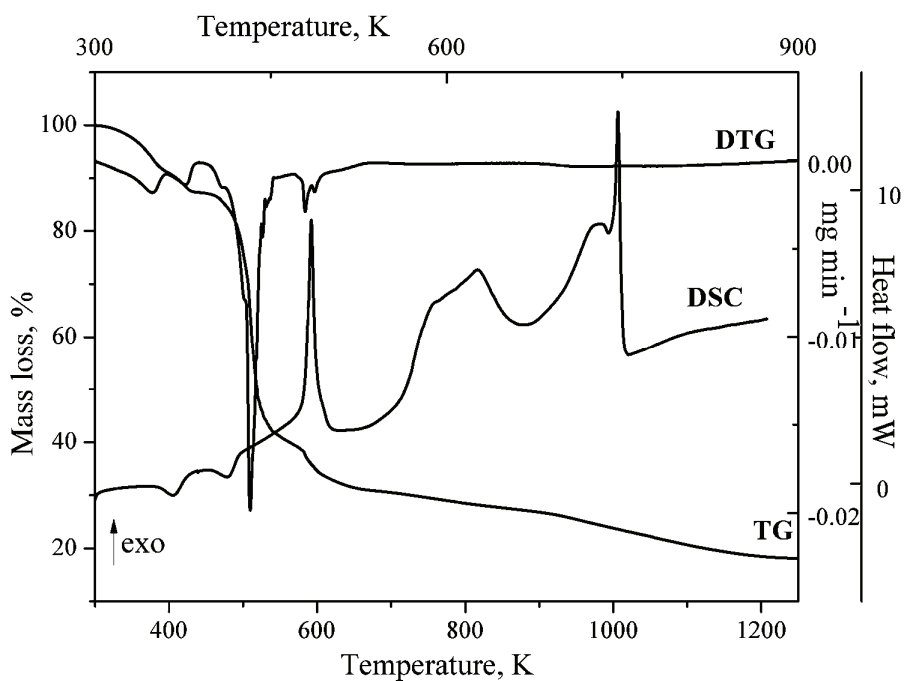
Fig. 5-S. TG/DTA and DSC curves of [Cu(INHCBA)$_2$(H$_2$O)$_2$](SO$_4$)·2H$_2$O.

Temperature, K
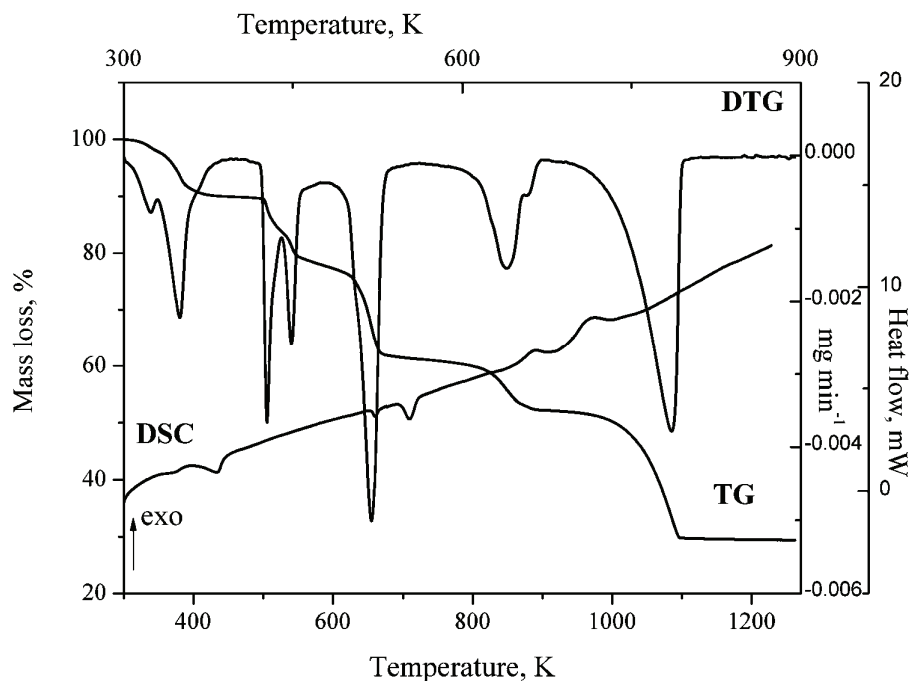
Fig. 6-S. TG/DTA and DSC curves of [Mn(INHCBA)$_2$(H$_2$O)$_2$](SO$_4$)·2.5H$_2$O.

Temperature, K
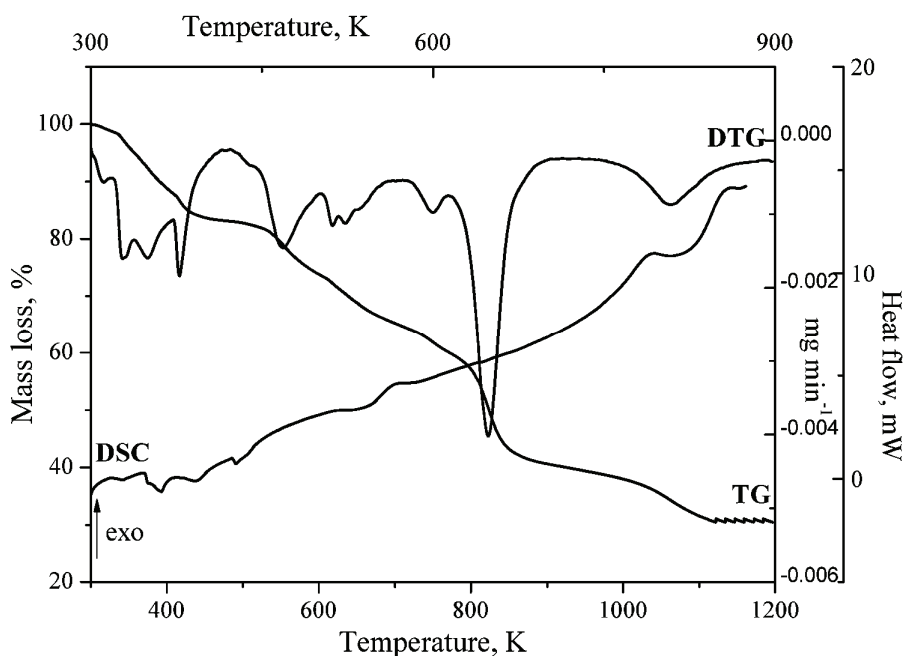
Fig. 7-S. TG/DTA and DSC curves of [Zn(INHCBA)$_2$(H$_2$O)$_2$](SO$_4$)·2.5H$_2$O.

A quantitative structure–activity relationship study of tetrabutylphosphonium bromide analogs as muscarinic acetylcholine receptors agonists

MEHDI NEKOEI[1]*, MAHMOUD SALIMI[2], MOHSEN DOLATABADI[3] and MAJID MOHAMMADHOSSEINI[1]

[1]*Department of Chemistry, Faculty of Science, Islamic Azad University, Shahrood Branch, Shahrood,* [2]*Department of Chemical Engineering, Faculty of Engineering, Islamic Azad University of Arak, Arak and* [3]*Department of Chemistry, Faculty of Science, University of Birjand, Birjand, Iran*

Abstract: Quantitative structure–activity relationship (QSAR) of tetrabutyl-phosphonium bromide (TBPB) analogs as muscarinic acetylcholine receptors (mAChRs) agonists was studied. A suitable set of molecular descriptors was calculated and stepwise multiple linear regression (SW-MLR) was employed to select those descriptors that resulted in the best fitted models. A MLR model with three selected descriptors was obtained. Furthermore, the MLR model was validated using the leave-one-out (LOO) and leave-group-out (LGO) cross-validation, and the *Y*-randomization test. This model, with high statistical significance (R^2_{train} = 0.982, F = 388.715, Q^2_{LOO} = 0.973, Q^2_{LGO} = 0.977 and R^2_{test} = 0.986) could predict the activity of the molecules with a percentage prediction error lower than 5 %.

Keywords: QSAR; muscarinic receptor; TBPB; multiple linear regression.

INTRODUCTION

Muscarinic acetylcholine receptors (mAChRs) are members of the GPCR family A that mediate the metabotropic actions of the neurotransmitter acetylcholine (ACh).[1–3] To date, five distinct subtypes of mAChRs (M1–M5) have been cloned and sequenced. M1, M3 and M5 activate phospholipase C and calcium through Gq, whereas M2 and M4 block the action of adenylyl cyclase through Gi/o.[1–3] mAChR-regulated cholinergic signaling plays a critical role in a wide variety of CNS and peripheral functions, including memory and attention mechanisms, motor control, nociception, regulation of sleep wake cycles, cardiovascular function, renal and gastrointestinal function and many others.[4–6] As a re-

---

* Corresponding author. E-mail: m_nekoei1356@yahoo.com

sult, agents that can selectively modulate the activity of specific mAChRs have therapeutic potential in multiple pathological states.[1–6]

Some novel tetrabutylphosphonium bromide (TBPB) analogs were recently reported as highly selective M1 allosteric agonists, which displayed robust efficacy in several preclinical antipsychotic models, as well as significant effects on the processing of amyloid precursor protein (APP) towards the non-amyloidogenic pathway and decreased Aβ production.[7,8]

Although there are several experimental methods available for screening the biological activity of chemicals (*e.g.*, *in vivo* and *in vitro* assay tests), and all have been performed using receptors and other biological materials of human, rat, mouse, and calf origin at least,[9] they are costly, time-consuming, and can potentially produce toxic side products from the experimental methods used today. This has meant that the development of computational methods as an alternative tool for predicting the properties of chemicals has been a subject of intensive study. Among the computational methods, quantitative structure–activity relationships (QSAR) have found diverse applications for predicting the properties of compounds, including biological activity prediction,[10] physical property prediction[11] and toxicity prediction.[12] QSAR models are essentially calibration models in which the independent variables are molecular descriptors that describe the structure of molecules and the dependent variable is the activity of interest.

In the present work, stepwise multiple linear regressions were employed for variable selection and model development in a QSAR analysis of the activity of some novel TBPB analogs. Finally, the accuracy of the proposed model was illustrated using leave-one-out (LOO) and leave-group-out (LGO) cross-validations and the *Y*-randomization technique.

DATA AND METHODOLOGY

The data used in this QSAR study consisted of the half maximal effective concentration (EC_{50}), which refers to the concentration of a TBPB analog that induces a response halfway between the baseline and maximum, that were reported by Bridges *et al.*[7,8] The activity data (EC_{50} (nM)) was converted to the logarithmic scale pEC_{50} ($-\log EC_{50}$ (M)) and then used for the subsequent QSAR analyses as the response variables. The *z*-matrices (molecular models) were constructed with HyperChem 7.0 and molecular structures were optimized using the AM1 algorithm.[13] In order to calculate the theoretical descriptors, the Dragon package version 2.1 was used.[14] For this propose the output of the HyperChem software for each compound was fed into the Dragon program and the descriptors were calculated. As a result, a total of 1481 theoretical descriptors were calculated for each compound in the data set (32 compounds).

The theoretical descriptors were reduced by the following procedure: 1) the descriptors that were constant were eliminated (308 descriptors); 2) in addition, to decrease redundancy existing in the descriptors, the correlation of the descriptors with each other and with the pEC_{50} of the molecules were examined, and collinear descriptors ($R > 0.9$) were detected. Among the collinear descriptors, the one that had the highest correlation with the pEC_{50} values was retained and the others were removed from the data matrix (736 descriptors).

Multiple linear regression analysis

The multiple linear regression method (MLR) is one of the most used modeling methods in QSAR. MLR regressions, a linear technique that can determine the relative importance of descriptors, are usually used to generate QSAR models. The MLR method provides an equation linking the structural features to the pEC_{50} of the compounds:

$$pEC_{50} = a_0 + a_i d_i + \cdot \ldots \cdot + a_n d_n \tag{1}$$

where the intercept (a_0) and the regression coefficients of the descriptors (a_i) are determined using the least-squares method. d_i has the usual definition, variable or descriptor in this case. The elements of this vector are equivalent numerical values of a 3D structure of the molecules or the structural descriptors. The program used for the MLR analysis was written in Matlab 6.5.[15]

Stepwise multiple regression

The stepwise multiple regression technique based on forward selection was used to select the most appropriate descriptors.[16] The variable considered for inclusion at any step was the one yielding the largest single degree of freedom *F*-ratio among the variables that were eligible for inclusion. The variable was included only if this value was larger than a fixed value F_{in}. Consequently, at each step, the jth variable was added to a *k*-size model if:

$$F_j = \max_j \left(\frac{RSS_k - RSS_{k+j}}{S^2_{k+j}} \right) > F_{in} \tag{2}$$

In the above inequality, *RSS* is the residual sum of squares and *S* is the mean square error. The subscript *k+j* refers to quantities computed when the jth variable was added to the *k* variables that were already included in the model.

Cross-validation technique

The consistency and reliability of a method can be explored using the cross-validation technique.[17] Two different strategies, leave-one-out (LOO) and leave-group-out (LGO), can be employed in this method. In the LOO strategy, by deleting each time one object from the training set, a number of models will be produced. Obviously, the number of models produced by the LOO procedure is equal to the number of available examples *n* (*n* = 26). The prediction error sum of the squares (*PRESS*) is a standard index to measure the accuracy of a modeling method based on the cross-validation technique. Based on the *PRESS* and *SSY* (sum of the squares of the deviations of the experimental values from their mean) statistics, Q^2 can be easily calculated from Eq. (3):

$$Q^2_{LOO} = \frac{PRESS}{SSY} = 1 - \frac{\sum_{i=1}^{n} \left(y_{exp} - y_{pred} \right)^2}{\sum_{i=1}^{n} \left(y_{exp} - \bar{y} \right)^2} \tag{3}$$

In the case of the LGO, *G* represents a group of randomly selected data points which would be left out at the beginning and would be predicted by the model which was developed using the remaining data points. Thus, *G* molecules are considered as a prediction set. The value of Q^2_{LGO} can be calculated using Eq. (4):

$$Q^2_{LGO} = \frac{PRESS}{SSY} = 1 - \frac{\sum_{i=1}^{test} \left(y_{exp} - y_{pred} \right)^2}{\sum_{i=1}^{test} \left(y_{exp} - \bar{y}_{train} \right)^2} \tag{4}$$

It is usual to choose 20 % of the total number of molecules to be left out. Therefore, in the present work, five data points were removed from the data set and the model was refitted; the predicted values for those points were then compared to their experimental values. Again, this was repeated until each data point had been omitted once. The higher the Q^2_{LOO} or Q^2_{LGO}, the higher is the predictive power of the model.

Y-*randomization test*

This technique ensures the robustness of a QSAR model.[18] The dependent variable vector (biological action) is randomly shuffled and a new QSAR model is developed using the original independent variable matrix. The new QSAR models (after several repetitions) are expected to have low R^2 and Q^2 values. If the opposite is the case, then an acceptable QSAR model cannot be obtained for the specific modeling method and data.

RESULTS AND DISCUSSION

For the selection of the most important descriptors, the stepwise multiple regression technique based on forward selection was used. According to a rule of thumb, at least five data points (compounds) should be included in the equation for every parameter (descriptor). On the other hand, the ratio of 5 training molecules for each descriptor must be included in the equation. In order to investigate the optimum number of descriptors to be used in a model for modeling pEC_{50}, the statistical parameters (R^2 and Q^2) for 1–5 parameter models were calculated. The results showed that the models with 4 and 5 descriptors did not significantly improve the statistics of the models, which determined that the optimum subset size had been achieved with a maximum of 3 descriptors.

Since colinearity between the variables degrades the performance of MLR--based QSAR models, before a multiparametric analysis was undertaken, the correlations between every one of the variables used in this study were examined. The correlation matrix itself showed how the employed descriptors were mutually correlated. The correlation matrix obtained in the present case is shown in Table I, from which it could be seen that the correlation coefficient value of each pair of descriptors was less than 0.60, which meant that the selected descriptors were independent.

TABLE I. The correlation coefficient matrix for the descriptors used in this study

	ATS8m	C-028	SIC2
ATS8m	1		
C-028	0.43	1	
SIC2	0.16	–0.58	1

Predictive power of the model

In order to build and test the models, a data set of 32 compounds was randomly separated into a training set of 26 compounds, which was used to build model and a test set of 6 compounds, which was applied to test the built model.

With the selected two descriptors, a linear model was built using the training set data, and the following equation was obtained:

$$pEC_{50} = 15.15(\pm0.34) - 5.88(\pm0.94)ATS8m - 2.18(\pm0.11)C\text{-}028 \qquad (5)$$
$$N = 26, R^2_{train} = 0.964, Q^2_{LOO} = 0.953, Q^2_{LGO} = 0.956,$$
$$F = 310.829, R^2_{test} = 0.984$$

In this and the following equations, N is the number of compounds, R^2 is the squared correlation coefficient, Q^2 is the squared cross-validation coefficient and F is the Fisher F statistic. The figures in parentheses are the standard deviations. Then the built model was used to predict the test set data. The statistical quality of Eq. (5) is good, but to gain better quality results, the MLR model was used with three descriptors and the following equation was obtained:

$$pEC_{50} = 24.91(\pm2.18) - 3.79(\pm0.83)ATS8m -$$
$$- 2.54(\pm0.12)C\text{-}028 - 13.62(\pm3.02)\ SIC2 \qquad (6)$$
$$N = 26, R^2_{train} = 0.982, Q^2_{LOO} = 0.973, Q^2_{LGO} = 0.977,$$
$$F = 388.715, R^2_{test} = 0.986$$

The prediction results and relative error percentages (RE / %) are given in Table II, from which it can be seen that the calculated values of pEC_{50} are in good agreement with those of the experimental values and also the variables used in this equation can predict the activity of the molecules with a prediction error percentage of lower than 5 %. The values of pEC_{50} for the compounds in the training and test sets calculated using the Eq (6) are plotted *versus* the corresponding experimental values in Fig. 1. A plot of the residuals for the calculated values of pEC_{50} in training and test sets *versus* the corresponding experimental values is illustrated in Fig. 2. As can be seen, the model did not show proportional and systematic error because the propagation of the residuals on both sides of zero are random.

The model obtained was validated using the leave-one-out (LOO) and leave-group-out (LGO) cross-validation processes. With the LOO cross-validation, a data point is removed from the set and the model is recalculated. The predicted activity for that point is then compared to its actual value. This is repeated until each data point is omitted once. For LGO cross-validation, 20 % of the data points are removed from the data set and the model is refitted; the predicted values for these points are then compared to their experimental values. Again, this is repeated until each data point has been omitted once. The cross-validation parameters are shown in Eq. (1). The crossvalidated correlation coefficient (Q^2) is 0.973 for the LOO and 0.977 for the LGO cross-validations. These confirm that the obtained regression model has a good internal- and external-predictive power.

However, the small data size may produce an overfitted model. In order to assess the robustness of the model, the *Y*-randomization test was applied. The de-

pendent variable vector pEC_{50} was randomly shuffled and a new QSAR model was developed using the original variable matrix. The new QSAR model is expected to show a low value for R^2_{train} and Q^2_{LOO}. Several random shuffles of the y vector were performed, for which the results are shown in Table III. The low R^2_{train} and Q^2_{LOO} values show that the good results in the original model were not due to a chance correlation or a structural dependency of the training set.
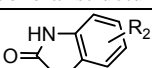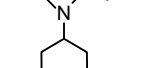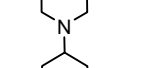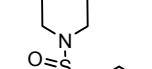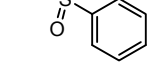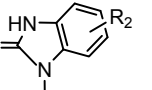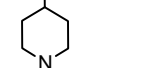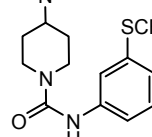
TABLE II. Chemical structures and the corresponding observed and predicted pEC_{50} values by MLR method

Compound No.	General structure	R_1	R_2	$pEC_{50(exp)}$	$MLR_{(pred)}$	RE^a / %
1[b]		2-MeBn	H	6.54	6.69	2.29
2[b]		CO_2Et	H	8.68	8.72	0.46
3[b]		2-MeBn	Cl	5.99	5.92	−1.17
4[b]		Bn	Cl	6.45	6.37	−1.24
5[b]		2-CF$_3$Bn	H	6.39	6.48	1.41
6[c]		2-CF$_3$Bn	Cl	5.82	5.71	−1.89
7[c]		2-ClBn	H	6.59	6.55	−0.61
8[b]		2-ClBn	Cl	5.74	5.90	2.79
9[b]		2-NO$_2$Bn	H	6.92	6.73	−2.75
10[b]		2-NO$_2$Bn	Cl	5.96	5.92	−0.67
11[c]		2-CNBn	H	6.31	6.58	4.28
12[b]		2-CNBn	Cl	5.80	5.78	−0.34
13[b]		CH$_3$	4-F	8.97	9.01	0.45
14[c]		CH$_3$	5-F	9.07	9.05	−0.22
15[b]		CH$_3$	6-F	9.12	9.17	0.55
16[b]		CF$_3$	4-F	8.77	8.83	0.68
17[b]		CF$_3$	5-F	8.98	8.87	−1.22
18[b]		2-CH$_3$	H	9.06	9.18	1.32
19[c]		2-CH$_3$	Cl	8.57	8.50	−0.82
20[b]		3-CH$_3$	H	9.29	9.08	−2.26
21[b]		3-CH$_3$	Cl	8.68	8.45	−2.65
22[b]		2-CF$_3$	H	9.04	9.00	−0.44
23[b]		2-CF$_3$	Cl	7.95	8.32	4.65
24[b]		3-Cl	H	9.03	8.81	−2.44
25[c]		3-Cl	Cl	8.15	8.37	2.70

TABLE II. Continued

Compound No.	General structure	R_1	R_2	$pEC_{50(exp)}$	$MLR_{(pred)}$	RE / % [c]
26[b]		–	4-F	8.59	8.55	–0.47
27[b]		–	5-F	8.64	8.59	–0.58
28[b]		–	6-F	8.48	8.74	3.07
29[b]		–	5-Cl	8.39	8.53	1.67
		–	5-Br	8.36	8.34	–0.24
30[b]						
31[b]		–	6-F	8.02	8.21	2.37
32[b]		–	5-Cl	8.44	8.07	–4.38

[a]Relative error percentage; [b]training set; [c]test set
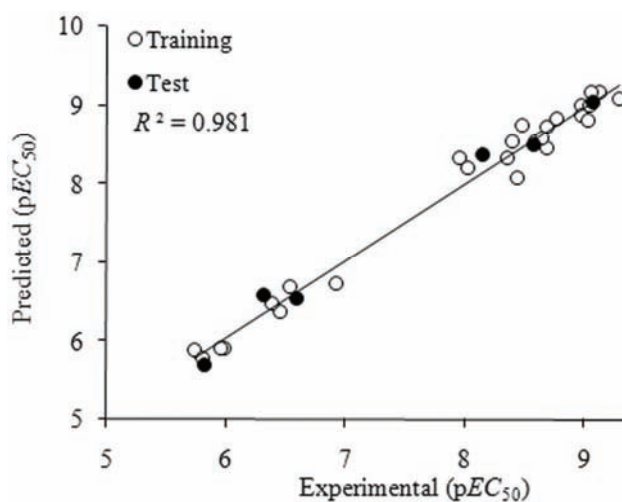
Fig. 1. The predicted *versus* the experimental pEC_{50} by MLR.

Besides demonstrating statistical significance, QSAR models should also provide useful chemical insights for drug design. For this reason, an acceptable interpretation of the QSAR results is provided below. By interpreting the descrip-

tors contained in the model, it is possible to gain some insight into factors which are related to the activity of the mAChRs selective compounds.
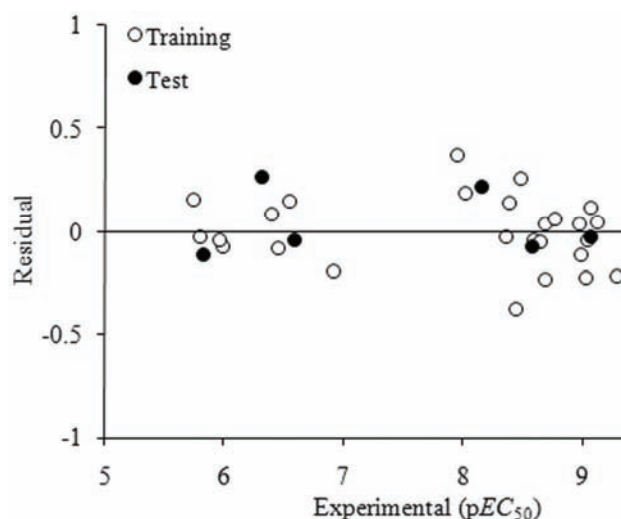
Fig. 2. The residual *versus* the experimental pEC_{50} by MLR.

TABLE III. R^2_{train} and Q^2_{LOO} values after several *Y*-randomization tests

Iteration	R^2_{train}	Q^2_{LOO}
1	0.156	0.004
2	0.087	0.059
3	0.399	0.219
4	0.108	0.009
5	0.108	0.010
6	0.279	0.064
7	0.347	0.171
8	0.149	0.002
9	0.171	0.002
10	0.077	0.058

To examine the relative importance as well as the contribution of each descriptor in the model, the value of the mean effect (*MF*) was calculated for each descriptor. The *MF* value indicates the relative importance of a descriptor in comparison with the other descriptors in the model. Its sign exhibits the variation direction in the values of the activities as a result of an increase (or reduction) of the value of this descriptor.

ATS8m is one of the 2D autocorrelation descriptors which appeared in the model. The 2D autocorrelation descriptor was successfully employed by Fernandez *et al.*[19,20] In these descriptors, the molecule atoms represent a set of discrete points in space, and the atomic property and function are evaluated at these

points. The symbol for each of the autocorrelation descriptors is followed by two indices d and w, whereby d stands for the lag, and w stands for the weight. Thus, for example, ATS8m means: the Broto–Moreau autocorrelation descriptor of lag 8 that is weighted by atomic mass. The lag is defined as the topological distance d between pairs of atoms. The topological distance between a pair of atoms (i,j) is given in the ij^{th} entry in the topological level matrix. The lag can have any value from the set $\{0,1,2,3,4,5,6,7,8\}$. The weight can be m (relative atomic mass), p (polarizability), e (Sanderson electronegativity) and v (Van der Waals volume). The relative mass is defined as the ratio of the atomic mass of an atom to that of carbon. Similarly, the other three weights p, e and v are scaled by the corresponding values for carbon. The physico–chemical property (weights) for ATS8m is atomic mass, which shows the mass of the atoms or molecules play the main role in this descriptor. The ATS8m mean effect ($MF = 0.083$) has a positive sign, which indicates that the pEC_{50} value is directly related to this descriptor. Hence, it was concluded that by increasing the molecular mass, the value of this descriptor increased, causing an increase of its pEC_{50} value.

C-028 is the second descriptor, appearing in the model. It is one of the atom--centered fragment descriptors that describes each atom by its own atom type and the bond types and atom types of its first neighbors.[21] The C-028 descriptor displays R-CR-X. This atom centered fragment descriptor is defined for each ring atom that has three neighbors. In this case, R-CR-X can be defined as a central carbon atom (C) on an aromatic ring that has one carbon neighbor (R) and one heteroatom neighbor (X) on the same aromatic ring and the third neighbor outside this ring is a carbon (R). The C-028 mean effect ($MF = 0.346$) has a positive sign, which indicates that the pEC_{50} value is directly related to this descriptor. Hence, it was concluded that by increasing the number of heteroatom (with R-CR-X format) in molecules the value of this descriptor increased, causing an increase of its pEC_{50} value.

The last descriptor appearing in the model is the second-order neighborhood structural information content (SIC2). It is calculated based on a hydrogen-depleted molecular graph and represents a measure of the structural complexity per vertex.[21] The positive sign of the descriptor mean effect ($MF = 0.571$) confirms that complex molecular structures with a diverse set of atoms in addition to carbon, such as nitrogen, oxygen, and halogens, which can establish covalent bonds in the lattice, have a high pEC_{50} value.

Summarizing, it is concluded that the mass, the number of heteroatoms, and the number of halogens play the main roles in determining the activity of mAChRs selective compounds.

CONCLUSIONS

Quantitative structure–activity relationships were applied on TBPB analogs as muscarinic acetylcholine receptors using the multiple parameter linear regression method. The separation of the data into two independent sets (training and test) showed that the obtained MLR model can predict external data with great accuracy. The proposed method, due to its high predictive ability, is a useful aid to costly and time consuming experiments for determining the activity of TBPB analogs. Selection of three variables, *i.e*., ATS8m, C-028 and SIC2, by the step-wise multiple regression technique indicates the complexity of the activity mechanism. Synthesis of the new proposed molecules and their biological evaluation will show if this procedure can be used as a general rational drug discovery tool.

ИЗВОД

СТУДИЈА КВАНТИТАТИВНОГ ОДНОСА СТРУКТУРА–АКТИВНОСТ ЗА АНАЛОГЕ ТЕТРАБУТИЛФОСФОНИЈУМ-БРОМИДА КАО АГОНИСТА МУСКАРИНСКИХ АЦЕТИЛХОЛИНСКИХ РЕЦЕПТОРА

MEHDI NEKOEI[1], MAHMOUD SALIMI[2], MOHSEN DOLATABADI[3] и MAJID MOHAMMADHOSSEINI[1]

[1]*Department of Chemistry, Faculty of Science, Islamic Azad University, Shahrood Branch, Shahrood,* [2]*Department of Chemical Engineering, Faculty of Engineering, Islamic Azad University of Arak, Arak u* [3]*Department of Chemistry, Faculty of Science, University of Birjand, Birjand, Iran*

Проучаван је квантитативни однос структура–активност (QSAR) за аналоге тетрабутил-фосфонијум-бромида (TBPB) као агониста мускаринских ацетилхолинских рецептора (mAChRs). Одређен је погодан скуп молекулских дескриптора и примењена поступна вишеструка линеарна регресија (SW-MLR). На тај начин су изабрани они дескриптори који дају најбоље слагање. Добијен је MLR модел са три дескриптора, који је даље тестиран помоћу LOO и LGO проступака, као и *Y*-насумичне расподеле. Овај модел, са добрим статистичким показатељима ($R^2_{\text{train}} = 0,982$, $F = 388,715$, $Q^2_{\text{LOO}} = 0,973$, $Q^2_{\text{LGO}} = 0,977$, $R^2_{\text{test}} = 0,986$), омогућује да се предвиди активност молекула са грешком мањом од 5 %.

(Примљено 22. новембра 2010)

REFERENCES

1. T. I. Bonner, N. J. Buckley, A. C. Young, M. R. Brann, *Science* **237** (1987) 527
2. C. C. Felder, F. P. Bymaster, J. Ward, N. J. De-Lapp, *J. Med. Chem*. **43** (2000) 4333
3. F. P. Bymaster, D. L. McKinzie, C. C. Felder, J. Wess, *Neurochem. Res.* **28** (2003) 437
4. R. M. Eglen, A. Choppin, M. P. Dillon, S. Hedge, *Curr. Opin. Chem. Biol.* **3** (1999) 426
5. N. J. M. Birdsall, N. M. Nathanson, R. D. Schwarz, *Trends Pharm. Sci.* **22** (2001) 215
6. R. A. Eglen, A. Choppin, N. Watson, *Trends Pharm. Sci.* **22** (2001) 409
7. T. M. Bridges, A. E. Brady, J. P. Kennedy, R. N. Daniels, N. R. Miller, K. Kim, M. L. Breininger, P. R. Gentry, J. T. Brogan, C. K. Jones, P. J. Conn, C. W. Lindsley, *Bioorg. Med. Chem. Lett.* **18** (2008) 5439
8. N. R. Miller, R. N. Daniels, T. M. Bridges, A. E. Brady, P. J. Conn, C. W. Lindsley, *Bioorg. Med. Chem. Lett.* **18** (2008) 5443

9. D. L. Hill, *The Biochemistry and Physiology of Tetrahymena*, First Academic Press, New York, 1972
10. O. Deeb, B. Hemmateenejad, *Chem. Biol. Drug Des.* **70** (2007) 19
11. R. P. Verma, A. Kurup, C. Hansch, *Bioorg. Med. Chem.* **13** (2005) 237
12. V. K. Agrawal, P. V. Khadikar, *Bioorg. Med. Chem.* **9** (2001) 3035
13. *HyperChem Release 7*, HyperCube, Inc., http://www.hyper.com
14. R. Todeschini, Milano Chemometrics and QSPR Group, http://michem.disat.unimib.it//chm/ (accessed in August, 2011)
15. *Matlab 6.5*, Mathworks, 1984–2002
16. M. A. Efroymson, in *Mathematical Methods for Digital Computers*, A. Ralston, H. S Wilf, Eds.,Wiley, New York, 1960
17. D. W. Osten, *J. Chemom.* **2** (1988) 39
18. S. Wold, L. Eriksson, in *Chemometrics Methods in Molecular Design*, H. Van de Water- beemd, Ed., VCH, Weinheim, 1995
19. M. Fernández, A. Tundidor-Camba, J. Caballero, *J. Chem. Inf. Model.* **45** (2005) 1884
20. J. Caballero, A. Tundidor-Camba, M. Fernández, *QSAR Comb. Sci.* **26** (2007) 27
21. R. Todeschini, V. Consonni, *Handbook of Molecular Descriptors*, Wiley-VCH, Wein- heim, 2000.

Effects of dopants on the isothermal decomposition kinetics of potassium metaperiodate

KARUVANTHODI MURALEEDHARAN*, MALAYAN PARAMBIL KANNAN
and THARAKKAL GANGADEVI

Department of Chemistry, University of Calicut, Kerala-673 635, India

Abstract: The isothermal decomposition and kinetics of potassium metaperiodate (KIO$_4$) were studied by thermogravimetry as a function of the concentration of dopants. The thermal decomposition of KIO$_4$ proceeds mainly through two stages: an acceleration period up to $\alpha = 0.50$ and a decay stage. The thermal decomposition data for both doped and untreated KIO$_4$ were found to be best described by the Prout–Tompkins Equation. The α–t data of doped and untreated samples of KIO$_4$ were subjected to isoconversional studies for the determination of the activation energy values. The isoconversional studies of the isothermal decomposition of untreated and doped samples of KIO$_4$ indicated that the thermal decomposition of KIO$_4$ proceeds through a single kinetic model, the Prout–Tompkins model, throughout the entire range of conversion, as opposed to earlier observations.

Keywords: doping; isoconversional analysis; isothermal decomposition; KIO$_4$.

INTRODUCTION

Thermal decomposition studies are one of the most common and widely used techniques employed to obtain insight into the elementary steps of solid-state reactions. The reactivity of solids is greatly modified by pre-treatment, such as doping, pre-compression, pre-heating, *etc*. The nature of influence of the pre-treatment provides valuable information of the elementary steps of solid-state reactions and thereby on the mechanism and control of solid-state reactions.[1,2] Kinetic studies are one of the important applications of thermal analysis. Solid-state kinetic data are of practical interest for a large and growing number of technologically important processes. A large number of reviews are available in the literature on such processes.[3–10]

The methods of kinetic analysis can be classified based on the experimental conditions selected and the mathematical analysis performed. Experimentally, either isothermal or non-isothermal methods can be used. The isothermal methods are based on the initial assumption that a single conversion function and a single set of Arrhenius parameters, A and E, apply over the full range of the degrees of conversion. The main problem in isothermal kinetic analysis is that a sample requires some time to reach the experimental temperature. We solved this problem by fabricating a thermobalance particularly for studying the isothermal kinetics of solid-state reactions. The effects of pre-treatments on the thermal reactivity of several high-energy solids, such as halates and perhalates, were reported[11–19] that throw light on the mechanism of their decomposition. Thermal decompositions of halates and perhalates, which occupy an important place in modern solid-state chemistry, are extremely sensitive to the presence of impurities, additives, *etc*., and more data of this kind are desirable.

According to thermoanalytical studies, KIO_4 decomposes in two steps.[20,21] At about 570 K, KIO_4 decomposes with heat evolution to potassium iodate (KIO_3) and oxygen. The decomposition of KIO_3 to KI occurs in the range 780––800 K. In the thermal decomposition of KIO_4, the identification of the six--valent iodine compound, K_2IO_4, analogous to the compounds, M_2IO_4 formed in the decomposition of lithium and sodium periodates has not been realised. The effects of several pre-treatments on the kinetics and mechanism of the thermal decomposition of KIO_4 have been studied. It was observed that KIO_4 decomposes *via* the Prout–Tompkins mechanism. Earlier investigations[13,16,18,19] showed that the isothermal decomposition of KIO_4 follows Prout–Tompkins kinetics at all temperatures studied and it was proposed that the probable rate determining step in the thermal decomposition of KIO_4 is the transfer of an electron from the periodate anion to the potassium cation, rather than the rupture of the I–O bond or the diffusion of cations/anions.

Studies on the effect of metal oxide (CuO, MnO_2 and TiO_2) additives on the thermal decomposition kinetics of potassium metaperiodate (KIO_4) to potassium iodate (KIO_3), in air by thermogravimetry under isothermal conditions,[18] revealed that irrespective of whether p- or n-type, the metal oxides had little or no influence on the rate of the decomposition, except for a small decrease when the oxide concentration was as high as 10 wt. %. The rate law for the decomposition of KIO_4 (Prout–Tompkins model) remained unaffected by the additives. The behaviour of mechanical mixtures of KIO_4 with n- and p-type semi-conducting oxides suggests that the electron work functions of these oxides might be smaller than that of KIO_4; hence, they lack electron acceptor property with respect to KIO_4 and thus fail to favour electron transfer processes.

In continuation of investigations on the thermal behaviour of periodates of alkali metals,[13,16–19] in this paper, the results of isoconversional analysis of the

isothermal decomposition kinetics of doped and untreated samples of KIO_4 in the temperature range 560–580 K are reported. Isoconversional kinetics rests upon the evaluation of the dependence of the effective activation energy on conversion and using this dependence for making kinetic predictions and for exploring the mechanism of thermal processes.

EXPERIMENTAL

All the employed chemicals were of AnalaR grade reagents from Merck. Doped samples of KIO_4, at four concentrations, *viz.*, 10^{-4}, 10^{-3}, 10^{-2} and 0.1 mol % were prepared by the method described earlier.[13,16] $BaCl_2$, $AlCl_3 \cdot 6H_2O$, K_2SO_4 and K_3PO_4 were used for doping Ba^{2+}, Al^{3+}, SO_4^{2-} and PO_4^{3-}, respectively. The thermogravimetric (TG) measurements in static air were performed on a custom fabricated thermobalance, [16] an upgraded version of Hooley.[22]

A major problem[23] in isothermal experiments is that the sample requires some time to reach the experimental temperature. During this period of non-isothermal heating, the sample undergoes some transformations that are likely to affect the results of the following kinetic analysis. The situation is especially aggravated by the fact that under isothermal conditions, a typical solid-state process has its maximum reaction rate at the beginning of the transformation. Hence a thermobalance was fabricated particularly for isothermal studies, in which loading of the sample is possible at any time after attaining the desired temperature. The operational characteristics of the thermobalance are: accuracy; balance: $\pm 1.0 \times 10^{-5}$ g, temperature: ± 0.5 K, sample mass: 5×10^{-2} g, particle size: 90–106 μm and crucible: platinum. The fraction of solid decomposed (α) was measured as a function of time (t) at five different temperatures, *viz.*, 560, 565, 570, 575 and 580 K.

The α–t data, in the α range 0.05–0.95, of doped and untreated samples of KIO_4 were subjected to isoconversional studies for the determination of the apparent activation energy as a function of α from the sets of isothermals obtained. The activation energy value (for a given value of α) of the decomposition reaction was calculated from a plot of ln t (t being the time required to reach a given value of α at a constant temperature T) *versus* the corresponding reciprocal of the temperature ($1/T$).

RESULTS AND DISCUSSION

The α–t curves for the decomposition of the pure and doped samples of KIO_4 at 560 K are shown in Fig. 1. Similar curves were obtained for all other samples of KIO_4 (doped and untreated) at all temperatures. The decomposition proceeded mainly through two stages: *i*) an acceleration period up to $\alpha = 0.50$ and *ii*) a decay stage.

The α–t data in the α range 0.05–0.95 were fitted to various solid state kinetic equations, given in Table S-I of the Supplementary material, using the method of weighted least squares, as described earlier.[13] The Prout–Tompkins Equation,[24] ln ($\alpha/(1-\alpha)$) = kt, which is the simplest case of an autocatalytic reaction, gave the best fits for all the studied temperatures. A typical fit for the Prout–Tomkin model for the decomposition of the untreated sample of KIO_4 at 560 K is shown in Fig. 2. Typical fits for all kinetic models described in Table S-I for the decomposition of the untreated sample of KIO_4 at 560 K are shown in Figs. S-1–S-4 of the Supplementary material. Similar fits were obtained for all

other samples of KIO_4 and at all temperatures (not shown). Separate kinetic analyses of the α–t data corresponding to the acceleration region (α range 0.05––0.5) and the decay region ((α range 0.5–0.95) showed that the acceleration stage was best fitted by the Prout–Tompkins equation itself, whereas the decay stage was better fitted by the contracting area equation.[13,16,19] Doping did not change the basic shape (sigmoid) of the α–t plots and the decomposition proceeded through the two stages mentioned in the case of pure KIO_4, obeying the same rate laws mentioned above for the two decomposition ranges.
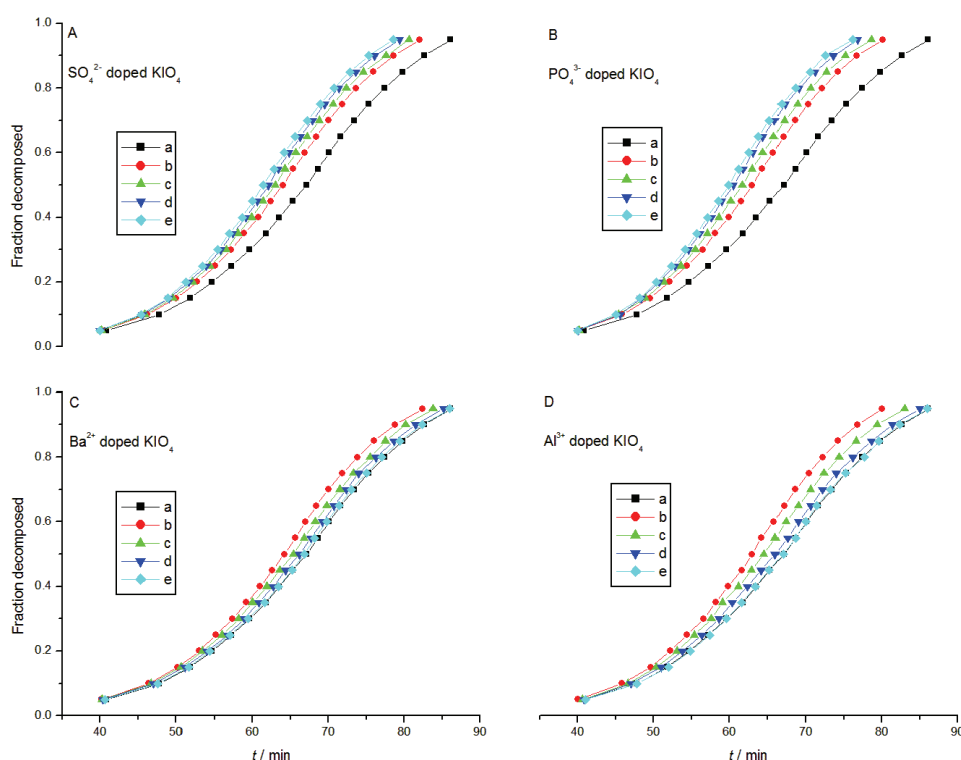
Fig. 1. The α–t curves for the isothermal decomposition of A: sulphate; B: phosphate; C: barium- and D: aluminium-doped KIO_4 at 560 K; 0 mol %, a, 10^{-4} mol %, b, 10^{-3} mol %, c, 10^{-2} mol %, d, 0.1 mol %, e; in C and D, curve a is superimposed on curve e.

The α–t data, in the α range 0.05–0.95 with an interval of 0.05, of the untreated and doped samples of KIO_4 were also subjected to isoconversional studies for the determination of the apparent activation energy as a function of α. A plot of ln t (t being the time required to reach a given value of α at a constant temperature T) *versus* the corresponding reciprocal of the temperature (1/T) leads to the activation energy for the given value of α. Typical isoconversional plots for the isothermal decomposition of sulphate doped KIO_4 (at different conver-

sions) are shown in Fig. 3. Similar plots were obtained for all other doped samples of KIO_4. Values of slope and correlation coefficient obtained for the isoconversional plots of sulphate and barium doped samples of KIO_4 at different dopant concentrations at different conversions are given in Tables I and II, respectively. Similar values were obtained for isoconversional plots of all other doped samples of KIO_4. In all cases, the isoconversional plots gave good correlations. A plot of the apparent activation energy *vs.* conversion for untreated KIO_4 is shown in Fig. 4 and those of the doped samples in Fig. 5.
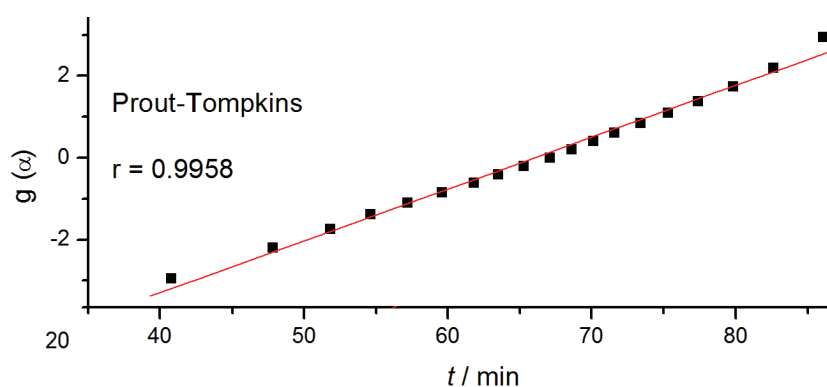
Fig. 2. Typical model fitting least square plot for the Prout–Tompkins model for the decomposition of KIO_4 at 560 K.

Philips and Taylor[25] proposed that the rupture of the I–O bond determines the rate of the decomposition of KIO_4 to KIO_3. Contrary to the observation of Hill,[26] they pointed out that the autocatalytic stage does not involve a diffusion chain and reported an activation energy (E) value of 191 kJ mol^{-1} for the decomposition of KIO_4. Our earlier investigations[13,16,18,19] showed that the isothermal decomposition of KIO_4 follows Prout–Tompkins kinetics at all temperatures studied with an E value of 206±3 kJ mol^{-1}. The acceleration stage was best described by the Prout–Tompkins equation itself, with an E value of 218±3 kJ mol^{-1}. However, the decay stage was best represented by the contracting area equation with an E value of 185±3 kJ mol^{-1}. Based on these previous results, we suggested that KIO_4 decomposes in accordance to the Prout–Tompkins model with two dimensional nucleus growth up to 50 % decomposition, and thereafter through the contracting area law. Several authors[17,25,27–30] reported such a description of the reaction kinetics using different rate laws for different ranges of α. We reported earlier that the rate law and the activation energy of the decomposition remained unaltered by doping and observed that the basic mechanism of the decomposition was not affected by doping, the only effect being a modification in the concentration of active sites.
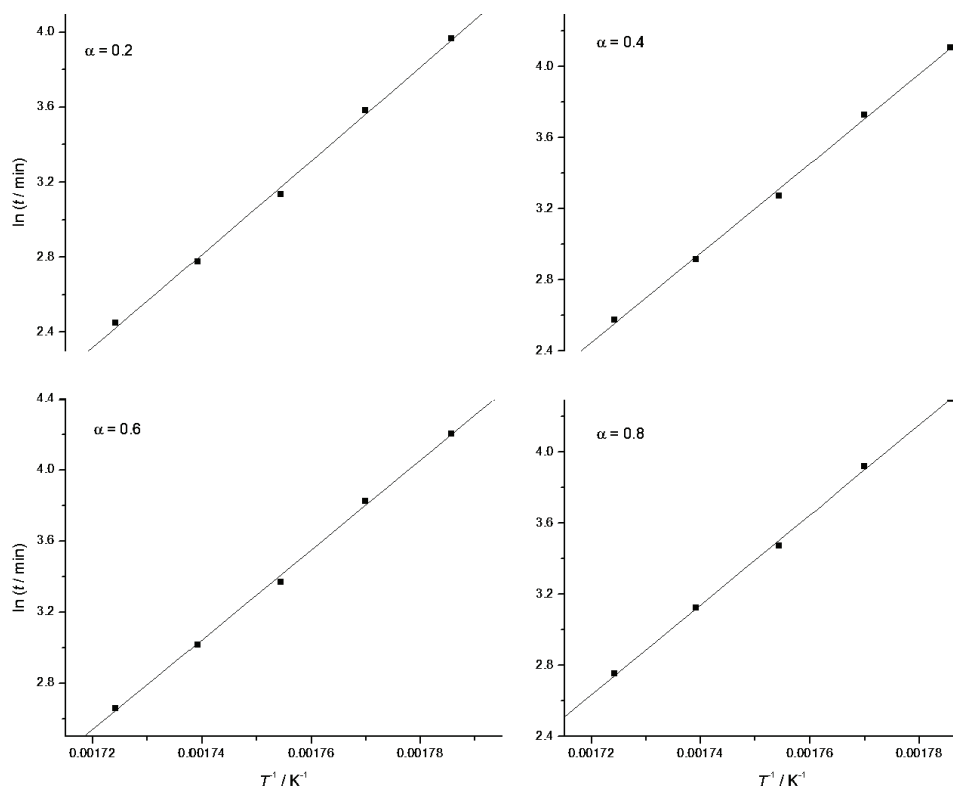
Fig. 3. Typical isoconversional plots for sulphate doped KIO_4 at 560 K.

TABLE I. Values of slope and correlation coefficient obtained for the isoconversional analysis of sulphate-doped samples of KIO_4 at different dopant content and at different conversions

α	Dopant content, mol %							
	10^{-4}		10^{-3}		10^{-2}		0.1	
	Slope, K^{-1}	r	Slope, K^{-1}	r	Slope, K^{-1}	r	Slope, K^{-1}	r
0.05	24351.5	0.9982	24492.5	0.9996	24598.1	0.9987	24596.9	0.9985
0.10	24609.0	0.9985	24822.4	0.9996	24914.3	0.9988	24908.9	0.9988
0.15	24835.5	0.9987	24973.9	0.9988	25066.0	0.9990	25123.3	0.9989
0.20	24923.0	0.9989	25008.7	0.9988	24764.7	0.9981	25203.3	0.9989
0.25	24954.1	0.9988	25146.2	0.9989	25351.4	0.9991	25314.1	0.9989
0.30	25025.9	0.9989	25231.0	0.9990	25365.8	0.9991	25352.1	0.9989
0.35	25126.7	0.9990	25269.2	0.9991	25405.5	0.9992	25352.0	0.9990
0.40	25182.6	0.9991	25372.0	0.9992	25464.2	0.9992	25450.5	0.9989
0.45	25251.1	0.9989	25388.8	0.9991	25494.5	0.9990	25512.0	0.9989
0.50	25273.1	0.9991	25424.0	0.9992	25525.6	0.9991	25572.9	0.9990
0.55	25302.6	0.9991	25398.9	0.9992	25530.6	0.9992	25565.2	0.9990
0.60	25243.2	0.9991	25380.1	0.9993	25490.4	0.9992	25529.7	0.9992
0.65	25262.9	0.9993	25366.1	0.9993	25506.2	0.9994	25517.6	0.9991
0.70	25237.6	0.9993	25384.7	0.9994	25520.8	0.9994	25535.4	0.9992

TABLE I. Continued

α	Dopant content, mol %							
	10^{-4}		10^{-3}		10^{-2}		0.1	
	Slope, K^{-1}	r	Slope, K^{-1}	r	Slope, K^{-1}	r	Slope, K^{-1}	r
0.75	25276.7	0.9993	25389.1	0.9993	25487.8	0.9994	25538.0	0.9994
0.80	25257.2	0.9994	25407.5	0.9993	25513.7	0.9996	25598.4	0.9994
0.85	25203.7	0.9994	25388.3	0.9994	25530.2	0.9996	25568.6	0.9996
0.90	25239.6	0.9995	25470.2	0.9995	25521.6	0.9996	25603.3	0.9996
0.95	25278.6	0.9996	25422.5	0.9996	25486.7	0.9997	25570.3	0.9998

TABLE II. Values of slope and correlation coefficient obtained for the isoconversional analysis of barium-doped samples of KIO_4 at different dopant concentrations and at different conversions

α	Dopant content, mol %							
	10^{-4}		10^{-3}		10^{-2}		0.1	
	Slope, K^{-1}	r	Slope, K^{-1}	r	Slope, K^{-1}	r	Slope, K^{-1}	r
0.05	24322.1	0.9996	24355.6	0.9986	24387.2	0.9995	24591.4	0.9987
0.10	24635.0	0.9987	24231.8	0.9982	24313.2	0.9981	24957.9	0.9988
0.15	24808.8	0.9985	24393.3	0.9988	24585.6	0.9989	24832.5	0.9990
0.20	24792.8	0.9987	24530.4	0.9989	24695.4	0.9990	24777.8	0.9991
0.25	24853.0	0.9989	24824.8	0.9992	24966.2	0.9993	24935.0	0.9989
0.30	24912.9	0.9990	24972.3	0.9992	25086.5	0.9993	25104.3	0.9990
0.35	24915.5	0.9989	24975.4	0.9991	25122.0	0.9992	25286.7	0.9993
0.40	25018.1	0.9988	25147.6	0.9993	25289.1	0.9993	25376.4	0.9994
0.45	25081.4	0.9990	25253.6	0.9993	25407.3	0.9995	25467.3	0.9995
0.50	25138.2	0.9989	25373.1	0.9992	25522.9	0.9995	25510.4	0.9995
0.55	25160.2	0.9991	25353.5	0.9990	25518.6	0.9994	25548.6	0.9995
0.60	25175.2	0.9991	25267.4	0.9993	25442.6	0.9995	25507.5	0.9995
0.65	25160.6	0.9992	25162.7	0.9993	25336.4	0.9995	25433.2	0.9994
0.70	25181.1	0.9992	25101.3	0.9993	25201.5	0.9994	25336.5	0.9997
0.75	25238.2	0.9993	25085.0	0.9992	25070.0	0.9994	25333.0	0.9997
0.80	25298.5	0.9996	25091.3	0.9995	25062.3	0.9995	25225.7	0.9997
0.85	25191.5	0.9993	24978.1	0.9995	24962.1	0.9995	25213.7	0.9997
0.90	25092.0	0.9994	24930.0	0.9995	24831.2	0.9993	25320.0	0.9998
0.95	25140.0	0.9994	24890.2	0.9995	24795.8	0.9995	25330.4	0.9997

We found that the apparent activation energy values obtained by the isoconversional method at different conversions (α range 0.05–0.95 with an interval of 0.05) for sulphate- and barium-doped samples of KIO_4 lie in the range 203–213 kJ mol^{-1}. However, in the case of the phosphate- and aluminium-doped samples of KIO_4, the apparent activation energy values varied only up to 210 kJ mol^{-1} from 203 kJ mol^{-1}. In the case of untreated KIO_4, the activation energy value increased from 203 kJ mol^{-1} with conversion, passed through a maximum ($\approx$210 kJ mol^{-1}), and decreased to the initial value (203 kJ mol^{-1}). In all cases, these values are in close agreement with the activation energy values obtained

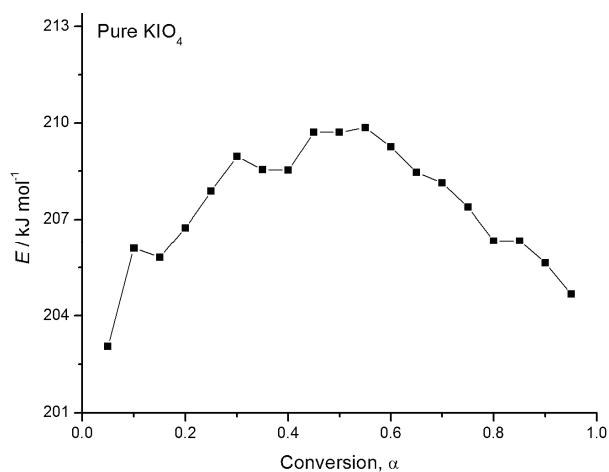from the model fitting method (206±3 kJ mol^{-1}) using the Prout–Tompkins model.

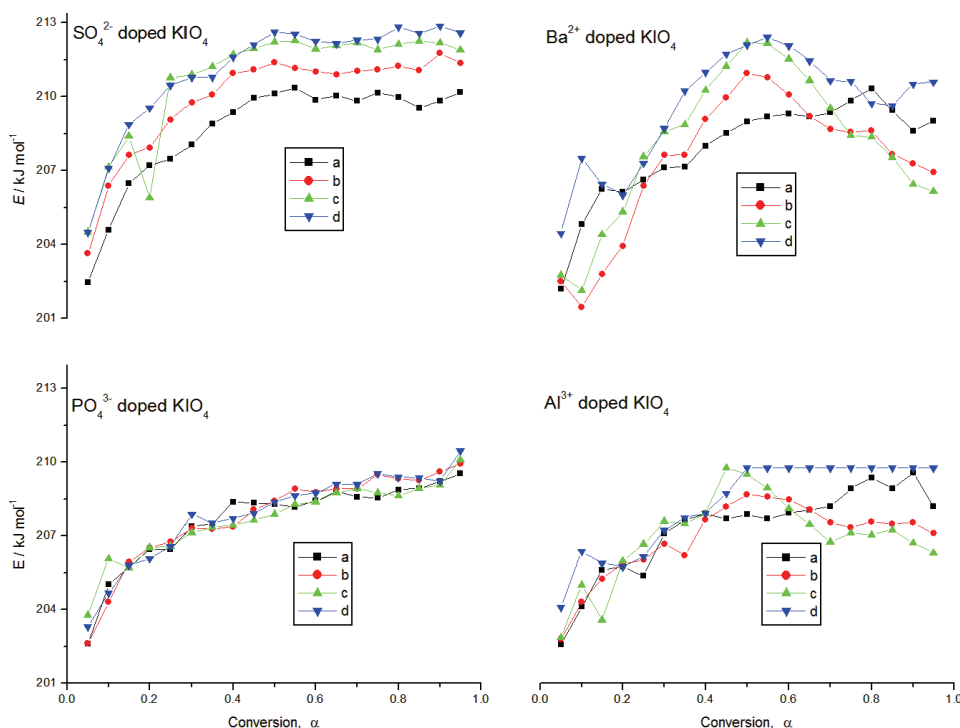Fig. 4. Plot of the apparent activation energy *vs.* conversion for pure KIO$_4$.

Fig. 5. Plot of the apparent activation energy *vs.* conversion for sulphate (A), barium (B), phosphate (C) and aluminium (D); 10^{-4} mol %, a, 10^{-3} mol %, b 10^{-2} mol %, c, 0.1 mol %, d.

Perusal of Tables I and II and Figs. 4 and 5 reveals that the deviation of activation energy with conversion is less than ±2 % for all samples of doped and untreated KIO$_4$. This indicates that the thermal decomposition of KIO$_4$ proceeds through a single kinetic model, the Prout–Tompkins model, throughout the entire conversion range, as opposed to our previous observation that the acceleration stage was best fitted by the Prout–Tompkins Equation and the decay stage was fitted better by the contracting area equation.[16,19]

CONCLUSIONS

The apparent activation energy values obtained previously by model fitting analysis of the isothermal decomposition of untreated and doped samples of KIO$_4$ are in good agreement with the present results. The isoconversional studies of the isothermal decomposition of untreated and doped samples of KIO$_4$ indicate that the thermal decomposition of KIO$_4$ proceeds through a single kinetic model, the Prout–Tompkins model, throughout the entire range of conversion, contrary to our earlier observations.

SUPPLEMENTARY MATERIAL

Table S-I and Figs. S-1–S-4 are available electronically at http://www.shd.org.rs/JSCS/, or from the corresponding author on request.

И З В О Д

УТИЦАЈ ДОДАТАКА НА ИЗОТЕРМСКУ КИНЕТИКУ РАЗЛАГАЊА КАЛИЈУМ-МЕТАПЕРЈОДАТА

KARUVANTHODI MURALEEDHARAN, MALAYAN PARAMBIL KANNAN и THARAKKAL GANGADEVI

Department of Chemistry, University of Calicut, Kerala-673 635, India

Изотермска кинетика разлагања калијум-метаперјодата (KIO$_4$) испитивана је термогравиметријски у функцији концентрације додатака. Термално разлагање се одвија углавном кроз два ступња: период убрзања до $\alpha = 0,50$ и ступањ разлагања. Термално разлагање KIO$_4$ са и без додатака се може описати Prout–Tompkins-овом једначином. Изоконвенционални метод је коришћен у одређивању енергије активације допираних и недопираних узорака. Изоконвенционална испитивања изотермске кинетике нетретираних и допираних KIO$_4$ узо–рака указују на то да се термално разлагање одвија само кроз један кинетички ступањ, Prout––Tompkins модел, у широком опсегу конверзије што је супротно нашим ранијим запажањима.

REFERENCES

1. P. J. Herley, P. W. M. Jacobs, P. W. Levy, *Proc. Roy. Soc*. **318A** (1970) 197
2. V. R. Pai Verneker, K. Rajeshwar, *J. Phys. Chem. Solids* **37** (1976) 63
3. V. A. Benderskii, D. E. Makarov, C. A. Wight, *Chemical Dynamics at Low Temperatures*, Wiley, New York, 1994, p. 385
4. M. E. Brown, D. Dollimore, A. K. Galwey, *Reactions in the Solid State*, *Comprehensive Chemical Kinetics*, Elsevier, Amsterdam**,** 1980, p. 340

5. T. B. Brill, K. J. James, *Chem. Rev.* **93** (1993) 2667
6. J. H. Flynn, in *Encyclopedia of Polymer Science and Engineering*, H. F. Mark, N. M. Bi-kales, C. G. Overberger, G. Menges, Eds., Wiley, New York, 1989, p. 690
7. J. Sestak, *Thermophysical Properties of Solids*, in *Comprehensive Analytical Chemistry Vol. XIID*, Elsevier, Amsterdam, 1984, p. 440
8. J. G. Fatou, in *Encyclopedia of Polymer Science and Engineering*, H. F. Mark, N. M. Bi-kales, C. G. Overberger, G. Menges, Eds., Wiley, New York. 1989, p. 231
9. A. K. Galwey, *Thermochim. Acta* **413** (2004) 139
10. D. Dollimore, *Chem. Rev.* **68** (1996) 63
11. M. P. Kannan, *J. Thermal. Anal.* **32** (1987) 1219
12. K. Muraleedharan, M. P. Kannan, *React. Kinet. Catal. Lett.* **39** (1989) 339
13. M. P. Kannan, K. Muraleedharan, *Thermochim. Acta* **158** (1990) 259
14. T. Gangadevi, M. P. Kannan, B. Hema, *Thermochim. Acta* **285** (1996) 269
15. M. P. Kannan, T. Gangadevi, *Thermochim. Acta* **292** (1997) 105
16. K. Muraleedharan, M. P. Kannan, *Thermochim Acta* **359** (2000) 161
17. M. P. Kannan, V. M. Abdul Mujeeb, *React. Kinet. Catal. Lett.* **72** (2001) 245
18. K. Muraleedharan, M. P. Kannan, T. Gangadevi, *J. Therm. Anal. Cal.* **100** (2010) 177
19. K. Muraleedharan, M. P. Kannan, T. Gangadevi, *Thermochim Acta* **502** (2010) 24
20. O. N. Breusov, N. J. Kashina, T. V. Rezvina, *Zh. Neorg. Khim.* **15** (1970) 612
21. P. Bianco, R. Subbah, G. Perinet, *Bull. Soc. Chim.* **9** (1967) 3437
22. J. G. Hooley, *Can. J. Chem.* **35** (1957) 374
23. S. Vyazovkin, C. A. Wight, *Annu. Rev. Phys. Chem.* **48** (1997) 125
24. E. G. Prout, F. C. Tompkins, *Trans. Faraday Soc.* **40** (1944) 488
25. B. R. Philips, D. Taylor, *J. Chem. Soc.* (1963) 5583
26. R. A. W. Hill, *Trans. Faraday Soc.* **54** (1958) 685
27. M. M. Markowitz, D. A. Boryta, *J. Phys. Chem.* **65** (1961) 1419
28. K. H. Stern, *High Temperature Properties and Thermal Decomposition of Inorganic Salts with Oxyanions*, CRC Press, Boca Raton, FL, 2001
29. A. K. Galwey, M. E. Brown, *Thermal Decomposition of Ionic Solids*, *Studies in Physical and Theoretical Chemistry*, Vol. 86, Elsevier, Amsterdam, 1999
30. F. Solymosi, *Structure and Stability of Salts of Halogen Oxyacids in the Solid Phase*, Wiley, London, 1977.

Effects of dopants on the isothermal decomposition kinetics of potassium metaperiodate

KARUVANTHODI MURALEEDHARAN*, MALAYAN PARAMBIL KANNAN
and THARAKKAL GANGA DEVI

Department of Chemistry, University of Calicut, Kerala-673 635, India

TABLE S-I. The different reaction models used to describe the reaction kinetics

Model No.	Reaction model	Function $g(\alpha)$
1	Power law	$\alpha^{1/4}$
2	Power law	$\alpha^{1/3}$
3	Power law	$\alpha^{1/2}$
4	Power law	$\alpha^{3/2}$
5	One-dimensional diffusion	α^2
6	Mampel (first order)	$-\ln(1-\alpha)$
7	Avrami–Erofeev	$(-\ln(1-\alpha))^{1/4}$
8	Avrami–Erofeev	$(-\ln(1-\alpha))^{1/3}$
9	Avrami–Erofeev	$(-\ln(1-\alpha))^{1/2}$
10	Three-dimensional diffusion	$(1-(1-\alpha)^{1/3})^2$
11	Contracting sphere	$1-(1-\alpha)^{1/3}$
12	Contracting area (cylinder)	$1-(1-\alpha)^{1/2}$
13	Prout–Tompkins	$\ln(\alpha/(1-\alpha))$
14	Second order	$(1-\alpha)^{-1}-1$

* Corresponding author. E-mail: kmuralika@gmail.com

S23

Fig. S-1. Typical model fitting least square plots (for models 1–4 given in Table S-I) for the decomposition of KIO_4 at 560 K.

Fig. S-2. Typical model fitting least square plots (for models 5–8 given in Table S-I) for the decomposition of KIO_4 at 560 K.
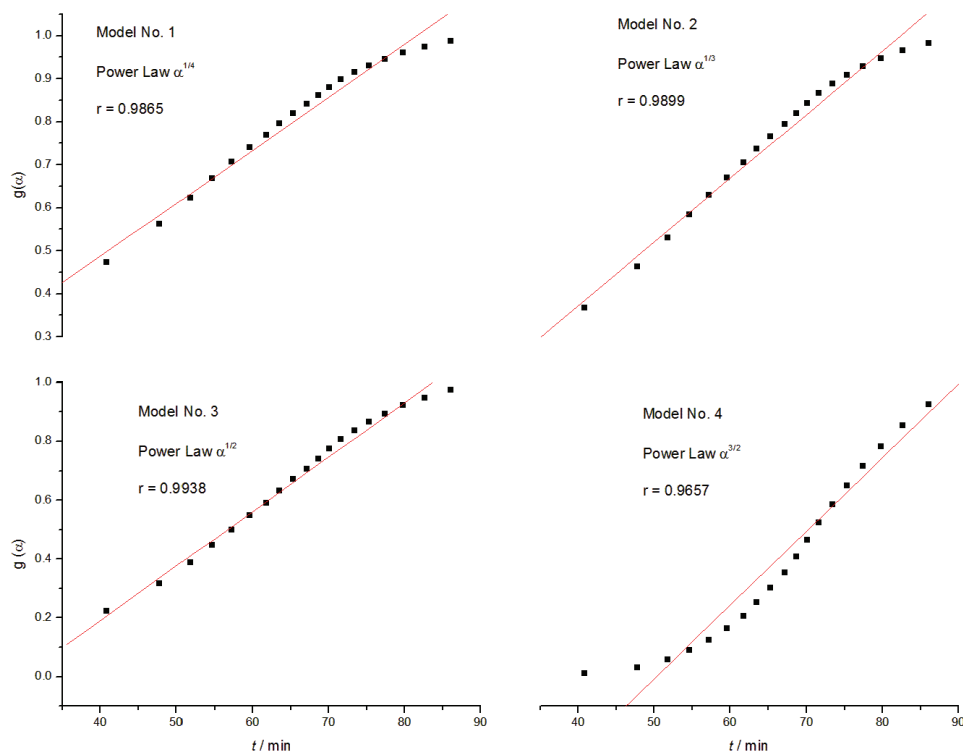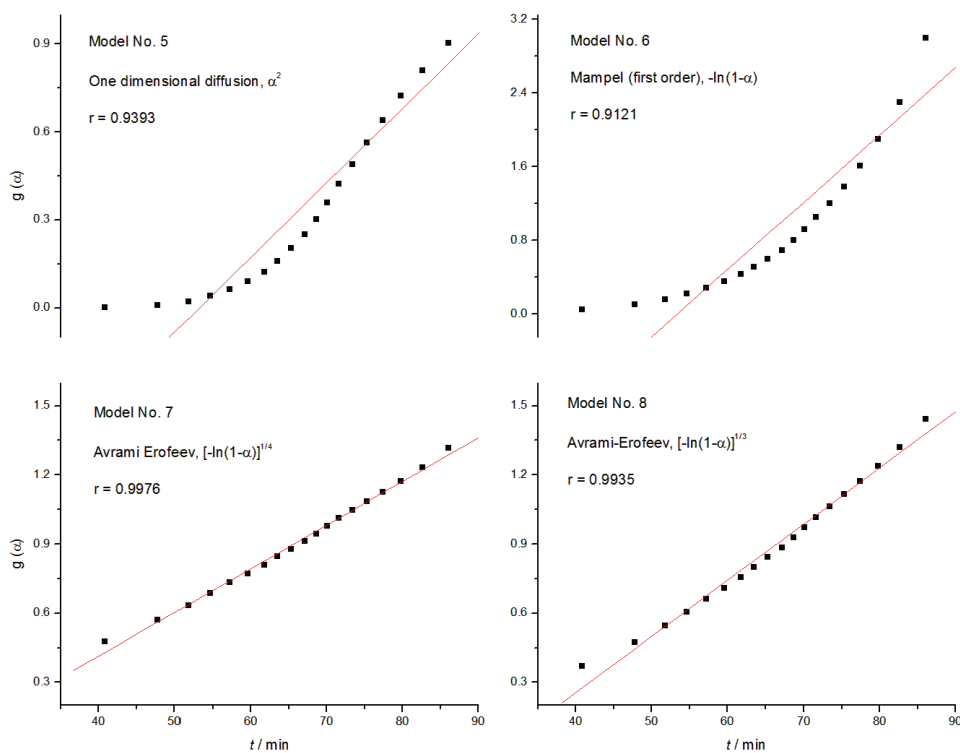
MURALEEDHARAN, KANNAN and DEVI
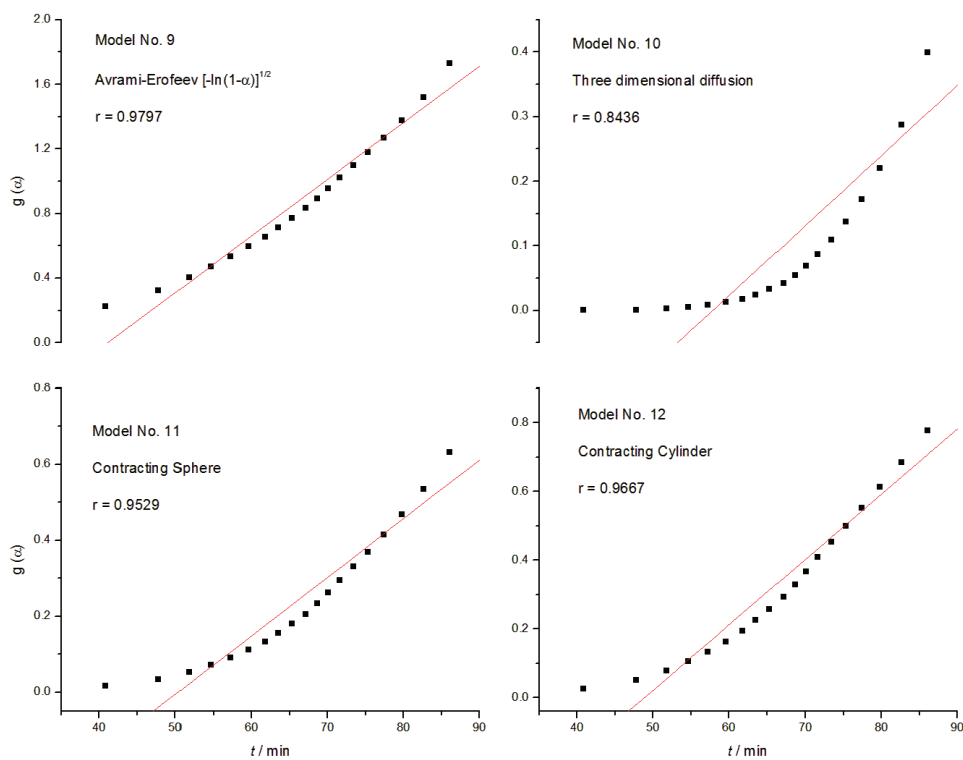

Fig. S-3. Typical model fitting least square plots (for models 9–12 given in Table S-I)
for the decomposition of KIO_4 at 560 K.
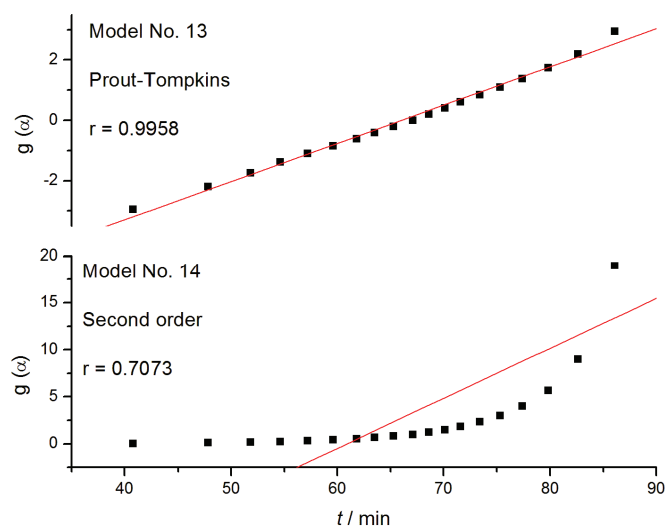

Fig. S-4. Typical model fitting least square plots (for models 13 and 14 given in Table S-I)
for the decomposition of KIO_4 at 560 K.

A novel platinum-based nanocatalyst at a niobia-doped titania support for the hydrogen oxidation reaction

NEVENKA R. ELEZOVIĆ[1*#], BILJANA M. BABIĆ[2], VELIMIR RADMILOVIĆ[3],
LJILJANA M. GAJIĆ-KRSTAJIĆ[4], NEDELJKO V. KRSTAJIĆ[5]
and LJILJANA M. VRAČAR[5]

[1]*Institute for Multidisciplinary Research, University of Belgrade, Kneza Višeslava 1, 11030 Belgrade,* [2]*Vinča Institute of Nuclear Sciences, P. O. Box 522, 11001 Belgrade, Serbia,* [3]*National Center for Electron Microscopy, LBNL University of California, Cyclotron Road CA 94720 - Berkeley, USA,* [4]*Institute of Technical Sciences-SASA, Knez Mihailova 35, Belgrade and* [5]*Faculty of Technology and Metallurgy, University of Belgrade, Karnegijeva 4, 11000 Belgrade, Serbia*

Abstract: The kinetics of the hydrogen oxidation reaction (HOR) was studied at Pt nanoparticles supported on niobia-doped titania (Pt/N–T). The catalyst support, with the composition of $0.05NbO_{2.5-\delta}$–$0.995TiO_2$ ($0 < \delta < 1$), was synthesized by a modified sol–gel procedure and characterized by the BET and X-ray diffraction (XRD) techniques. The specific surface area of the support was found to be 70 m^2 g^{-1}. The XRD analysis revealed the presence of the anatase TiO_2 phase in the support powder. No peaks indicating the existence of Nb-compounds were detected. Pt/N–T nanocatalyst was synthesized by the borohydride reduction method. Transmission electron microscopy revealed a quite homogenous distribution of the Pt nanoparticles over the support, with a mean particle size of about 3 nm. The electrochemical active surface area of Pt of 42±4 m^2 g^{-1} was determined by the cyclic voltammetry technique. The kinetics of the HOR was investigated by linear sweep voltammetry at a rotating disc electrode in 0.5 mol dm^{-3} $HClO_4$ solution. The determined value of the Tafel slope of 35 mV dec^{-1} and an exchange current density of 0.45 mA cm^{-2} per real surface area of the Pt are in good accordance with those already reported in the literature for the HOR at polycrystalline Pt and Pt nanocatalysts in acid solutions. This new catalyst exhibited better activity for the HOR in comparison with Pt nanocatalyst supported on Vulcan® XC-72R high area carbon.

Keywords: niobia-doped titania support; Pt nanocatalyst; hydrogen oxidation reaction; fuel cell.

1139

INTRODUCTION

In spite of the fact that proton exchange membrane fuel cells (PEMFCs) are promising future energy providers, many requirements regarding both the catalyst support and the catalyst material remain still unresolved. The main goals of contemporary research in this field are the development of inexpensive electrocatalysts for anode and cathode reactions, with high activity and satisfactory corrosion and chemical stability.

Platinum and Pt-based catalysts have been recognized as excellent catalysts for the hydrogen oxidation reaction.[1–3] The role of the supporting material for the functioning of a catalyst is very important, as it could affect both the catalytic activity and the durability of the catalyst. The catalyst support properties should be a combination of high surface area, excellent chemical stability and corrosion resistance. Hitherto, the most widely used supporting materials for Pt-based catalysts for the hydrogen oxidation reaction were carbon-based supports.[4–7] Carbon-based supports provide high electronic conductivity, an adequate physical surface for the dispersion of nanoparticles that is necessary to achieve a high surface area, also diminishing the catalyst loading. However, corrosion of a carbon support that could proceed either during recharge of a regenerative fuel cell at the air electrode at high overpotentials, or by start/stop of a simple fuel cell[8] is one of the main factors that could decrease the life time of PEMFCs. In the presence of water, carbon can also be consumed through the heterogeneous reaction: $C + H_2O \rightarrow H_2 + CO$,[9] especially in the presence of Pt which catalyses this reaction. The reaction product CO might poison the Pt catalyst. The above-mentioned disadvantages of carbon-based supports imply the need for new supporting materials, in order to prevent damage of the Pt nanocatalysts, enhance the reliability and reduce the total lifetime costs of PEMFC.

Several titanium oxide phases, mainly Ti_4O_7 and Ti_5O_9, known as Magneli phases, have been reported as promising catalyst supports for Pt-based nanocatalysts, for electrochemical reactions in PEMFCs.[10–12] The main disadvantage of the above-mentioned titanium oxides as supporting materials are their very low specific surface area. Namely, the maximum obtained value of the surface area is too low to achieve high dispersion and compositional homogeneity of the Pt nanoparticles over the support, which are important requirements for enhanced electrocatalytic activity. Ioroi *et al.* reported good corrosion stability of a Ti_4O_7-supported Pt catalyst, as well as almost the same catalytic activities as the XC-72/Pt catalyst for both the hydrogen oxidation reaction and the oxygen reduction reaction.[13]

According to the literature,[14] niobium oxide nanoparticles could be a promising material for catalyst support for Pt-based nanaocatalysts, owing its excellent chemical stability in acid solutions.

The aim of this work was to test a Pt nanocatalyst supported on a novel niobia-doped titania support (Pt/N–T) for the hydrogen oxidation reaction (HOR) and to compare the obtained results with those already reported for carbon-supported Pt-based nanocatalysts. A support with the composition $0.05NbO_{2.5-\delta}-0.995TiO_2$ $(0 < \delta < 1)$ was synthesized and completely characterized by the nitrogen adsorption/desorption isotherm and X-ray diffraction (XRD) techniques. A Pt nanocatalyst was synthesized on this support using the borohydride reduction method and characterized by the transmission electron microscopy (TEM) technique. This catalyst has already been tested for the oxygen reduction reaction and enhancements of the specific and mass activities were found.

EXPERIMENTAL

Synthesis of N–T support

The N–T support was synthesized by a modified sol–gel procedure proposed by Boujday *et.al.*[15] This procedure considers the acid-catalyzed sol–gel method in a non-aqueous medium. The sol was prepared by adding 0.9 ml of a 37 % solution of hydrochloric acid (Zorka, Serbia) to 40 ml of a 97 % solution of titanium tetra-isopropoxide, $Ti(O–iPr)_4$ (Alfa Aesar, Germany), and the appropriate volume of 0.17 ml of 99.95 % niobium(V) ethoxide (Aldrich, Germany) under vigorous stirring (0.5 % Nb in a Nb/Ti atomic ratio to obtain a $Nb_{0.005}Ti_{0.995}O_2$ solid solution). Finally, 4.8 ml of deionized (D.I.) water was added under continuous stirring. The mixture was placed in glass tubes, sealed and left at room temperature for 5 days. In the presence of such an amount of hydrochloric acid, the hydrolysis proceeded without the formation of a precipitate, leading to a transparent sol. Gellification of the sol was achieved by adding an appropriate amount of water.

The sample was freeze-dried using a Modulyo Freeze Dryer System, Edwards, England, consisting of a freeze dryer unit and a high vacuum pump E 2 M 8, Edwards. The sample was pre-frozen in a freezer at –30 °C for 24 h. Subsequently, the sample was freeze-dried in the acrylic chamber with the shelf arrangements mounted directly on the top of the condenser of the freeze dryer. The vacuum during the twenty-hour freeze-drying was around 4 mbar. The dried sample was heated at 400 °C for 2 h in a conventional furnace to obtain crystallized anatase phase and to remove traces of organics. After the treatment, the furnace was cooled to room temperature. Finally, to activate the Nb-donor dopant in the TiO_2, the nanoparticles were additionally annealed at 400 °C for 2 h under a pure H_2 gas flow and cooled to room temperature under a H_2 gas atmosphere.[16]

Synthesis of the Pt/N–T catalyst

The Pt/N–T catalyst containing 20 mass % Pt was prepared by means of the borohydride reduction method.[16] An appropriate amount of H_2PtCl_6 was dissolved in D.I. water. The support powder was dispersed in D.I. water and then the metal salt solution was added under constant stirring. The mixture of metal salt and the support was reduced by using an excess of sodium borohydride solution. The precipitate was washed with D.I. water and then dried at 80 °C.

The Pt/XC catalyst (with a real active Pt surface area of 96 m^2 g^{-1}, determined by cyclic voltammetry), which was used for comparison of the activities for the HOR, was synthesized by a modified ethylene glycol method on commercial carbon (Vulcan XC-72R) support. The details of the synthesis have already been reported.[5]

Cell and electrode preparation

Pt/N–T catalyst (20 mg) was ultrasonically suspended in 9.5 ml of water and 0.5 ml of Nafion solution (5 mass %, Aldrich solution) to prepare a catalyst ink. Then, 20 μl of ink was transferred with an injector to a gold disk electrode (5 mm diameter). After volatilization of the water, the electrode was heated at 80 °C for 10 min. The so-prepared electrodes were always characterized by cyclic voltammetry in order to confirm their similar real Pt surface area (estimated from the H underpotential deposition (upd) region). The reproducibility (10 %) of the determined real Pt surface area was very good; hence, the amount of Pt on the electrode was considered to be 8.0±0.8 μg.

For the electrochemical measurements, a conventional rotating disk electrode (RDE) three-compartment cell was used. The working electrode compartment was separated from the other two compartments by fritted glass discs. The counter electrode was a platinum sheet of 5 cm^2 geometric area. All measurements were performed with a Pt/H$_2$ reference electrode (RHE) in the same solution, at the same temperature as the working electrode. The RHE was kept in a compartment separated from the working electrode by a wetted, closed glass stopcock and purified hydrogen was bubbled continuously through the solution.

Electrode characterization

Adsorption and desorption isotherms. The nitrogen adsorption and desorption isotherms were measured on the N–T support at –196 °C, using the gravimetric McBain method. The specific surface area, S_{BET}, and the pore size distribution were calculated from the isotherms. Pore size distribution was estimated by applying the Barrett–Joyner–Halenda (BJH) method.[17]

XRD Analysis. Structural analysis (XRD) was realized using a Siemens D-500 diffractometer. Cu Kα radiation was used in conjunction with a Cu Kβ nickel filter. The XRD pattern was used to evaluate the crystallite size of the Nb–TiO$_2$ support. The average crystallite size, D, was calculated from the Scherrer formula: $D = 0.9\lambda/\beta\cos\theta$, where λ is the wavelength of the X-rays, θ is the diffraction angle, $\beta = (\beta_m^2 - \beta_s^2)$, β is the corrected half-width, β_m the observed half-width and β_s is the half-width of a standard Si sample (provided by Siemens).

TEM Measurements. Transmission electron microscopy (TEM) measurements were performed at the National Center for Electron Microscopy (NCEM-Berkeley) using a FEI (Fillips electronic instruments)-CM200 super-twin and CM300 ultra-twin microscopes operating at 200 and 300 kV and equipped with Gatan 1k×1k and 2k×2k CCD cameras, respectively. Specimens were prepared for TEM by making suspensions of the catalyst powder in ethanol, using an ultrasonic bath. These suspensions were dropped onto clean holey carbon grids, and then air-dried.

The particle size distribution was determined from images of, on average, 20 different regions of the catalyst; each region contained 10–20 particles. The particle shapes were determined by real space crystallography with the use of high-resolution images taken from particles near or on the edge of the N–T substrate, and/or by numerical Fourier filtering of the digitized image intensity spectrum of particles on top of the support.

Electrochemical characterization. The cyclic voltammetry experiments were performed in the potential range between hydrogen and oxygen evolution (0.04–1.4 V *vs.* RHE), in 0.5 mol dm^{-3} HClO$_4$ solution, with various scan rates at the Pt/N–T and Pt/XC electrodes. Prior to recording the cyclic voltammograms, the electrode surface was stabilized by repetitive cycling from 0.04 to 1.4 V *vs.* RHE. The solution (HClO$_4$, Spectrograde, Merck) was prepared in D.I. water ("Millipore"– 18 MΩ cm resistivity), at a temperature of 25 °C, which was saturated with high purity nitrogen by continuously bubbling through the working electrode compartment during the experiments.

Linear sweep voltammetry curves for the HOR in 0.5 M $HClO_4$ solution saturated with pure hydrogen, continuously bubbling through the working electrode compartment, were recorded at 10 mV s^{-1} sweep rate. A PAR universal programmer, model 175, was used to provide the potentiodynamic voltage time program addressed to a PAR model 371 potentiostat/ /galvanostat.

RESULTS AND DISCUSSION

BET and XRD analysis of N–T support

The nitrogen adsorption isotherm for the N–T support, according to the IUPAC classification, belongs to type IV, associated with mesoporous materials. The specific surface area of the support powder calculated by the BET equation was determined to be 70 m^2 g^{-1}. The pore size distribution is presented in Fig. 1.
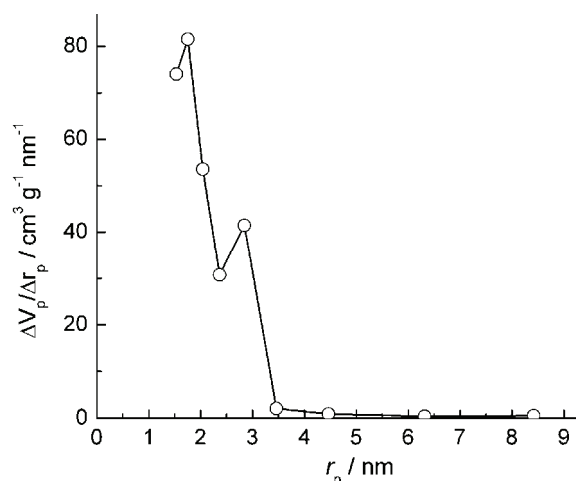
Fig. 1. Pore size distribution for the N–T support.

The X-ray pattern of the N–T support sample is shown in Fig. 2. It could be seen that all peaks present belong to the anatase phase of titanium dioxide. No peaks corresponding to niobium compounds were detected. The broad peaks indicate to nano-sized particles. The obtained values for lattice parameters were $a = b = 0.37854$ nm and $c = 0.94835$ nm. The determined values of the lattice parameters for anatase titanium oxide were enlarged compared to those of pure anatase (JCPDS 21-1272), indicating niobium incorporation into the lattice. It is well known that Nb (or V and Ta) can be substitutionally incorporated within the TiO_2 lattice.[18,19] Investigation of the structural properties of niobia-doped titania even up to 38 % of Nb, showed the existence of only a pure anatase or rutile phase, depending on the growth temperature.[20] In the present study, in order to activate the Nb-donor dopant in TiO_2, the nanoparticles were additionally annealed at 400 °C and XRD analysis showed the existence of anatase TiO_2. This result is in good accordance with literature results which reported that up to 550

°C, only anatase was present, while at 800 °C and higher, pure rutile phase was obtained.[20]
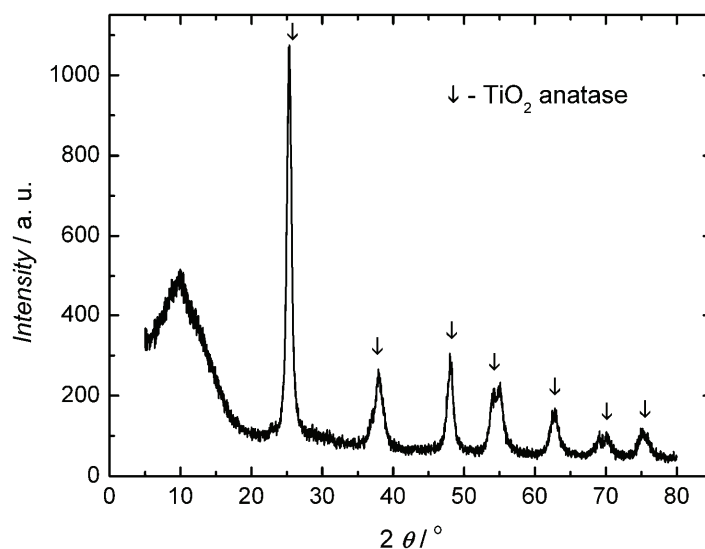
Fig. 2. XRD Diffraction results for the N–T support.

TEM Analysis of the Pt/N–T catalyst

TEM Micrographs of the N–T-supported Pt nanocatalyst are presented in Fig. 3. Figure 3a shows a low-magnification transmission electron micrograph of

(a)   (b)
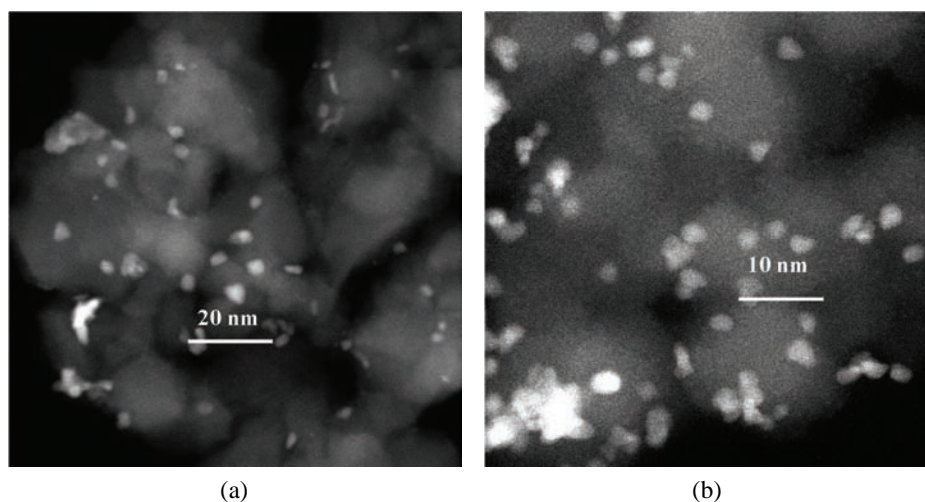
Fig. 3. TEM micrographs of the Pt/N–T nanocatalyst: a) low magnification image showing a homogeneous distribution of Pt particles on the catalyst support; b) high resolution dark field image of the catalyst, showing no pronounced agglomeration of the particles.

the Pt nanoparticles on the N–T support. It is evident that the Pt nanoparticles are globular in shape and quite uniformly distributed over the N–T support. Using these results, it was possible to determine the Pt particle size distribution, as well as to calculate the total surface area of the particles by analyzing the images from different regions of the catalyst, taking into account the hypothesis that all the particles are globular in shape and have the same average particle size. A high resolution electron microscopy image of the Pt/N–T sample is shown in Fig. 3b. There is no evidence of pronounced particle agglomeration. The determined average size of the nanoparticle was about 3 nm.

Cyclic voltammetry results

The cyclic voltammetry responses at the N–T support, and the Pt/N–T and the Pt/XC nanocatalysts were recorded in the potential range between oxygen and hydrogen evolution in 0.5 mol dm^{-3} HClO$_4$ solution. The obtained results are presented in Fig. 4. The cyclic voltammetry response of the N–T support (Fig. 4 inset) shows the rectangular shape that is expected for an ideal electrochemical double-layer capacitor. No significant peaks revealing the presence of oxidative–reductive processes were observed. This result proves that N–T was an electrochemically inert support over the whole range of applied potential (0.04––1.40 V *vs*. RHE). The cyclic voltammetric curve of the Pt/N–T electrode (Fig.
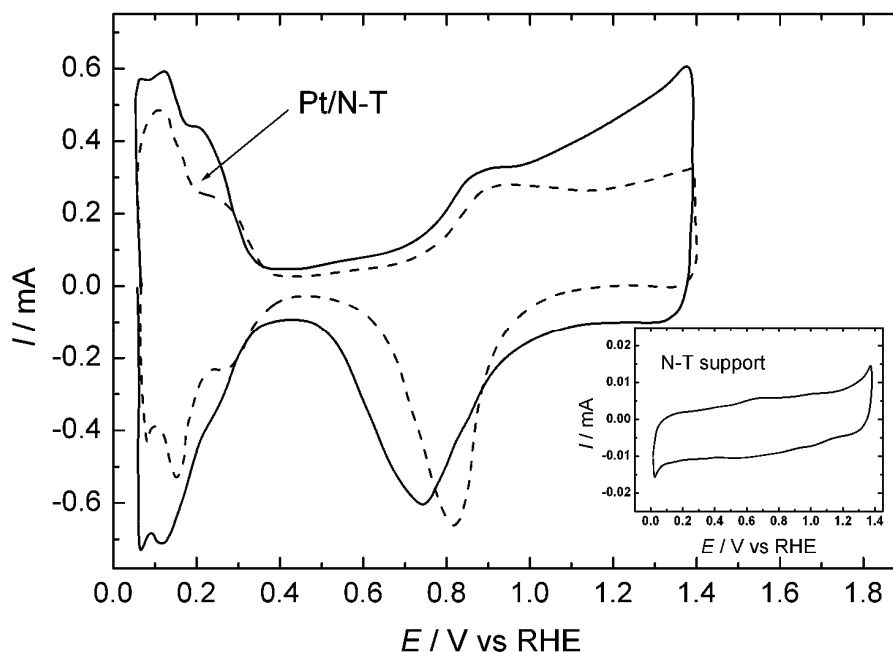
Fig. 4. Cyclic voltammograms obtained at the N–T support, and the Pt/N–T and Pt/XC nanocatalysts in nitrogen-purged, 0.5 mol dm^{-3} HClO$_4$, using a 0.1 V s^{-1} sweep rate, at 25 °C.

4), in the same solution saturated with N_2, has a typical voltammogram shape for Pt in acid solution, with very clear hydrogen adsorption–desorption and PtOH formation and reduction regions. The cyclic voltammogram of the Pt/XC nanocatalyst, under the same experimental conditions, is also presented in Fig. 4. A similar Pt-like shape could be observed and a lower specific surface area of Pt in the Pt/N–T catalyst, estimated based on the desorption charge of hydrogen in the under potential deposition region. The Pt/N–T catalyst in comparison with the Pt/XC was also characterized by a very narrow, symmetric double layer region, as a consequence of its lower capacitance current contribution.

The electrochemically active surface area of Pt for the Pt/N–T catalyst was determined from the adsorption/desorption charge of hydrogen atoms, after subtraction of the double layer charge, taking the reference value of 210 μC cm^{-2} for a charge of full coverage with adsorbed hydrogen species at Pt.[21] This calculation gave the value of specific electrochemical active area of 42±4 m^2 g^{-1} Pt for the Pt/N–T electrode.

Hydrogen oxidation reaction at Pt/N–T electrode

It is well known that hydrogen oxidation on Pt-based electrodes in acid solution is one of the fastest electrochemical reactions. The measured currents reach the diffusion limitation rising to the diffusion-limited level within less than 0.10 V *vs*. RHE, even at a RDE. For this reason, the mixed controlled potential region must be analyzed in order to collect kinetic information from experimentally obtained results.

The basic assumption of the analysis is that the measured current is determined by the overall resistance that consists of three components: one related to electron transfer kinetics, the two others result from mass transport limitations. According to this, the kinetically controlled current, I_k, at a given potential E can be determined from RDE curves using the equation proposed by Lawson:[22]

$$\frac{1}{I} = \frac{1}{I_k} + \frac{1}{I_L} + \frac{1}{I_f} \tag{1}$$

and

$$I_L = 0.62nFD^{2/3}cv^{-1/6}\omega^{1/2} \tag{2}$$

where I_k is the kinetic current in the absence of any mass-transfer effects, and I_L is the so-called Levich current, controlled mainly by diffusion. Other parameters have their usual significance in the conventional Levich Equation. I_f represents the diffusion current controlled by reactant diffusion through the Nafion film and is equal to:

$$I_f = nFD_f c_f L^{-1} \tag{3}$$

where D_f, c_f and L stand for the diffusion coefficient and the concentration of dissolved hydrogen in the Nafion film, and the film thickness, respectively. At a sufficiently large potential, E, and if the rotation rate of the electrode is increased enough ($\omega \to \infty$), the kinetic current, I_k and I_L become very large and under such conditions, the measured current I is equal to I_f. Based on the above consideration, it is possible to obtain the value of I_f from the intercept of $1/I_{L.lim}$ axis by extrapolating the relationship of $1/I_L$ $vs.$ $\omega^{-1/2}$, where $I_{L.lim}$ represents the diffusion-limited current density at a given rotation rate.

The potentiodynamic curves for the oxidation of H_2 on the Pt/N–T electrode at different rotation rates in 0.5 mol dm^{-3} HClO$_4$ solution at 25 °C are presented in Fig. 5. It can be seen that the HOR starts at 0.0 V $vs.$ RHE and reach the diffusion-limited current at approximately 0.05 V. Linear sweep voltammograms for the HOR at two different rotation rates for the Pt/XC and Pt/N–T electrodes are presented in Fig. 6. Although very similar values of currents were observed, Pt/N–T catalyst is characterized by a higher specific activity for the HOR, expressed in terms of the current density, taking into account its lower real surface area, determined by cyclic voltammetry. It should be mentioned that it is not common to refer to catalytic activity for the HOR at Pt based catalyst in terms of current density value at any given potential, as it is usually reported for the oxygen reduction reaction.
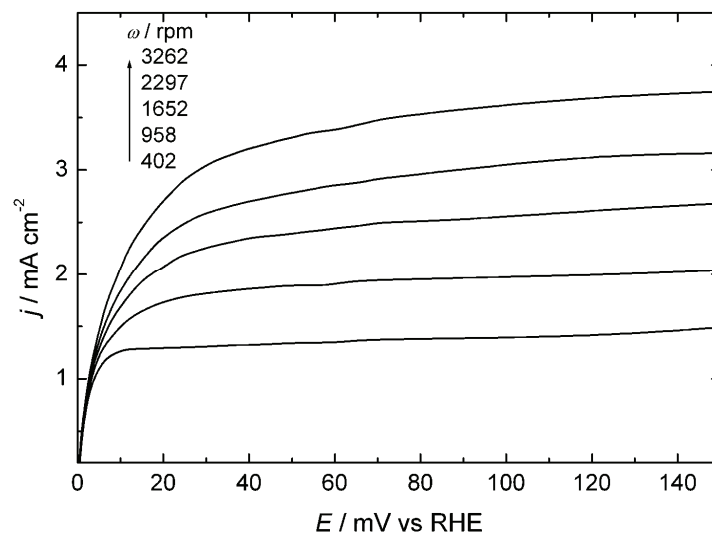
Fig. 5. Linear-sweep voltammograms for the HOR at the Pt/N–T nanocatalyst (current density expressed per geometric surface area), for different rotation rates in 0.5 mol dm^{-3} HClO$_4$ solution saturated with pure H$_2$ (scan rate 0.01 V s^{-1}) at 25 °C.

A Levich–Koutecky plot based on the experimental data at 0.15 V is shown in Fig. 7. The value of the current density controlled by diffusion of the reactant

through the Nafion film, determined from the intercept in Fig. 6, was about 55 mA cm^{-2} (the current density is expressed per geometric surface area). Nevertheless, its contribution to the measured current densities is negligible if the values of I_k determined from Eq. (1) are less than 10 % of the minimum value of I_f. This means that is not possible to obtain accurately a polarization curve for the HOR from the corresponding modified Levich–Koutecky plots.
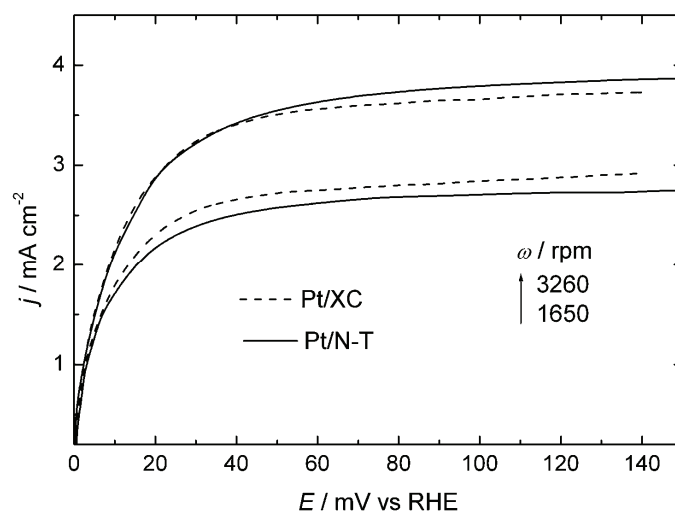
Fig. 6. Linear sweep voltammograms for the HOR at the Pt/N–T and Pt/XC nanocatalysts (current density expressed per geometric surface area) at two different rotation rates in 0.5 mol dm^{-3} HClO$_4$ solution saturated with pure H$_2$ (scan rate 0.01 V s^{-1}) at 25 °C.
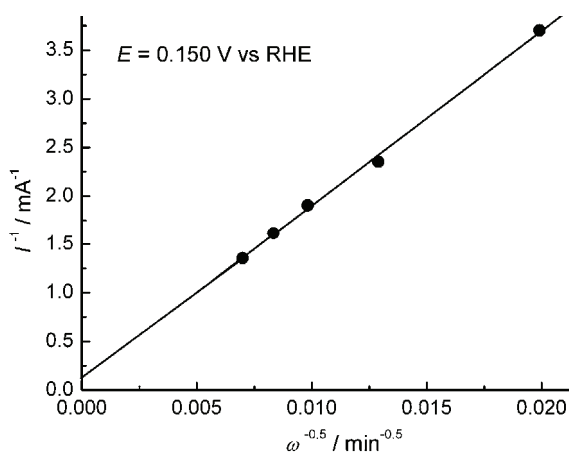
Fig. 7. Levich–Koutecky plot for the HOR at a Pt/N–T RDE in 0.5 mol dm^{-3} HClO$_4$ solution at 25 °C, in the diffusion-limited potential region at $E = 0.15$ V *vs.* RHE.

Tafel plots are commonly used to obtain kinetic information for the HOR.[1,23,24] A summary of the theoretically predicted values of the Tafel slopes

for different types of mechanisms for the HOR at platinum electrodes in acid solutions are presented in Table I. For the HOR on platinum electrodes, the most widely accepted mechanism is chemical adsorption (Tafel step) or electrochemical adsorption (Heyrovsky step), followed by adsorbed hydrogen discharge (Volmer step), as is presented by the following equations:[3]

$$H_2 + 2M \rightarrow 2MH \qquad \text{(Tafel step)} \qquad (4)$$

$$H_2 + M \rightarrow MH + H^+ + e^- \qquad \text{(Heyrovsky step)} \qquad (5)$$

$$MH \rightarrow M + H^+ + e^- \qquad \text{(Volmer step)} \qquad (6)$$
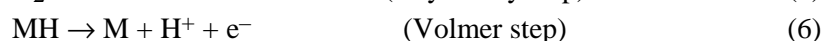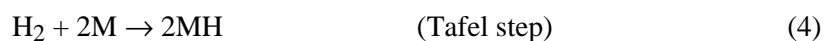
TABLE I. Theoretical values of the Tafel slopes ($b = 2.303RT/\beta F$) and mechanisms for the HOR in acid solutions at 25 °C

Mechanism	b / mV dec^{-1}	Rate-determining step
Tafel–Volmer	30	Tafel
Heyrovsky–Volmer	118	Heyrovsky
Tafel–Volmer and Heyrovsky–Volmer	59	Volmer

In order to obtain information about the kinetics of the HOR at the Pt/N–T catalyst, the RDE polarization data were analyzed in terms of mass transport corrected Tafel diagrams and the obtained results are presented in Fig. 8.
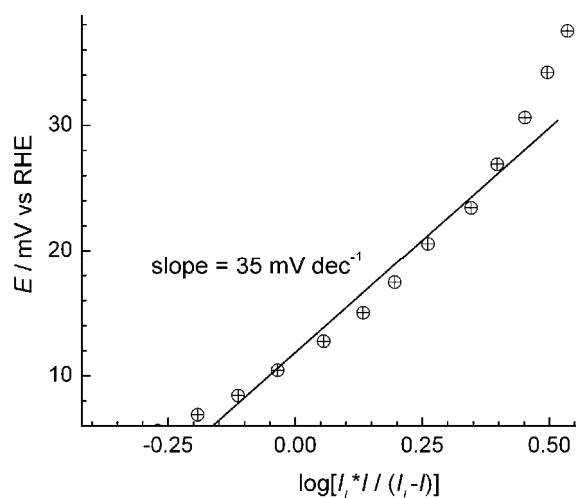
Fig. 8. Mass corrected Tafel plot for the HOR at a Pt/N–T RDE in 0.5 mol dm^{-3} HClO$_4$, at 25 °C.

The Tafel slope of 35 mV dec^{-1} is in good accordance with the already reported slope for the hydrogen oxidation reaction at platinum single crystals,[23] smooth platinum[25] and platinum nanocatalysts in acid solutions.[3,5]

It is not possible to determine the exchange currents (I_0) simply by extrapolating the Tafel lines to the reversible potential due to the absence of a well-defined Tafel region. The exchange current was estimated from the slope of the

linear polarization response and after correction for diffusion, using the following equation:[5]

$$\frac{\Delta E}{\Delta I} = \frac{RT}{nF}\left(\frac{1}{I_0} + \frac{1}{I_{L,lim}}\right) \qquad (7)$$

where $n = 2$ and $I_{L,lim}$ is the limiting current.

This calculation assumes that the HOR and the hydrogen evolution reaction (HER) follow the same reaction mechanism around the equilibrium potential. The obtained value for the exchange current density of 0.45 mA cm^{-2} is in good accordance with previously reported values for the HOR at Pt in acid solutions,[23,26] determined using the RDE technique. The determined exchange current density, expressed per real surface area, is twice as high as that obtained for the HOR at a Pt nanocatalyst on a carbon support.[5]

This new catalyst was already tested for the oxygen reduction reaction and a five times enhancement in the catalytic activity per mass Pt loaded, as well as ten times enhancement in the specific activity (per real electrochemically active surface area) were reported.[27] Bearing in mind that the overall cell performance in PEMFCs is influenced much more by the oxygen reduction reaction, owing to its much higher overvoltage compared with the hydrogen oxidation reaction, it could be concluded that this new catalyst is promising for applications in PEMFCs.

CONCLUSIONS

An N–T support was successfully synthesized by a modified sol–gel procedure. The specific surface area of the support, determined by the BET technique, was found to be 70 m^2 g^{-1}. The presence of anatase TiO$_2$ in the synthesized catalyst support powder was determined by XRD measurements. No peak corresponding to Nb-compounds was detected.

A Pt/N–T nanocatalyst was successfully synthesized by the borohydride reduction method. TEM Analysis revealed a quite homogenous distribution of Pt nanoparticles on the N–T support, with an average particle size of about 3 nm.

The electrochemically active surface area of the Pt in the Pt/N–T nanocatalyst, determined by the cyclic voltammetry technique, was found to be 42±4 m^2 g^{-1}.

Electrochemical characterization of the fabricated catalyst for the HOR revealed a Tafel slope of 35 mV dec^{-1} and an exchange current density of 0.45 mA cm^{-2}. This value of the Tafel slope and the exchange current density are of the same order of magnitude already accepted in literature for the HOR at a platinum-based catalyst in acid solutions. The determined exchange current density was two-times higher than the corresponding value obtained for the hydrogen oxidation reaction at a Pt carbon supported catalyst.

И З В О Д

НОВИ Pt КАТАЛИЗАТОР НА НОСАЧУ НА БАЗИ ТiO₂ ЗА РЕАКЦИЈУ ОКСИДАЦИЈЕ ВОДОНИКА

НЕВЕНКА Р. ЕЛЕЗОВИЋ[1], БИЉАНА М. БАБИЋ[2], ВЕЛИМИР РАДМИЛОВИЋ[3], ЉИЉАНА М. ГАЈИЋ-КРСТАЈИЋ[4], НЕДЕЉКО В. КРСТАЈИЋ[5] и ЉИЉАНА М. ВРАЧАР[5]

[1]*Институт за мултидисциплинарна истраживања, Универзитет у Београду,Кнеза Вишеслава 1, 11030 Београд,* [2]*Институт за нуклеарне науке Винча, п. пр. 522, Београд,* [3]*National Center for Electron Microscopy, LBNL University of California, Cyclotron Road, CA 94720- Berkeley, USA,* [4]*Институт техничких наука САНУ, Кнез Михаилова 35, 11000 Београд и* [5]*Технолошко–металурски факултет Универзитета у Београду, Карнегијева 4, Београд*

Кинетика електрохемијске оксидације водоника је испитивана на Pt нанокатализатору на носачу састава 0,05NbO$_{2,5-\delta}$–0,995TiO₂ ($0 < \delta < 1$) (у тексту Pt/N–T). Носач катализатора је синтетисан применом модификованог сол–гел поступка и окарактерисан BET методом и методом дифракције X-зрака. Специфична површина носача је била 70 m² g⁻¹. Дифракцијом X-зрака је утврђено присуство TiO₂ у форми анатаза, док пикови који би указивали на присуство једињења Nb нису детектовани. Нанокатализатор Pt/N–T је синтетисан методом редукције помоћу бор-хидрида. Применом трансмисионе електронске микроскопије је показана хомогена расподела наночестица Pt на носачу, са просечном величином честица око 3 nm. Применом цикличне волтаметрије је одређена електрохемијска активна површина катализатора приближне вредности 42±4 m² g⁻¹. Кинетика реакције оксидације водоника је испитивана применом линеарне скенирајуће волтаметрије на ротирајућој диск електроди у раствору 0,5 mol dm⁻³ HClO₄. Добијене вредности Тафеловог нагиба и густине струје измене од 35 mV дек⁻¹ и 0,45 mA cm⁻² (обрачунато по електрохемијски активној површини Pt) су у сагласности са литературним вредностима за реакцију оксидације водоника на поликристалној Pt и на наночестицама Pt у киселим растворима. Нови катализатор Pt/N–T је показао већу активност за оксидацију водоника од Pt нанокатализатора на носачу од угља развијене површине (Vulcan® XC-72R).

(Примљено 26. августа 2010, ревидирано 15. јануара 2011)

REFERENCES

1. R. M. Q. Mello, E. A. Ticianelli, *Electrochim. Acta* **42** (1997) 1031
2. J. Shim, C. R. Lee, H. K. Lee, J. S. Lee, E. J. Cairns, *J. Power Sources* **102** (2001) 172
3. A. F. Innocente, A. C. D. Angelo, *J. Power Sources* **162** (2006) 151
4. S. J. Lee, S. Mukerjee, E. A. Ticianelli, J. McBreen, *Electrochim. Acta* **44** (1999) 3283
5. B. M. Babić, Lj. M. Vračar, V. Radmilović, N. V. Krstajić, *Electrochim. Acta* **51** (2006) 3820
6. R. B. Lin, S. M. Shih, *J. Chin. Inst. Chem. Eng.* **38** (2007) 365
7. J. Kim, J. H. Jang, Y. H. Lee, Y. U. Kwon, *J. Power Sources* **193** (2009) 441
8. C. A. Reiser, L. Bregoli, T. W. Patterson, S. Yi. Jung, J. D. Yang, M. L. Perry, T. D. Jarvi, *Electrochem. Solid-State Lett.* **8** (2005) A273
9. Y. Shao, G. Yin, Y. Gao, *J. Power Sources* **171** (2007) 558

10. G. R. Dieckmann, S. H. Langer, *Electrochim. Acta* **44** (1998) 437
11. L. He, H. F. Franzen, J. E. Vitt, D. C. Johnson, *J. Appl. Electrochem.* **26** (1996) 785
12. E. E. Farndon, D. Pletcher, *Electrochim. Acta* **42** (1997) 1281
13. T. Ioroi, Z. Siroma, N. Fujiwara, S. Yamazaki, K. Yasuda, *Electrochem. Commun.* **7** (2005) 183.
14. K. Sasaki, L. Zhang, R. R. Adzic, *Phys. Chem. Chem. Phys*. **10** (2008) 159
15. S. Boujday, F. Wunsch, P. Portes, J. F. Bocquet, C. Colbeau-Justin, *Sol. Energ. Mat. Sol. C.* **83** (2004) 421
16. K. W. Park, K. S. Seol, *Electrochem. Commun.* **9** (2007) 2256
17. E. P. Barret, L. G. Joyner, P. P. Halenda, *J. Am. Chem. Soc*. **73** (1951) 373
18. D. Morris, Y. Dou, J. Rebane, C. E. J. Mitchell, R. G. Egdell, *Phys. Rev., B* **61** (2000) 13445
19. E. Antolini, E. R. Gonzalez, *Solid State Ionics* **180** (2009) 746
20. Y. Gao, *Thin Solid Films* **346** (1999) 73
21. J. T. Hwang, J. S. Chung, *Electrochim. Acta* **38** (1993) 2715
22. D. R. Lawson, L. D. White, C. R. Martin, M. N. Szentirmay, J. I. Song, *J. Electrochem. Soc.* **135** (1988) 2247
23. N. M. Markovic, B. N. Grgur, P. N. Ross, *J. Phys. Chem., B* **101** (1997) 5405
24. P. M. Quaiano, M. R. G. De Chialvo, A. C. Chialvo, *Phys. Chem. Chem. Phys*. **6** (2004) 4450
25. B. E. Conway, B. V. Tilak, *Electrochim. Acta* **47** (2002) 3571
26. N. R. Elezovic, B. M. Babic, V. R. Radmilovic, Lj. M. Vracar, N. V. Krstajic, *Phys. Chem. Chem. Phys.* **11** (2009) 5192
27. N. R. Elezovic, B. M. Babic, Lj. Gajic-Krstajic, V. Radmilovic, N. V. Krstajic, Lj. Vracar, *J. Power Sources* **195** (2010) 3961.

PMMA–Y_2O_3 (Eu^{3+}) nanocomposites: optical and mechanical properties

SALAH S. MUSBAH[1], VESNA J. RADOJEVIĆ[1*], NADEŽDA V. BORNA[1],
DUŠICA B. STOJANOVIĆ[1], MIROSLAV D. DRAMIĆANIN[2],
ALEKSANDAR D. MARINKOVIĆ[1#] and RADOSLAV R. ALEKSIĆ[1]

*[1]Faculty of Technology and Metallurgy, University of Belgrade, Karnegijeva 4, Belgrade and
[2]Institute of Nuclear Sciences "Vinča", P. O. Box 522, Belgrade, Serbia*

Abstract: The results of a study related to the processing and characterization of poly(methyl methacrylate) (PMMA)–Y_2O_3 (Eu^{3+}) nanocomposites are presented herein. The nanocomposite samples were prepared using a laboratory mixing molder with different contents of Eu-ion doped Y_2O_3 nanophosphor powder. The influence of particle content on the optical and dynamic mechanical properties of the nanocomposites was investigated. The intensity of the luminescence emission spectra increased as the nanophosphor content in the composite increased. The results of dynamic mechanical analysis revealed that the storage modulus, loss modulus and glass transition temperature (T_g) of the polymer composites increased with increasing content of the nanophosphor powder. The microhardness data also confirmed that the hardness number increased with nanoparticles concentration in the PMMA nanocomposites. The obtained results revealed a relatively linear relationship between T_g and the Vickers hardness.

Keywords: nanocomposites; luminescence; mechanical properties; dynamic mechanical analysis; microhardness.

INTRODUCTION

Nanocomposites are a distinct form of composite materials, which involve embedding nano- or molecular domain-sized particles into organic polymer, metal or ceramic matrix materials.[1,2] The intimate inclusion of nanoparticles in these matrices can greatly change the mechanical, electrical, optical or magnetic properties of these materials. The reason for this is that with such small in-

---

1153

clusions, a large amount of interfacial phase material exists in the bulk of these nanocomposites.

This paper is related to the processing and characterization of polymer––nanophosphor composites, as promising materials for the production of nanocomposite fibers. Plastic optical fibers (POF) can be used for a number of applications, such as light transmission for signs and illumination, sensors and data communication.[3–5] Signal attenuation of commercial polymer fibers is much higher than that of glass fibers. In order to improve POF optical efficiency, research and processing are being developed in the direction of nanocomposite POF doped with dyes, and fluorescent or phosphorescent nanopowder.[6]

The optical properties of nano-sized phosphors are significantly improved in comparison to bulk materials (stronger luminescence emission and modified radiative lifetime).[7–20] Poly(methyl methacrylate), PMMA, nanocomposites containing Y_2O_3 doped with rare earths (RE) ions have been investigated and it was suggest that doped Y_2O_3 nanocrystals embedded in PMMA would have potential for various photonic applications, including laser systems and optical communication devices.[21,22] Nanocomposites PMMA–Y_2O_3:RE were successfully prepared by mixing Y_2O_3/Eu^{3+},Yb^{3+} or Y_2O_3/Eu^{3+} with PMMA for infrared cards.[22] The Eu-ion doped Y_2O_3 nanophosphor is useful for nanocomposite POF light guides because the luminescence wavelength of the Eu-ion (611 nm) is in the visible range of spectrum. It is very important to preserve their optical properties for a synergetic effect in functional nanocomposites.

In this work, Eu-ion doped Y_2O_3 nanophosphor powder was dispersed in PMMA as the host. The influence of the content of nanopowder on the optical properties, dynamic mechanical properties, transition temperature, T_g, and microhardness of the nanocomposites was investigated.

When an amorphous polymer is heated, it undergoes a phase transition from the glassy state to the rubbery state at the T_g, when abrupt jumps in the thermal expansion and heat capacity occur. The temperature coefficients of the molar volume, free volume and enthalpy change of the glass–rubber transition are closely related to the cohesive energy density of the polymer. The glass transition temperature, T_g is linearly related to the cohesive energy density (CED) by the following equation:[23]

$$T_g = (2E_C/mR) + C_1 \qquad (1)$$

where E_C is the CED, T_g is the glass transition temperature (in K), m a parameter that describes the internal mobility of the groups in a single chain, R is the gas constant and C_1 is a constant. The CED is also the main factor determining hardness, H, which results in an almost linear relationship between T_g and H for a number of amorphous glassy polymers:[24–26]

$$H = kT_g + C \qquad (2)$$

where C and k are experimental fitting parameters.

The nanoparticles penetrate into the polymer matrix and establish cohesive forces between the polymer chains and decrease the segmental mobility thereby increasing the T_g value.[27] Therefore, it is to be expected that the microhardness will also be increased. The expression for the Vickers hardness (HV) is:

$$HV = 1.854Pd^{-2} \qquad (3)$$

where P is the applied load and d is the mean diagonal length of the diamond--shaped indent.

Dynamic mechanical analysis (DMA) is a sensitive technique that characterizes the mechanical response of materials by monitoring property change with respect to the temperature and frequency of an applied sinusoidal stress. This technique separates the dynamic response of materials in to two distinct parts: an elastic part (E') – storage modulus and a viscous component (E'') – loss modulus. The loss factor, tan δ, is the ratio of the energy dissipated to the energy stored. The transition temperature (T_g) of a polymer is associated with the onset of the storage modulus – $T_{g(E')}$; the loss modulus peak – $T_{g(E'')}$ and the tan δ peak – $T_{g(\tan \delta)}$. The onset of E' occurs first at the lowest temperature and relates to mechanical failure. The E'' peak occurs next and is associated with the T_g as the temperature of the onset of segmental motion. The tan δ peak occurs at the highest temperature and represents a good measure of the "leather like" midpoint between the glassy and rubbery state.[28,29]

EXPERIMENTAL

The nanopowder was synthesized by a complex polymer solution method (PCS), employing poly(ethylene glycol) (PEG) fuel. The particle size was about 30–40 nm.[30]

The nanocomposites were prepared by melt compounding in a Laboratory Mixing Molder (Atlas, USA), at a working temperature of 250 °C and a rotor speed of 180 rpm for 20 min. The polymer component of the composite was extrusion grade PMMA pellets, Acryrex® CM-205, Chi Mei Corporation, Taiwan. Samples with different contents of (Eu^{3+})Y$_2$O$_3$ powder: 0.1, 0.5, 1.0 and 1.5 % by weight were processed.

The infrared (IR) spectra of the powder, pure PMMA and the composites were obtained by Fourier transform infrared (FT-IR) spectroscopy (Hartmann & Braun, MB-series) in KBr discs. The scanning range was between 4000 and 400 cm^{-1} with a resolution of 4 cm^{-1}.

The emission spectra of the PMMA-Y$_2$O$_3$ (Eu^{3+}) nanocomposites were collected at room temperature after excitation into the $^7F_0 \rightarrow {}^5D_2$ absorption band. The excitation source was an Optical Parametric Oscillator (O.P.O.) pumped by the third harmonic of an Nd:YAG laser. The emission was analyzed using an HR250 monochromator (Jobin-Yvon) and then detected by an ICCD camera (Princeton Instrument).

The microhardness measurements were performed at the room temperature using a Vickers microhardness tester Leitz, Kleinharteprufer Durimet I. The Vickers microhardness test uses a square based pyramidal indenter with an apex of $\alpha = 136°$, producing a diamond-shaped indent on the surface. A press load of 490 mN, a press time of 15 s, and a holding time of 5 s after completing the indentation were used. Individual Vickers microhardness values (HV) were calculated as the mean value of at least five indentations.

A dynamic mechanical analysis (DMA) instrument (TA Instruments Q800) was used to determine the dynamic mechanical properties of the samples. The experiments were realized in the single-cantilever mode over a temperature range from 25 to 160 °C at a fixed frequency of 1 Hz. The heating ramp rate was 3 °C min^{-1}. The temperature dependence of the storage modulus, loss modulus and tan δ were obtained.

RESULTS AND DISCUSSION

The FT-IR transmission spectra of the powder, PMMA and composites are illustrated in Fig. 1. The peaks at 2946 and 1735 cm^{-1} are assigned to C–H and C=O stretching vibrations in PMMA, respectively. The absorption bands of PMMA (1439, 840, 750 and 440 cm^{-1}), and the vibration bands of PMMA (3458, 1385, 1133 and 974 cm^{-1}), were observed in the spectra. In the spectrum of Y_2O_3 (Eu^{3+}), the transmission band centered at 560 cm^{-1} is attributed to Y–O lattice vibrations. This peak also appeared in all the spectra of all the composites.
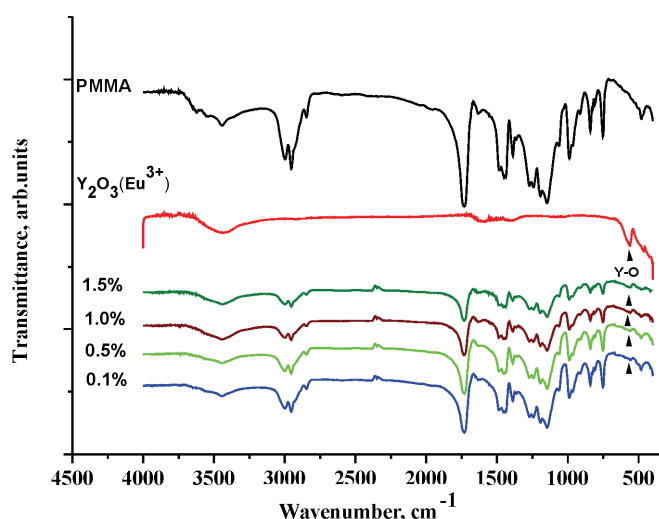
Fig. 1. FT-IR Spectra of Y_2O_3 (Eu^{3+}), PMMA and the composites with different contents of Y_2O_3 (Eu^{3+}).

The emission luminescence spectra of nanocomposite are presented in Fig. 2. The spectra exhibit groups of distinctive emission peaks in the 580–711 nm range. These emission peaks can be related to each of the $^5D_0 \rightarrow {}^7FJ$ ($J = 0, 1, 2, 3$ or 4) transitions of Eu^{3+}, which are characteristic for Eu^{3+} within a crystallized cubic phase. The strongest emission peak at 611 nm is caused by the electron dipole transition of Eu^{3+} ($^5D_0 \rightarrow {}^7F_2$), corresponding to the red luminescence. The intensity of the emission peak increased with increasing powder content in composite. It is very important that the nano-phosphors maintain their optical properties in the composites. The strongest emission peak at 611 nm was obtained in the range of wavelengths where the maximum signal attenuation of

PMMA optical fiber is expected to be found. This feature will improve the transmission properties of POF and will prolong the length of a light guide.
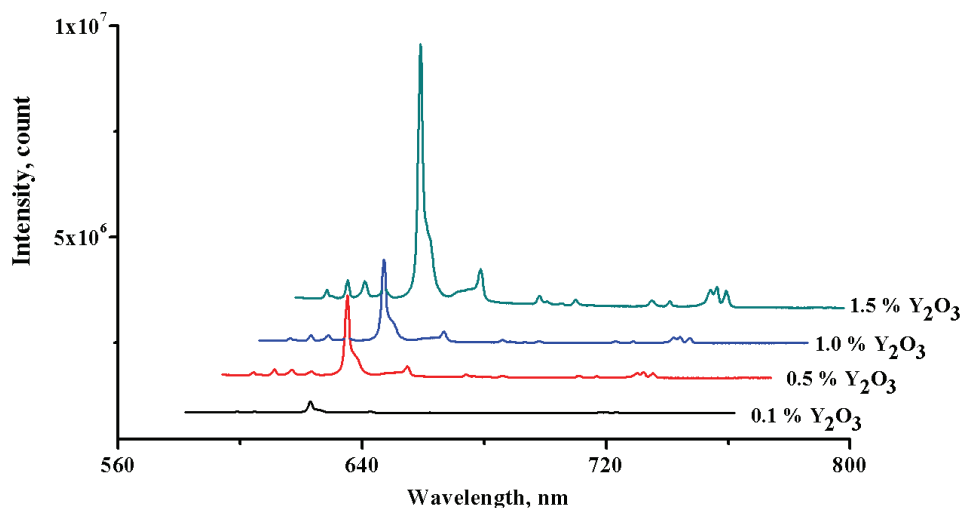
Fig. 2. Emission spectra of the PMMA–Y$_2$O$_3$ (Eu^{3+}) nanocomposites
at room temperature.

Investigations of the dynamic mechanical properties of the samples provided information on the transitions occurring in the materials (Fig. 3). The DMA results revealed that the storage modulus of the all the composite samples were higher than that of a pure PMMA at 30 °C (Table I). The increase of nanopowder content up to 1 % increased the storage modulus of composite by 15.5 % compared to that of pure PMMA. With 1.5 % of the nanophosphor, the storage modulus of the composite was only 5.1 % higher than that of PMMA, because of agglomeration of the nanoparticles. The corresponding loss moduli were between 175 and 200 MPa and obviously increased with increasing content of nanopowder in the same manner as the storage modulus. The T_g values of the PMMA––Y$_2$O$_3$ (Eu^{3+}) composites were also higher than that of PMMA and increased with increasing content of the nanoparticles. The results suggested that the nanoparticles did not disperse individually but as aggregates; however, notable increases in the glass transition temperature in the order of 2 to 8 °C were evidenced.

The hardness (H) of a material is a measure of its resistance to shear stresses under local volume compression. The hardness number increased with Y$_2$O$_3$ (Eu^{3+}) concentration in the PMMA nanocomposites. The increased resistance to surface deformation of the PMMA nanocomposites may be due to a decrease in the free volume of the matrix associated with the formation of apparent physical cross-linking and entanglements. The T_g is linearly related to the microhardness
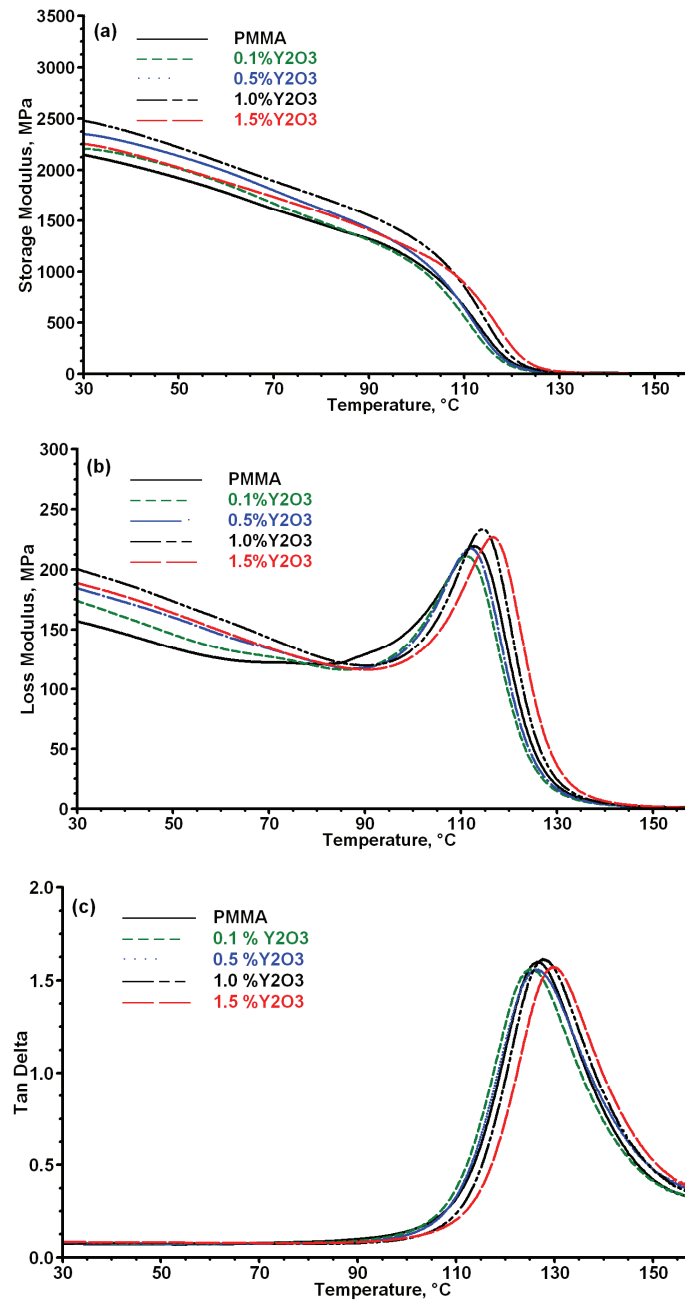
Fig. 3. Temperature dependence of a) the storage modulus, b) the loss modulus and c) tan δ for composites with different contents of Y_2O_3 (Eu^{3+}).

TABLE I. Results of DMA: E' and E" at 30 °C, values of T_g obtained by E' onset, E" maximum, tan δ maximum and microhardness (HV)

$c_{Y_2O_3}$ / %	E' / MPa	ΔE' / %	E" / MPa	$T_{g(E')}$ / °C,	$T_{g(E'')}$ / °C	$T_{g(\tan \delta)}$ / °C	HV / MPa
0	2147	–	156.9	100.68	112.70	126.40	254.87
0.1	2199	2.4	175.0	102.05	111.33	125.48	259.256
0.5	2352	9.5	184.6	103.29	111.84	126.20	269.812
1.0	2481	15.5	200.6	105.71	114.44	127.60	276.631
1.5	2256	5.1	189.0	108.47	116.73	129.70	280.139

according to Eq. (2). The correlations between HV and the T_g derived from the DMA curves by the E' onset, by the E" peak and by the tan δ peak are presented in Fig. 4. The fitting coefficients of these correlations, C, k and R^2 are presented in Table II for all three lines. The value of R^2 of the linear correlation between HV and $T_{g(E')}$ is the highest. This means that the E' onset is the most sensitive to local shear stresses and it exhibits the best linearity with microhardness.
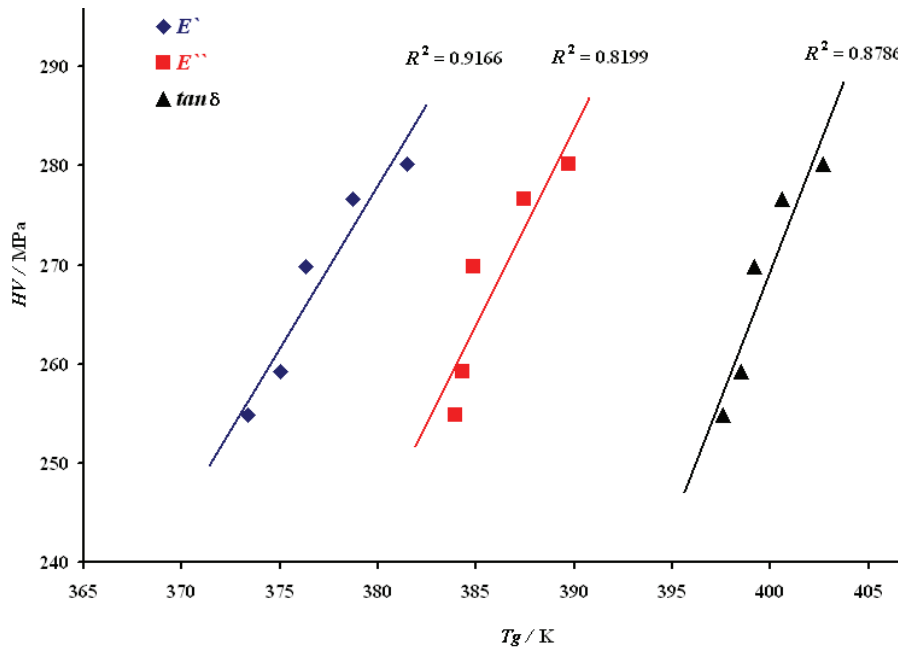
Fig. 4. Linear correlations of HV and T_g obtained from the DMA results – $T_{g(E')}$, $T_{g\,(E'')}$ and $T_{g(\tan \delta)}$

TABLE II. Fitting parameters of the T_g–HV correlations

Fitting parameter	$HV - T_{g(E')}$	$HV - T_{g(E'')}$	$HV - T_{g(\tan \delta)}$
C / MPa	–969.28	–1272.6	–1773.6
k / MPa K^{-1}	3.2825	3.9911	5.108
R^2	0.9166	0.8199	0.8786

CONCLUSIONS

The optical and mechanical properties of PMMA–Y_2O_3 (Eu^{3+}) nanocomposites were investigated. The luminescence spectra of the nanocomposites revealed that the phosphorescence of the powder remained on compositing and the emission intensity was enhanced as the content of the powder in the composites increased. The results obtained from the DMA showed that on the addition of nanopowder, the T_g of the PMMA increased, but only by a few degrees; this also suggests that the nanoparticles did not disperse individually but as aggregates. The microhardness number increased with increasing Y_2O_3 (Eu^{3+}) content in the PMMA nanocomposites. A nearly linear correlation between T_g and microhardness was obtained, because both properties are closely related to the cohesive energy density. This result is in accordance with previously reported results for amorphous glassy polymers, and now this linear correlation is applicable to similar composite configurations.

ИЗВОД

НАНОКОМПОЗИТ PMMA–Y_2O_3 (Eu^{3+}): ОПТИЧКА И МЕХАНИЧКА СВОЈСТВА

SALAH S. MUSBAH[1], ВЕСНА Ј. РАДОЈЕВИЋ[1], НАДЕЖДА В. БОРНА[1], ДУШИЦА Б. СТОЈАНОВИЋ[1], МИРОСЛАВ ДРАМИЋАНИН[2], АЛЕКСАНДАР Д. МАРИНКОВИЋ[1] и РАДОСЛАВ Р. АЛЕКСИЋ[1]

[1]*Технолошко−металуршки факултет, Унивезитет у Београду,, Карнеѓијева 4, Београд и* [2]*Институт за нуклеарне науке "Винча", п. пр. 522, Београд*

У оквиру овог рада презентовано је истраживање процесирања и карактеризације нанокомпозитног материјала поли(метил-метакрилат) (PMMA)–Y_2O_3 (Eu^{3+}). Узорци са различитим садржајем нанофосфора Y_2O_3 допираног са Eu јонима процесирани су у лабораторијском уређају за умешавање термопластичних полимера. Испитиван је утицај удела наночестица на оптичка и динамичко−механичка својства композита. Интензитет луминисцентног емисионог спектра композита расте са уделом нанофосфора. Резултати DMA показују да модул депоноване енергије, модул губитака и температура трансформације расту са повећањем удела наночестица. Микротврдоћа композита такође расте са повећањем удела наночестица у композиту и показује скоро линеарну зависност од температуре трансформације (T_g).

REFERENCES

1. D. R. Paul, L. M. Robeson, *Polymer* **49** (2008) 3187
2. S. C. Tjong, *Mater. Sci. Eng., R* **53** (2006) 73
3. Y. Osada, D. E. D. Rossi, *Polymer Sensors and Actuators*, Springer-Verlag, Heidelberg, Germany, 2000
4. S. M. Vaezi-Nejad, *Selected Topics in Advanced Solid State and Fiber Optic Sensors*, IEE, London, UK, 2000

5. R. J. Bartlett, R. Philip-Chandy, P. Eldridge, D. F. Merchant, R. Morgan, P. J. Scully, *Trans. Inst. Meas. Control* **22** (2000) 431

6. K. Mohomed, T. G. Gerasimov, H. Abourahma, M. J. Zaworotko, J. P. Harmon, *Mater. Sci. Eng., A* **409** (2005) 227

7. H. Eilers, B. M. Tissue, *Chem. Phys. Lett.* **251** (1996) 74

8. B. Bihari, H. Eilers, B. M. Tissue, *J. Lumin.* **75** (1997) 1

9. T. Ye, Z. Guiwen, Z. Weiping, X. Shangda, *Mater. Res. Bull*. **32** (1997) 501

10. Q. Li, L. Gao, D. Yan, *Nanostruct. Mater*. **8** (1997) 825

11. D. K. Williams, B. Bihari, B. M. Tissue, J. M. McHale, *J. Phys. Chem., B* **102** (1998) 916

12. A. Konrad, T. Fries, A. Gahn, F. Kummer, U. Herr, R. Tidecks, K. Samwer *J. Appl. Phys.* **86** (1999) 3129

13. T. Igarashi, M. Ihara, T. Kusunoki, K. Ohno, T. Isobe, M. Senna, *Appl. Phys. Lett.* **76** (2000) 1549

14. G. Wakefield, E. Holland, P. J. Dobson, J. L. Hutchison, *Adv. Mat*. **13** (2001) 1557

15. D. Matsuura, *Appl. Phys. Lett.* **81** (2002) 4526

16. T. L. Phan, M. H. Phan, N. Vu, T. K. Anh, S.-C. Yu, *Phys. Status Solidi, A* **201** (2004) 2170

17. N. Nguyen, M. H. Nam, T. K. Anh, L. Q. Minh, and E. Tanguy *Adv. Nat. Sci*. **6** (2006) 119

18. N. Vu, T. K. Anh, G.-C. Yi, W. Strek, *J. Lumin.* **122**–**123** (2007) 776

19. E. Ritzhaupt-Kleissl, J. Boehm , J. Hausselt, T. Hanemann, *Mater. Sci. Eng., C* **26** (2006) 1067

20. T. K. Anh, N. Vu, M. H. Nam, L. Q. Minh, *Adv. Nat. Sci.* **7** (2006) 63

21. K. S. Dhiraj, S. Chandra, J. B. Gruber, W. Gorski, M. Zhang, J. H. Shim, *J. Appl. Phys.* **105** (2009) 093105

22. T. K. Anh, P. Benalloul, C. Barthou, L. T. K. Giang, N. Vu, L. Q. Minh, *J. Nanomaterials* (2007) 2

23. B. Crist, in *Materials Science and Technology*, Vol. 1, E. L. Thomas, Ed., VCH, Weinheim, Germany, 1993, p. 427

24. F. J. Baltá-Calleja, A. Flores, F. Ania, in *Mechanical properties of polymers based on nanostructure and morphology*, G. H. Michler, F. J. Baltá-Calleja, Eds., Taylor and Francis, London, UK, 2005, p. 285

25. A. Flores, F. Ania, F. J. Baltá-Calleja, *Polymer* **50** (2009) 729

26. S. Fakirov, F. J. Balta-Calleja, M. Krumova, *J. Polym. Sci., B* **37** (1999) 1413

27. A. K. Adiyodi, X. Joseph, P. V. Jyithy, G. Jose, N. V. Unnikrishnan, *Materials Science – Poland* **27** (2009) 297

28. E. A. Turi, *Thermal Characterization of Polymeric Materials*, Vol. I, 2nd ed., Academic Press, New York, 1997, p. 980

29. M. Dixit, S. Gupta, V. Mathur, K. S. Rathore, K. Sharma, N. S. Saxena, *Chalcogenide Lett.* **6** (2009) 131

30. Z. Antic, R. Krsmanovic, I. Zekovic, M. D. Dramicanin, in *Proceeding of Electroceramics XI*, (2008), University of Manchester, Manchester, UK, Abstracts and CD proceedings, 2008, C-038-P.

Modelling the process of Al(OH)$_3$ crystallization from industrial sodium aluminate solutions using artificial neural networks

RADENKO SMILJANIĆ[1], DRAGICA LAZIĆ[2], MILADIN GLIGORIĆ[2], MILOVAN JOTANOVIĆ[2], ŽIVAN ŽIVKOVIĆ[2] and IVAN MIHAJLOVIĆ[3]*

[1]Alumina Factory Birač A.D., Zvornik, [2]Faculty of Technology in Zvornik, University of East Sarajevo, Bosnia and Herzegovina and [3]Technical Faculty in Bor, University of Belgrade, Serbia

Abstract: This paper presents an attempt to define the non-linear correlation dependence between the degree of decomposition of the aluminate solution, the average diameter of the crystallized gibbsite, the total Na$_2$O content in the obtained alumina and the specific utilization level of the process on the one hand and important input parameters of the process on the other. As input parameters having an influence on the process, the concentration of Na$_2$O (caustic), the caustic ratio and the crystallization ratio, the starting and final temperature of the process, the average diameter of the crystallization seed and the duration of the decomposition process were considered. As the result of measurements of these process parameters and the acquisition of the resulting output parameters of the process, a database with 500 data lines was obtained. To define the correlation dependence, with the aim of predicting the process parameters of the decomposition process of the sodium aluminate solution, the artificial neural network (ANN) methodology was applied.

Keywords: aluminate solution; crystallization; modelling; artificial neural networks.

INTRODUCTION

In 1888, Karl Josef Bayer developed and patented a process which has become the cornerstone of the aluminium production industry worldwide.[1] The Bayer process involves the digestion of crushed bauxite in a concentrated sodium hydroxide (caustic) solution at temperatures of up to 270 °C.[2] The temperature depends on the mineral composition of the bauxite.[3] Under these conditions, the majority of the aluminium bearing species from the ore are dissolved leaving an insoluble residue (red mud) composed primarily of quartz, iron oxides, sodium

---

1163

aluminosilicates, calcium carbonate and titanium dioxide, which is removed by settling/filtration.[3]

The dissolved aluminium is precipitated entirely in the form of gibbsite (Al(OH)$_3$) with the characteristics of the final grains depending on the initial (seeding) material used and the conditions of the process.[4,5] This is achieved by cooling the solution to 52–55 °C and seeding with gibbsite grains, essentially reversing the initial dissolution process. The crystallization of aluminium hydroxide (Al(OH)$_3$) from caustic aluminate solution is the rate determining step within the Bayer cycle, which is used for alumina production.[6,7] In addition, due to the complexity of Bayer liquor speciation, the mechanisms of Al(OH)$_3$ crystallization are still not completely understood and are the subject of considerable research effort.[8]

The kinetics of gibbsite crystallization from the caustic sodium aluminate solution, as well as the size and the shape of the obtained particles, depend on the following process parameters: temperature, alumina/caustic ratio, amount and size distribution of the crystallization seeds, stirring speed and the presence of activation ions added to the solution.[9–12]

Most of the results published recently concerning gibbsite crystallization from the sodium aluminate solutions were obtained from laboratory investigations using the synthetic solutions,[9,10,13] in this way only simulating the conditions in the industrial Bayer process.[14] The industrial conditions of gibbsite crystallization are much more complex than those in laboratory experiments. At the same time, the process of gibbsite crystallization is much slower compared with other processes in the Bayer technology of alumina production,[6] which is another reason why this process demands further analysis under industrial conditions.

The main motive for the investigations presented in this paper was to draw conclusions about the possibilities of predicting the results of gibbsite crystallization from caustic sodium aluminate solutions under industrial conditions. The outputs of the process, the possibilities of prediction of which were analysed, are degree of decomposition of the solution, average diameter of the obtained gibbsite grains; content of Na$_2$O in the produced alumina and the specific utilization level of the process. As input parameters the concentration of caustic soda in the starting solution and its caustic ratio, the crystallization ratio of the solution (ratio between the content of Al(OH)$_3$ introduced into the solution in pulp form as crystallization seeds and the Al(OH)$_3$ content in the caustic sodium aluminate solution); the starting and the final temperatures of the process; the average diameter of the crystallization seeds and the duration of the process were considered. Defining the correlation dependence between the outputs and the inputs of this industrial process, with significant values of the correlation coefficient (R^2), presents a possibility for improved management of gibbsite crystallization from sodium aluminate solutions, as a part of the Bayer technology for alumina production.

THEORETICAL BACKGROUND AND THE METHODOLOGY OF THE INVESTIGATIONS

Parameters influencing the decomposition process of the caustic sodium aluminate solutions

The precipitate from a dilute aluminate solution is Bayerite, α-Al(OH)$_3$, and from a saturated solution, Gibbsite, Al(OH)$_3$.[8] The content of Na$_2$O (caustic) in the starting industrial solutions ranges between 150 and 160 g dm^{-3} with a caustic ratio (Na$_2$O/Al$_2$O$_3$ molar ratio) in the range 1.45–1.60. The starting temperature is in the range 60–70 °C, while the temperature at the end of the decomposition process ranges between 50 and 55 °C, which were reported to be the optimal temperatures of the process.[9,15] The amount of added crystallization seeds (CS) at the beginning of the process is determined by the crystallization ratio (CR), which presents the relationship: $\eta = $ Al$_2$O$_{3(CS)}$/Al$_2$O$_{3(AS)}$ (where AS is the content of Al$_2$O$_3$ in the aluminate solution). Increasing CR positively influences the rate of the process, as does increasing the CS average diameter of the CS, under constant CR.[9,10,12,14]

Under industrial conditions, CR is in the range 2–2.5, with an average particle diameter of 100–120 μm. With time, the rate of the process decreases and the time required for 80 % of the Al(OH)$_3$ to precipitate is about 70 h under laboratory conditions.[9,12,16] Under industrial conditions, the degree of decomposition is even lower, ranging between 45 and 55 %, during 70–80 h. In addition, if producing coarse alumina (Sandy type), the granulation of the final product should be above 100 μm with an as low as possible content of Na$_2$O$_{(total)}$ ($\leq$ 0.4 %).[7]

RESULTS AND DISCUSSION

Modelling the dependence between the outputs (results) and the inputs (parameters of the process)

Industrial practice of the alumina production suggests that the input parameters of the process should be controlled on a daily basis because all have an influence on the kinetics of the decomposition of the sodium aluminate solution, the granulation of the produced Al(OH)$_3$ and the Na$_2$O content in the resulting alumina. Their synergetic action results in the output of the process, which determines its efficiency and effectiveness.

For the modelling of technological processes with established mathematical dependences between its results (dependent variables) and the predictors (process parameters), multiple linear regression analysis (MLRA), nonlinear regression (NLR) and artificial neural networks (ANNs) are the most employed methods.[17–23] Comparative analysis of the results of these statistical methods, indicate that the best results are usually obtained using ANNs.[20,21] For this reason, this methodology was used in the investigations presented in this paper.

Data from the factory Birač, Zvornik (Bosnia and Herzegovina), were used for modelling the process of the decomposition of aluminate solutions. The data were collected during the years 2008–2009 by measuring the input and output process parameters under stable operation of the production line. A total number of 500 data sets were collected this way, comprising the following:

a) Input parameters of the process. the Na$_2$O (caustic) content in the solution (g dm^{-3}) – X_1; the caustic ratio (α_k) of the solution – X_2; the crystallization

ratio – X_3; the starting temperature of the solution (°C) – X_4; the final temperature of the solution (°C) – X_5; the average diameter of the crystallization seed (μm) – X_6 and the duration of the crystallization process (h) – X_7.

b) Output parameters of the process. degree of decomposition of the solution (%) – Y_1; average diameter of the crystallized gibbsite (μm) – Y_2; total Na_2O content in the calcined alumina (%) – Y_3; and the specific level of solution utilization (t m^{-3}) – Y_4.

The values of the measured input parameters of the technological process (X_1–X_7) and the process quality indicators – outputs of the process (Y_1–Y_4), are presented in Table I in the form of the results of descriptive statistics.

TABLE I. Values of the input (X_i) and the output (Y_i) variables of the process of industrial sodium aluminate solution decomposition – descriptive statistics of 500 data sets

Parameter	Range	Minimum	Maximum	Mean		Standard deviation	Variance
				Statistic	Standard error		
X_1	12.330	144.000	156.330	150.944	0.076	1.703	2.900
X_2	0.180	1.470	1.650	1.530	0.001	0.033	0.001
X_3	3.410	1.260	4.670	2.285	0.030	0.662	0.438
X_4	11.000	58.000	69.000	64.656	0.054	1.199	1.437
X_5	22.200	36.300	58.500	50.582	0.184	4.112	16.909
X_6	37.710	87.220	124.930	106.473	0.381	8.510	72.416
X_7	76.000	49.000	125.000	77.080	0.624	13.944	194.426
Y_1	24.330	32.300	56.630	46.658	0.124	2.775	7.699
Y_2	37.630	86.520	124.150	107.703	0.382	8.552	73.135
Y_3	0.270	0.220	0.490	0.309	0.002	0.055	0.003
Y_4	0.039	0.052	0.091	0.076	0.000	0.005	0.000

It should be noted that one of the input parameters (X_2) has a small variance (Table I). However, it presents the caustic ratio of the solution that is one of the most important parameters of the Bayer process; thus, it cannot be omitted from the analysis. A small change in X_2 leads to a considerable change in the value of the output parameters, especially the degree of decomposition of the solution (Y_1).

For defining the correlation dependence in the form: outputs of the process (Y_1–Y_4) as function of the inputs of the process (X_1–X_7), a bivariate correlation analysis was performed. As the result of this analysis, the Pearson correlation (*PC*) coefficients with the corresponding statistical significance were calculated (Table I-S, Supplementary material).

To finally define the dependence of the output parameters as functions of the input parameters, using linear regression analysis (LRA) with an acceptable level of fitting (strong correlation), the value of *PC* must be above 0.5 or less than –0.5 with statistical significance ($p \leq 0.05$).[24,25]

The data presented in Table I-S reveals that this constraint is attained only in following cases: Y_1 (degree of aluminate solution decomposition) and X_5 (final

temperature of the process) with $PC = -0.720$ and $p = 0.000$ and X_7 (duration of the process) with $PC = 0.661$ and $p = 0.000$; Y_2 (average diameter of the crystallized gibbsite) and X_6 (average diameter of the crystallization seed) with $PC = 0.921$ and $p = 0.000$; Y_3 (Na$_2$O – total in the produced alumina) and X_2 (caustic ratio) with $PC = -0.602$ and $p = 0.000$; Y_4 (specific utilization level) and X_5 (final temperature of the process) with PC $= -0.583$ and $p = 0.000$, and X_7 (duration of the process) with $PC = 0.555$ and $p = 0.000$. This was also the case for the following interdependence between outputs of the process: Y_1 (degree of aluminate solution decomposition) and Y_4 (specific utilization level of the process) with $PC = 0.900$ and $p = 0.000$.

Considering that only a small number of variables had an acceptable level of correlation (PC) and statistical significance ($p \leq 0.05$), it was concluded that the MLRA approach should not be considered as an adequate tool for modelling the investigated process because it would result in inadequate data fitting. In such cases, ANNs usually offer much better results.[20,21]

ANN Modelling

An artificial neural network is a network with nodes or neurons analogous to biological neurons.[26,27] ANNs have become a powerful tool for many complex applications, such as function approximation, optimization, non-linear system identification and pattern recognition. Artificial neural networks have seen an explosive growth in the last decade and are still being developed at a breathtaking pace. These methods represent a class of tools that can facilitate the exploration of large systems in ways not previously possible. Although neural networks originated outside the field of statistics, and have even been seen as an alternative to statistical methods in some circles, there are sings that this viewpoint is making way for an appreciation of the ways in which neural networks complement classical statistics.[28]

Owing to several attractive characteristics, ANNs have been widely used in chemical engineering applications, such as steady state and dynamic process modelling, process identification, yield maximization, non-linear control, and fault detection and diagnosis.[29–32] The most widely utilized ANN paradigm is a multi-layered perception (MLP) that approximates non-linear relationships existing between an input set of data (causal process variables) and the corresponding output (dependent variables) data set. A three layer MLP with a single intermediate (hidden) layer housing a sufficiently large number of neurons (also termed nodes or processing elements) can approximate (map) any non-linear computable function to an arbitrary degree of accuracy. It learns the approximation through a numerical procedure called "network training" wherein network parameters (weights) are adjusted iteratively so that the network, in response to the input patterns in an example set, accurately produces the corresponding outputs. A number of algo-

rithms,[28] each possessing certain positive characteristics, are employed to train an MLP network, *e.g*., the most popular error back-propagation (EBP), quickprop and resilient back-propagation (RPROP).[33]

Error back-propagation has been applied to a wide variety of practical problems and it has proven very successful in its ability to make non-linear relationships. A typical back-propagation net, which was used for modelling procedure described in this paper, is presented in Fig. 1.

Hidden layer activation function: Sigmoid

Output layer activation function: Sigmoid
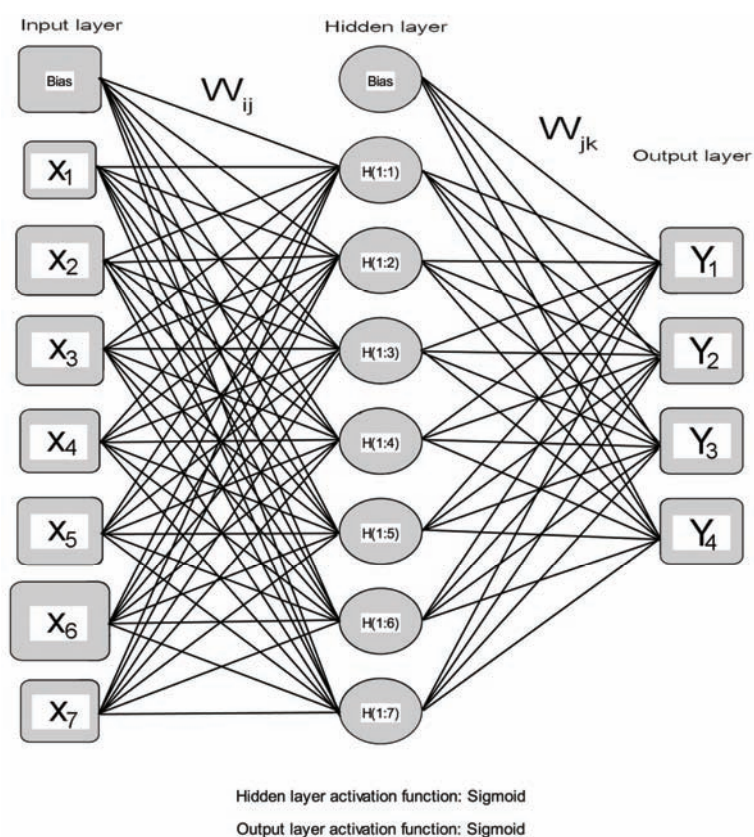
Fig. 1. The ANN architecture for the determination of Y_1, Y_2, Y_3 and Y_4 in the industrial process of decomposition of sodium aluminate solutions.

Generally, a MLP–EBP neural network contains one input layer, one or more hidden layers, and one output layer. Each layer comprises one or more neurons. The neurons are interconnected using weight factors. A neuron in a given layer receives information from all the neurons in the preceding layer (Fig. 1). It sums information, weighted by factors corresponding to the connection and the bias of the network, and transmits this sum to all neurons of the next layer using a mathematical function.[21,23]

As shown in the ANN architecture depicted in Fig. 1, the network used for modelling in this work consisted of three layers of neurons. The layers described as input, hidden and output layers comprise i, j and k numbers of processing nodes, respectively. Each node in the input (hidden) layer is linked to all the nodes in the hidden (output) layer using weighted connections. In addition to the i and j numbers of input and hidden nodes, the ANN architecture also houses a bias node (with a fixed output + 1) in its input and hidden layers and they provide additional adjustable parameters (weights) for model fitting. The number of the nodes i in the ANN network input layer is equal to the number of inputs in the process and the number of output nodes k equals the number of the process outputs. However, the number of hidden nodes j is an adjustable parameter the magnitude of which is determined by issues such as the desired approximation and generalization capabilities of the network model.[26,34]

The back-propagation algorithm modifies the network weights to minimize the mean squared error between the desired and the actual outputs of the network. Back-propagation uses supervised learning in which the inputs, as well as desired the outputs, are controlled and selected.[27]

The use of an ANN usually comprises three phases. First is the training phase, which is facilitated on 70 to 80 % randomly selected data from the starting data set. During this phase, the correction of the weighted parameters of the connections is achieved through the number of iterations to attain the minimal mean squared error between the calculated and measured outputs of the network. During the second phase, the remaining 20–30 % of the data is used for testing the "trained" network. In this phase, the network uses the weighted parameters determined during the first phase. These data lines, excluded during the teaching of the network, are now incorporated in it as new input values X_i which are then transformed to new outputs Y_k. The third phase is the validation of the network on a new data set. This data set consists of already measured data or data from new experimental measurements. The validation phase presents the final level of successful or unsuccessful prediction using the network developed in the previous two stages on a new database.[20,21]

Accordingly, ANN methodology was applied for modelling the process of sodium aluminate solution dissociation under industrial conditions using available data, the descriptive statistics of which is presented in Table I. The assembly of 500 input and output data sets was divided into two groups. The first group, which was used to train the network, consisted of 350 (70 %) randomly selected data lines, while the second group consisted of the remaining 150 (30 %) remaining from the starting database and was used to test the network.

For the development of the relational ANN configuration (Fig. 1), previously defined input parameters X_1–X_7 and output parameters Y_1–Y_4 were used as the elements of the network architecture. The ANN presented in Fig. 1 consists of

three layers: input, output and hidden layer. The neurons of the input layer are presenting the information on input process parameters, X_i (independent variables), while the neurons of the output layer generate the output information, *i.e.*, process quality indicators, Y_k (dependent variables). In the present case, $i = 7$ and $k = 4$. In addition, the best results of the model fitting were obtained with 7 neurons in hidden layer, *i.e.*, $j = 7$. The appropriate number of neurons in the hidden layer was determined by training and testing several networks. This process is necessary because too few neurons in the hidden layer produce high training and testing errors because of underfitting and statistical bias. On the contrary, too many hidden layer neurons leads to a low training error but high testing error as a result of overfitting and high variance. In this study, an iterative approach was employed to determine the optimal number of hidden layer neurons, yielding minimum model prediction error on the "test data set". In this way, 13 different network architectures were tried, ranging from 2 to 14 neurons in the hidden layer. The best results were obtained with the network architecture presented in Fig. 1.

The input to any neuron j, in the hidden layer, without its bias, is given by:

$$I_i = \sum W_{ij} X_j \tag{1}$$

where W_{ij} is the weight of the interconnection between neuron i and j and X_j represents the signal at the connection concerned.

An important component of an ANN is its activation function appearing after the input layer. Each hidden node and output node applies the activation function to its net input. For the case in question in this paper, a log sigmoid activation function was chosen. This function was most frequently used one for modelling similar systems:[20,21,34]

$$F(x) = 1/(1 - e^{-x}) \tag{2}$$

The overall transfer function of a neuron is thus structured as:

$$O_j = A_j = f(\Sigma W_{ij} X_j) \tag{3}$$

where O_j is the output of the neuron, A_j is its activation, X_j is the input to the neuron in the hidden layer, which is identical to the output of the preceding neuron with index j of the observed element.

The aim of the learning process is to minimize the overall network error:

$$E = 1/2\Sigma(y_j - O_j)^2 \tag{4}$$

where y_j is the target output value.

Adaptation of the weights is affected according to the equation:[35]

$$\Delta W_{ij} = W_{ij}(t + 1) - W_{ij}(t) = -\alpha \partial E / \partial W_{ij} \tag{5}$$

where α is defined as the learning rate. This results in:

$$\Delta W_{ij} = \alpha \beta_j X_j \tag{6}$$

where the local error of a hidden element is calculated *via*:

$$\beta_j = f(I_j)\Sigma\beta_k W_{jk} \tag{7}$$

The β_k components represent the errors of the elements in the subsequent layer, while W_{jk} represent the connection weights for these elements. The error of a neuron of the output layer is obtained *via*:

$$\beta_k = f(I_k)(y_k - O_k) \tag{8}$$

The error is first calculated and then back-propagated into the hidden layer located before the output layer.

The connection weights can then be modified according to the calculated ΔW_{ij} in the concluding stage of this process. To resolve a problem of a local minimum of the error space, a momentum term was introduced. The equation for the adoption of a weight is modified as follows:

$$\Delta W_{ij}(t) = \alpha\beta_j X_j + \mu\Delta W_{ij}(t-1) \tag{9}$$

where μ is defined as the momentum, t is the current learning step and $(t-1)$ the previous learning step.

The training used in this study is summarized in Fig. 2, for the benefit of the Y values in the investigated process.

In this way, in the training phase of the network, the necessary number of iteration was performed until the error between the measured outputs of the decomposition process of an industrial sodium aluminate solution (Y_1–Y_4) and the calculated values were not minimized and remained constant. The obtained results from the training stage can be evaluated by comparison of the calculated Y_1–Y_4 values with the measured ones. The obtained coefficients of determination, R^2: 0.729, 0.868, 0.785 and 0.732 for Y_1, Y_2, Y_3 and Y_4, respectively, present satisfactory fitting of the calculated and measured values obtained during the training phase and can be used in subsequent testing and validation.

After the development of this kind of "trained" network, the testing stage was performed using the second part of the database (a total of 150 vectors). In this phase, all 13 hidden layer structures were involved until a minimum model prediction error was obtained. The ANN structure presented in Fig. 1, with seven neurons in the hidden layer, resulted in the minimum model prediction error. During the ANN testing phase, the calculated coefficients of determination (R^2) were slightly increased in comparison with the training phase and equalled: 0.801, 0.91, 0.857 and 0.802, respectively, for Y_1, Y_2, Y_3 and Y_4. A comparative presentation of the measured and the values calculated using the ANN approach for the investigated process is presented in Figs. 1-S and 2-S, Supplementary material. The improvement in the fit obtained on the test set compared to that obtained on the training set suggests that most of the extreme points that are more difficult to model were in the training set. The selection of the variables for the

training and the testing stage was performed using a random number generator and hence, was not subjectively influenced.
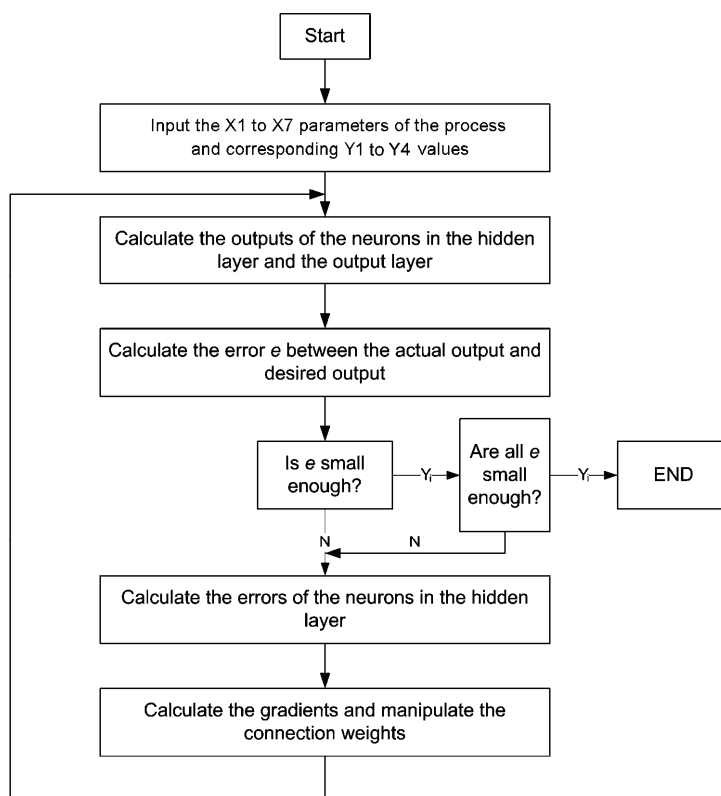
Fig. 2. Flow chart of the back-propagation learning algorithm.

According to the results presented in Figs. 1-S and 2-S, it could be concluded that the output variable Y_2 (average diameter of the crystallized gibbsite) has the best modelling potential, while other output variables, Y_1; Y_3 and Y_4, have to some extent smaller potentials for modelling. However, all the calculated coefficients of determination (R^2) were large enough to advocate that the investigated process can be adequately modelled using the approach presented in this paper.

Furthermore, the obtained results of the non-linear correlation defined using the ANN methodology enables a ranking of each individual input parameter (X_1–X_7) according to the degree of significance of their influence on the output results (Y_1–Y_4), Fig. 3.

The significances of the influence of the input parameters on the decomposition process of the industrial sodium aluminate solution are: $X_6 = 0.26$; $X_2 = = 0.175$; $X_3 = 0.165$; $X_5 = 0.155$; $X_4 = 0.105$; $X_7 = 0095$ and $X_1 = 0045$. The

obtained results could be quite important for managing the process of decomposition of industrial sodium aluminate solutions, concerning the minimization of Y_3, maximization of Y_1 and Y_4 and optimization of the Y_2 values.
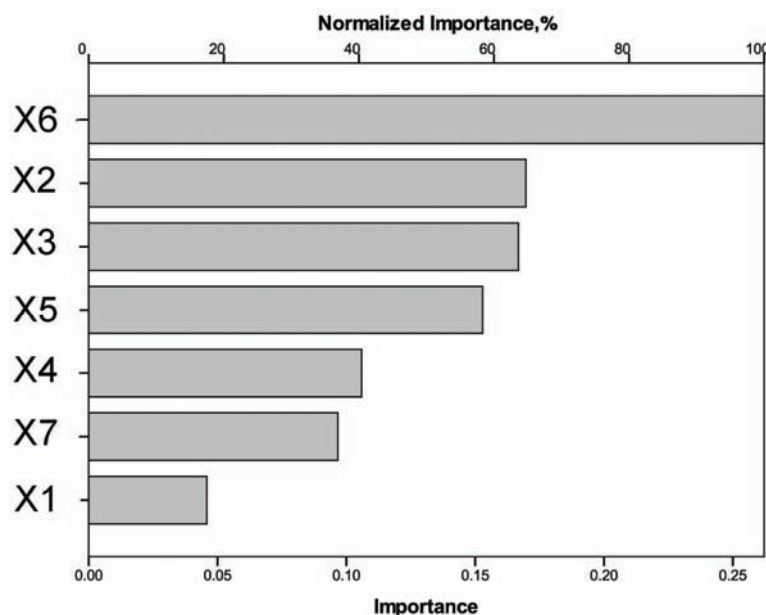
Fig. 3. Degree of significance of the individual input parameters (X_1–X_7) on the values of the output parameters (Y_1–Y_4).

CONCLUSIONS

Values of the degree of decomposition of an industrial sodium aluminate solution, the average diameter of crystallized gibbsite grains, the total Na$_2$O content in calcined alumina and the specific level of solution utilization (Y_1 to Y_4, respectively), under industrial conditions in the factory Birač, Zvornik (Bosnia and Herzegovina) were determined using MLRA methodology. The values of the coefficient of determination (R^2) were 0.801, 0.91, 0.857 and 0.802, respectively, for Y_1, Y_2, Y_3 and Y_4. These results indicated a highly acceptable degree of fitting of the dependence $Y_i = f(X_1$–$X_7)$, obtained using an ANN procedure as a part of the SPSS software application, version 18 (PASW Statistics). The selected ANN structure consisted of 350 (70 %) samples for training and 150 (30 %) for testing the network.

The significances of the influence of the input parameters of the process of the decomposition of the industrial sodium aluminate solution are: $X_6 = 0.26$, $X_2 = 0.175$, $X_3 = 0.165$, $X_5 = 0.155$, $X_4 = 0.105$, $X_7 = 0095$ and $X_1 = 0045$.

The variables with highest influence on the process output are the average diameter of the crystallization seeds and the caustic ratio of the solution. In addi-

tion to these parameters, the starting and final temperatures of the solution also have a large influence. The remaining inputs of the process demonstrated less importance on outcome of the process (Y_i), under industrial conditions of the Bayer technology for alumina production. The defined elements of the ANN structure can be applied generally to conditions in any factory that uses the Bayer technology for alumina production.

Since the training of the ANN structure could be facilitated on 70 to 80 % randomly selected data from the starting data set, further research will include the possibility of ANN training with different training set sizes. In this way, the influence of increasing the training set size from 70 to 75 or 80 % on the outcome of the model will be investigated.

SUPPLEMENTARY MATERIAL

Table I-S and Figs. 1-S and 2-S are available electronically at http://www.shd.org.rs/ /JSCS/, or from the corresponding author on request.

И З В О Д

МОДЕЛОВАЊЕ ПРОЦЕСА КРИСТАЛИЗАЦИЈЕ Al(OH)$_3$ ИЗ ИНДУСТРИЈСКОГ НАТРИЈУМ-АЛУМИНАТНОГ РАСТВОРА ПОМОЋУ ВЕШТАЧКИХ НЕУРОНСКИХ МРЕЖА

РАДЕНКО СМИЉАНИЋ[1], ДРАГИЦА ЛАЗИЋ[2], МИЛАДИН ГЛИГОРИЋ[2], МИЛОВАН ЈОТАНОВИЋ[2], ЖИВАН ЖИВКОВИЋ[2] и ИВАН МИХАЈЛОВИЋ[3]

[1]Фабрика алуминијума Бирач А.Д., Зворник, [2]Универзитет у Источном Сарајеву, Технолошки факултет у Зворнику, Босна и Херцеговина и [3]Универзитет у Београду, Технички факултет у Бору

У овом раду је приказан покушај дефинисања нелинеарне корелационе зависности између степена разлагања алуминатног раствора, просечне величине пречника кристалисаног зрна гибсита, укупног садржаја Na$_2$O у добијеној глиници и специфичног степена искоришћења процеса на једној страни, и важних улазних параметара процеса, на другој. Као улазни параметри који утичу на процес у обзир су узети: концентрација каустичног Na$_2$O, каустични однос, кристализациони број, полазна и крајња температуре процеса разлагања, просечна величина пречника кристализационих центара и трајање процеса кристализације. Као резултат мерења и контроле наведених технолошких параметара, као и бележења резултујућих излазних величина, формирана је база података са 500 линија уноса. Како би се дефинисале корелације са циљем предвиђања технолошких параметара процеса разлагања алуминатних раствора, коришћена је метода вештачких неуронских мрежа.

(Примљено 31. октобра, ревидирано 30. децембра 2010)

REFERENCES

1. T. G. Pearson, *The Chemical Background of the Aluminium Industry,* The Royal Institute of Chemistry, London, England, 1957, p. 103
2. A. R. Hind, S. K. Bhargava, S. C. Grocott, *Colloids Surf., A* **146** (1999) 359
3. I. Djuric, I. Mihajlovic, Z. Zivkovic, *Can. Metall. Q.* **49** (2010) 209
4. D. Lazić, Ž. Živković, D. Grujičić, *J. Min. Metall., B* **34** (1998) 111
5. X. Zhi-Peng, L. Ji-Wei, Y. Huang, Y. B. Cheng, *Mater. Lett.* **57** (2003) 2501

6. F. Habashi, *Handbook of Extractive Metallurgy*, vol. 1, Wiley-VCH, Weinheim, Germany, 1997, p. 1143
7. F. Habashi, *J. Min. Metall., B* **45** (2009) 1
8. H. Li, J. Addai-Mensah, C. J. Thomas, R. A. Gerson, *J. Cryst. Growth* **279** (2005) 508
9. I. Seyssiecq, S. Veesler, R. Boistelle, J. M. Lamerant, *Chem. Eng. Sci.* **53** (1998) 2177
10. I. Blagojević, D. Blečić, R. Vasiljević, *J. Cryst. Growth* **200** (1999) 558
11. J. Li, C. A. Clive, J. Addai-Menach, *J. Cryst. Growth* **219** (2000) 451
12. G. H. Chen, Q. Y. Chen, Z. L. Yin, Z. M. Yin, *Trans. Nonferrous Met. Soc. China* **16** (2006) 483
13. Z. Wang, S. Bi, Y. Yang, Z. Zuan, *J. Cryst. Growth* **274** (2005) 218
14. S. J. Freij, G. M. Parkinson, *Hydrometallurgy* **78** (2005) 246
15. B. Dash, B. C. Tripathy, I. N. Bhattacharya, S. C. Das, C. R. Mishra, B. S. Pani, *Hydrometallurgy* **88** (2007) 121.
16. S. Cao, Y. Zhang, Y. Zhang, *Hydrometallurgy* **98** (2009) 298
17. E. Sayan, M. Bayramoglu, *Hydrometallurgy* **57** (2000) 181
18. G. Bloch, T. Denoeux, *ISA Trans.* **42** (2003) 39
19. M. Paliwal, U. A. Kumar, *Expert Syst. Appl.* **36** (2009) 2
20. D. Liu, Z. Yuan, S. Liao, *Expert Syst. Appl.* **36** (2009) 10397
21. Ž. Živković, I. Mihajlović, Dj. Nikolić, *Serb. J. Manage.* **4** (2009) 143
22. Ž. Živković, N. Mitevska, I. Mihajlović, Đ. Nikolić, *J. Min. Metall., B* **45** (2009) 23
23. P. Đorđević, I. Mihajlović, Ž. Živković, *Serb. J. Manage.* **5** (2010) 189
24. R. N. Meroney, *J. Wind Eng. Ind. Aerodyn.* **77** and **78** (1998) 543
25. W. D. Nelson, K. Viele, B. C. Lynn, *Bioinformatics: Application Note* **24** (2008) 2103
26. H. Demuth, M. Beale, *Neural Network Toolbox for use with MATLAB*, Natick, MA, USA, 2002, p. 32
27. G. Dreyfus, *Neural Networks, Methodology and Applications*, Springer-Verlag, Berlin, Germany, 2004, p. 199
28. R. C. Eberhart, R. W. Dobbins, *Neural Network PC Tools: A Practical Guide*, Academic Press, New York, USA, 2002, p. 10
29. D. R. Baughman, Y. A. Liu, *Neural Networks in Bioprocessing and Chemical Engineering*, Academic Press, New York, USA, 1995
30. S. S Tambe, B. D Kulkarni, P. B. Deshpande, *Elements of Artificial Neural Networks with selected applications in Chemical Engineering and Chemical and Biological Sciences*, Simulations & Advanced Controls, Louisville, KY, 1996
31. A. B. Bulsari, *J. Syst. Eng*. **4** (1994) 131
32. K. Huang, X. L. Zhan, F. Q Chen, W. Lu, *Chem. Eng. Sci.* **58** (2003) 58
33. G. Stephanopoulos, C. Han, *Comp. Chem. Eng.* **20** (1996) 743
34. M. Riedmiller, H. Braun, in *Proceedings of the IEEE Int. Conf. On Neural Networks*, San Fransisco, CA, 1993
35. B. Zhang, J. Li, Q. Chen, G. Chen, *Miner. Eng*. **22** (2009) 853
36. H. S. Meradi, S. Bouhousche, M. Lahreche, in *Proceedings of World Acad. Sci. Eng. Technol.,* Vol. 17, 2006, p. 319.

Modelling the process of Al(OH)$_3$ crystallization from industrial sodium aluminate solutions using artificial neural networks

RADENKO SMILJANIĆ[1], DRAGICA LAZIĆ[2], MILADIN GLIGORIĆ[2], MILOVAN JOTANOVIĆ[2], ŽIVAN ŽIVKOVIĆ[2] and IVAN MIHAJLOVIĆ[3]*

[1]Alumina Factory Birač A.D., Zvornik, [2]Faculty of Technology in Zvornik, University of East Sarajevo, Bosnia and Herzegovina and [3]Technical Faculty in Bor, University of Belgrade, Serbia

TABLE I-S. Correlation matrix for the input (X_1–X_7) and the output (Y_1–Y_4) variables of the industrial sodium aluminate solution dissociation process (number of data points for each variable was 500)

Parameter	Correlation	X_1	X_2	X_3	X_4	X_5	X_6	X_7	Y_1	Y_2	Y_3	Y_4
X_1	Pearson	1										
	Sig. (2-tailed)											
X_2	Pearson	–.319[a]	1									
	Sig. (2-tailed)	.000										
X_3	Pearson	–.149[a]	.361[a]	1								
	Sig. (2-tailed)	.001	.000									
X_4	Pearson	–.150[a]	.209[a]	–.030	1							
	Sig. (2-tailed)	.001	.000	.500								
X_5	Pearson	.090[b]	–.252[a]	–.489[a]	.214[a]	1						
	Sig. (2-tailed)	.045	.000	.000	.000							
X_6	Pearson	.115[a]	–.084	.458[a]	–.040	.066	1					
	Sig. (2-tailed)	.010	.061	.000	.372	.139						
X_7	Pearson	–.125[a]	.159[a]	.421[a]	–.156[a]	–.716[a]	–.147[a]	1				
	Sig. (2-tailed)	.005	.000	.000	.000	.000	.001					

* Corresponding author. E-mail: imihajlovic@tf.bor.ac.rs

SMILJANIĆ *et al.*

TABLE I-S. Continued

Para-meter	Correlation	X_1	X_2	X_3	X_4	X_5	X_6	X_7	Y_1	Y_2	Y_3	Y_4
Y_1	Pearson	−.143[a]	.073	.447[a]	−.108[b]	−.720[a]	−.227[a]	.661[a]	1			
	Sig. (2-tailed)	.001	.101	.000	.016	.000	.000	.000				
Y_2	Pearson	.124[a]	−.121[a]	.424[a]	−.016	.079	.921[a]	−.129[a]	−.222[a]	1		
	Sig. (2-tailed)	.005	.007	.000	.729	.079	.000	.004	.000			
Y_3	Pearson	.307[a]	−.602[a]	−.121[a]	−.489[a]	.031	.098[b]	.006	−.011	.110[b]	1	
	Sig. (2-tailed)	.000	.000	.007	.000	.490	.029	.886	.805	.014		
Y_4	Pearson	.149[a]	−.328[a]	.270[a]	−.198[a]	−.583[a]	−.173[a]	.555[a]	.900[a]	−.154[a]	.250[a]	1
	Sig. (2-tailed)	.001	.000	.000	.000	.000	.000	.000	.000	.001	.000	

[a]Correlation is significant at the 0.01 level (2-tailed); [b]correlation is significant at the 0.05 level (2-tailed)

(a)
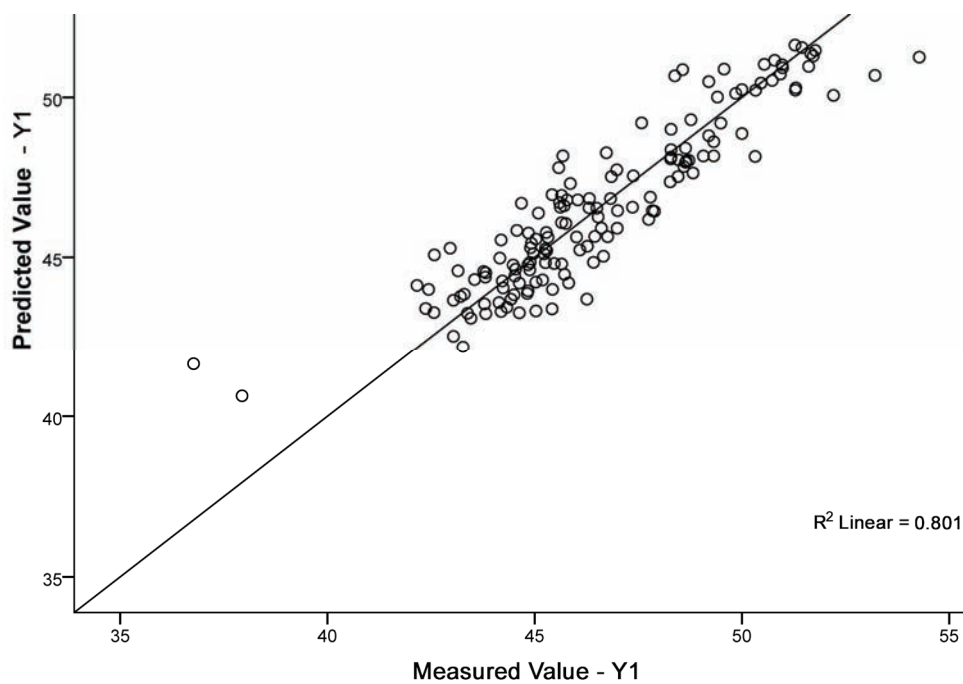
Fig. 1-S. Comparison of the measured and the values calculated using the ANN: a) the degree of decomposition of the industrial sodium aluminate solution (Y_1).
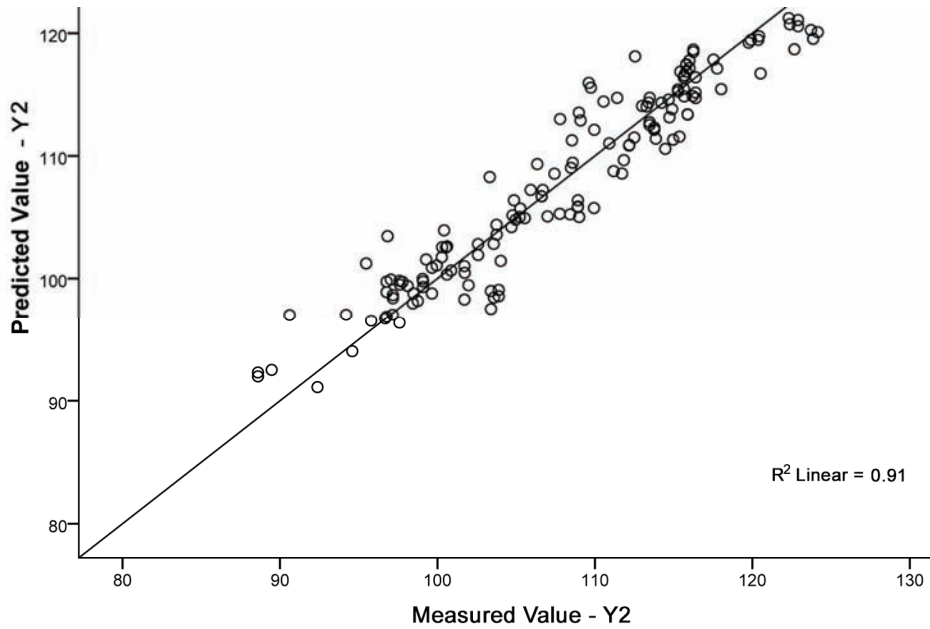
(b)

Fig. 1-S (continued). Comparison of the measured and the values calculated using the ANN:
b) average diameter of the gibbsite grains (Y_2).
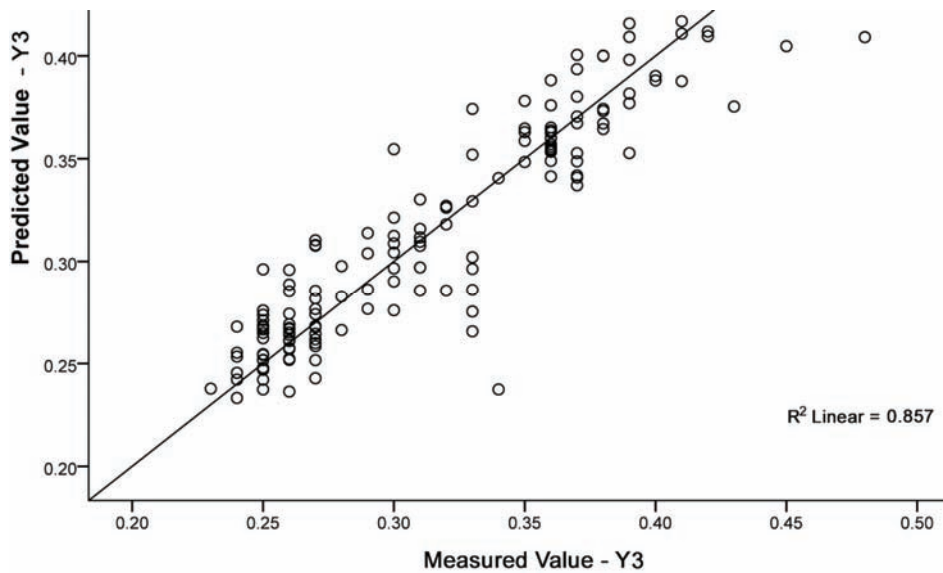
(a)

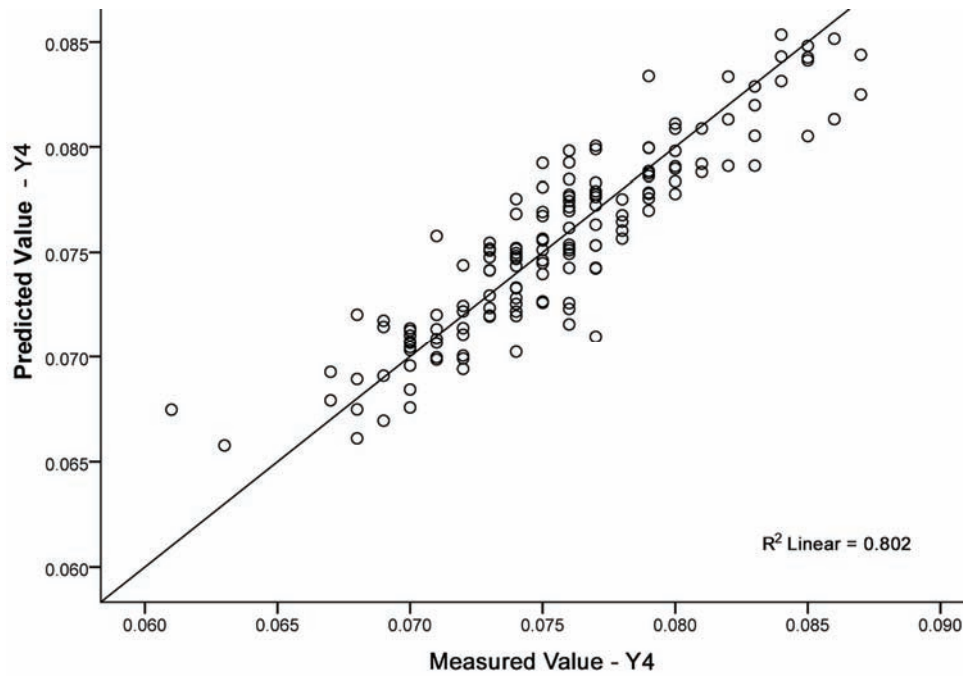Fig. 2-S. Comparison of the measured and the values calculated using the ANN:
a) Na$_2$O (total) content in the alumina (Y_3).

(b)

Fig. 2-S (continued). Comparison of the measured and the values calculated using the ANN: b) specific utilization level of the process (Y_4).

Distribution and forms of manganese in vertisols of Serbia

JELENA Ž. MILIVOJEVIĆ[1], IVICA G. ĐALOVIĆ[2*#], MIODRAG Ž. JELIĆ[3], SREĆKO R. TRIFUNOVIĆ[4§], DARINKA M. BOGDANOVIĆ[5], DRAGIŠA S. MILOŠEV[5], BRANISLAV D. NEDELJKOVIĆ[6] and DRAGANA Đ. BJELIĆ[2]

[1]*Center for Small Grains of Kragujevac, Sava Kovacević St. 31, 34000 Kragujevac,* [2]*Institute of Field and Vegetable Crops, Maksim Gorki St. 30, 21000 Novi Sad,* [3]*Faculty of Agriculture, University of Kosovska Mitrovica, Jelene Anžujske bb, Zubin Potok 38228,* [4]*Department of Chemistry, Faculty of Science, University of Kragujevac, Radoje Domanović St. 12, 34000 Kragujevac,* [5]*Faculty of Agriculture, University of Novi Sad, Dositej Obradović St. 8, 21000 Novi Sad and* [6]*Zastava Car Factory, Trg Topolivaca 4, 34000 Kragujevac, Serbia*

Abstract: Soil samples taken from the Ap horizont of arable land and meadows at ten different localities were analyzed for different forms of manganese, including total (HF), pseudo-total (HNO_3), 0.1 M HCl-extractable and diethylentriaminepentaacetic acid (DTPA)-extractable. A sequential fractional procedure was used for Mn portioning into fractions: water soluble and exchangeable Mn (I), specifically adsorbed Mn with carbonates (II), reductant releasable Mn in oxides (III), Mn bonded with organic matter (IV) and Mn structurally bonded in silicates (residual fraction) (V). Serbian vertisols have a normal Mn content, comparable with similar soils. The total (HF) and pseudo-total (HNO_3) Mn contents were not correlated with soil properties, whereas the humus content positively influenced the 0.1 M HCl-extractable Mn in soil ($r = 0.49$). Soil pH and $CaCO_3$ ($r = 0.57$ and 0.43) showed significant negative correlations with the DTPA-extractable Mn, respectively. The different extraction methods showed similar patterns of Mn content in arable and meadow soils. The sequential fractional procedure showed that reductant releasable Mn occluded in oxides of Fe and Mn was the prevailing Mn fraction in soil, however, water soluble and exchangeable Mn and Mn bonded with organic matter had significant correlations with most of the examined soil characteristics. Potential Mn toxicity in vertisols could be observed under lower pH and saturated conditions.

Keywords: soil; manganese solubility; plant availability; adsorption; distribution of manganese.

INTRODUCTION

Being a multi-complex system, soil comprises mineral, organic, organic-mineral, liquid and gaseous phases and it possesses certain physical, chemical and biological properties. The original geologic substrate and subsequent geochemical and pedogenic impacts determine the total levels of micronutrients in soils. The total levels are rarely indicative of plant availability, because availability depends on soil pH, organic matter content, adsorptive surfaces, and other physical, chemical, and biological conditions in the rhizosphere.[1]

The accumulation of heavy metals in soils represents a potential risk to human health due to the transfer of these elements to aquatic media, their uptake by plants and their subsequent introduction into the food chain. Chemical fractionation schemes for partitioning trace metals in soils and sediments have been used extensively since the 1970s and are based on three to six fractions,[2–5] many of them being slightly modified Tessier's schemes.[2] Chemical extraction is employed to assess operationally defined metal fractions, which can be related to chemical species, as well as to potentially mobile, bioavailable or ecotoxic phases of a sample. The sequential extraction procedure for environmental studies provides an important tool for the determination of the different chemical forms or ways of binding between trace metals and soil components.[6] It is generally accepted that the ecological effects of metals (*e.g.*, their bioavailability, ecotoxicology and risk of groundwater contamination) are related to their mobile fractions rather than to the total concentrations.[7] Sequential extraction was confirmed as a convenient method for the investigation of heavy metals in agro–ecological conditions.[8]

Manganese (Mn) is an essential micronutrient for plant growth. Through its involvement in various enzymes and other physiologically active molecules, this micronutrient affects the gene expression, biosynthesis of proteins, nucleic acids, growth substances, chlorophyll and secondary metabolites, metabolism of carbohydrates and lipids, stress tolerance,[9] *etc.* of plants. Mn oxides are not only an important solid phase component of soil micronutrients, but also play an important role in the redistribution of micronutrients in soils. Changes in the redox status and consequent transformation of mineral forms of Mn act as an important driving force for the redistribution of trace elements and other heavy metals in soils.[10] Patrick and Jugsujinda,[11] and Han and Banin[12] found significant transformations and redistribution of heavy metals among the solid-phase components in soils due to the redistribution of Mn during incubation under a saturated regime. High values of Mn are usually attributed to the presence of Mn-oxides concentrations due to locally reduced conditions.[13] Therefore, proper land use, *i.e.*, cropped soil, permanent crops or meadows, can strongly influence the soil moisture regime.

The aim of this study was to assess the distribution and forms of manganese occurring in vertisol soils under the environmental conditions of Serbia using different extraction methods and a sequential extraction procedure.

EXPERIMENTAL

Samples of the Ap horizon of vertisol soil were taken from the following ten locations in Serbia: 1) Milutovac, 2) Priština, 3) Trnava, 4) Rekovac, 5) Vranje (Neradovac), 6) Zaječar, 7) Bela Crkva, 8) Blace, 9) Salaš and 10) Kragujevac (Fig. 1). Sub-samples were taken from field and meadow ecosystems, from a depth of 0 to 20 cm, after which they were air-dried and crushed in a porcelain mortar to particles of 2 mm in size. A stainless steel screen was used in the preparation for characterization and Mn-fraction analyses.

Fig. 1. Geographical location of the investigated soil samples in the Republic of Serbia.

Determination of the soil characteristics

Soil pH was determined in a suspension with water and 1 M KCl mixture, with the ratio of soil:solution 1:2.5 after a 30-min equilibration period; the organic content was determined using the humus method of Kotzmann,[14] the available P_2O_5 and K_2O contents were determined by the AL method of Egner–Riehm.[15] Cation exchange capacity (*CEC*) was determined using the method with 1 M NH_4OAc, pH 7, and the particle size distribution was determined

by a pipette method.[16–17] The total manganese was determined by atomic adsorption spectro-photometry (AAS, Carl Zeis Jena, model AAS 1N). The cold extraction method was used for the determination of the total and pseudo-total manganese where 0.5±0.001 g of sample was transferred into a centrifuge tube, and then 10 cm^3 of 0.5 M HCl were added. The solution was shaken and centrifuged for a short time and then placed on a shaking-table and agitated for 1 h. After agitation, the solutions were centrifuged at 3000 rpm (1,900×g) for 15 min, and then filtered through a 0.45-μm syringe filter to remove particulates.

Sequential fractional procedures

Manganese (Mn) in different soil fractions was extracted using the procedure proposed by Tessier *et al.*[2] The methods used for the fractionation procedure are outlined below.

1. Water soluble and exchangeable Mn was determined by extraction with 0.1 M CaCl$_2$ (pH 7.0); 10 g of soil were agitated in plastic pots with 100 cm^3 of solution for 20 min and then filtered.

2. Specifically adsorbed Mn and Mn bonded with carbonates were determined utilizing extraction with 1 M NaOAc (pH 5.0). Again, 10 g of soil were added to 100 cm^3 of solution, and agitated for 5 h at room temperature and then filtered. In this case, the sum of 1. and 2. was calculated and the value of fraction 2 was obtained by subtraction.

3. Reductant releasable Mn occluded in Fe and Mn oxides was determined in the 2.5 mg of soil placed in a centrifuge tube. After extraction of fractions 1. and 2., 50 cm^3 of 0.04 M hydroxylamine hydrochloride were added (in 25 % HOAc, pH 3). The tubes were then kept in a water bath for 6 h at 85 °C under stirring. Subsequently, the total volume of 50 cm^3 was attained by adding distilled water, and the tubes were closed, agitated for 10 min, and centrifuged for 10 min at 3000 rpm. The clear supernatant was removed from the reagent bottles and the remains of the soil were rinsed with 20 cm^3 of distilled water.

4. Mn bonded with organic matter was determined in the following way: 7.5 cm^3 of 0.02 M HNO$_3$ and 12.5 ml of H$_2$O$_2$ pH 2.0 were added to the centrifuge tubes with the soil remaining from the previous three extractions. The tubes were kept in a water bath at 86 °C for 2 h and then stirred. After cooling, 7.5 cm^3 of 30 % H$_2$O$_2$ were added and again the suspension was kept at 86 °C for 3 h. After cooling, 12.5 cm^3 of 3.2 M NH$_4$OAc in 20 % HNO$_3$ were added. The final volume was set by adding distilled water and then the tubes were closed. They were then shaken for 30 min and centrifuged for 10 min at 3000 rpm. The resulting clear supernatant was transferred to reagent bottles.

5. Mn structurally bonded in silicates (residual fraction) was determined by calculating the difference between the total content determined with HNO$_3$–HF–HClO$_4$ and the sum of the first four fractions.

The total Mn content was determined by destructing the samples with a mixture of the acids HNO$_3$, HClO$_4$ and HF. Through this procedure, all the forms of Mn present in the soil were transferred into solution. The pseudo-total content of the Mn was obtained by application of concentrated HNO$_3$ and H$_2$O$_2$.[18–20]

The distribution of manganese in various chemical fractions (1.–4.) was determined by flame atomic absorption spectrometry (AAS).

Statistical analysis

The results obtained for the different contents of manganese (total, accessible and different chemical fractions) in the vertisol samples were statistically processed by the Student's *t*-test and Pearson correlation coefficients.[21]

RESULTS AND DISCUSSION

Basic soil characteristics of the investigated vertisols are given in Table I. The vertisols showed marked heterogeneity in terms of pH. Most of the studied soil samples were acid to slightly alkaline. In terms of the content of readily available phosphorus, the selected samples belonged to the class of soils with a low P availability, but the observed levels of P_2O_5 varied widely among the samples: from 0.6–28.0 mg 100 g^{-1} soil in the samples from cultivated fields to 0.8–17.8 mg 100 g^{-1} soil in the samples from meadows. The investigated soils showed a moderate to high content of available K_2O. The selected sampling sites also differed in the humus concentration with an average range from 3.3 % (field) to 3.5 % (meadow) and with a high capacity for cation adsorption, ranging from 15.5 to 34.7 meq per 100 g soil.

TABLE I. Examined physical-chemical characteristics of vertisol in Serbia (mean, standard deviation and range)

Soil characteristic	Field			Meadow		
	Mean	Range	Standard deviation	Mean	Range	Standard deviation
pH (H_2O)	7.1	5.8–8.1	0.9	6.9	5.6–8.1	0.9
pH (KCl)	6.0	4.6–6.9	0.9	5.8	4.7–7.0	0.9
Humus content, %	3.3	2.5–4.0	0.5	3.5	2.0–5.6	1.1
P_2O_5 content, mg 100g^{-1}	7.7	0.6–28.0	8.5	4.2	0.8–17.8	5.0
K_2O content, mg 100g^{-1}	34.4	19.0–59.6	11.8	31.1	20.4–53.5	10.4
CEC, m.e 100g^{-1}	25.1	15.5–31.5	5.6	23.8	16.9–34.7	6.6
Sand content, %	29.6	21.4–36.0	4.8	32.2	22.3–50.5	9.0
Silt content, %	24.6	18.8–31.2	3.6	22.8	11.9–29.4	5.6
Clay content, %	45.8	33.5–54.4	7.2	44.9	28.9–64.3	11.1
Silt + clay content, %	70.4	64.0–78.6	4.8	67.7	49.5–77.7	9.0

The mean value of the total Mn content in the field and meadow vertisols amounted to 927 and 882 mg kg^{-1}, respectively (Table II). However, the examined samples showed high heterogeneity regarding the total Mn content.

TABLE II. Manganese content in the tested vertisols of Serbia determined using different extraction methods ($X\pm SD$ and interval, mg kg^{-1})

Location	HF	HNO_3	0.1 M Hcl	0.005 M dtpa
Field ($n = 10$)	927±311	850±306	117±17.1	52.5±21.7
	650–1675	550–1600	89.0–154.0	21.0–90.0
Meadow ($n = 10$)	882±252	803±286.5	113±32	59.8±22.2
	560–1460	500–1490	49–178	28.0–106.0
t-Test (field and meadow)	0.40[b]	0.35[b]	0.05[a]	0.74[b]

[a]The Student t-test showed that there a statistical significance between the examined characteristic of the field and meadow soil; [b]The Student t-test showed that there was no statistical significance between the examined characteristic of the field and meadow soil

The average values of Mn extraction from the samples of arable land, when mild extraction agents were used, were 117.0 mg kg^{-1} in 0.1 M HCl and 52.5 mg kg^{-1} in 0.005 M diethylentriaminepentaacetic acid (DTPA), indicating that the soils were sufficiently provided with this element. The high values of available Mn in the arable soil samples indicated a low strength of its binding with the solid soil phase. The meadow soil samples were also adequately supplied with readily available Mn, although the Mn concentrations found by 0.1 M HCl extraction (113 mg kg^{-1}) were slightly lower and by DTPA extraction (59.8 mg kg^{-1}) slightly higher compared with the corresponding values found for the arable vertisols. Thus, a solution of 0.1 M HCl extracted twice the amount of Mn extracted by a DTPA solution.

On average, about 91 % of the total content of Mn in vertisols from arable land and meadows was extracted with HNO$_3$ (pseudo-total content), *i.e.*, 850 and 803 mg kg^{-1}, respectively (Table III). Conversely, 0.1 M HCl extracted about 13.5 % of the total content of Mn in vertisol from the arable and the meadow samples. The relative values of the individual Mn extractions with 0.1 M HCl solution, between the two land uses, varied over a wide range (7.6–16.5 % from the arable soil samples and 5.8–21.7 % from the meadow samples).

The average relative values of Mn extracted with DTPA were 5.6 (arable soil) and 7.4 % (meadow). The individual values varied widely and were related to the soil pH. The highest relative amount of DTPA-extractable Mn was extracted from the soil with the lowest pH value. The extraction with 0.1 M HCl and DTPA 0.005 extracted much greater amounts of Mn (2–3 times more) from the arable land samples 7 and 10.

These results are in agreement with a number of previous observations.[22] Han and Banin[23] reported that Mn in arid-zone soils was mainly in the easily reducible oxide-bound fraction and it redistributed into the carbonate-bound and soluble plus exchangeable fractions after a year of water saturation. The EDTA-extractable Mn in savanna soils ranges from 13 to 54 mg kg^{-1} soil, which is far greater than the 1.0 mg kg^{-1} considered critical for most soils, suggesting that savanna soils have adequate reserves of available Mn.[24]

Generally, the contents of total and readily available Mn in the analyzed vertisols were not dependent on the properties of the investigated soils. However, this finding was not confirmed for Indian vertisols, where the total Mn was negatively correlated with coarse clay and silt but positively correlated with fine clay. Contrary to this, the DTPA-available form of Mn was negatively correlated with pH (r = –0.55 and –0.57) and the CaCO$_3$ content (–0.43). Similar results for DTPA-Mn were presented by Verma *et al.*[25] and for Indian vertisols.[26] From this association, it can be inferred that the addition of organic matter increases the availability of Mn and, as the soil become coarser, Mn deficiency becomes a problem.[27] Manganese extracted with 0.1 M KCl is positively correlated with the

humus content ($r = 0.49$). Bloom[28] reported that Mn^{2+} formed outer-sphere complexes (non-specific sorption) with the carboxyl groups of the soil organic matter (SOM); this mechanism explains the weak association of Mn with the soil organic matter. The Mn content in soil showed no relation with the soil texture of the investtigated vertisols. Some studies also found that Mn movement is independent of clays, as shown by the weak correlation between Mn and the clay distribution in soils.[29,30]

TABLE III. The relative content of manganese in different extraction agents (in % of HF-total)

Locality	Extraction method			
	HF	HNO$_3$	0.1 M HCl	0.005 m dtpa
Field				
Milutovac	720	81.9	14.4	3.8
Priština	1675	95.5	7.6	5.0
Trnava	778	99.6	14.0	4.6
Rekovac	780	83.3	13.7	5.1
Vranje	740	94.6	16.5	3.9
Zaječar	760	97.4	15.5	7.0
Bela Crkva	650	84.6	13.7	7.1
Blace	1020	97.0	11.8	5.4
Salaš	950	96.3	12.5	6.8
Kragujevac	1200	82.9	12.8	7.5
X	927	91.3	13.3	5.6
Meadow				
Milutovac	813	87.9	14.4	7.4
Priština	1460	102.0	9.0	4.1
Trnava	1041	86.9	11.5	6.4
Rekovac	764	85.7	15.8	6.8
Vranje	800	93.8	13.6	5.6
Zaječar	620	80.6	15.3	7.4
Bela Crkva	560	88.4	21.2	15.2
Blace	995	97.0	9.5	4.9
Salaš	900	99.4	5.8	3.3
Kragujevac	820	86.6	21.7	12.9
X	877.3	90.8	13.8	7.4

Sequential extraction analysis

Considering that the tested vertisols from Serbia were established at locations with manganese deficiency in the parent material, sequential extraction enabled the determination the form of its presence in the soil, allowing a clear understanding of its potential mobility and accessibility to plants. The Mn distribution among the various chemical fractions of the examined vertisols showed that Mn was predominantly located in the fraction of oxides of Fe and Mn(III). Its presence in this fraction was 56.4 % of its total content in the meadow vertisols and 54.2 % in the arable soils. Similar Mn values in the fraction of metals

associated with Fe and Mn oxides were found by other authors. Sims *et al.*[31] found that the reduced fraction contained approximately 45 % of the total content of Mn, and Maria Isabel *et al.*[32] found 33.1 % in oxide-bound phase according to a modified Tessier procedure and 48.9 % according to Community Bureau of Reference Protocol for Spanish Soils. The high content of extractable Mn in this fraction was derived from the fixed Mn and Mn coupled with oxides (MnO and MnO_2).[2] The individual samples from the fields and meadows showed a marked heterogeneity in terms of the Mn content in this fraction, which could be explained by the fact that the content of Mn in this fraction occurs in samples with larger Mn contents.

The fraction of specifically adsorbed Mn and Mn bound to carbonates (II) was the second largest Mn pool. In the arable soil samples, this fraction accounted for 13.7 % of the total Mn content, while in the meadow vertisols, the value was 15.45 %. The higher relative content of Mn in the meadow samples might indicate that the Mn in the arable soils could have a stronger association to the solid phase of the soil, despite its higher content. This finding was confirmed by the fact that the relative content of Mn in the arable soils was significantly lower in the exchangeable fraction of adsorbed metal (fraction I), which leads to weak associations with the soluble part of the total Mn, which is directly accessible to plants. In addition, the extracted amount of Mn and its relative prevalence in this fraction, in individual samples, varied over a wide range, which were significantly higher in samples of the arable soils (9.7–28.4 %) compared with the meadow soil. It was also found that the largest amounts of Mn were extracted from samples with the highest total content. Contrary to the above, the samples with the highest total contents of Mn had lower values of relative Mn abundance, indicating that the increase in the total Mn content reduces its percentage in the fractions of specifically adsorbed Mn and Mn bonded to carbonates. Based on those findings, it could be assumed that the potential availability of Mn is determined by specific soil properties and less by its total content.

In the arable vertisols, the relative content of Mn in the organic (IV) fraction averaged 13.2 %, while in the meadow vertisols, the average was 12.8 %. Similar differences were observed for the Mn content in the third fraction. These differences probably derived from the chemical and mineralogical properties of the individual soil samples and, similarly, the lowest soil pH values led to the least amount of organically bound Mn. Another observation was that the samples with the highest relative content of organically bound Mn were the highest in K_2O, the texture clay fraction and the *CEC*. This could be explained by the fact that the complexes of organic matter with Mn can be easily adsorbed to the clay particles of soil, which affects the content of organically bound Mn. The positive relationship between the organic bound Mn and the available potassium is probably due to their appearance in the same forms of bonds, since the investigated vertisols

had sufficient clay contents, which explains the considerable amount of potassium in the soil.

The fraction of exchangeable adsorbed metal (fraction I) was relatively high in Mn (3.7 % of the total content of Mn) in the arable land samples (35.9 mg kg^{-1}) and 5.6 % of the total Mn content in the meadow samples (42.3 mg kg^{-1}). This fraction is dependent on soil pH, content of K$_2$O, clay (*CEC*), silt and CaCO$_3$, respectively.

The *t*-test found no significant differences between the respective chemical fractions for both uses of the vertisols, indicating the same geochemical origin of the soils at the examined locations and no effects of cropping technology on the distribution of Mn among the different fractions.

Positive correlation coefficients for the Mn content were found between fractions I and II, III and IV, III and the total content and IV and the total content, whereas negative correlations were observed between fractions I and IV, II and IV and the total content (Table IV). The negative correlation between the content of Mn in fractions I and IV indicates that the increase of Mn in the organic matter (fraction IV) was a result of the high complexation of Mn and its decrease in the soluble fractions. The results also showed that all of the stable fractions (II, III and IV) were correlated with the total Mn, but not with the residual fraction. Medium to high correlations ($r = -0.51$ and 0.96) were observed between total Mn and Mn in fractions II–IV. The coefficients indicate that the individual forms of Mn were in a state of dynamic equilibrium.

TABLE IV. Correlation coefficient between the manganese content in different chemical fractions in the soil from fields and meadows

Fraction	I	II	III	IV	V	Mn content total (HF)
I	1.00					
II	0.52[a]	1.00				
III	NS[b]	NS	1.00			
IV	–0.61[c]	NS	0.57[c]	1.00		
V	NS	–0.51[c]	NS	NS	1.00	
Mn content total	NS	–0.46	0.96[c]	0.53[a]	NS	1.00

[a]Statistically significant at the probability level of 0.05; [b]there is no statistical significance, [c]statistically significant at the probability level of 0.01

The correlation coefficients between the Mn content in different chemical fractions and selected soil properties are presented in Table V. The analysis showed that the content of Mn in fraction I decreased significantly (–0.49 and –0.90) as the soil pH and the contents of clay (*CEC*), K$_2$O and CaCO$_3$ increased. Conversely, plots with high values of silt had an increased Mn content in fraction I ($r = 0.52$).

The high negative correlation coefficients between the content of Mn in the first fraction and soil properties, such as pH, clay content (*CEC*) and K$_2$O, in-

dicated that these soil properties had a dominant influence on the distribution of Mn in this fraction. When the pH value of the soil is high, Mn is less soluble due to the oxidation process that occurs in an alkaline reaction and the transition of Mn oxides into the more inaccessible forms. As the clay content and pH influence the *CEC* to a large extent, the increase of *CEC* strengthens the bond between cations (Mn) and the solid phase of soil, which reduces the mobility and solubility of Mn in this fraction.

TABLE V. Correlation coefficient between the manganese content in different chemical fractions and some soil characteristics

Soil characteristic	Fraction					
	I	II	III	IV	V	Mn content total
pH (H$_2$O)	–0.90[a]	NS[b]	NS	0.71[a]	NS	NS
pH (nKCl)	–0.90[a]	NS	NS	0.70[a]	NS	NS
Humus content	NS	NS	NS	NS	–0.46[c]	NS
P$_2$O$_5$	NS	NS	NS	NS	NS	NS
K$_2$O	–0.60[a]	NS	NS	0.57[a]	NS	NS
CEC	–0.64[a]	NS	NS	0.76[a]	NS	NS
Sand	NS	NS	NS	–0.61[a]	NS	NS
Silt	0.52[c]	NS	NS	–0.61[a]	NS	NS
Clay	–0.49[a]	NS	NS	0.79[a]	NS	NS
Silt + clay	NS	NS	NS	0.61[a]	NS	NS

[a]Statistically significant at the probability level of 0.01; [b]there is no statistical significance; [c]statistically significant at the probability level of 0.05

The positive correlation between the Mn content in fraction I and silt is caused by weaker bond strengths between the silt and Mn, since silt particles are coarse and positioned at the junction between sand and clay. It could be assumed that the solubility of Mn (fraction I) is higher in soil with a coarser texture than clay soil with a similar total content of Mn. Specifically adsorbed Mn and Mn bound to carbonates (fraction II) and Mn bound to oxides (fraction I) were not significantly correlated with any of the studied soil properties (Table V).

The amounts of Mn extracted from the organic fraction (IV) had significantly high positive correlations with soil pH, clay (*CEC*) and K$_2$O (from 0.57 to 0.79), and negative correlations with coarse soil particles (silt and sand). The high and positive correlation of Mn in the organic fraction and clay showed that most of the Mn was associated with clay organic matter. Therefore increasing the content of fine particles (clay with organic matter) results in increases in the free surface, and therefore the *CEC*, as well as bond strength compared to the coarser particles (silt and sand).

The positive correlation ($r = 0.70$ and 0.71) between soil pH and Mn content in the organic fraction indicates that the pH had a positive effect on the Mn con-

tent in the organic fraction. These results are similar to the results of other authors.[25,33–35]

Based on the correlation coefficients shown in Table VI, it was found that the applied extraction techniques extracted significantly higher amounts of dissolved Mn compared with the amounts that plants could adopt. With 0.005 M DTPA and 0.1 M HCl addition, besides the water-soluble + exchangeable amounts of Mn, specifically adsorbed forms also dissolve. HF and HNO_3 dissolve metals that are bound with much stronger bonds (fraction II–V). These metals are not accessible to plants and, therefore, this method cannot be used as an indicator of Mn accessibility to plants. The availability of micronutrients to crops is controlled by many soil factors, such as pH, soil organic matter, temperature and moisture.[36–37] Increased microbial activity can also result in a decrease in the oxidation–reduction potential of the soil, increasing Mn availability; consequently, manganese (II) forms only relatively weak bounds with organic ligands.[38] According to Fageria *et al.*, the main ionic Mn species in a soil solution is Mn^{2+}, and its concentrations decrease 100-fold per unit increase in soil pH.[37] This is in agreement with the results obtained in other studies on Brazilian soils.[37,39]

TABLE VI. The correlation coefficients between the content of manganese in different chemical fractions of soil and its contents obtained by using different extraction procedures

Extraction procedure	Fraction				
	I	II	III	IV	V
HF	NS[a]	0.512[b]	0.959[c]	0.534[b]	NS
HNO_3	NS	0.443[b]	0.966[c]	0.572[c]	NS
0.1 M HCl	0.516[b]	0.703[c]	NS	NS	NS
0.005 M DTPA	0.786[c]	0.882[c]	NS	NS	NS

[a]There is no statistical significance; [b]statistically significant at the probability level of 0.05; [c]statistically significant at the probability level of 0.01

CONCLUSIONS

The contents of Mn (total and pseudo-total) were found to be similar in the samples of field and meadow vertisols and to have similar levels as the average values determined in other studies. The extraction of Mn with NHO_3 produced values similar to the real total content (about 90 %). The availability of Mn (DTPA–Mn) depends on the pH value and $CaCO_3$ content, since negative correlations were observed. Reductant releasable Mn occluded in the oxides of Fe and Mn was found to be the most abundant fraction of Mn according to sequential extraction procedures, however, the Mn bonded with organic matter had significant correlations with most of the examined soil properties. Mn availability in soil could be controlled by appropriate water regime and management practices that modify the pH value of soil.

И З В О Д

ДИСТРИБУЦИЈА И ФОРМЕ МАНГАНА У ВЕРТИСОЛИМА СРБИЈЕ

ЈЕЛЕНА Ж. МИЛИВОЈЕВИЋ[1], ИВИЦА Г. ЂАЛОВИЋ[2], МИОДРАГ Ж. ЈЕЛИЋ[3], СРЕЋКО Р. ТРИФУНОВИЋ[4], ДАРИНКА М. БОГДАНОВИЋ[5], ДРАГИША С. МИЛОШЕВ[5], БРАНИСЛАВ Д. НЕДЕЉКОВИЋ[6] и ДРАГАНА Ђ. БЈЕЛИЋ[2]

[1]*Ценѣар за сѣрна жиѣа, Саве Ковачевића 31, 34000 Краѓујевац,* [2]*Инсѣиѣуѣ за раѣарсѣво и йоврѣарсѣво, Максима Горкоѓ 30, 2100, Нови Сад,* [3]*Пољойривредни факулѣеѣ, Универзиѣеѣ у Косовској Миѣровици, Јелене Анжујске бб, 38228 Зубин Поѣок,* [4]*Инсѣиѣуѣ за хемију, Природно–маѣемаѣички факулѣеѣ, Универзиѣеѣ у Краѓујевцу, Радоја Домановића 12, 34000 Краѓујевац,* [5]*Пољойривредни факулѣеѣ, Универзиѣеѣ у Новом Саду, Досиѣеја Обрадовића 8, 21 000 Нови Сад и* [6]*Фабрика ауѣомобила Краѓујевац, Трѓ Тойоливаца 4, 34 000 Краѓујевац*

У циљу одређивања различитих облика мангана у вертисолима са подручја Србије (оранице и ливаде) пореклом са десет различитих локалитета анализиран је укупан садржај мангана (HF), псеудо-укупан садржај (HNO₃), 0,1 M HCl растворљив и DTPA растворљив манган. Секвенцијалном екстракцијом извршено је раздвајање фракција мангана на раствор-љив у води и размењив манган (I), специфично адсорбован са карбонатима (II), оклудован у оксидима (III), манган везан за органску материју (IV) и манган структурно везан у сили-катима (резидуални део) (V). Садржај мангана у анализираном земљишту (вертисол) поређен је са добијеним резултатима на сличним земљиштима. Укупан садржај мангана (HF) и псеу-до-укупан садржај (HNO₃) нису били у корелацији са испитиваним својствима земљишта, док је садржај хумуса позитивно утицао на 0,1 M HCl растворљив манган (*r* = 0,49). Земљишни pH и CaCO₃ (*r* = 0,57 и 0,43) су показали високо значајну негативну корелацију са DTPA растворљивим манганом. Различита екстракциона средства су испољила сличан ефе-кат на садржај Mn у обрадивом земљишту и ливадама. Секвенциона екстракциона анализа је показала да манган оклудован у оксидима чини процентуално највећу фракцију у земљишту, истовремено постоје статистички значајне корелације између мангана растворљивог у води и мангана везаног за органску материју и већине својстава земљишта. Потенцијал екотокси-чности мангана се може испољити само у случајевима ниске pH вредности земљишта и по-јаве засићања земљишта са водом.

(Примљено 29. децембра 2010, ревидирано 12. априла 2011)

REFERENCES

1. A. Kabata-Pendias, A. Pendias, *Trace elements in soils and plants*, 2nd ed., CRC press, Boca Raton, FL, USA, 2001
2. A. Tessier, P. G. C. Campbell, M. Bisson, *Anal. Chem.* **51** (1979) 844
3. C. Ianni, N. Ruggieri, P. Rivaro, R. Frache, *Anal. Sci.* **17** (2001) 1273
4. F. X. Han, A. Banin, W. L. Kingery, G. B. Triplett, L. X. Zhou, S. J. Zheng, W. X Ding, *Adv. Environ. Res.* **8** (2003) 113
5. J. T. Hlavay, M. Prohaska, W. Weisz, G. Wenzel, J. Stingeder, *Pure Appl. Chem.* **76** (2004) 415
6. G. J. Rauret, F. Lopez–Sanchez, A. Sahuquillo, R. Rubio, C. Davidson, A. Ure, P. Que-vauviller, *J. Environ. Monit.* **1** (1999) 57

7. E. Cordos, R. Rautiu, C. Roman, M. Ponta, T. Frentiu, A. Sarkany, L. Fodorpataki, K. Macalik, C. McCormick, D. Weiss, *Eur. J. Miner. Process. Environ. Prot.* **3** (2003) 324
8. Dj. Petrović, M. Todorović, D. Manojlović, V. D. Krsmanović, *J. Serb. Chem. Soc.* **75** (2010) 1005
9. Z. Rengel, in *Nutrient Cycling in Terrestrial Ecosystems*, P. Marschner, Z. Rengel, Eds., Springer-Verlag, Heidelberg, 2007, p. 121
10. F. X. Han, A. Banin, *Commun. Soil Sci. Plant Anal*. **31** (2000) 943
11. W. H. Patrick Jr., A. Jugsujinda, *Soil Sci. Soc. Am. J.* **56** (1992) 1071
12. F. X. Han, A. Banin, W. L. Kingery, G. B. Triplett, L. X. Zhou, S. J. Zheng, W. X. Ding, *AES BIOFLUX* **8** (2003) 113
13. C. S. Aydinalp, S. Marinova, *Polish J. Environ. Stud.* **12** (2003) 629
14. M. Jakovljevic, M. Pantovic, S. Blagojevic, *Laboratory Manual of Soil and Water Chemistry*, Faculty of Agriculture, Belgrade, 1995, p. 57 (in Serbian)
15. A. M. Ure, in *Heavy metals in soils*, 2nd ed., B. J. Allovay, ed., Blackie Academic & Professional, Glasgow, UK, 1995, p. 58
16. USDA-NRCS, *Soil survey laboratory methods manual*, Soil Survey Investigation Report 42, ver. 3.0, National Soil Survey Center, Lincoln, NE, USA, 1996
17. JDPZ, *Soil survey laboratory methods manual*, Book 5, Belgrade, 1997 (in Serbian)
18. D. C. Martens, W. L. Lindsay, in *Soil Testing and Plant Analysis*, 3rd ed., Soil Science Society of America, Madison, WI, USA, 1980
19. R. J. Haynes, *J. Agric. Sci*. **129** (1997) 325
20. J. J. Wang, D. L. Harrell, R. E. Henderson, P. F. Bell, *Commun. Soil Sci. Plant Anal*. **35** (2004) 145
21. R Mead, R. N. Curnow, A. M. Hasted, *Statistical methods in agriculture and experimental biology*, Chapman & Hall, London, 1996, p. 410
22. B. Li, Q. Wang, B. Huang, S. Li, *Anal. Sci*. **17** (2001) 1561
23. F. X. Han, A. Banin, *Soil Sci. Soc. Am. J*. **60** (1996) 1072
24. W. L. Lindsay, W. L. Norvell, *Soil Sci. Soc. Am. J*. **42** (1978) 421
25. V. K. Verma, R. K. Setia, P. K. Sharma, C. Singh, A. Kumar, *Int. J. Agric. Biol*. **7** (2005) 243
26. B. D. Sharma, S. S. Mukhopadhyay, J. C. Katyal, *Commun. Soil Sci. Plant Anal*. **37** (2006) 653
27. V. K. Nayyar, U. S. Sadana, P. N. Takkar, *Fertil. News* **8** (1985) 173
28. V. P. R. Bloom, *Chemistry in the Soil Environment, ASA Special Publication 40*, Soil Science Society of America, Madison, WI, USA, 1983, p. 129
29. A. Swarup, S. Anand, *Fertil. News* **34** (1989) 21
30. F. X. Han, W. L. Kingery, J. E. Hargreaves, T. W. Walker, *Geoderma* **142** (2007) 96
31. J. L. Sims, I. W. H. Patrich, *Soil Sci. Soc. Am. J*. **42** (1978) 258
32. R. M. Isabel, J. M. Alvarez, L. M. Lopez-Valdivia, A. Novillo, J. Obrador, *Soil Sci.* **174** (2009) 94
33. V. H. Nguyen, S. Vega, J. A. Silva, *Soil Sci. Soc. Am. J.* **65** (2001) 153
34. P. Polić, P. Pfendt, *J. Serb. Chem. Soc*. **61** (1996) 1001
35. M D. Marjanović, M. M. Vukčević, D. G. Antonović, S. Dimitrijević, Đ. M. Jovanović, M. N. Matavulj, M. Đ. Ristić, *J. Serb. Chem. Soc*. **74** (2009) 697
36. J. C. Katyal, B. D. Sharma, *Geoderma* **49** (1991) 165
37. N. K. Fageria, V. C. Baligar, R. B. Clark, *Adv. Agron.* **77** (2002) 185

38. H. Marschner, *Mineral nutrition of higher plants*, 2nd ed., Academic Press, San Diego, CA, USA, 1995
39. E. Vidal-Vázquez, R. Caridad-Cancela, M. M. Taboada-Castro, A. Páz–Donzález, C. A. Abreu, *Commun. Soil Sci. Plant Anal.* **36** (2005) 717.